Stony Brook University

Flow kinematics and dynamics controlling tracer movement and shallow-water wave propagation in the Hudson River

A Dissertation Presented

by

Jindong Wang

to

The Graduate School

in Partial Fulfillment of the

Requirements

for the Degree of

Doctor of Philosophy

in

Marine and Atmospheric Science

Stony Brook University

August 2012

Stony Brook University

The Graduate School

Jindong Wang

We, the dissertation committee for the above candidate for the

Doctor of Philosophy degree, hereby recommend

acceptance of this dissertation.

Robert E. Wilson – Dissertation Advisor
Associate Professor, School of Marine and Atmospheric Sciences

Dong-Ping Wang – Chairperson of Defense
Professor, **School of Marine and Atmospheric Sciences**

Malcolm J. Bowman
Professor, School of Marine and Atmospheric Sciences

Alan F. Blumberg
Professor
Civil, Environmental and Ocean Engineering, Stevens Institute of Technology

Robert J. Chant
Associate Professor
Institute of Marine and Coastal Sciences, Rutgers University

Frank Aikman
Chief of Marine Modeling and Analysis Programs
NOAA/NOS Coast Survey Development Laboratory

This dissertation is accepted by the Graduate School

Charles Taber
Interim Dean of the Graduate School

Abstract of the Dissertation

Flow kinematics and dynamics controlling tracer movement and shallow-water wave propagation in the Hudson River

by

Jindong Wang

Doctor of Philosophy

in

Marine and Atmospheric Science

Stony Brook University

2012

Analyses of ship borne ADCP, salinity and dye tracer data from a 2002 experiment in a reach of the lower Hudson Estuary emphasize the influence of bottom topography on halocline position within the water column and dye tracer movement relative to isohalines. Halocline slope and halocline position within the water column during both flood and ebb and their relationship to bottom topography and bottom friction are described in terms of both the quasi-steady two-layer frictional hydraulics and tidally generated internal waves. Hindcast simulations using ROMS for the same reach provide detailed description of 3D velocity field and salinity field to support the analyses. The spatially and temporally-varying vertical shear, strain rate and Richardson Number are estimated from both the observed and model data. The results indicate that halocline fluctuations and vertical tracer movement are significantly enhanced especially at the maximum ebb and flood and are closely related to strong vertical advection induced by the bottom valleys and hills. In addition, tracer dispersion is mainly controlled by vertical mixing

induced by strong current shear. Strong vertical mixing regions are present not only within the bottom boundary layer during flood but also at the upstream slope of the bottom valleys and hills during ebb and at the current frontal zone during the transition from ebb to flood. The model results also suggest that the sudden release of the internal wave leads to enhanced vertical mixing in the vicinity of the halocline during the transition from ebb to flood.

Analyses of extensive observations from ADCPs moored in the channel extending from the lower Hudson to the upper reaches near Troy reveal significant overtides and longitudinal variation in tidal amplitude and phase. The results show that the tides and overtides are strongly influenced by local topographic variations and the longitudinal position in the river dependent on the ratio of tidal wavelength to channel length. Analyses of water level observations from gauges distributed along the river from the Battery to Troy compliment the current observations. Mechanisms of overtide generation and tidal wave propagation are investigated by both one-dimensional model following Parker (1984) and two-dimensional ROMS model. Results emphasize the importance of nonlinear terms in over-tide generation, the influence of variations in channel depth and cross-section, and the importance of tidal wavelength to channel length. These results motivated further study of the interactions between storm surge, river pulse, and tide in the Hudson River. Hindcast simulations using both one-dimensional and two-dimensional models provide detailed description of water elevation and current throughout the Hudson River from the Battery to Troy to support the analyses. In addition, longitudinal variation in surge height and surge timing, and the effects of nonlinearity and channel morphology change on surge, will be discussed based on the model results in both a generic channel and the Hudson River.

Table of Contents

List of Figures

Chapter 2

List of Tables

Acknowledgments

I would like to thank my advisor, Dr. Robert E. Wilson, for his guidance, patience, support and encouragement during my research and study at Stony Brook University.

I would also like to thank my committee: Dr. Dong-Ping Wang, Dr. Malcolm J. Bowman, Dr. Alan F. Blumberg, Dr. Robert J. Chant, and Dr. Frank Aikman. Their thorough reviews of my dissertation and insightful comments and suggestions improved this work tremendously. Especially Dr. Robert J. Chant provided both dye tracer experiment data in the Hudson Estuary and very important suggestions.

Special thanks to Dr. Frank Aikman for offering me an excellent position in NOAA/National Ocean Service, which make it possible for me to continue my research and exploration in physical oceanography.

I thank Dr. Roger D. Flood for providing high-resolution bathymetry data and water level data at very important locations in the Hudson River. I also thank Dr. Charles N. Flagg for providing the multiprocessor computer, allowing me to do model simulations much faster.

I would like to acknowledge support from New York Sea Grant under award R/CE-30-NYCT to Dr. Robert E. Wilson. I also acknowledge New York State Foundation and U.S. EPA for their financial support of scholarship.

I thank the faculty at SoMAS for their inspiring teaching and help. In particular, I thank Dr. Kamazima Lwiza, Dr. Henry Bokuniewicz, Dr. Sultan Hameed, Dr. Brain Colle, and Dr. Marvin Geller. I also thank the staff at SoMAS for their generous assistance. Special thanks to Carol Dovi and Mark Lang.

I also thank my colleagues and friends for their help and friendship during my study at Stony Brook University. I particularly thank Yanluan Lin, Fanghua Xu, Peng Cheng, Younjoo Lee, Jianhua Hao, Yan Hao, Jun Wei, Xiaona Li, Xiaolin Li, Zhenrui Cao, Yuan Liu, Bingqi Cheng, Yanjuan Guo, Jie Gong, Owen Doherty, Joseph Ching, Dongming Yang, Ling Liu, Weilei Wang, Yigang Fang, Chunling Wang, Wenqian Xu, Jiuan Wei, Jianping Zhang, Wei Li, Wei Zhao, Jing Zhou, Zhijia Yuan, Yimin Mao, and Junyi Zhu.

Most of all, I would like to thank my family, especially my parents and my wife Xi Chen. Their love and support have been with me every step of my life and make me to be more than I can.

Chapter 1
Introduction

Analyses of ship borne ADCP, salinity and dye tracer concentration data from a 2002 experiment in the lower Hudson Estuary emphasize the influence of bottom topography on halocline position within the water column and tracer movement along isohalines. Chant et al. (2007) analyzed these data with a focus of bottom boundary layer entrainment during flood. In their analyses they applied scaling for bottom boundary layer structure during flood [Trowbridge, 1992] and ebb [Stacey and Ralston, 2005]. Geyer et al. (2008) analyzed these data to characterize longitudinal dispersion within the bottom boundary layer associated with the combined effects on vertical and lateral current shear. One of the objectives of the present study is to evaluate the processes by which fluid entrained into the bottom boundary layer during flood tide is detrained and injected into the halocline during ebb tide. Our hypothesis is that the injection of fluid into the halocline is controlled by vertical advection amplified by the bottom topographic features and the deformation associated with the vertical shear in the horizontal current.

Halocline slope and halocline position within the water column during both flood and ebb and their relationship to bottom topography and bottom friction are described in terms of both the quasi-steady two-layer frictional hydraulics [Lawrence, 1990; Chant and Wilson, 2000; Engel, 2009] and tidally generated internal waves [Hibiya, 1986; Wang, 2006]. The lower Hudson Estuary is highly stratified during the neap tide, which is suitable for the use of the quasi-steady two-layer frictional hydraulics to estimate the vertical displacement of the halocline, especially during the maximum ebb or flood. In addition, the halocline exhibits significant vertical excursions over the tidal cycle, leading to the formation of arrested lee waves over the bottom valleys and hills especially during the maximum ebb. The behavior of the internal waves

varies within a tidal cycle, leading to the significant changes in vertical mixing and vertical advection in the water column.

Hindcast simulations using ROMS for the same reach provide detailed description of three-dimensional velocity field and salinity field to support the analyses. Blumberg et al. (2004) and Warner et al. (2005) used ECOM and ROMS respectively to simulate the velocity and salinity fields in the lower Hudson River, providing very useful information to this study. In this study, we also used a new method combining the two-dimensional barotropic simulations with the three-dimensional baroclinic simulations. In order to get better estimates of water levels and currents at the open boundary, a two-dimensional barotropic model was implemented and validated in the Hudson River from the Battery, NY up to the Troy, NY. The output water levels and currents from the two-dimensional model provide the open boundary values for the three-dimensional baroclinic simulations. This method compensates the absence of the observed current data at the open boundary, leading to more stable and accurate three-dimensional baroclinic simulations.

Analyses of current observations from moored ADCPs in a lateral section in the lower Hudson Estuary reveal strong over-tide production. The M_4 harmonic shows a strong maximum in the vicinity of the halocline indicating the importance of baroclinic effects and tidal period variations in two layer flow, while the M_6 current shows a minimum in the vicinity of halocline. Analyses of extensive observations from ADCPs moored in the channel extending from the lower Hudson to the upper reaches near Troy reveal similar strong over-tides. The results show that the over-tides are strongly influenced by local topographic variations and the longitudinal position in the estuary dependent on the ratio of tidal wavelength to channel length. Analyses of water level observations from gauges distributed along the estuary from the Battery to Troy compliment the current observations. Mechanisms of over-tide generation and their spatial variation are modeled following Parker (1984). Results emphasize the importance of nonlinear terms in over-tide generation, the influence of variations in channel depth and cross-section, and the importance of tidal wavelength to channel length.

These results motivated further study of the interactions between storm surge, river pulse, and tide in the Hudson River. Analyses of the observed water level data during historical hurricanes emphasize the influence of surge-tide interaction on potential coastal flooding. Storm surge associated with tropical and extra-tropical cyclones is generated in the ocean and propagates across the continental shelf and into coastal waters, bays and estuaries. Storm surge can cause severe flooding and tremendous loss of life and property in coastal areas especially when its peak occurs at the time of a high tide. In addition, heavy precipitation associated with storms can lead to a river pulse resulting in a surge especially in the upstream reaches of an estuary. The river-pulse-induced surge can be superimposed by the surge propagating from the ocean, resulting in even more severe flooding. Longitudinal variation in surge height and surge timing, and the effects of nonlinearity and channel geometry change on surge are further investigated by use of Parker's model.

The dissertation is organized into an introductory chapter and three main chapters. Chapter 2 addresses the effects of bottom topography on halocline position, tracer movement and tidal period internal motion in the lower Hudson Estuary. In Chapter 3, the mechanisms of overtide generation and tidal wave propagation in the Hudson River are investigated by use of both one-dimensional model and two-dimensional ROMS model. Chapter 4 presents the interactions between storm surge, river pulse and tide in the Hudson River by use of the observations and the numerical experiments.

Chapter 2
Tracer movement and tidal period internal motion in the Hudson Estuary

Abstract

Analyses of ship borne ADCP, salinity and dye tracer concentration data from a 2002 experiment in a reach of the lower Hudson Estuary with strong bottom topography emphasize the influence of bottom topography on tidal variations in halocline position within the water column and the movement the dye tracer relative to isohalines. The halocline exhibits significant vertical excursions over the tidal cycle, leading to the formation of arrested lee waves over the bottom valleys and hills especially during the maximum ebb. The lee waves are then released when currents decelerate. Dyer tracer movement emphasizes the importance of vertical motion at bottom salinity fronts and injection into the halocline and movement along isohalines. Halocline slope and halocline position within the water column during both flood and ebb and their relationship to bottom topography and bottom friction are described in terms of both quasi-steady two-layer frictional hydraulics and transient tidally generated internal waves using hindcast ROMS simulations for the reach. The spatially and temporally-varying vertical shear, strain rate and Richardson Number are estimated from both the observed and modeled data. The results indicate that the enhanced halocline fluctuations and vertical tracer movement during the maximum ebb and flood and are closely related to strong vertical advection induced by the topographic features. In addition, tracer dispersion is mainly controlled by vertical mixing induced by strong current shear. Lee waves significantly enhance vertical shear and thereby vertical mixing in the bottom boundary layer at the upstream slope of the bottom valleys and hills during ebb. In addition, the model results also suggest that the sudden release of lee waves

leads to enhanced vertical mixing in the vicinity of the halocline during the transition from ebb to flood.

2.1 Objectives and Introduction

The objective of this chapter is to evaluate the bottom topographic effects on stratified tidal flow and tracer movement and the processes by which fluid entrained into the bottom boundary layer during flood tide is detrained and injected into the halocline during ebb tide.

Estuaries typically have complicated bottom topographic features like valleys and hills caused by dredging, piling-up, bedform erosion or sediment accumulation. The stratified tidal flow passes over and interacts with these features, leading to significant changes in local hydrodynamics [Baines, 1995]. When the bottom topographic features are relatively small in both horizontal and vertical scale and can only be seen as "rough bottom", turbulent mixing induced by tidal flow tends be intensified within the bottom boundary layer. But the halocline position would not change significantly. When the bottom topographic features reach as large as kilometers in horizontal scale and meters in vertical scale, the wave-like fluctuations of the halocline following these features are usually observed at the certain time period during the tidal cycle [Farmer and Smith, 1980; Kranenburg, 1991; Geyer and Nepf, 1996]. Topographic effects in stratified flow are important for better understanding estuarine transport and the related biogeochemical processes.

Analyses of ship borne ADCP, salinity and dye tracer data from a 2002 experiment in the lower Hudson Estuary emphasize the influence of bottom topography on halocline position within the water column and tracer movement along isohalines. Halocline slope and halocline position within the water column vary in time from ebb to flood. The halocline fluctuations coincide with the bottom topographic features, obviously seen from the longitudinal salinity structure especially when it is around the maximum ebb (Figure 2.2). Generally the halocline is depressed over a valley and is elevated over a hill. The vertical displacement of the halocline can reach as high as ~4 meters at the region with the mean depth of 16 meters. On the other hand, the halocline fluctuations tend to be straightened during the slack water. Correspondingly

the dye tracer movement shows different characteristics at different times during the tidal cycle. The dye tracer tends to move along isohalines, resulting in a tongue-like structure during the ebb. At the same time vertical fluctuations of the dye tracer also can be observed over the bottom topographic features. However, during the flood the dye tracer patch is confined by the halocline and be well-mixed within the bottom boundary layer. After a few tidal cycles, the dye tracer volume tends to be significantly dispersed and enlarged in both vertical and horizontal directions. The dye tracer movement also provides insights into the estuarine hydrodynamics from the Lagrangian perspective.

Chant et al. (2007) analyzed the dye experiment data with a focus of bottom boundary layer entrainment during flood. In their analyses they applied scaling for bottom boundary layer structure during flood [Trowbridge, 1992] and ebb [Stacey and Ralston, 2005]. Geyer et al. (2008) analyzed these data to characterize longitudinal dispersion within the bottom boundary layer associated with the combined effects on vertical and lateral current shear.

The stratified tidal flow over bottom topographic features can be analyzed from two aspects in terms of both the quasi-steady two-layer frictional hydraulics [Armi, 1986; Lawrence, 1990; Engel, 2009] and tidally generated internal waves [Hibiya, 1986; Wang, 2006]. The quasi-steady two-layer frictional hydraulics is based on combination of one-dimensional continuity and momentum equations under assumption of the quasi-steady ($\partial u / \partial t = 0$) two-layer flow. The composite Froude number composed of layer Froude numbers is introduced as criteria to describe the flow status (internally supercritical or subcritical). The halocline fluctuations represented by thinning or thickening of each layer can be related through hydraulic response to the longitudinal changes in channel geometry (bottom topography and cross-section area) and local bottom friction. Halocline fluctuations as hydraulic response are also shown to have significant effects on estuarine salt flux [Geyer and Nepf, 1996; Engel, 2009].

The halocline fluctuations also can be seen as tidally generated internal waves. As the tidal current accelerates and exceeds the first-mode internal wave speed, the internal waves are triggered and amplified over bottom topographic features. As the tidal flow reduces or reverses in the direction, the locally-generated internal wave may leave the topographic feature and begin

to propagate, evolving into a train of internal solitary waves. Farmer and Smith (1980) obtained in situ evidence of halocline fluctuations by use of acoustic echo-sounding systems and explained halocline fluctuations as quasi-steady lee waves. Hibiya (1986) explained halocline fluctuations as transient internal waves generated in response to a time-varying tidal flow by using analytical ray-tracing method. Wang (2006) simulated the internal wave generation in a generic partially mixed estuarine environment by use of a three-dimensional model POM and confirmed the time-evolving characteristics of the internal wave for tidal flow over bottom topographic features.

In this study, both the quasi-steady two-layer frictional hydraulics and the tidally generated internal waves will be used to analyze the observed data from a 2002 dye experiment in the lower Hudson. The effect of halocline fluctuations on tracer movement will also be discussed. In order to further investigate the mechanisms of halocline fluctuations, we also calculated the horizontal velocity gradient and estimated the strain rate. Hindcast simulations using three-dimensional model ROMS for the reach provide detailed description for the 3D velocity field and salinity field to support the analyses. The chapter is organized as follows. The dye experiment and data processing are described in section 2.2. The analyzing results of the observed data are discussed in section 2.3. The ROMS model setup is described in section 2.4. The skill assessment and the 3D model results are analyzed in section 2.5. Quasi-steady two-layer hydraulics and the relationship between internal waves and vertical mixing are discussed in section 2.6. This chapter is summarized in 2.7.

2.2 Dye tracer experiments and data processing

The dye experiments were carried out in the Hudson River Estuary in May 2002 [Chant et al., 2007; Geyer et al., 2008; Lerczak et al., 2006]. The segment of channel for the dye study was located north to the George Washington Bridge, relatively straight and uniform in the along-channel direction (Figure 2.1). Tidal currents induced by a progressive tidal wave can reach approximately 1 m/s. The surface and bottom salinity difference is approximately 5 psu during the spring tide and 15 psu during the neap tide. River discharge during the experiments ranged from 500 m^3s^{-1} to 2000 m^3s^{-1}, with the mean value close to 800 m^3s^{-1}.

The dye experiments were complemented with the observed time series from April 22 to June 6, 2002 of velocity, salinity, and pressure by the use of moored instruments including four 1.2-MHz ADCPs, 12 Seabird CT sensors and 2 Paroscientific pressure sensors. The mooring time series cover in sequence strong spring tide, neap tide, weak spring tide, neap tide and strong spring tide [Chant et al., 2007]. The mooring array was deployed across the channel approximately 3 km north of the George Washington Bridge.

Four injections were conducted at different tidal phases. The first one was at the early ebb during the first neap tide. The second one was at the mid flood of the ending of the first neap tide. The third one was at the early ebb during the transition from the second neap tide to the second strong spring tide. And the fourth one was at the early flood during the second strong spring tide. For each of injections, ~44 kg of Fluorescein dye was diluted with ambient salt water in the Hudson River and then released at 2~3 m above the bottom of the deep channel on the eastern side of the river within approximately 15 minutes. In the end, an initial stripe of dye was produced, with approximately one meter in the vertical direction, several meters in the along-channel direction, and several hundreds of meters in the cross-channel direction. Following the injection, two boats were involved in surveying of the dye patch. Each boat was equipped with a 1200-KHz RDI ADCP (acoustic Doppler profiler) and a CTD (conductivity, temperature, depth recorder) with a Chelsea fluorometer. All the sensors were calibrated before the survey to mitigate the influence of the background fluorescence on estimating dye concentration. The two boats tracked the dye patch in the along-channel direction and in the cross-channel direction, respectively. The surveys were designed to get the three dimensional distribution of dye concentration, salinity and velocity within one or two tidal cycles.

The along-channel velocity, salinity and dye concentration observed in the longitudinal surveys were mainly used in this study. The along-channel velocity u was transformed from the original ADCP eastward velocity and northward velocity. The channel direction was mainly determined by following the direction of the thalweg of the lower Hudson reaches. It was assumed that the lateral variations were negligible for the longitudinal surveys mainly over the thalweg. The vertical strain rate $\partial w/\partial z$ was estimated by using the continuity equation

$\partial u/\partial x + \partial w/\partial z = 0$ in the x-z plane. In order to estimate the tendency of vertical mixing in the water column, the gradient Richardson numbers at the surveyed positions were calculated by using the formula

$$Ri = \frac{-(g/\rho)(\partial\rho/\partial z)}{(\partial u/\partial z)^2} \tag{2.1}$$

In order to estimate the effect of pressure gradient force on the water current and the related tracer movement in the water column, we did the following analysis. The pressure at a certain point z in the water column is estimated by integrating the salinity from z to the water surface, i.e.

$$p(x,z) = g\beta\int_z^\eta s(x,z)\,dz \tag{2.2}$$

where β is the saline contraction coefficient and η is the surface water elevation. Then the horizontal pressure gradient is estimated by

$$\frac{\partial p}{\partial x} = g\beta\frac{\partial\int_z^\eta s\,dz}{\partial x} \tag{2.3}$$

which includes both the barotropic pressure gradient $g\dfrac{\partial\eta}{\partial x}$ and the baroclinic pressure gradient. The barotropic pressure gradient cannot be directly estimated from the observed data since the water elevations were not measured during the ship surveys. The barotropic pressure gradient will be analyzed later based on the 3D model results. Thus only the baroclinic pressure gradient can be estimated based on the measured salinity profile. The measurement of salinity s in the water column at each of the surveyed positions is supposed to start at a common reference level z_r, which should be close to the water surface. Then the horizontal baroclinic pressure gradient can be estimated by discretizing (2.3) and neglecting the barotropic pressure gradient:

$$g\beta\Delta z\frac{\partial\sum_z^{z_r} s}{\partial x} \tag{2.4}$$

Neglecting the constant coefficient $g\beta\Delta z$, we call $\partial\sum_z^{z_r} s/\partial x$ as the baroclinic gradient. The baroclinic gradient values were then calculated at the longitudinally-surveyed positions for the following discussions.

2.3 Analyses of observations

The hydrodynamics in the lower Hudson Estuary show significant tidal variations from neap to spring and ebb to flood. The complicated bottom topography in the estuarine channel exerts additional significant influence on the estuarine processes. The water column is much more stratified during neap tide than spring tide. The ebb-flood asymmetry in the velocity and salinity fields is also more obvious during neap tide than spring tide. During ebb the vertical shear of the along-channel velocity remains strong through the water column from the bottom to the surface. The halocline tends to be expanded in the vertical direction and shows strong fluctuations over bottom topographic features. During flood the subsurface maximum of velocity occurs coinciding with the halocline position. The vertical shear is mainly strong within the well-developed bottom boundary layer. And the vertical shear is reversed above the halocline. The vertical extension of the halocline tends to be narrowed down. The halocline fluctuations are not as obvious as those during ebb. On the other hand, the vertical shear of the along-channel velocity remains strong through the water column during both ebb and flood of spring tide. The water column tends to be well-mixed from bottom to surface. As a result, the stratification is significantly reduced. In the next discussion, our focus will be mainly put onto neap tide.

Three groups of variables of salinity, dye concentration, velocity, strain rate, baroclinic gradient and Richardson number at different times during the same tidal cycle of the neap tide are shown in Figure 2.2~2.10. They correspond to the maximum ebb, the early flood, and the maximum flood, respectively. For each of them, the variables are contoured in a longitudinal (x) and vertical (z) plane with the background of the thalweg bottom topography. In addition, only the salinity and dye concentration are contoured in a longer longitudinal section, showing the results at the maximum flood (Figure 2.11) and the maximum ebb (Figure 2.12) approximately three tidal cycles later than the tidal cycle mentioned above. As a comparison, the salinity and dye tracer are shown at the same longer longitudinal section but during the transition time from neap to spring (Figure 2.13). Finally the contoured variables are also shown in a lateral section across the big valley during the maximum ebb (Figure 2.14), providing the view of lateral variations in salinity, dye concentration and velocity u.

2.3.1 Maximum ebb

As shown in Figure 2.1 and 2.2, the first longitudinal section extended from 18 km to 26 km north of the Battery. The data for this section were observed about one and a half hours later than the maximum ebb and about three hours later than the releasing time. In the longitudinal section figures, the normal thalweg depth is ~14 m for this particular reach. A big valley is located between 20 km and 22 km with the cross-channel width of ~250 m and with the bottom depth of ~20 m. Thus the spatial scale of this big valley is 2 km long, 250 m wide, and 6 m deep. A relatively small hill is located at ~24 km, with the spatial scale of 1 km long, 250 m wide, and 3 m high. Generally a series of valleys and hills with different size are distributed along the thalweg of this particular reach.

As seen in the upper panel of Figure 2.2, the halocline clearly showed a wave-like pattern following the bottom valleys and hills. A halocline wave crest and a wave trough were present over the seaward edge and the landward edge, respectively of the big valley at ~21 km. The halocline was displaced by ~4 m from the crest to the trough. In addition, the halocline over the small hill at ~23 km was also significantly elevated, representing another halocline wave crest. The 9 psu isohaline (the black dashed line in this and the following figures) was generally consistent with the most stratified positions in the water column and was used as the middle line of the halocline. The 14 psu isohaline (the black dotted line in the following figures) was used to show the relative position of the dye patch.

The dye patch (the lower panel of Figure 2.2) extended approximately 7.5 km along the channel. The dye patch was clearly separated into at least three parts in the longitudinal direction. A big dye gap at ~21.5 km, i.e. over the landward edge of the big valley, lied in between two main parts of the dye patch, corresponding to the halocline wave trough. The dye at ~20.2 km, i.e. over the seaward edge of the big valley, intruded upward to ~7 m depth, following the elevated halocline. The dye over the small hill at ~23 km also intruded upward. In addition, a relatively small dye gap over a small valley at ~24 km separated the highly concentrated dye patch into two parts. Generally the uppermost limit of the dye patch followed

the 14 psu isohaline (the black dotted line) very well, showing wave-like fluctuations over the bottom topographic features.

Correspondingly the along-channel velocity *u* contours (the upper panel of Figure 2.3) also showed a wave-like pattern following the bottom valleys and hills. There occurred significant vertical and longitudinal variations in $\partial u / \partial x$. Over the landward edge of the big valley at ~21 km, there was horizontal convergence ($\partial u / \partial x$ <0) above the halocline and horizontal divergence ($\partial u / \partial x$ >0) below the halocline, suggesting the presence of a downward advection around the halocline. Conversely there was horizontal divergence above the halocline and horizontal convergence below the halocline over the seaward edge of the big valley, leading to an upward advection around the halocline.

The strain rate pattern in the lower panel of Figure 2.3 is consistent with the fluctuated halocline, providing an additional hint of the structure of vertical advection *w*. Over the landward edge of the big valley at ~21 km, the strain rate values were negative under the halocline and positive above the halocline. Thus vertical advection should decrease upward from the bottom to the halocline and then increase upward from the halocline to the surface, suggesting the minimum *w* occurring around the halocline. This minimum *w* was reasonably to be negative, i.e. a downward advection. Conversely an upward advection should be present over the seaward edge of the big valley. The estimated vertical advection here is consistent with the horizontal convergence and divergence mentioned above. Thus vertical advection plays a significant role in moving the halocline position in the vertical direction over the bottom topographic features during the maximum ebb.

One question may be asked is whether vertical mixing rather than vertical advection contributes to the wave-like pattern of the tracer. In the *Ri* contours (the lower panel of Figure 2.4), the deep blue regions (*Ri*<=0.25) indicating relatively high turbulent mixing were mainly located within the subsurface layer and the certain places in the bottom layer over the seaward edges of the bottom valleys. The red regions (*Ri*>1) indicating very limited vertical mixing dominated the whole x-z section, especially the place over the landward slope of the big valley.

Thus the tracer movement over the landward slope of the valley was mainly induced by vertical advection rather than vertical mixing during the maximum ebb.

The contoured along-channel velocity, salinity, and dye concentration are also shown in Figure 2.14 for a cross-channel section over the big valley at ~21.5 km. The data were measured during the maximum ebb of the second dye release experiment, when flow condition and stratification were similar to those for the above longitudinal section. The halocline was significantly depressed with the lateral scale of ~200 m coinciding with the width of the big valley. Correspondingly the dye was separated into two main parts with a big gap in between. The along-channel velocity was strengthened in the lower layer coinciding with the depressed halocline, leading to very strong lateral shear on either side of the channel. The strong lateral shear of *u* may significantly enhance the tracer dispersion on both sides of the big valley.

2.3.2 Early flood

Figure 2.5 ~ 2.7 show variables in similar longitudinal section but at the early flood, about two and a half hours later than the time in 2.3.1. The previously fluctuating halocline (the upper panel of Figure 2.5) was almost straightened probably due to the reverse effect of the bottom topography. The previous halocline wave trough induced by the bottom valley was elevated by the bottom hill during this time period. The dye patch (the lower panel of Figure 2.5) as a whole still maintained the longitudinal extension of ~7.5 km and was advected landward by ~1.5 km. The dye previously intruding upward was squeezed by ~1 m downward to the bottom layer due to descending of the halocline. But the dye patch still clearly maintained three separate parts corresponding to those parts around the maximum ebb in 2.3.1. This also provides us with a good moving coordinate system to evaluate the tracer pattern in the Lagrangian perspective. The dye gap at ~23 km was located over a hill rather than a valley, indicating that this dye gap was the same one previously located at ~21.5 km around the maximum ebb and was moved here. On the other hand, the 14 psu isohaline and the halocline above it at ~23 km were almost straightened. This also confirms the reverse effect of the bottom hill on the previous wave trough. However the dye in the bottom layer responded in a slower way to this reverse effect, which allowed the maintenance of its wave-like structure. In addition,

the dye gap and the related halocline trough at ~25.5 km may first be elevated by the hill at ~24.5 km and then be lowered by the valley at ~25.5 km.

The along-channel velocity *u* (the upper panel of Figure 2.6) showed clearly subsurface maximum at the bottom of the halocline. The velocity *u* generally had positive vertical shear ($\partial u/\partial z>0$) within the bottom boundary layer and has negative vertical shear ($\partial u/\partial z<0$) within the upper water column. The vertical and longitudinal variations in $\partial u/\partial x$ were much weaker than those around the maximum ebb. So were the horizontal convergence and divergence. The estimated strain rate $\partial w/\partial z$ (the lower panel of Figure x) was also reduced in magnitude relative to that in 2.3.1. But the strain rate pattern was still related to the bottom valleys and hills. The baroclinic gradient $\partial\sum_z^\eta s/\partial x$ (the upper panel of Figure 2.7) had predominantly negative values with relatively small magnitude through the bottom boundary layer, suggesting accelerating of the bottom flooding current. However, there were relatively big positive values over the landward edges of the small valley at ~26 km, suggesting decelerating of the bottom flooding current. In addition, vertical mixing represented by the Richardson number (the lower panel of Figure 2.7) became strong within the bottom boundary layer and the subsurface layer where there were relatively stronger vertical current shear and relatively weaker stratification.

2.3.3 Maximum flood

Figure 2.8 ~ 2.10 show variables in a further landward longitudinal section with relatively uniform bottom topography during the maximum flood, about three hours later than the time in 2.3.2. The halocline (the upper panel of Figure 2.8) changed very little in longitudinal pattern and vertical position from that in the early flood but was more concentrated due to upward extension of the bottom boundary layer. The halocline still maintained some wave-like perturbations even over the relatively uniform bottom topography. But the wave range was significantly reduced.

The dye patch (the lower panel of Figure 2.8) did not have obvious separate parts any more but rather had a single main part, still maintaining the longitudinal length of ~7.5 km. There are two possible reasons. The relatively strong vertical shear of *u* in the bottom boundary

layer (the upper panel of Figure 2.9) makes it possible that the dye at smaller depths is moved faster than that at bigger depths during the flood. Thus the dye previously intruding upward is now moved faster than the bottom dye. In addition, much stronger bottom layer turbulence (the lower panel of Figure x) during the flood tends to make the dye patch well-mixed within the bottom boundary layer. Thus the dye at smaller depths caught up and mixed with the deeper dye. As a result, the dye patch previously separated by the topographic features was reunited over relatively uniform bottom during the flood.

It should also be noted that the dye mass center moved landward by ~5.2 km within ~3.5 hours. Thus the mean advection rate was approximately 0.41 m/s. However, the landward front of the 14 psu isohaline only moved by ~3.5 km within ~3.5 hours at the rate of ~0.28 m/s. Actually the dye patch not only moved landward but also extended upward into the halocline bottom. As a result, both the landward part and the upper part of the dye patch were significantly freshened. Chant et al. (2007) attributed the freshening of the dye mass to be entrainment of the halocline fresher water into the bottom saltier water. We think that both the estuarine circulation and the vertical shear of current play an important role in tracer movement. The dye patch was mostly within the bottom boundary layer, where the mean estuarine current was landward due to the dominating landward baroclinic pressure gradient force. Thus it can be expected that the dye mass center would not come back to the releasing site after a tidal cycle. Instead the dye mass center would be farther and farther landward away from the releasing site. In addition, as mentioned in the last paragraph, the vertical shear makes it possible that the dye previously intruding upward to the smaller depths is advected landward faster and then is mixed with the lower dye. Thus the dye patch as a whole was freshened. Even the upper part of the dye patch was able to go into the bottom of the halocline, it was hard for it to go further upward since the vertical shear was reversed above the middle halocline and the vertical mixing within the halocline was very weak.

The general pattern of the along-channel velocity (the upper panel of Figure 2.9) was still characterized by the presence of the subsurface maximum coinciding with the middle halocline. There were also some wave-like perturbations around the halocline and within the bottom boundary layer. Upward advection and downward advection estimated from the strain rate (the

lower panel of Figure 2.9) were still present at the wave crest and trough, respectively. But the strain rate magnitude was much smaller than that previously estimated over the bottom valleys or hills during the maximum ebb, suggesting weaker vertical advection.

Figure 2.11 shows the salt and the dye structure during the maximum flood approximate three tidal cycles later than the time in 2.3.3. The dye mass center was moved landward by approximate 10 km. The mean speed was ~0.07 m/s. The longitudinal length of the dye patch reached ~15 km, almost double in size of the dye patch three tidal cycles before. Geyer et al. (2008) calculated the horizontal dispersion rate for the same data sets by use of Taylor's formula and found the theoretical results significantly underestimate the observed dye expansion. We think the combining effects of the bottom-topographic-features-induced vertical advection and vertical shear of *u* mainly contribute to the dye expansion. The dye front already exceeded the 9 psu isohaline. The front of the 14 psu isohaline also moved landward by ~3 km within three tidal cycles, further lagging behind the dye front. The bottom boundary layer expanded upward significantly. The upward extension of the dye patch was still limited by the middle halocline.

Figure 2.12 shows the salt and the dye structure during the maximum ebb, approximate 5 hours later than the maximum flood mentioned in the last paragraph. Generally the halocline was obviously inclined, leading to a big landward slope. At the same time, the halocline was also displaced in the vertical direction over a big valley as deep as 2~4 m and extending from ~34 km to ~41 km. A halocline wave trough was present at ~40 km over the landward edge of the big valley. A halocline wave crest was present at ~34 km over the seaward edge of the big valley. The dye patch generally moved along the isohalines and intruded both landward and upward, leading to a tongue-like pattern. Geyer et al. (2008) attributed this tongue-like distribution to the strong vertical shear and the weak vertical mixing during the ebb. We think the relatively strong upward advection over the landward edge of the big valley also played an important role in building the tongue-like dye patch. Strong upward advection tended to be limited within a relatively short longitudinal distance [Hibiya, 2004] over the seaward edge of the big valley, where the dye tended to intrude upward into the bottom of the halocline. The dye in the upper water column was then carried seaward at a faster rate by the stronger ebbing currents there, while the dye in the bottom layer lagged behind.

As a comparison to the patterns during the neap tides, the salinity field and the dye patch at the maximum ebb during the transition from the neap tide to the spring tide are shown in Figure 2.13. The water column was already mixed to a relatively large extent due to the relatively strong tidal currents. As a result, the halocline almost disappeared. The isohaline slope was significantly enlarged in the landward direction. Correspondingly, the dye patch still looked like a tongue and intruded upward to a relatively large extent, almost reaching the water surface. At this moment, both the upward vertical advection induced by the bottom topographic slope at ~34 km and the relatively strong vertical mixing should affect vertical expansion of the dye patch.

2.4 Model description and setup

ROMS (The Regional Ocean Model System) was used to simulate the three-dimensional flow field and salinity field in the lower Hudson Estuary. ROMS is a free-surface, terrain-following, primitive equations ocean model [Haidvogel et al., 2000]. The primitive equations are time-discretized using a third-order accurate predictor (Leap-Frog) and corrector (Adams-Molton) time-stepping algorithm which allows larger time steps [Shchepetkin and McWilliams, 2005]. In the vertical, the primitive equations are discretized using stretched terrain-following coordinates which is capable of maintaining high resolution in the bottom layer over variable topography. In the horizontal, the primitive equations are discretized using boundary-fitted, orthogonal curvilinear coordinates on a staggered Arakawa C-grid. ROMS provides users with various options for advection schemes and turbulent closure schemes [Warner et al., 2005a], which allows appropriate simulations under different circumstances. Here we use a third-order upstream advective scheme for the horizontal momentum transport and the Generic Length Scale k-ε turbulence closure for parameterization of subgrid-scale mixing.

The model domain covers the Hudson River, extending nearly 250 km from the Battery, NY to the Troy, NY. The curvilinear grid with 2200 (longitudinally) × 60 (laterally) × 30 (vertically) cells was generated by use of a MATLAB GUI tool SeaGrid. The grid resolution is approximately 150 m × 40 m × 0.5 m for the lower Hudson Estuary. The grid bathymetry is

interpolated from the high-resolution multi-beam sounding data by courtesy of Dr. Roger Flood in Stony Brook, NY.

ROMS tends to be more stable and have a better performance for a 3D baroclinic simulation if both water elevation and depth-averaged currents are provided at the open boundaries. Under this condition, the free surface Chapman and the depth-averaged momentum Flather conditions can be applied. However, we only have observed time series of water elevation at the Battery as the open boundary forcing. Thus we do a 2D barotropic simulation first. The free surface clamped condition and the depth-averaged momentum reduced condition are specified at the south open boundary. The 2D barotropic simulation, validated by the observed water elevation and currents (Figure 2.17 and Table 2.1), is able to provide relatively accurate estimates of water elevation and depth-averaged currents in the vicinity of the south open boundary. Then a new south open boundary for the 3D baroclinic simulation is put at ~1.5 km north of the 2D barotropic south open boundary. Thus the water elevation and depth-averaged currents at the 3D south open boundary, which are output from the 2D simulation, can be used for driving the 3D baroclinic run. In addition, the daily-averaged discharge data collected by USGS at the Green Island, NY are specified at the north boundary for both 2D and 3D simulations.

The salinity time series observed at the moored array mentioned above are used to calculate the salinity values at the 3D south open boundary. It is assumed that a time varying longitudinal salinity gradient is present between the moored site and the 3D south open boundary. It is also assumed that the longitudinal gradient depends on the stratification, i.e. the bottom-surface salinity difference. This is confirmed by the longitudinal observations during the neap and spring tides. Generally the horizontal salinity gradient is smaller during the neap tide when the stratification is larger. Thus the horizontal salinity gradient is assumed to be inversely related to the bottom-surface salinity difference. A couple of longitudinal salinity fields observed by ship-borne CTD are then combined with the salinity time series at the moored site to estimate the time varying horizontal salinity gradient and thus the time varying salinity values at the 3D south open boundary. During the processing, the high-frequency noises in the observed

salinity time series have been removed by a low-pass (lower than 1/3 hours^{-1}) Fourier filter for modeling stability.

2.5 Model results

2.5.1 Model skill assessment

The 3D baroclinic simulation starts from the rest with a stratified salinity field specified in the lower Hudson Estuary. Hydrodynamic conditions are simulated for 16 days covering a spring-neap cycle. The first 5 days are for hydrodynamic adjustment. The last 11 days are used for skill assessment. The time series of surface salinity, bottom salinity, surface current, bottom current, and depth-averaged current from both the 3D model and the observations at the moored site have been shown in Figure 2.18. The related skill and the root-mean-squared errors (RMSE) have been shown in Table 2.1. The skill parameter is defined following Warner et al. (2005). Generally the model reproduces the observations very well with high skill (all higher than 0.89). However, the model tends to underestimate the surface salinity during spring and the transition from spring to neap which may be due to the underestimated surface layer mixing because of the absence of wind forcing in the model. In addition, the model tends to overestimate the bottom current probably due to the underestimated bottom friction coefficient. The effects of wind forcing and bottom friction coefficient on the modeling results will be further considered in the future studies. Our focus will be put onto neap tide in this study. On the other hand, the depth-averaged currents from both 3D simulation (the bottom panel of Figure 2.18) and previous 2D simulation (the bottom panel of Figure 2.17) are closely in agreement with the observed currents, suggesting the effectiveness of the method of using 2D output currents to drive 3D simulation at the open boundary in the lower Hudson.

In addition, vertical profiles of salinity and current from the model and observations during ebb and flood of neap tide in the vicinity of the moored site have been shown in Figure 2.19. Generally the model captures the vertical structure of both salinity and current very well. However, the model tends to underestimate the stratification especially during ebb which may be due to inadequate turbulent parameterization [Warner et al., 2005] or the underestimated surface

mixed layer. Further improvement of modeling stratification will be considered in the future studies. The overestimated bottom flooding current may indicate the underestimated bottom friction coefficient.

2.5.2 Tidal period internal motion

The 3D simulation has been output every six minutes for four days during neap tide. The results of one tidal cycle during the first dye release experiment have been used for analysis. Both spatial and temporal variations of fourteen parameters have been shown in Figure 2.20~2.55. The fourteen parameters include salinity *s*, along-channel current *u*, vertical advection *w*, logged viscosity $\log_{10}Kv$, Brunt–Väisälä frequency N^2 and its local time rate $\partial N^2/\partial t$, vertical shear $\partial u/\partial z$, Richardson Number R_i, available potential energy APE (ref. 2.6.3) and its local time rate ∂APE$/\partial t$, pressure gradient force F_{pg} and its power P_{pg}, barotropic pressure gradient force F_{BTpg} and baroclinic pressure gradient force F_{BCpg}.

Figure 2.20~2.26 show the fourteen parameters in the longitudinal section at the maximum ebb. Figure 2.27~2.32 show the longitudinal parameters at the early flood. Figure 2.33~2.35 show the longitudinal parameters at the maximum flood. Figure 2.36 and 2.37 show the longitudinal parameters at the end of flood. Two positions (S1 and S2) are selected to show temporal variations of these parameters within a tidal cycle. S1 is at 21.58 km north of the Battery and over the landward slope of the big valley. S2 is at the upstream of the big valley about 750 m north of S1. S2 is in vicinity of the moored site. Figure 2.38~2.44 show tidal variations at S1. Figure 2.45~2.51 show tidal variations at S2. In addition, Figure 2.52~2.55 show horizontal distribution of depth-integrated energy and power.

Maximum ebb

Vertical displacement of halocline (Figure 2.20 upper panel) over bottom topographic features reaches its maximum around the maximum ebb, which is mainly due to strong vertical advection (Figure 2.21 upper panel). There are mainly four places with depressed halocline in the lower Hudson reach: 21.5 km, 26 km, 30.5 km, and 36 km away from the Battery, NY.

Correspondingly, water surface over the depressed halocline is significantly elevated (upper black dotted line in Figure 2.20~2.26), producing very strong barotropic pressure gradient force in a relatively short distance. The barotropic pressure gradient force (Figure 2.26 middle panel) over the landward edge of the big valley is as high as 6×10^{-4} m^2/s^2, almost seven times stronger than the reach-mean F_{BTpg} at the early flood.

Around the maximum ebb, the model internal waves, i.e. the halocline fluctuations induced by the bottom topography are very strong, which is consistent with the observations. The halocline (the upper panel of Figure 2.20) is significantly depressed over the landward edge of the big valley at ~21.5 km. Correspondingly, strong downward advection (the upper panel of Figure 2.21) is present over the valley edge and strong upward advection is present over the valley. This is also consistent with the analyzed strain rate (the lower panel of Figure 2.3) from the observed data. The eddy viscosity (the lower panel of Figure 2.21) is relatively low through the reach except the patched higher values at the bottom where the internal wave is also present. This is generally consistent with the estimated Richardson numbers (the lower panel of Figure 2.4). Thus the internal wave also tends to increase the bottom turbulent mixing to some extent.

Along-channel current (the lower panel of Figure 2.20) also show vertical fluctuations corresponding to halocline fluctuations, producing relatively strong vertical shear (the upper panel of Figure 2.23) within both the bottom and surface layers. Within the bottom layer of the halocline depression regions, strong shear and relatively weak stratification (the upper panel of Figure 2.22) lead to relatively strong mixing represented by both eddy viscosity (the lower panel of Figure 2.21) and Richardson Number (the lower panel of Figure 2.23). Thus the presence of halocline depression tends to enhance the bottom layer mixing. However, vertical mixing decreases sharply above the bottom layer, where vertical advection plays a more important role. Within the upper layer, vertical mixing is relatively weak due to strong stratification in most regions except very limited region over the landward edge of the big valley. However certain regions in the upper layer tend to be further-stratified or de-stratified (the lower panel of Figure 2.22) very quickly due to halocline fluctuations.

Sharp water surface slope over the landward edge of the big valley leads to strong barotropic pressure gradient force through the water column (Figure 2.26). F_{BTpg} is much larger than F_{BCpg} within the surface layer and smaller than F_{BCpg} within the bottom layer. As a result, total pressure gradient force F_{pg} (the upper panel of Figure 2.26) reverses from the surface to the bottom. Within the surface layer, F_{pg} decelerates the ebbing currents over the landward side of isohaline trough and accelerates the ebbing currents over the seaward side of halocline trough. While within the bottom layer, F_{pg} accelerates the ebbing currents over the landward edge of the big valley. Thus F_{pg} tends to strengthen horizontal divergence of the ebbing currents within both the surface and bottom layers, leading to strong downward advection in the middle water. Correspondingly pressure gradient power changes very quickly within the surface layer over the landward edge of the big valley. The kinetic energy first decreases and then increases when the surface layer ebbing currents go through the edge. Part of the lost kinetic energy is transferred into available potential energy (the lower panel of Figure 2.24) at the bottom of the surface layer during this process.

Early flood

Isohaline fluctuations (the upper panel of Figure 2.27) especially within the bottom layer tend to be decreased in magnitude and be moved landward due to the bottom flooding currents (the lower panel of Figure 2.27). The effects of bottom topographic features on the bottom flooding currents lead to relatively strong upward advection (the upper panel of Figure 2.28), which elevates the previously-depressed isohalines.

Vertical shear (the upper panel of Figure 2.30) is very strong in between the surface layer ebbing currents and the bottom layer flooding currents. This stripe of strong shear decreases in depth from the halocline to the bottom in the landward direction, producing a landward inclined "tunnel" with strong vertical mixing (the lower panel of Figure 2.30 and the lower panel of Figure 2.28). The tunnel of strong mixing is surrounded by the regions with very weak mixing. This may be one of the reasons for the tongue-like structure of the dye patch during ebb (Figure 2.12 in draft thesis).

Both the stratification tendency (Figure 2.29) and the surface layer pressure gradient force (the upper panel of Figure 2.32) indicate that halocline fluctuations have propagated landward. Pressure gradient power (the lower panel of Figure 2.32) generally increases kinetic energy within the bottom layer and decreases kinetic energy within the surface layer.

At the slack before flood, the magnitude of the internal wave is generally reduced. The currents (the lower panel of Figure 2.20) begin to flood in the bottom layer but still ebb in the upper layer, producing very strong shear around the halocline. As analyzed above, the strong shear tends to reduce the isohaline fluctuations. Vertical advection (the upper panel of Figure 2.21) induced by the bottom topographic features is still present mainly in the bottom layer but is significantly decreased in magnitude. In addition, as seen in the lower panel of Figure 2.21, the previously-patched turbulent regions begin to connect with each other and extend through the bottom layer due to the bottom flooding currents.

Maximum flood

During the maximum flood (Figure 2.33) the internal wave is again strengthened over the landward edge of the big valley. However, the wave amplitude is not as large as that during the maximum ebb. This may be because the maximum flooding currents tend to be present at the bottom of the halocline while the maximum ebbing currents are present at the water surface. Vertical shear is inversed above the halocline during the flood and is relatively strong to reduce the internal wave amplitude to some extent. On the other hand, the upward advection (the upper panel of Figure 2.34) is significantly enhanced through the water column over the big valley at ~21.5km. There is also strong downward advection within the bottom boundary layer over the landward side of the bottom hills. The low values of the Richardson number (the lower panel of Figure 2.34) all through the bottom boundary layer suggesting very strong vertical mixing there. The pressure gradient force (Figure 2.35) tends to strengthen horizontal divergence of the flooding currents within both the surface and bottom layers, leading to strong upward advection in the middle water.

End of flood

At the end of flood (Figure 2.36), the surface currents start ebbing while the lower flooding currents are decelerating. As a result, the internal wave is released and tends to propagate downstream. However, the internal wave amplitude is reduced due to the strong vertical shear at the top of the halocline. Correspondingly, both vertical advection and vertical mixing especially in the surface layer is significantly reduced (Figure 2.37). In addition, the halocline is more concentrated than that at the early flood due to bottom boundary layer development during the flood.

Tidal-cycle variations at the landward slope (S1) of the big valley

The halocline (the upper panel of Figure 2.38) is depressed by ~6 m from the early ebb to the maximum ebb and is elevated back to the maximum flood. A well-mixed middle layer is developed above the halocline around the maximum ebb due to the lowered stratification (the upper panel of Figure 2.40). The well-mixed middle layer is then elevated from 7 m deep at the maximum ebb to the surface at the maximum flood. The bottom layer is also well-mixed at the maximum ebb. But the well-mixed bottom layer is limited to the very bottom, totally separated by strong halocline from the well-mixed middle layer. Thus there is little connection between the bottom and middle layers during ebb at the landward slope (S1) of the big valley.

There are strong downward advection during ebb and strong upward advection during flood (the upper panel of Figure 2.39). Sudden upward advection is present through the water column especially in the deeper region at the end of ebb (6.1 hour), which leads to sudden elevation of isohalines. This may coincide with the releasing of the arrested internal wave.

Tidal-cycle variations at the upstream (S2) of the big valley

The obvious isohaline depression (~2 m) (the upper panel of Figure 2.45) only appears after the releasing (6.1 hour) of the internal wave at S1, leading to significant de-stratification of the middle layer (Figure 2.47). Sudden upward advection is present about 40 minutes later than that at station S1. As a result, the halocline is quickly elevated after the internal wave trough

passes by. At the same time the relatively strong shear above the flooding currents leads to strong vertical mixing in the vicinity of the halocline (Figure 2.48). This well-mixed middle layer continues to be elevated toward the surface during flood.

Pressure gradient force (Figure 26 upper panel) is suddenly reversed when the isohalines are elevated. Around the maximum flood, baroclinic pressure gradient force exceeds barotropic pressure gradient force, leading to seaward pressure gradient force, which decelerates the flooding currents.

2.6 Discussion

2.6.1 Quasi-steady two-layer hydraulics

A quasi-steady two-layer stratified flow over longitudinally-varying channel morphology can be described [Engel, 2009; Chant and Wilson, 2000; Lawrence, 1993; Stommel and Farmer, 1953] by a composite equation coming from the momentum and continuity equations.

The quasi-steady momentum equations for each layer:

$$U_1\frac{\partial U_1}{\partial x} = -g\frac{\partial \eta}{\partial x} - \frac{C_i \mid \Delta U \mid (U_1 - U_2)}{D_1} \tag{2.5}$$

$$U_2\frac{\partial U_2}{\partial x} = g'\frac{\partial h_i}{\partial x} - g\frac{\rho_1}{\rho_2}\frac{\partial \eta}{\partial x} + \frac{C_i \mid \Delta U \mid (U_1 - U_2)}{D_1} - \frac{C_d \mid U_2 \mid U_2}{D_2} \tag{2.6}$$

The continuity equations for each layer:

$$\frac{\partial (U_1 D_1 b)}{\partial x} = D_1 b\frac{\partial U_1}{\partial x} + bU_1\frac{\partial D_1}{\partial x} + D_1 U_1\frac{\partial b}{\partial x} = 0 \tag{2.7}$$

$$\frac{\partial (U_2 D_2 b)}{\partial x} = D_2 b\frac{\partial U_2}{\partial x} + bU_2\frac{\partial D_2}{\partial x} + D_2 U_2\frac{\partial b}{\partial x} = 0 \tag{2.8}$$

A composite equation can be obtained by substituting the continuity equations into the momentum equations and subtracting (2.6) from (2.5):

$$\frac{\partial D_1}{\partial x}(G^2 - 1) = F_2^2\left(\frac{\partial h}{\partial x} + \frac{\partial \eta}{\partial x} \pm C_d\right) - \frac{1}{bg'}\frac{\partial b}{\partial x}(U_1^2 - U_2^2) + \frac{C_i \mid \Delta U \mid (U_1 - U_2)}{g'}\left(\frac{1}{D_1} + \frac{1}{D_2}\right) \tag{2.9}$$

An equivalent equation can be obtained by replace D_1 with h_i in the above equation (2.9):

$$\frac{\partial h_i}{\partial x}(G^2-1) = F_2^2(\frac{\partial h}{\partial x} \pm C_d) + (F_2^2+1)\frac{\partial \eta}{\partial x} - \frac{1}{bg'}\frac{\partial b}{\partial x}(U_1^2 - U_2^2) + \frac{C_i \mid \Delta U \mid (U_1 - U_2)}{g'}(\frac{1}{D_1} + \frac{1}{D_2}) \quad (2.10)$$

where $D_1 = \eta + h_i$ and $D_2 = h - h_i$ are layer thickness. U_1 and U_2 are layer mean velocity. b and h are the channel width and depth. h_i is the interface depth relative to the mean sea level. η is the water elevation. g' is the reduced gravity $g\Delta\rho/\rho$. C_d and C_i are bottom and interfacial friction coefficients. The sign before C_d is plus for the ebb and minus for the flood. C_d is assumed to be a constant for the interest estuarine reach. G^2 is the composite Froude number, the sum of the layer Froude numbers,

$$G^2 = F_1^2 + F_2^2 = \frac{U_1^2}{g'D_1} + \frac{U_2^2}{g'D_2} \quad (2.11)$$

In addition, the longitudinal variation of channel width can be neglected here since the segment of channel for the dye study was relatively straight and uniform in the longitudinal direction. The interfacial friction term is neglected due to the relatively small magnitude. The water elevation slope is also small for short distance surveys and can be ignored. Thus the effects of bottom friction and longitudinal variation in bottom topography on vertical displacement of the halocline position, i.e. thinning or thickening of the upper layer, can be evaluated by the reduced equation:

$$\frac{\partial h_i}{\partial x} = \frac{F_2^2}{G^2 - 1}(\frac{\partial h}{\partial x} \pm C_d) \quad (2.12)$$

This equation is only valid for $G^2 \neq 1$. When the condition $G^2=1$ is fulfilled, an alternative formula [Lawrence, 1993] can be used. For each time in a tidal period, the middle halocline is extracted from the contoured salinity field as the interface between the upper layer and the lower layer. The Froude numbers at all surveyed positions in the longitudinal channel are then calculated.

During the maximum ebb (the upper panel of Figure 2.15), the lower layer Froude number (F_2) is much smaller than the upper layer Froude number (F_1) due to the smaller velocity magnitude. The currents are generally supercritical ($G^2>1$) for most of the places in the reach but are subcritical ($G^2<1$) over the big valley at ~21.5 km. The currents in the lower layer tend to overcome the bottom friction and be accelerated in both the seaward and the downward

directions following the slope, leading to both horizontal divergence and thus downward advection. Thus the halocline tends to be depressed first over the landward edge of the valley when the supercritical water flows following the downward slope. The subsequent thickening of the upper layer tends to retard the currents in the upper layer due to the continuity effect, leading to horizontal convergence which intensifies downward advection and halocline displacement. Then the halocline tends to be elevated over the valley due to the internal hydraulic jump [Lawrence, 1993] when the supercritical water hits the subcritical water. This may also be one of the reasons for relatively high turbulent mixing over the seaward edge of the valleys (see the lower panel of Figure 2.4), where the kinetic energy is consumed to increase the potential energy. The slope of the landward edge of the big valley is $\partial h / \partial x \approx -0.009$ according to the surveyed position 11 and 12. The bottom friction effect (C_d) is opposite to the bottom topographic effect. Thus the halocline is displaced by $\Delta h_i \approx 2.4$ m if C_d=0.0015 or $\Delta h_i \approx 1.8$ m if C_d=0.003 between the surveyed position 11 and 12. This estimated value is consistent with the observed halocline displacement. On the other hand, the bottom friction effect is superimposed onto the bottom topographic effect over the landward edge of the big valley. Thus the halocline tends to be elevated in the seaward direction ($\partial h_i / \partial x > 0$) over the seaward edge of the big valley.

At the early flood (the middle panel of Figure 2.15), the lower layer Froude number is generally much bigger than the upper layer Froude number since the flooding currents occur earlier and have larger magnitude at the bottom than the upper water column. The currents are mostly subcritical through the reach. It also can be imagined that the subcritical ($G^2<1$) currents are all through the reach during the slack before flood. At the same time the bottom friction effect ($-C_d$) is superimposed onto the bottom topographic effect over the landward slope of the big valley. Thus the previously-depressed halocline tends to be elevated ($\partial h_i / \partial x > 0$) over the slope, leading to an inversed effect of the bottom topography on the halocline displacement relative to that during the maximum ebb. This may be one of the reasons that the fluctuated halocline during the maximum ebb was almost straightened at the early flood.

During the maximum flood (the lower panel of Figure 2.15), the lower layer Froude number is comparable to the upper layer Froude number since the mean currents within each layer are in similar magnitude. The currents are supercritical ($G^2>1$) all through the reach. The

generally-landward inclined halocline tends to be elevated in the landward direction ($\partial h_i / \partial x < 0$) due to the bottom friction effect ($-C_d$) over longitudinally-uniform bottom ($\partial h / \partial x \approx 0$). In addition, it can be imagined that the halocline tends to be elevated ($\partial h_i / \partial x < 0$) over the landward slope of the big valley ($\partial h / \partial x < 0$), which is consistent with the model result shown in Figure 2.22.

Generally the quasi-steady two layer hydraulics can be successfully used to explain some halocline behaviors induced by both the longitudinal variation in bottom topography and bottom friction. However, it is hard to quantify the effect of the longitudinal variation in channel width on the halocline displacement since the cross channel shape is rarely rectangular but more like a U, V, or half U and half V and the along-channel currents have significant lateral variations (Figure 2.14). It is also hard to quantify the effect of the vertical shear on the halocline behavior since the vertical resolution (two layers) is too coarse to resolve the vertical shear which tends to be much stronger at the top and the bottom of the halocline than that within either upper or lower layer. Thus part of future studies will be focused on how to improve the above aspects of the estuarine hydraulics.

2.6.2 Internal waves and vertical mixing

The first-mode internal wave speed at all surveyed positions in the longitudinal channel are calculated by use of the MATLAB program dynmodes.m developed by Dr. John Klinck. This program was designed for continuous density profiles in the water column. Then the ratio between the squared depth-averaged velocity U^2 and the squared first-mode internal wave speed c_1^2 are used as criteria for judging that the flow is supercritical ($U^2 / c_1^2 > 1$) or subcritical ($U^2 / c_1^2 < 1$).

During the maximum ebb (the upper panel of Figure 2.16), the currents are generally supercritical but are subcritical over the big valley. Similar to the above hydraulic analysis, the halocline was first depressed over the landward slope of the big valley and then elevated over the seaward slope, leading to a relatively large internal wave. As mentioned by Hibiya (1984), the

internal wave induced by the bottom topographic features is produced during the accelerating stage of tidal currents and is then amplified when tidal currents exceed the first-mode internal wave speed. Thus the internal wave amplitude, i.e. the vertical displacement of the halocline has been significantly amplified over the landward edge of the big valley during the maximum ebb. There also should be strong downward advection within a relatively short longitudinal distance over the landward edge of the big valley [Baines, 1973; Hibiya, 2004], which directly leads to the production of the internal wave trough.

In addition, the amplified internal wave tends to be arrested over the big valley. The previous studies paid little attention to the mechanisms of the internal wave being arrested over the bottom topographic feature. As shown in the upper panel of Figure 2.4, the baroclinic gradient $\partial \sum_z^{\eta} s / \partial x$ is closely related to the fluctuated halocline. The negative gradient values on the seaward side of the halocline trough at ~21.5 km indicate that the baroclinic pressure gradient was decelerating the ebbing currents. Conversely the positive gradient values on the landward side of the halocline trough indicate that the baroclinic pressure gradient was accelerating the ebbing currents. Since the velocity wave trough is consistent with the halocline wave trough, thus the accelerating and decelerating of the baroclinic pressure gradient tend to move the velocity wave trough landward, i.e. in the opposite direction of the ebbing currents. Similarly the baroclinic effect also tends to move the wave crest in the opposite direction of the ebbing currents. On the other hand, the ebbing currents tend to advect the wave seaward. Thus the balance between the baroclinic effect and the advection effect may be the main reason for the bottom-topography-induced wave being arrested during the maximum ebb.

Once the ebbing currents decreased and became subcritical (the middle panel of Figure 2.16), the baroclinic effect exceeded the advection effect, leading to the landward propagation of the internal wave. However the internal wave amplitude diminished very quickly so that it became very small at the early flood (Figure 2.5 and Figure 2.20). As mentioned above, the two layer hydraulics provides a possible explanation for the halocline being straightened after the maximum ebb. The other possible reason may be the relatively strong shear at the top of the halocline (the upper panel of Figure 2.6). The flooding currents occur earlier at the bottom than

the upper water column, leading to the presence of negative strong shear, which tends to deform the internal wave.

During the maximum flood, there were also wave-like perturbations (the upper panel of Figure 2.8) around the halocline and within the bottom boundary layer. The currents are generally supercritical but tend to become subcritical at the seaward edge of another big valley at ~34 km (the lower panel of Figure 2.16). An internal wave with relatively small magnitude was correspondingly present. As seen in the upper panel of Figure 2.10, the positive baroclinc gradient values tend to appear on the landward side of the wave trough, decelerating the flooding currents. The negative baroclinc gradient values tend to appear on the seaward side of the wave trough, accelerating the flooding currents. Thus the decelerating and accelerating of the baroclinic gradient tend to move the wave trough in the opposite direction of the flooding currents. The baroclinic effect also tends to move the wave crest in the opposite direction of the flooding currents. Similar to the above analysis, the competition between the baroclinic effect and the advection effect influences the internal wave propagation.

Based on the Richardson Number figures (Figure 2.23, Figure 2.30, Figure 2.41 and Figure 2.48), we can see a possible way for inter-halocline mixing to connect the bottom layer with the surface layer. Internal motions induced by topographic features play very important role during this process. Around the maximum ebb, the bottom ebbing currents at the seaward side of the isohaline trough are significantly slowed down by either elevated bottom (e.g. 20.5 km and 34 km) or widened channel (e.g. 30.6 km), leading to relatively strong shear over relatively weak stratification. As a result, very strong vertical mixing is produced at the seaward side of the isohaline trough. From the maximum ebb to the early flood, both the isohaline trough and the current trough are elevated due to development of the bottom flooding currents. However the shear increases more rapidly than the stratification especially at the current front zone where the bottom flooding currents meet the upper ebbing currents. Thus strong vertical mixing is developed along the current front zone, connecting the previously developed bottom mixed layer at the landward side with the previously developed middle mixed layer at the seaward side. From the early flood to the maximum flood, subsurface maximum of the flooding currents produces

zero shear zone, separating the newly developed bottom boundary layer from the upper mixing zone. The previously developed middle mixed layer is now further elevated to the surface.

2.6.3 Tidal period variations in available potential energy

Available potential energy (APE) has been widely used to study the energetics of internal waves [Lamb, 2007; Kang and Fringer, 2010]. The APE is the fraction of potential energy that can be converted into kinetic energy (KE), which ultimately contributes to mixing. The APE for an incompressible fluid is defined as the difference between the instantaneous potential energy and the minimum value of this quantity that could be achieved by a redistribution of mass through adiabatic processes [Lorenz, 1955]. The change of APE in the water column can be related to the mixing in stratified fluids [Winters et al., 1995]. Generally the KE is consumed through the mixing to produce upward buoyancy flux and increase the APE as the water column becomes more mixed. On the other hand, the APE is transferred back into the KE as the water column becomes more stratified. In order to estimate the mixing associated with internal tide motion induced by abrupt bottom topographic variations, the APE and the time rate change of APE are calculated in a tidal cycle in the water columns of the lower Hudson reach. In addition, the pressure gradient power is calculated to estimate the change of KE. The bottom dissipation rate is calculated to estimate the consumed energy of the total water column by the quadratic bottom friction.

Available potential energy APE is defined following Gill (1982):

$$APE = \frac{g^2 \rho'^2}{2\rho_0 N_r^2} \tag{2.13}$$

where $\rho'(x, y, z, t) = \rho(x, y, z, t) - \rho_r(z)$ is the perturbed density relative to the reference density.

$$N_r^2 = -\frac{g}{\rho_0}\frac{\partial \rho_r}{\partial z} \tag{2.14}$$

The reference density represents the status of the minimum potential energy at certain depth within a time period. In this study we first interpolate the model output density onto uniform vertical levels z_i with a half meter interval. The temporal minimum of density at each vertical level within a tidal cycle is used as the reference density at that level.

Pressure gradient force (F_{pg}) includes both barotropic (F_{BTpg}) and baroclinic (F_{BCpg}) pressure gradient forces:

$$F_{pg} = -\frac{1}{\rho}\nabla p = -\frac{g}{\rho}\nabla(\int_z^\eta \rho\, dz) \tag{2.15}$$

$$F_{BTpg} = -g\nabla\eta \tag{2.16}$$

$$F_{BCpg} = F_{pg} - F_{BTpg} \tag{2.17}$$

Pressure gradient power is the dot product of pressure gradient force and velocity, which indicates the effects of the pressure gradient force on variation of kinetic energy:

$$P_{pg} = F_{pg} \cdot V = -\frac{1}{\rho}\frac{\partial p}{\partial x}u - \frac{1}{\rho}\frac{\partial p}{\partial y}v \tag{2.18}$$

Bottom dissipation rate is calculated using the quadratic friction law:

$$Diss = \rho C_d(\sqrt{u_b^2 + v_b^2})^3 \tag{2.19}$$

The quadratic friction coefficient C_d is set to be 0.002.

Around the maximum ebb, available potential energy (the upper panel of Figure 2.24) is relatively low at most regions except the upstream regions of the halocline depressions where the stratification is lowered down. At the same time, available potential energy continues to decrease with time (the lower panel of Figure 2.24) for most regions within the bottom layer due to the enhancing tendency of stratification.

A quick increase of APE (the lower panel of Figure 2.42) is present at the bottom of the halocline due to the upward buoyancy flux, suggesting possible presence of inter-halocline mixing. However this quick increase of APE only lasts about half an hour. At this short transition time, the direction of pressure gradient force (the upper panel of Figure 2.43) is quickly reversed due to the sudden reduced surface slope, leading to the sudden increase of kinetic energy (the lower panel of Figure 2.43) within the surface layer. In addition, pressure gradient force is dominated by barotropic pressure gradient force within the surface layer and baroclinic pressure gradient force within the bottom layer especially during ebb (Figure 2.44).

Available potential energy (Figure 19 upper panel) reaches the maximum at the bottom of the halocline around the ending flood when the well-mixed bottom boundary layer is fully developed upward. APE then quickly decreases during the beginning ebb.

At the early flood, available potential energy (Figure 13 upper panel) almost reaches the minimum at most regions. However APE in both the halocline and the bottom layer increases suddenly (Figure 13) over the upstream (S2) of the big valley due to the releasing and landward movement of isohaline fluctuations.

Available potential energy (the lower panel of Figure 2.49) increases suddenly within both the halocline layer and the bottom layer when the isohalines are elevated (the upper panel of Figure 2.45) by sudden strong upward advection (the upper panel of Figure 2.46). This indicates strong upward buoyancy flux within both the halocline layer and the bottom layer. The magnitude of APE change with time within the halocline layer is about half of that within the bottom layer.

Horizontal distribution of depth-integrated energy and power

At the maximum ebb (t1), depth-integrated available potential energy (the upper panel of Figure 2.52) has very high values over the upstream of the big valley, extending longitudinally from 21.5 km to 24 km and laterally about 1 km. Depth-integrated APE (the lower panel of Figure 2.52) decreases with time at most regions. Depth-integrated pressure gradient power (the upper panel of Figure 2.53) has a sharp change not only over the landward edge of the big valley but also extending largely from the thalweg to the seaward shoal region. Bottom dissipation rate (the lower panel of Figure 2.53) also shows lateral extension. Thus the internal motions induced by bottom topographic features not only affect the very local energy budget and related mixing but also have laterally extended effects.

At the early flood (t2), depth-integrated APE (the upper panel of Figure 2.54) has dropped to the minimum at most regions. However APE is still very high at the upstream edge surrounding the big valley due to elevation of previously-depressed isohalines and releasing of

internal waves. In addition, APE increases quickly and suddenly (the lower panel of Figure 2.54) not only at the edge (21.5 km) of the big valley but also at the upstream (22.2 km) of the big valley, suggesting the extended effects of internal motion on mixing. Depth-integrated pressure gradient power (the upper panel of Figure 2.55) has positive values along the thalweg indicating the increase in kinetic energy of deeper flooding currents and has negative values in the shoal regions indicating the decrease in kinetic energy of shallower ebbing currents. Bottom dissipation rate (the lower panel of Figure 2.55) also shows larger values along the thalweg indicating larger bottom currents.

2.7 Summary and conclusions

In a partially-mixed estuary, isohaline slope is generally landward inclined and is smaller during the neap tide than during the spring tide. During the neap tide, the water is more stratified and the obvious halocline is present. Halocline position is significantly affected by the bottom topographic features especially during the maximum ebb and flood. Generally the halocline tends to be depressed over the upstream slope of a bottom valley or the downstream slope of a bottom hill, where downward advection is correspondingly present due to horizontal convergence in the upper layer and horizontal divergence in the lower layer. Conversely the halocline is elevated over the downstream slope of a valley or the upstream slope of a bottom hill, where upward advection is present. The flow condition (supercritical or subcritical) tends to be changed over the downstream edge of the bottom slope, where an internal hydraulic jump may be present if the supercritical currents hit the subcritical currents. As a result, the kinetic energy is consumed to increase the potential energy.

The production and propagation of the halocline fluctuations induced by the bottom topographic features are well explained by use of both the quasi-steady two layer hydraulics and the internal wave theories. The internal wave, i.e. the halocline fluctuations, begins to be produced during the accelerating stage and is significantly amplified during the maximum ebb or flood when the supercritical condition is fulfilled. The internal wave tends to be arrested over the bottom topographic features due to the balance between the baroclinic effect and the advection effect. When the tidal currents reduce to be subcritical, the internal wave begins to

propagate upstream. The internal wave amplitude tends to be diminished during the upstream propagation due to the inverse effect of the bottom topographic feature and the relatively strong shear at the top of the halocline.

Corresponding to the halocline behavior, the movement of the dye patch is also affected by the bottom topography. Generally the dye is significantly moved upward/downward where there is relatively strong upward/downward advection induced by the bottom slope. The dye intruding upward during the ebb is then advected landward at a faster rate, catching up and mixing with the landward bottom dye due to the relatively strong shear in the bottom layer during the flood. As a result, the dye patch as a whole is moved and expanded in both the landward and upward directions. In addition, the dye patch is expanded upward to a larger extent during the spring tide than during the neap tide due to less stratified water column and stronger turbulent mixing.

The three-dimensional baroclinic simulation well reproduced the flow and the salinity fields at the interest reach. The model vertical advection induced by the bottom topographic features is consistent with the analysis of the observed data. The model results indicate that strong vertical mixing regions are present not only within the bottom boundary layer during flood but also at the upstream slope of the bottom valleys and hills during ebb and at the current frontal zone during the transition from ebb to flood. The model results also suggest that the sudden release of the internal wave during the transition from ebb to flood leads to enhanced vertical mixing in the vicinity of the halocline.

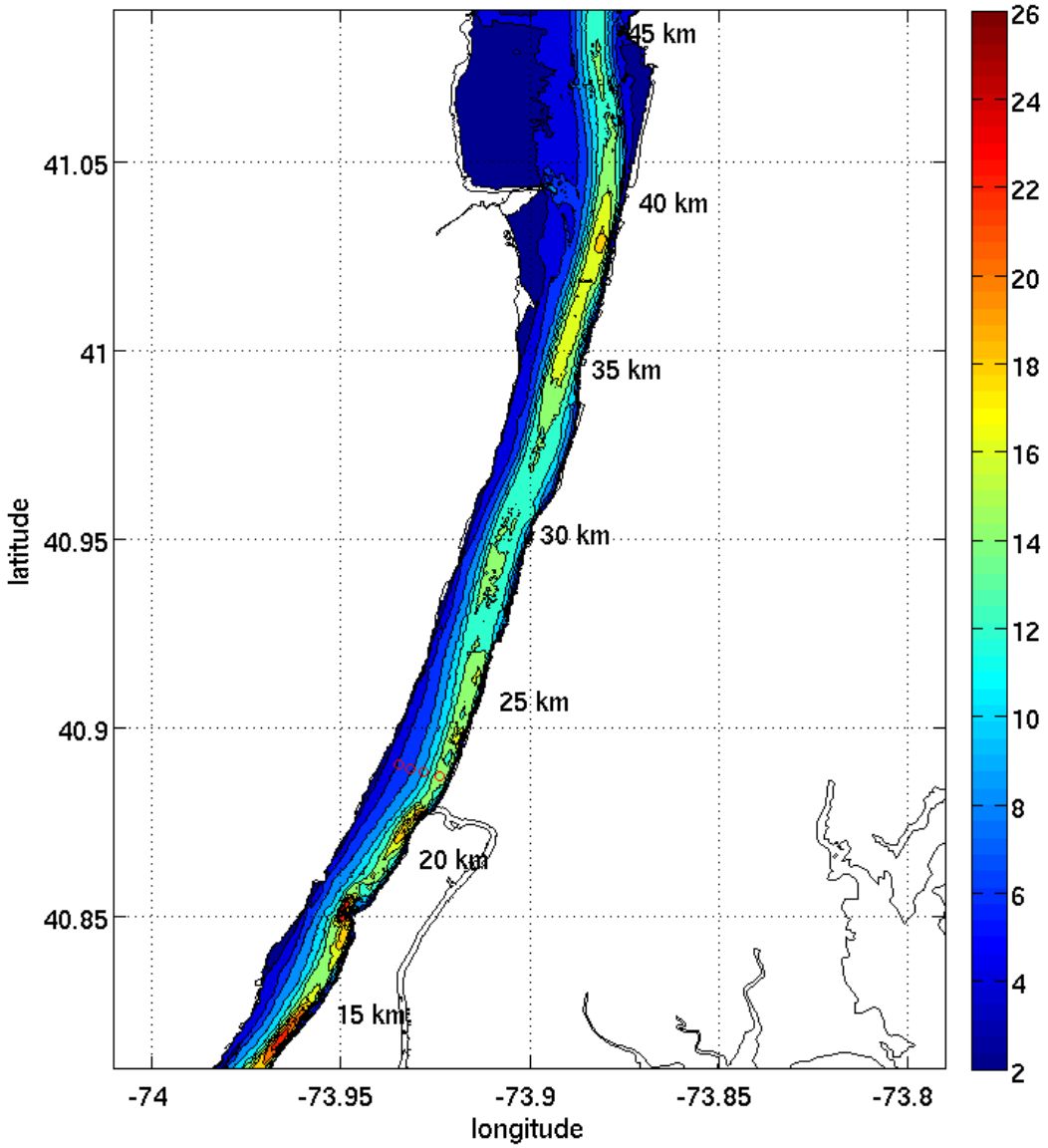

Figure 2.1 Bottom topography of the lower Hudson Estuary. The red circles show the position of moored ADCPs. The 2002 dye tracer experiments were mainly carried out at 15~40 km away from the Battery, NY.

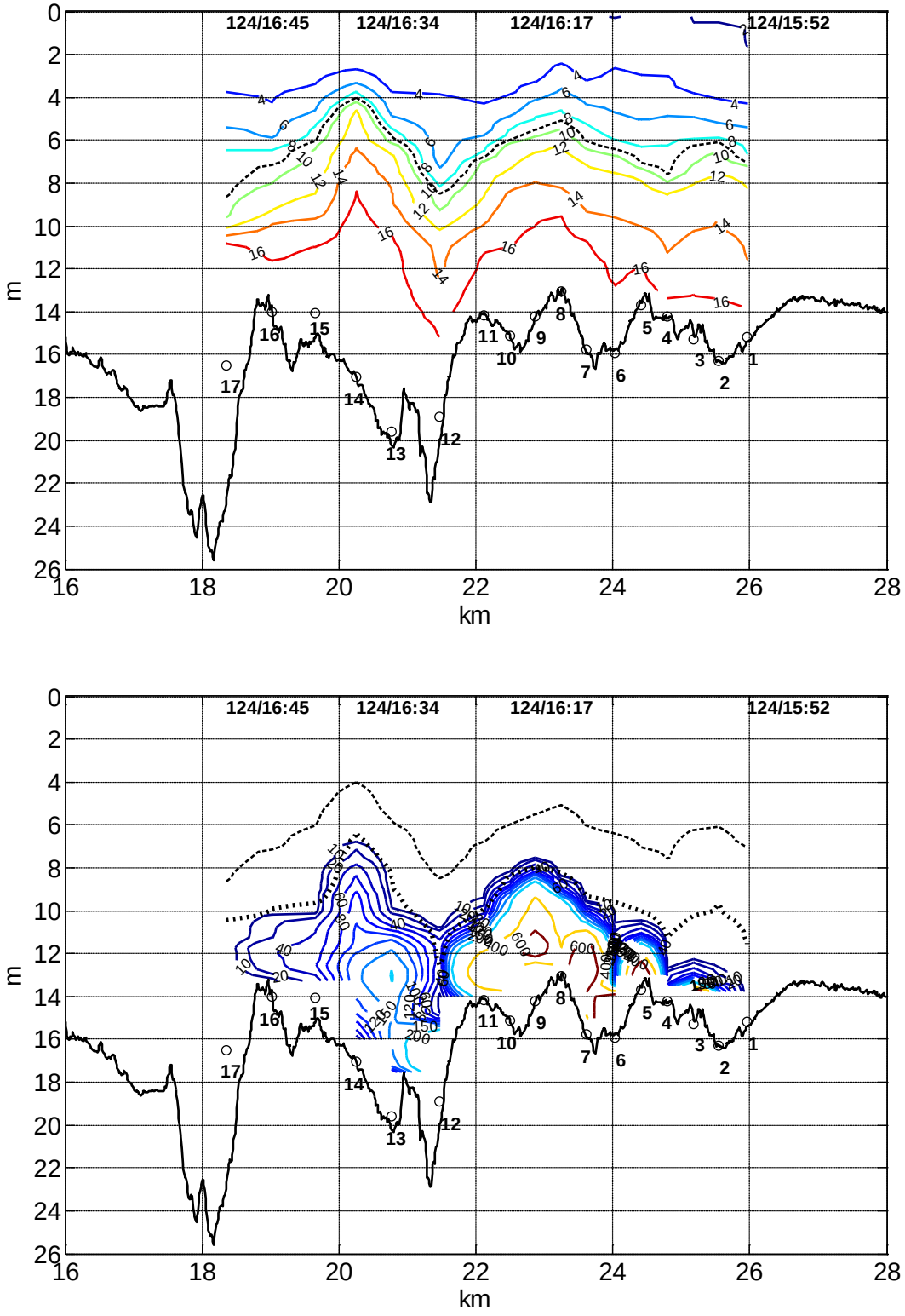

Figure 2.2 Salinity [*psu*] (upper panel) and dye concentration (lower panel) in a longitudinal section at the maximum ebb of neap tide. The dashed black line is 9 *psu* isohaline. The dotted black line is 14 *psu* isohaline. The data are from the first dye release experiment.

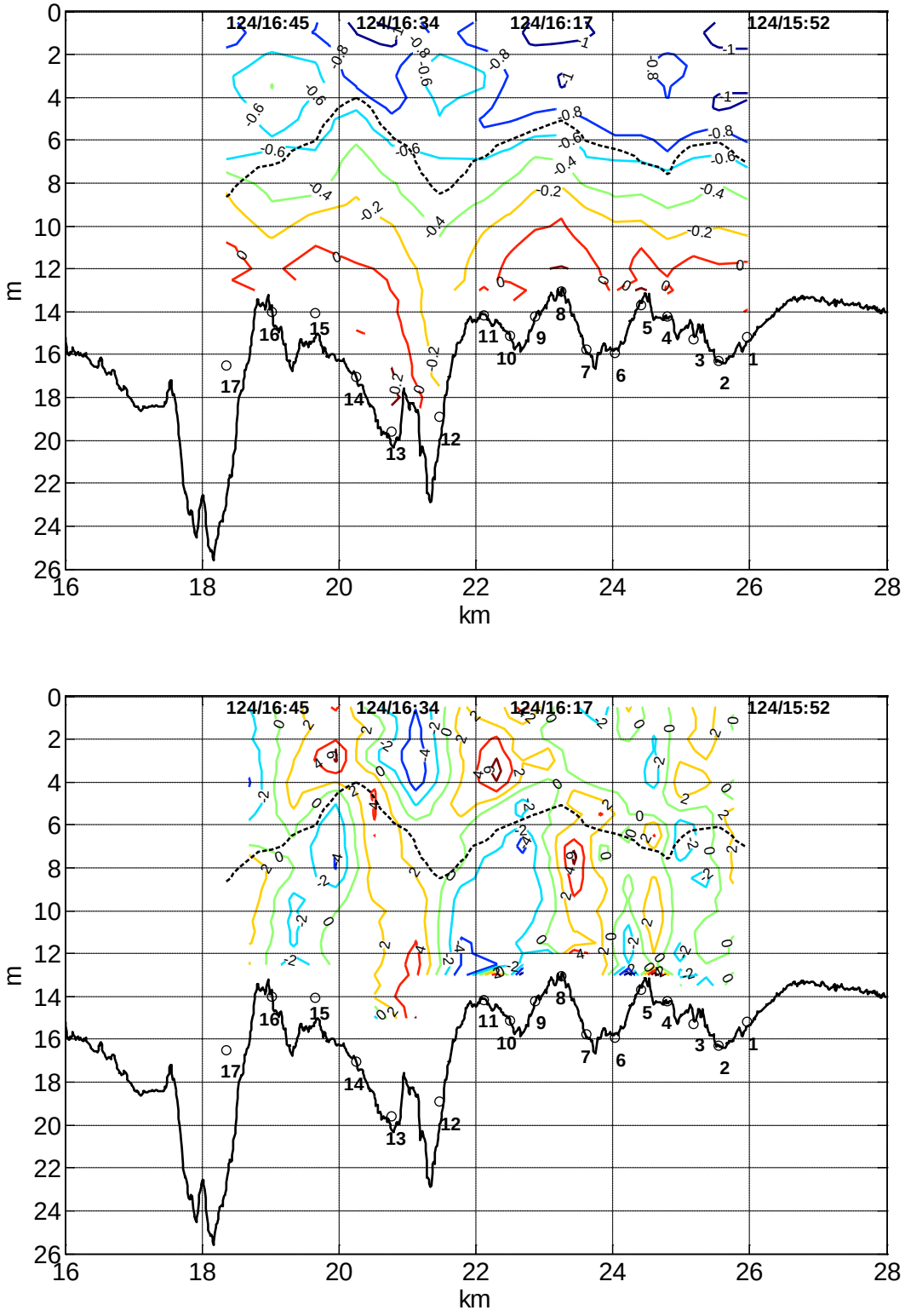

Figure 2.3 Along-channel velocity u [m/s] (upper panel) and strain rate $\partial w / \partial z$ i.e. negative horizontal divergence $-\partial u / \partial x$ [$10^{-4}\, s^{-1}$] (lower panel) in a longitudinal section at the maximum ebb of neap tide. The dashed black line is 9 *psu* isohaline.

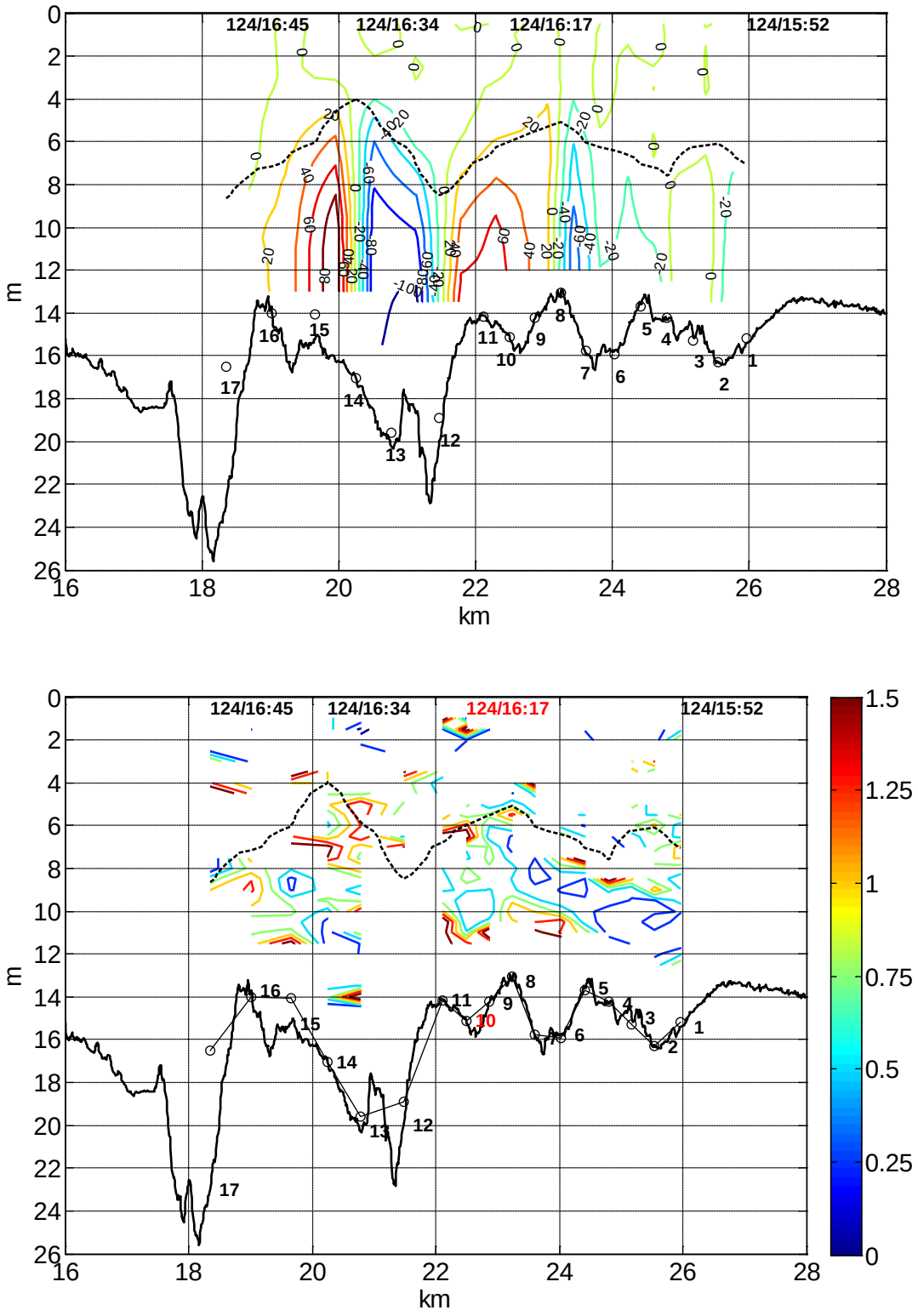

Figure 2.4 Baroclinic gradient $\partial \sum_{z}^{z_r} s / \partial x$ [10^{-4} *psu/m*] (upper panel) and Richardson number R_i (lower panel) with 9 *psu* dashed in a longitudinal section at the maximum ebb of neap tide.

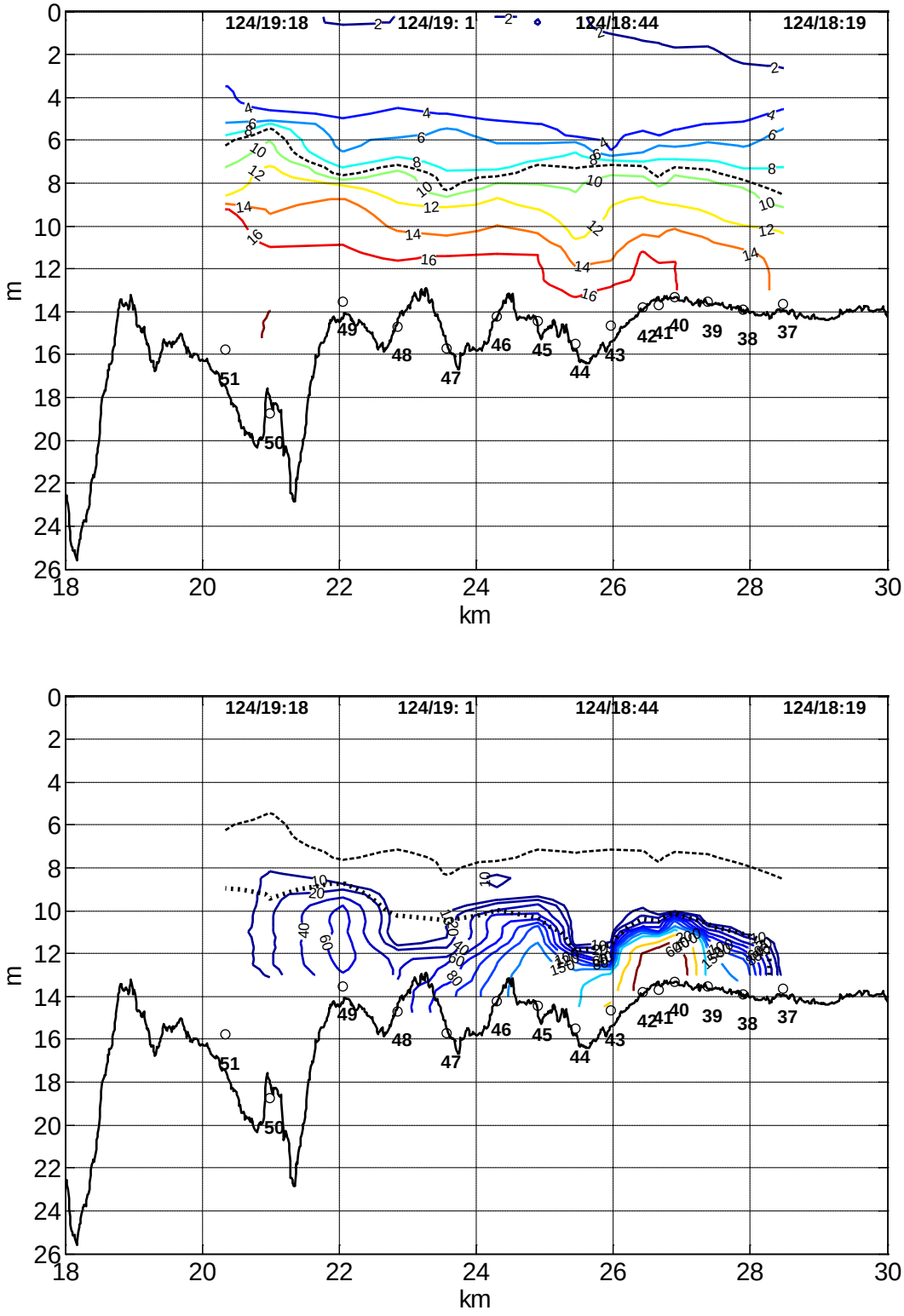

Figure 2.5 Salinity [*psu*] (upper panel) and dye concentration (lower panel) in a longitudinal section at the early flood of neap tide. The dashed black line is 9 *psu* isohaline. The dotted black line is 14 *psu* isohaline. The data are from the first dye release experiment.

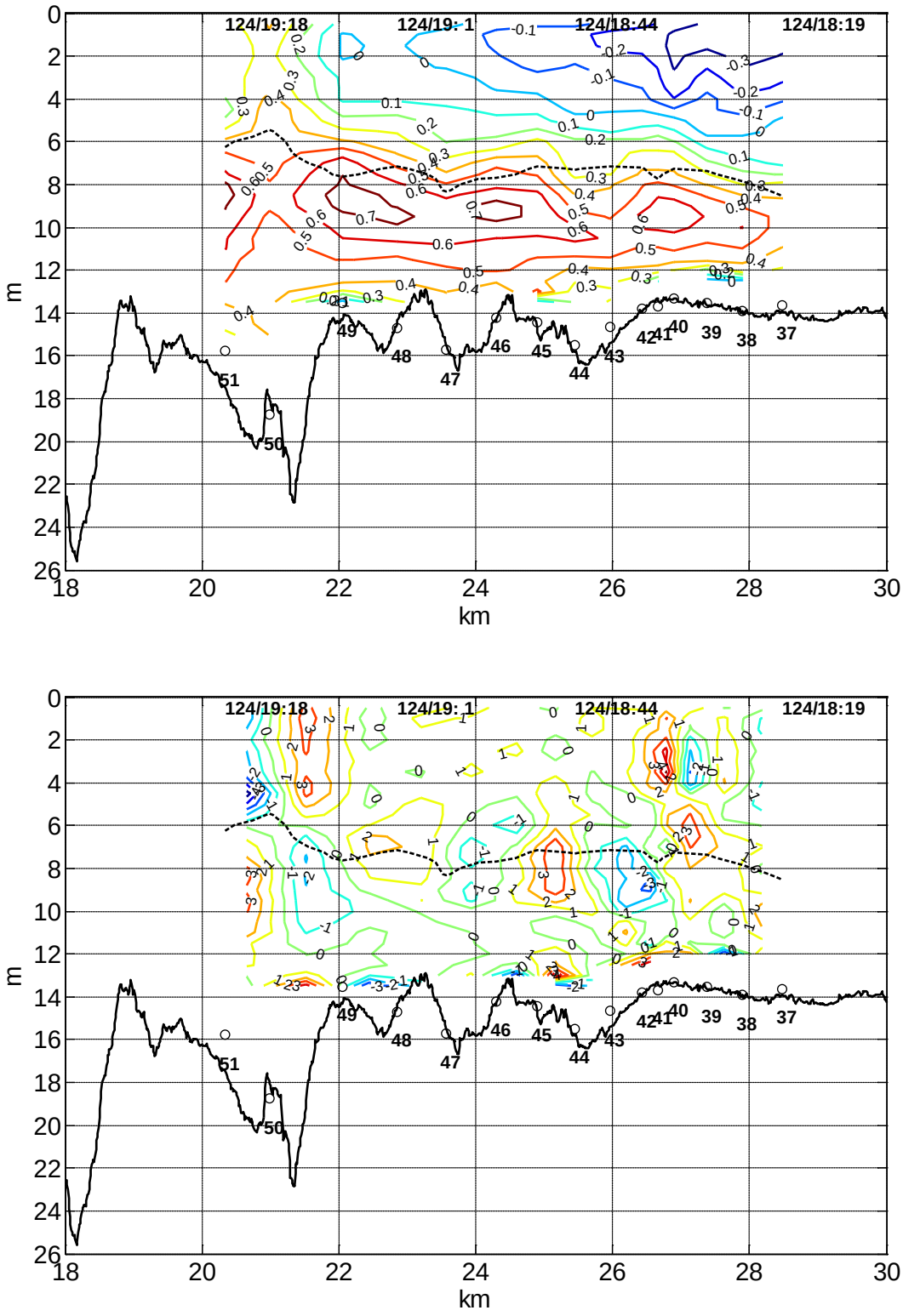

Figure 2.6 Along-channel velocity u [m/s] (upper panel) and strain rate $\partial w / \partial z$ i.e. negative horizontal divergence $-\partial u / \partial x$ [$10^{-4}\ s^{-1}$] (lower panel) in a longitudinal section at the early flood of neap tide. The dashed black line is 9 *psu* isohaline.

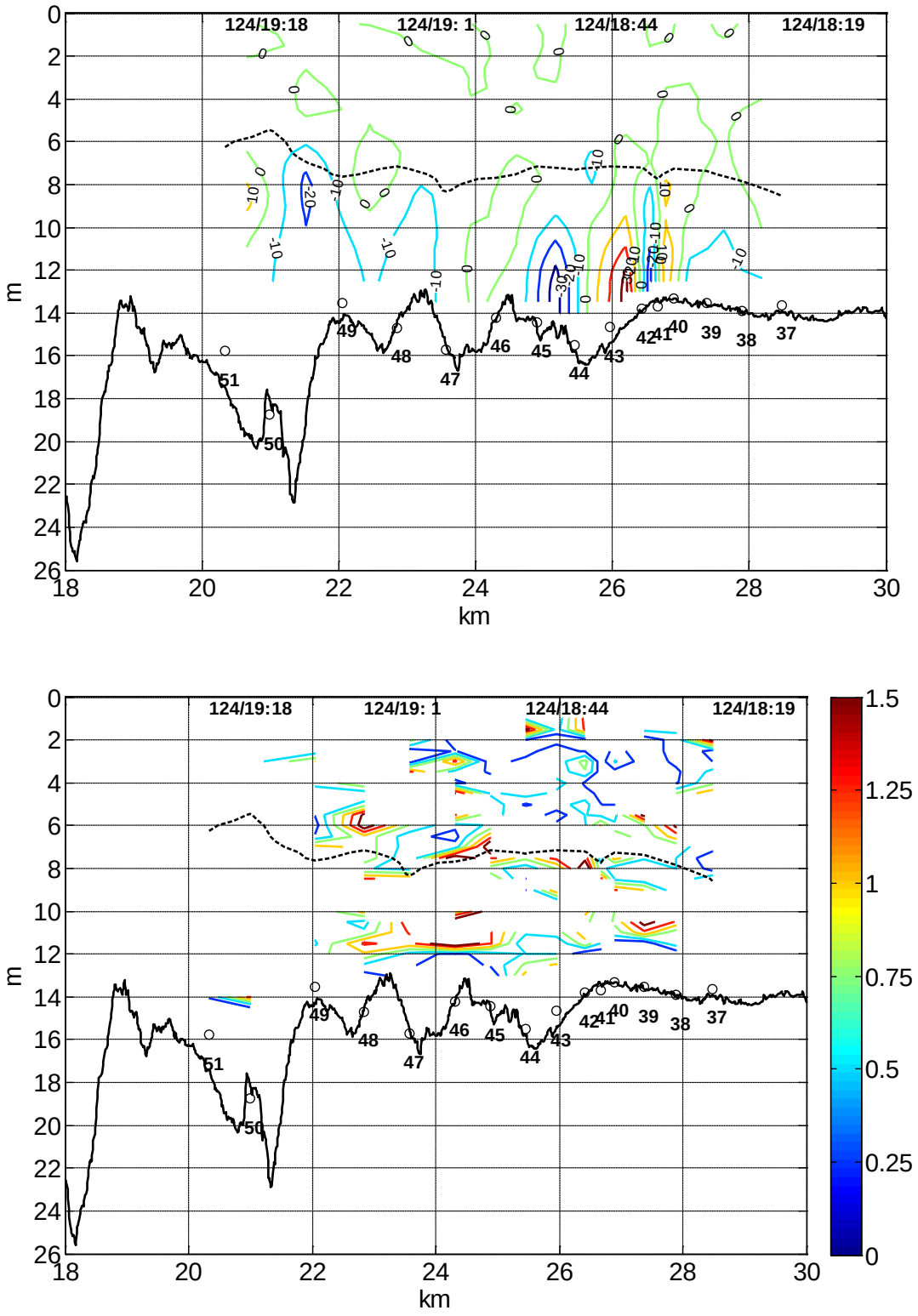

Figure 2.7 Baroclinic gradient $\partial \sum_{z}^{z_r} s / \partial x$ [10^{-4} *psu/m*] (upper panel) and Richardson number R_i (lower panel) with 9 *psu* dashed in a longitudinal section at the early flood of neap tide.

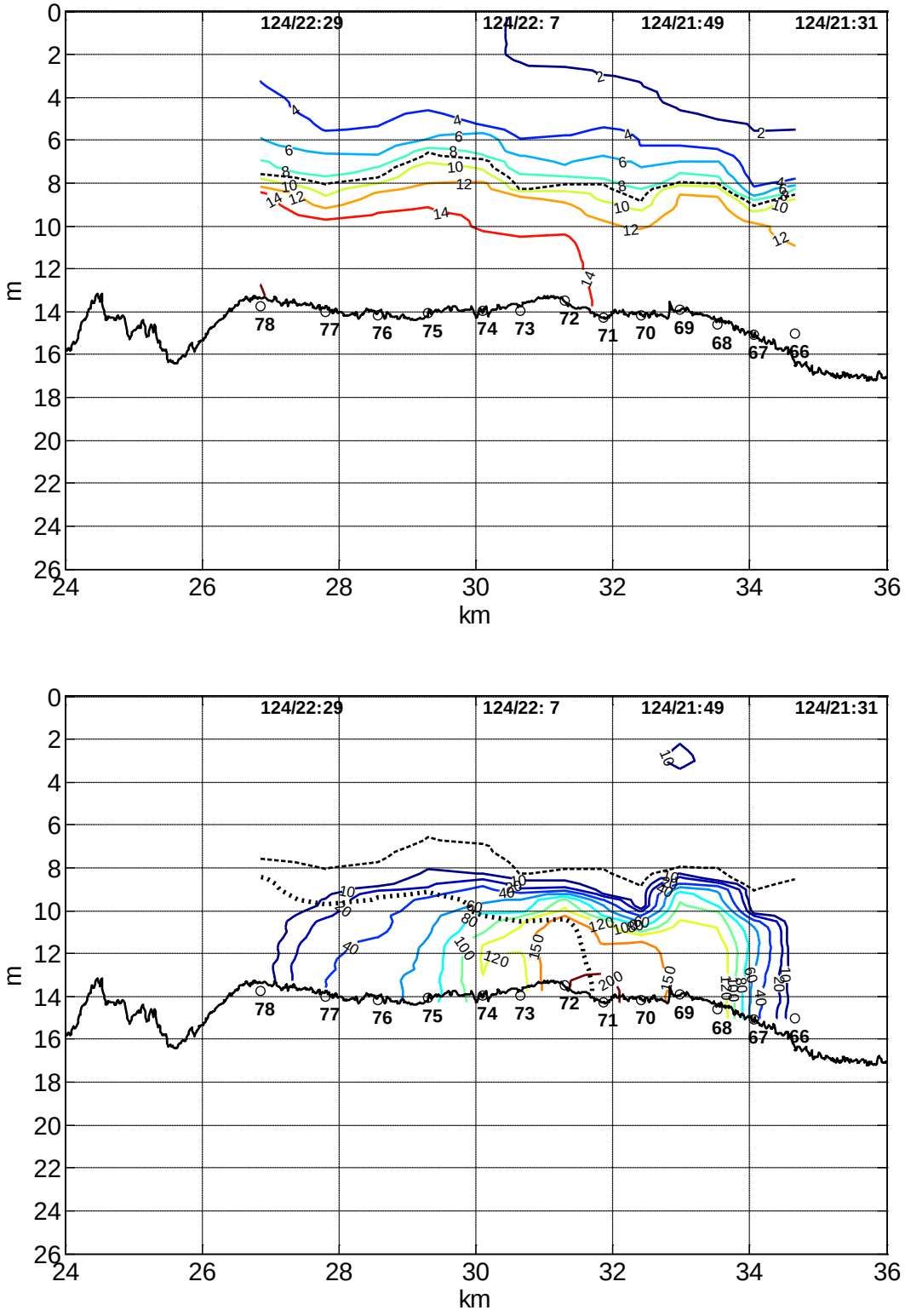

Figure 2.8 Salinity [*psu*] (upper panel) and dye concentration (lower panel) in a longitudinal section at the maximum flood of neap tide. The dashed black line is 9 *psu* isohaline. The dotted black line is 14 *psu* isohaline. The data are from the first dye release experiment.

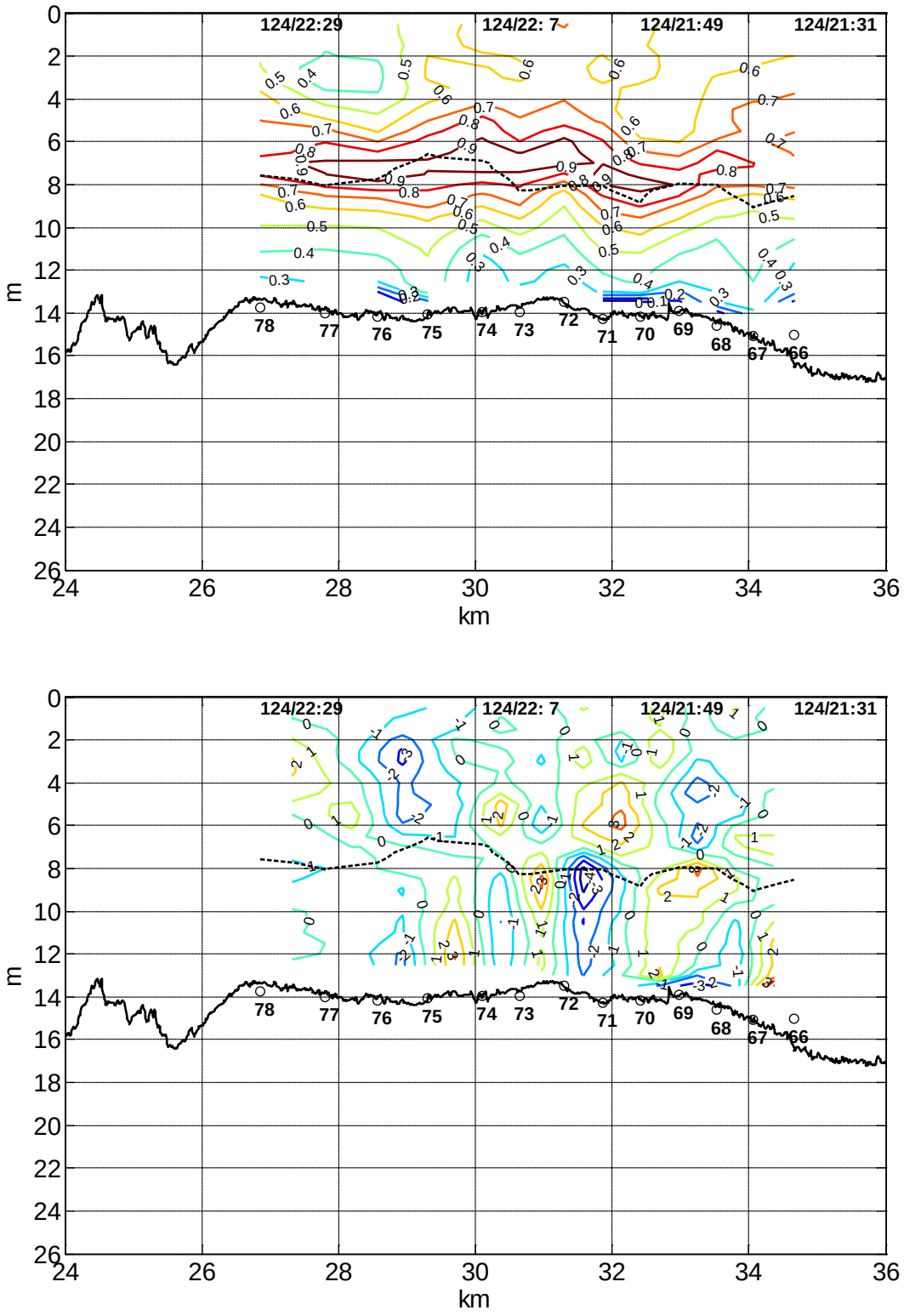

Figure 2.9 Along-channel velocity u [m/s] (upper panel) and strain rate $\partial w / \partial z$ i.e. negative horizontal divergence $-\partial u / \partial x$ [$10^{-4}\ s^{-1}$] (lower panel) in a longitudinal section at the maximum flood of neap tide. The dashed black line is 9 *psu* isohaline.

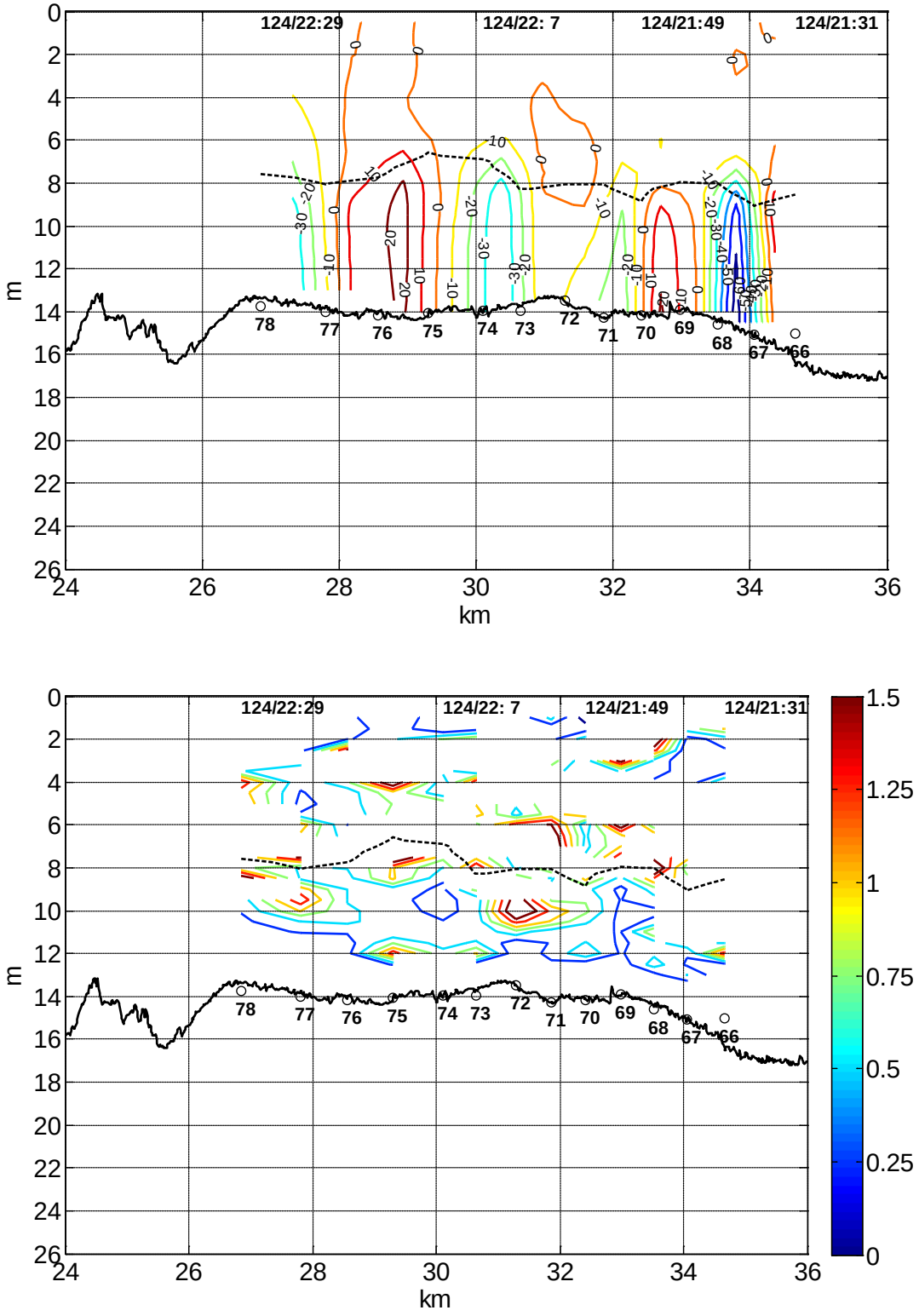

Figure 2.10 Baroclinic gradient $\partial \sum_z^{z_r} s / \partial x$ [10^{-4} *psu/m*] (upper panel) and Richardson number R_i (lower panel) with 9 *psu* dashed in a longitudinal section at the maximum flood of neap tide.

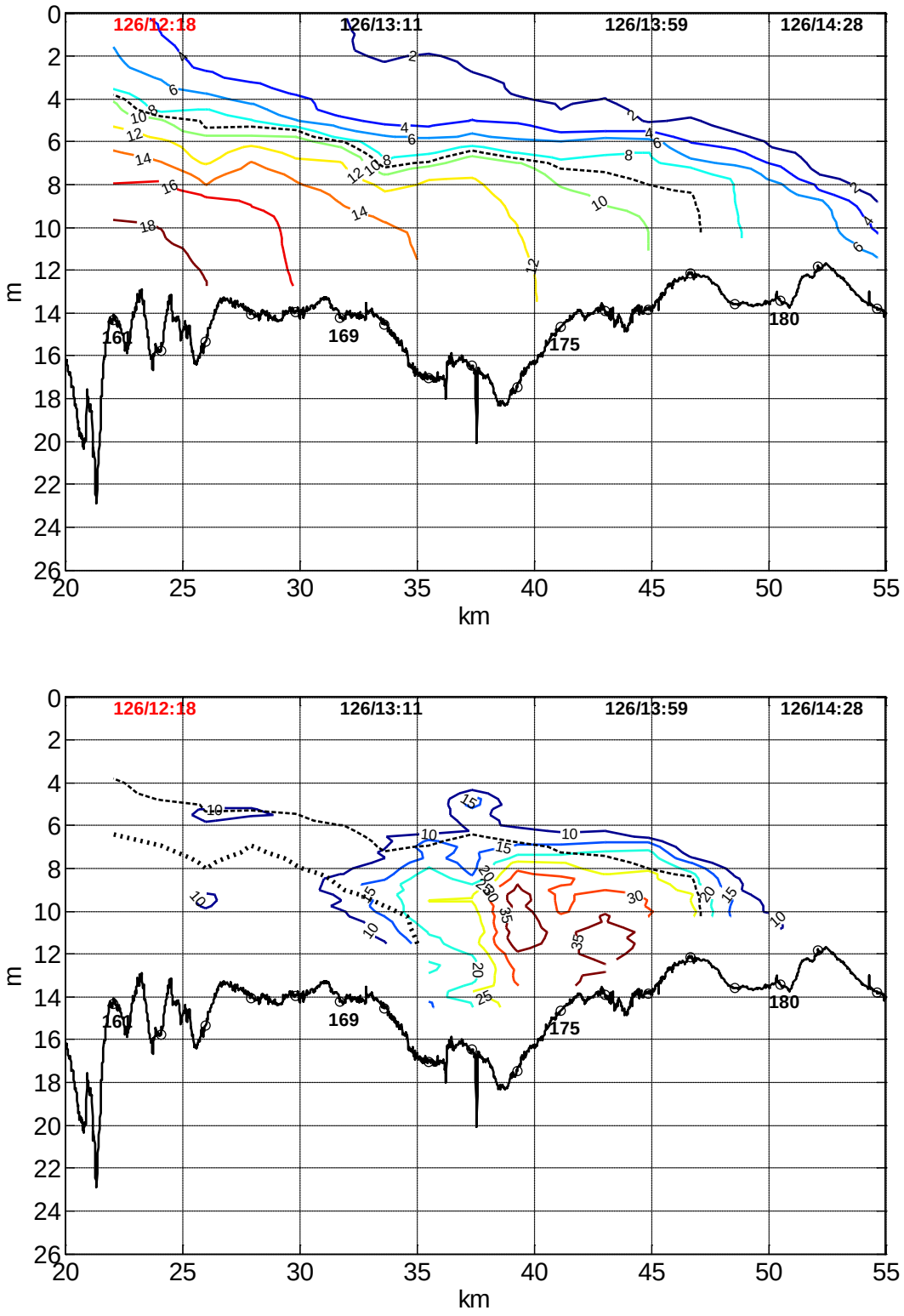

Figure 2.11 Salinity [*psu*] (upper panel) and dye concentration (lower panel) with 9 *psu* dashed and 14 *psu* dotted in a longitudinal section at the maximum flood of neap tide after three tidal cycles. The data are from the first dye release experiment.

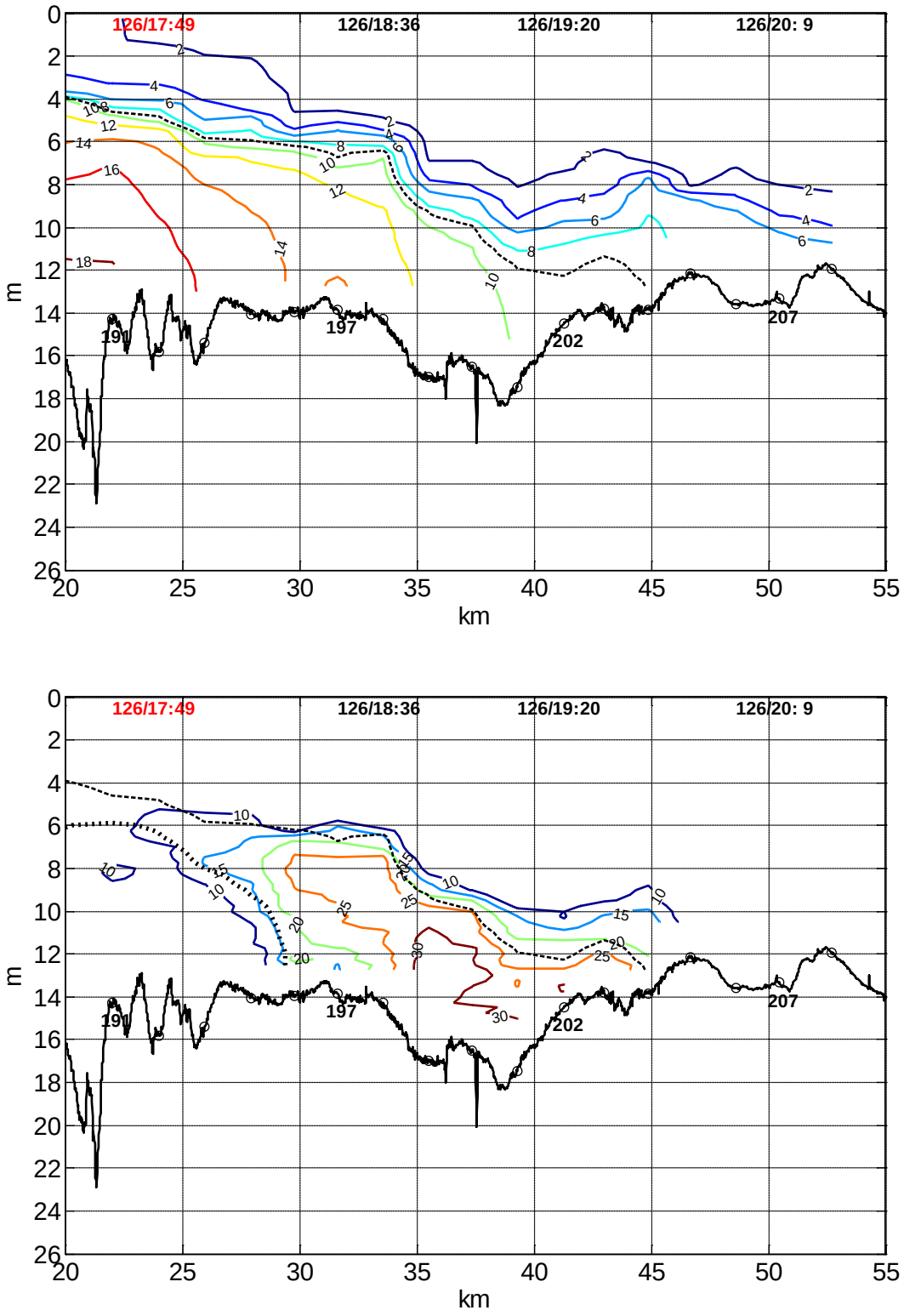

Figure 2.12 Salinity [*psu*] (upper panel) and dye concentration (lower panel) with 9 *psu* dashed and 14 *psu* dotted in a longitudinal section at the maximum ebb of neap tide after three tidal cycles. The data are from the first dye release experiment.

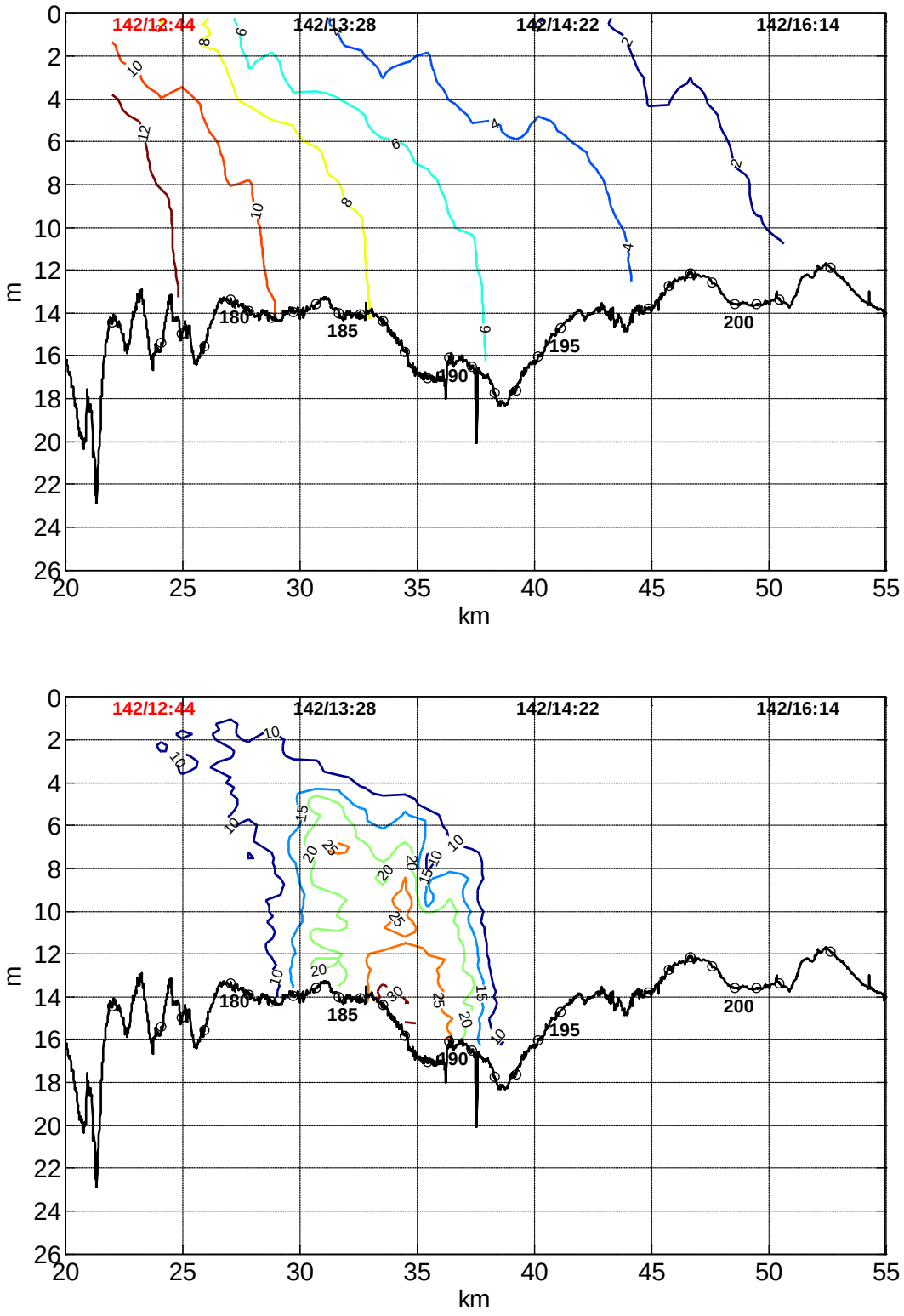

Figure 2.13 Salinity [*psu*] (upper panel) and dye concentration (lower panel) in a longitudinal section during transition from the neap to spring tides. The data are from the third dye release experiment.

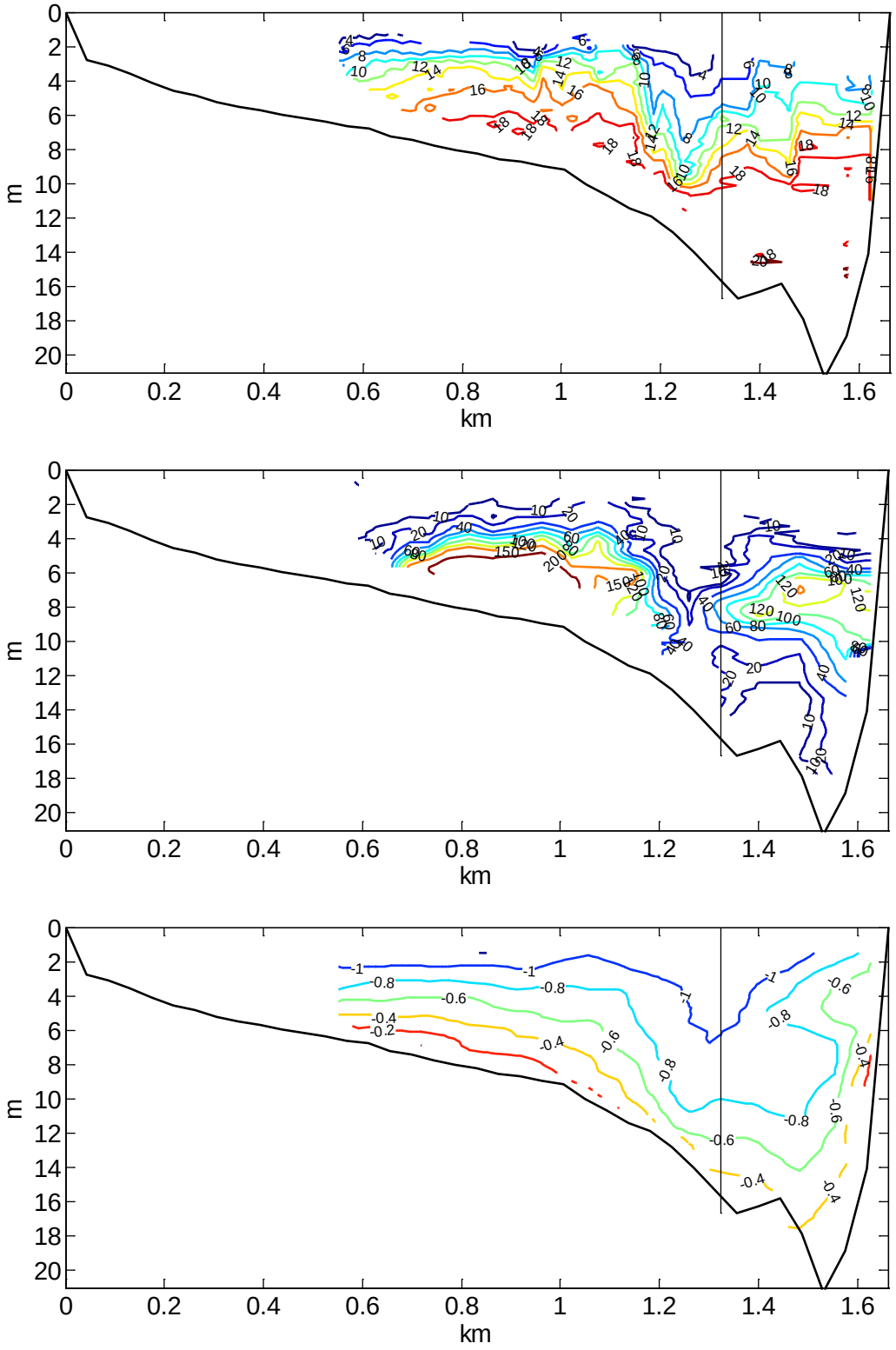

Figure 2.14 Salinity [*psu*] (upper panel), dye concentration (middle panel), and along-channel velocity u [*m/s*] (lower panel) in a lateral section across the big valley at ~21 km at the maximum ebb of neap tide. The thin black line shows where the along-channel survey passed. The data are from the second dye release experiment.

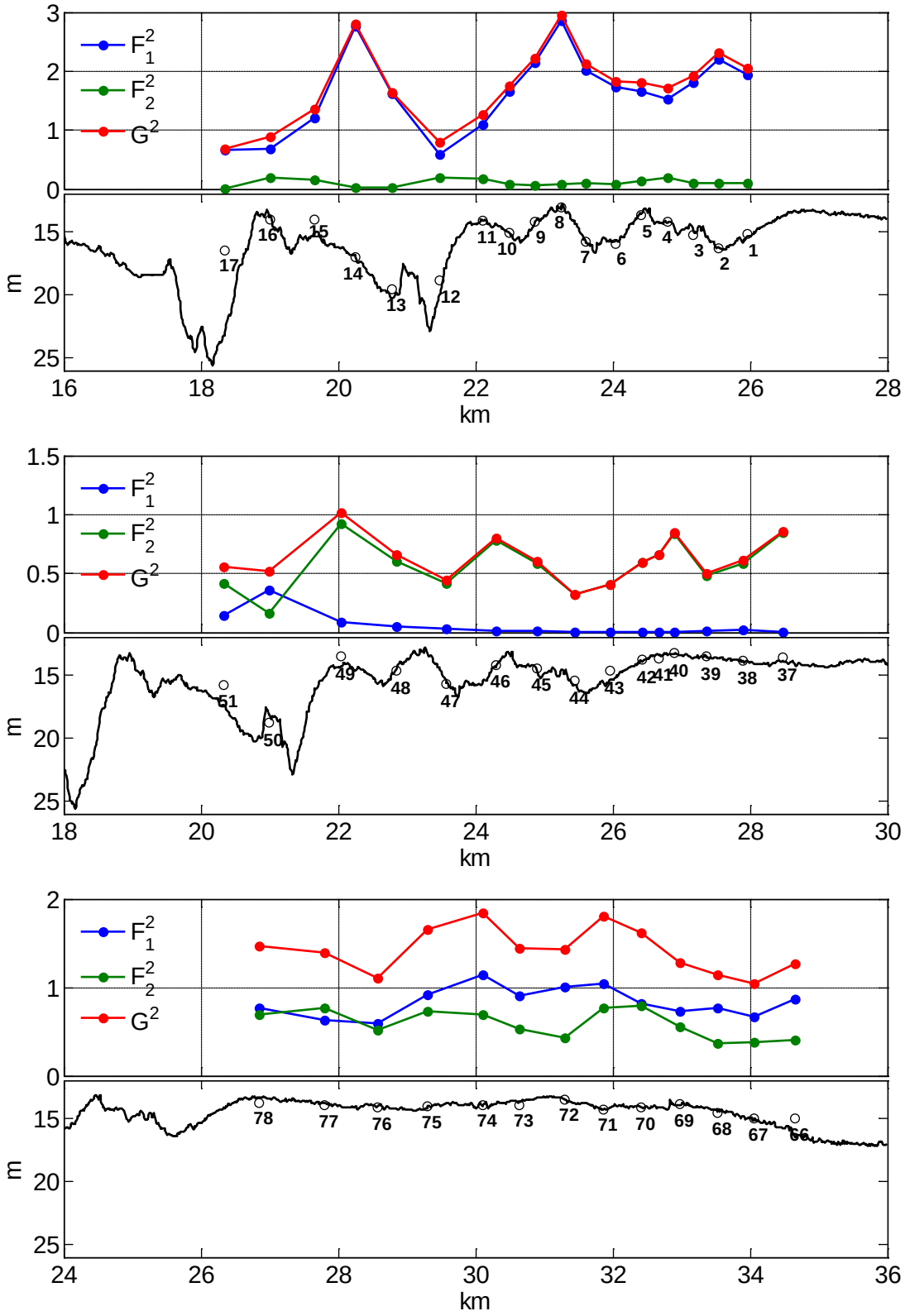

Figure 2.15 Squared layer Froude numbers F_1^2 and F_2^2 and squared composite Froude number G^2 in the longitudinal sections for the maximum ebb (upper panel), the early flood (middle panel), and the maximum flood (lower panel), of neap tide respectively.

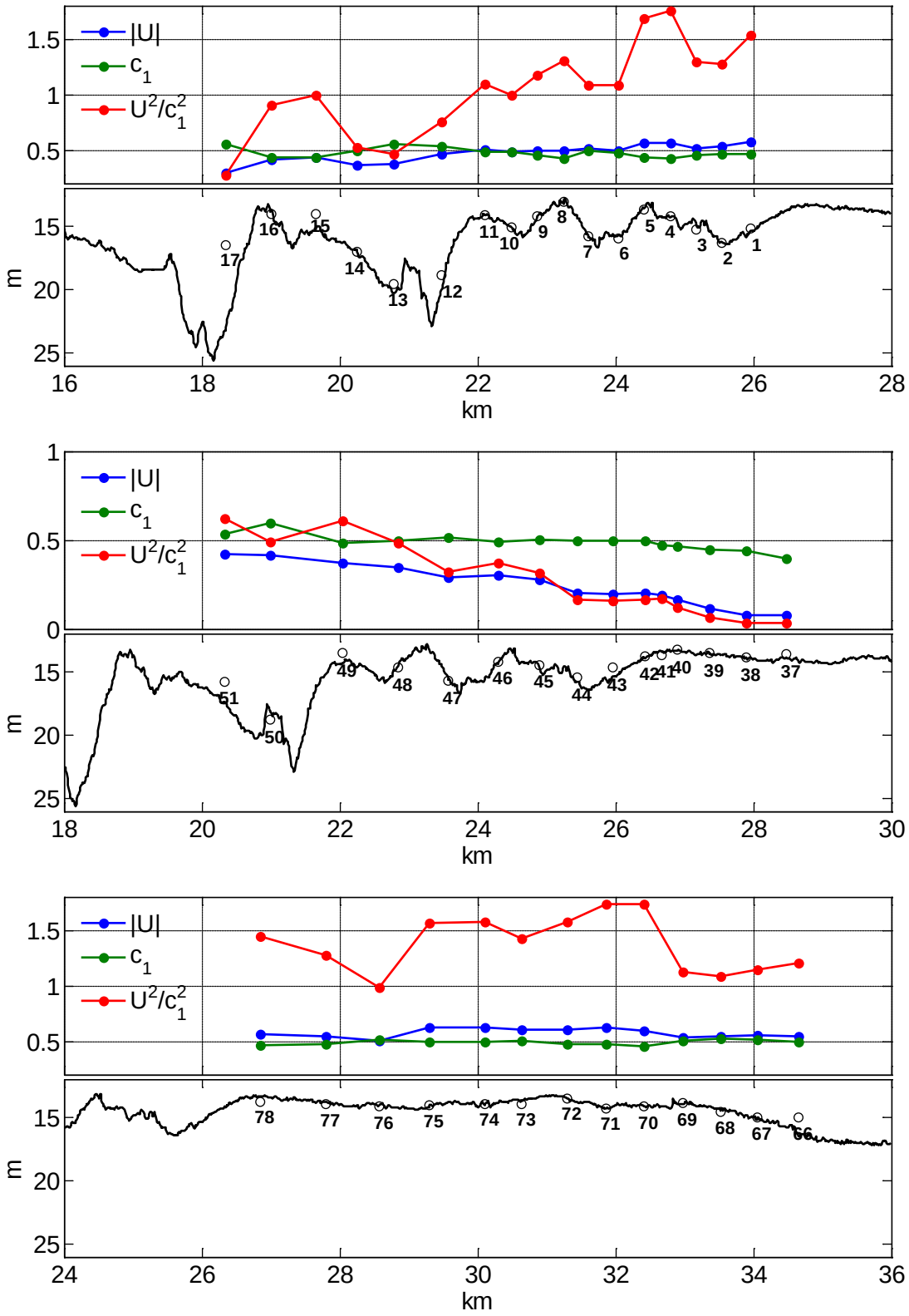

Figure 2.16 Depth-averaged along-channel velocity |*U*| [*m/s*], the first-mode internal wave speed c_1 [*m/s*], and their ratios in longitudinal sections for the maximum ebb (upper panel), the early flood (middle panel), and the maximum flood (lower panel), of neap tide respectively.

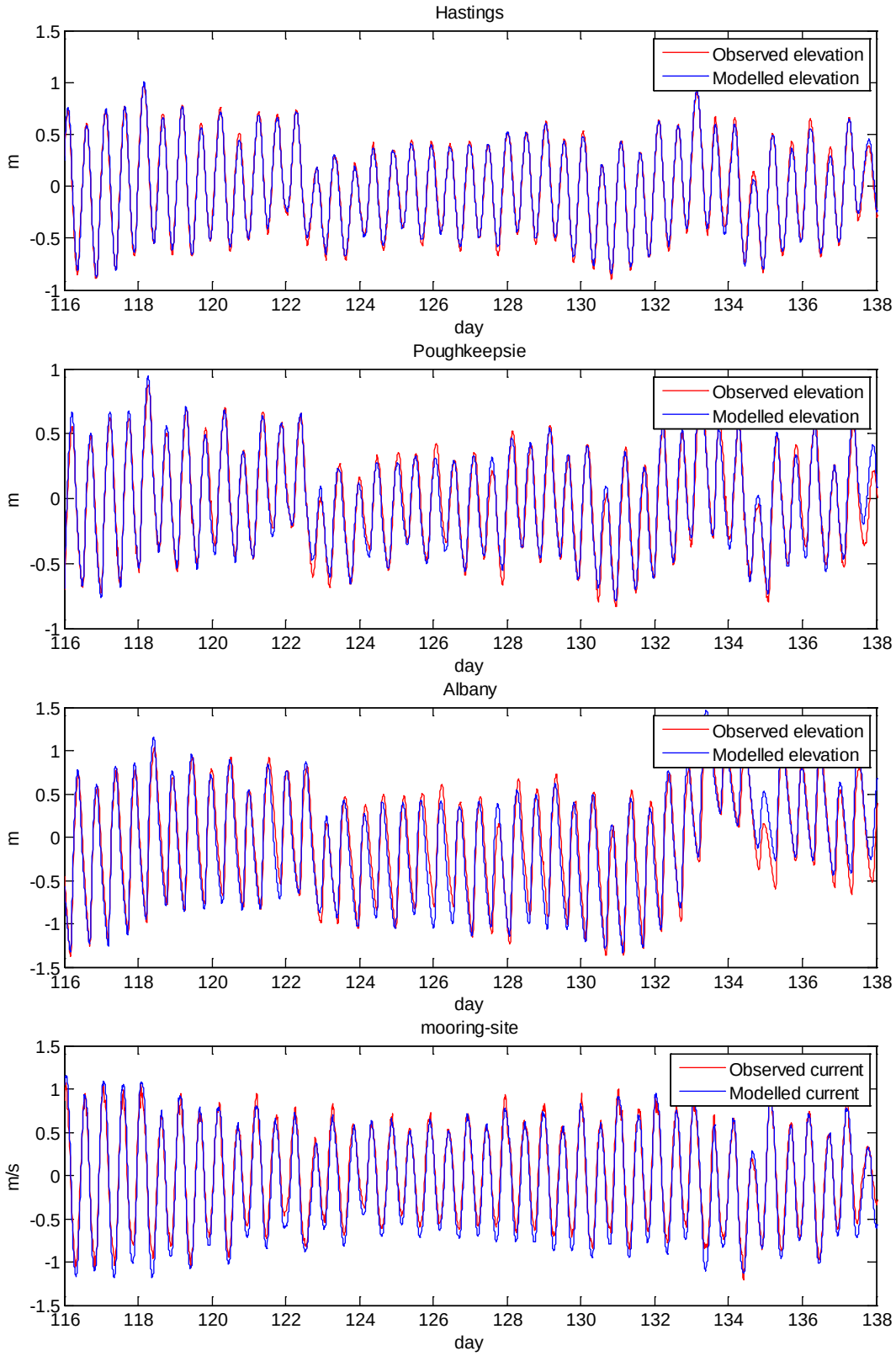

Figure 2.17 Comparison of water levels (upper three panels) and depth-averaged current (bottom panel) between the ROMS barotropic simulation and the observations at the Hastings, Poughkeepsie, Albany, and the moored site in the Hudson River (ref. Figure 3.1 for locations).

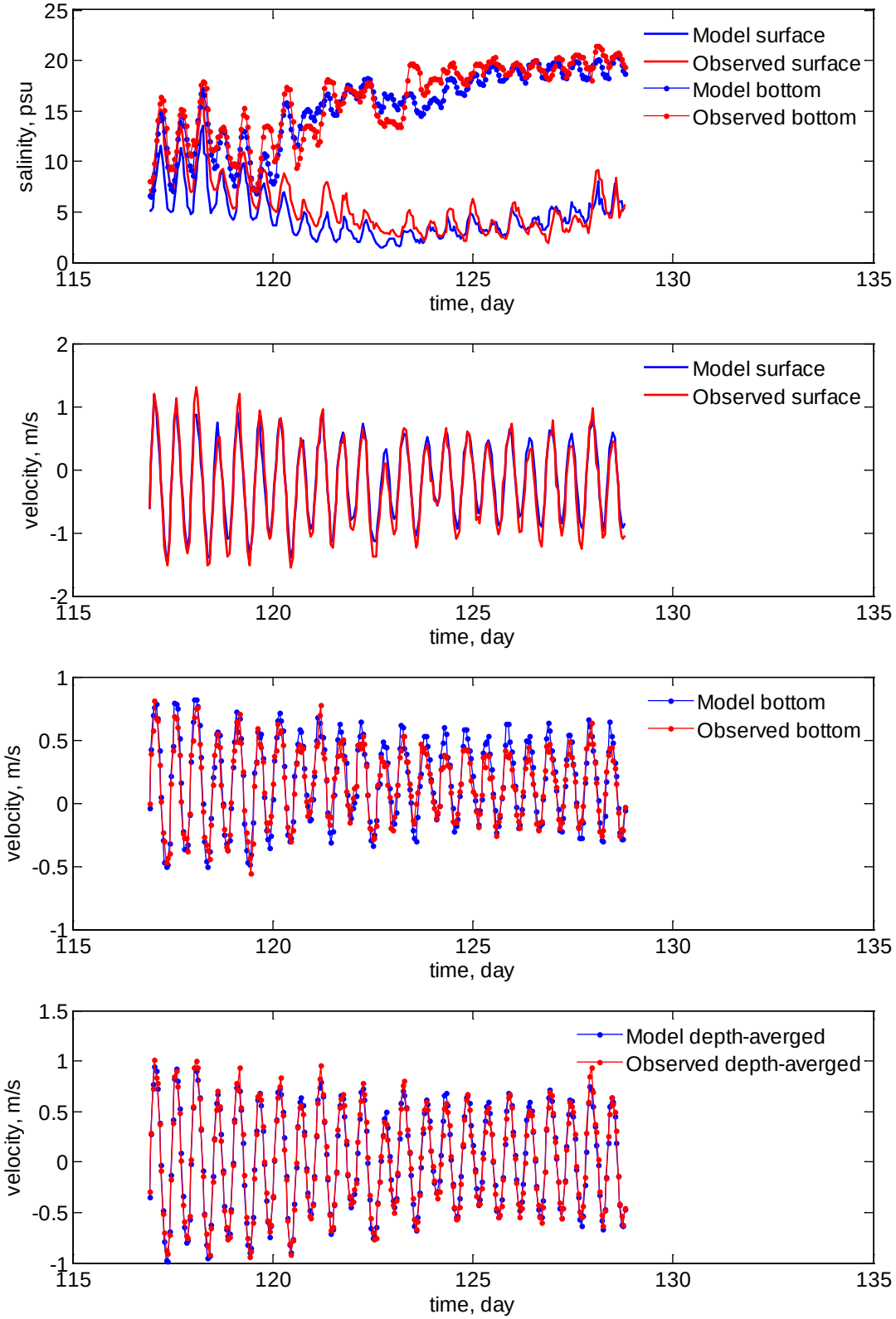

Figure 2.18 Comparison of time series of salinity (top panel) and currents (lower three panels) between the ROMS 3D simulation and the observations at the moored site of the lower Hudson.

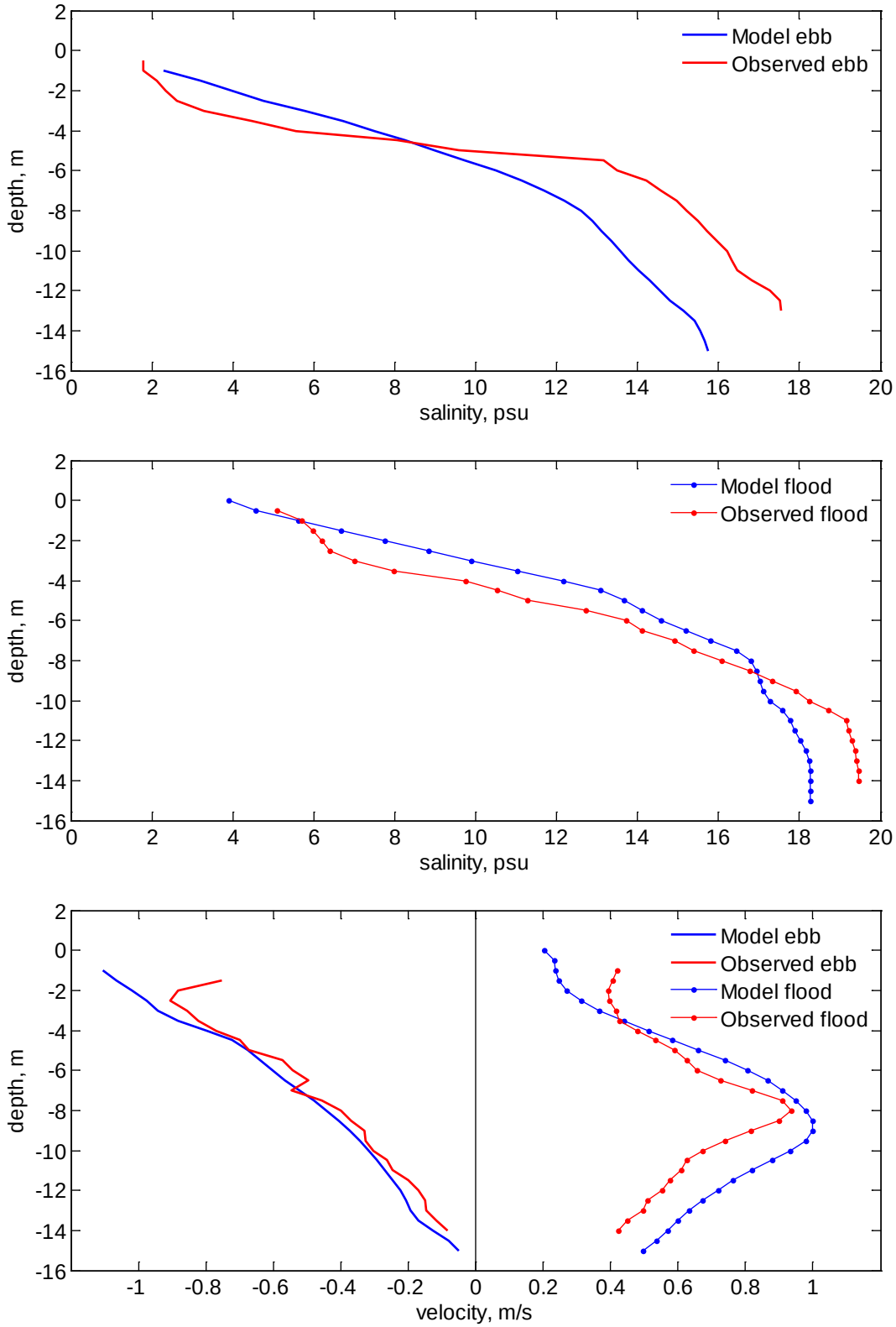

Figure 2.19 Comparison of vertical profiles of salinity (upper two panels) and currents (bottom panel) between the ROMS 3D simulation and the observations in the vicinity of the moored site of the lower Hudson.

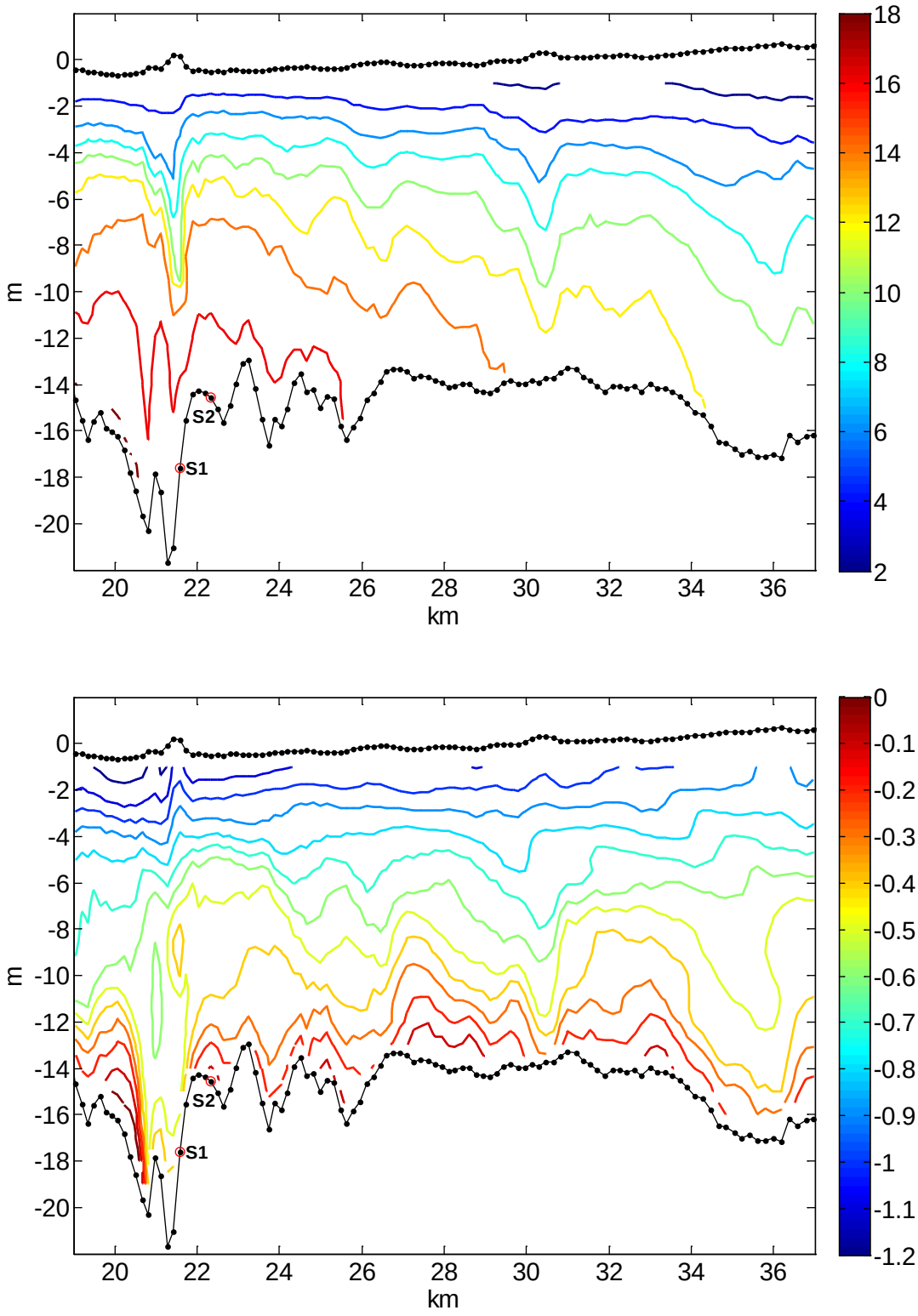

Figure 2.20 Model salinity [*psu*] (upper panel) and along-channel velocity *u* [*m/s*] (lower panel) in a longitudinal section at the maximum ebb (**t1** in tidal cycle Figures 2.38~2.51) of neap tide. Free surface (exaggerated by 30 times) and bottom topography have been shown as dotted lines.

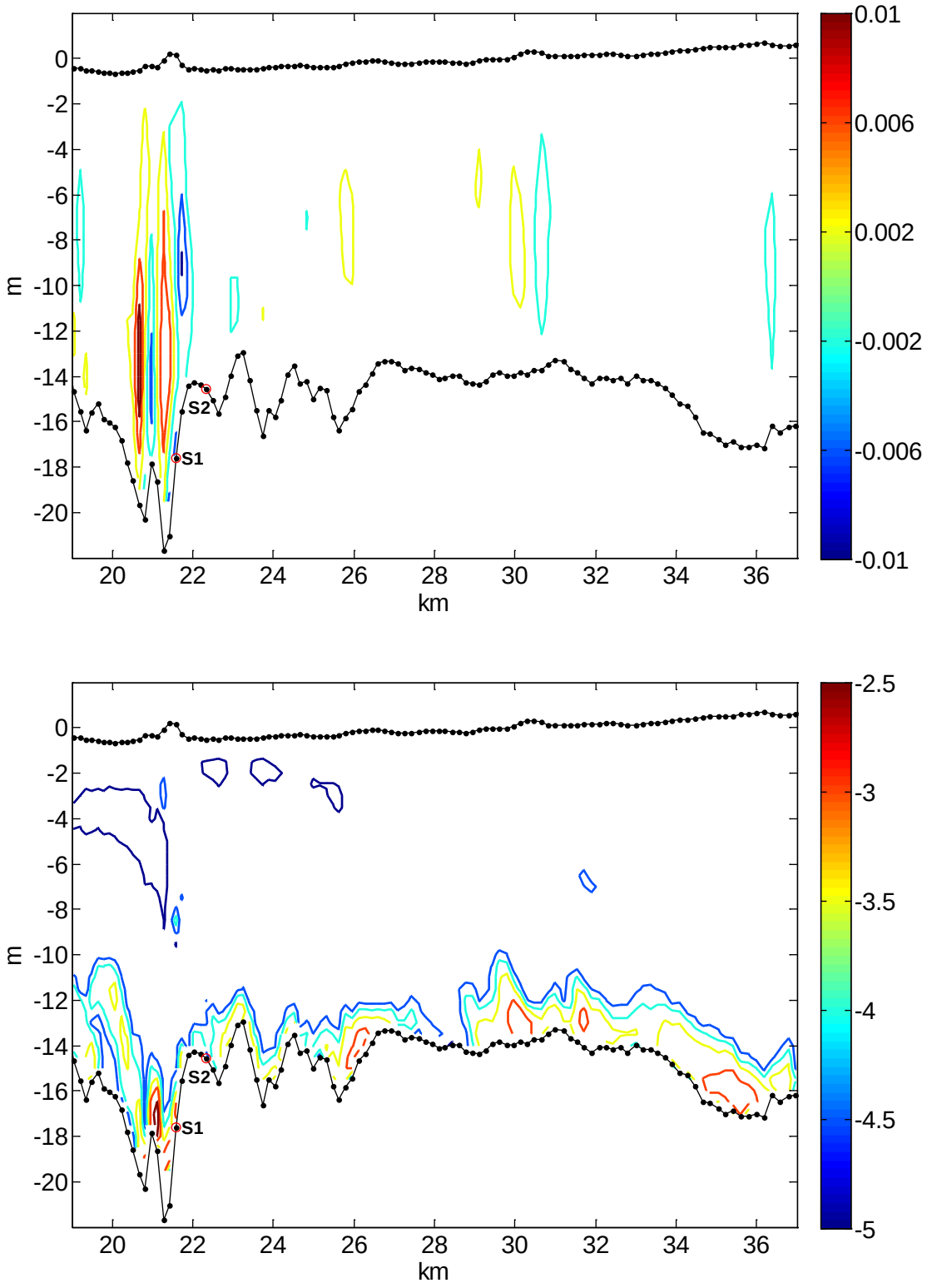

Figure 2.21 Model vertical advection *w* [*m/s*] (upper panel) and logged viscosity [m^2/s] (lower panel) in a longitudinal section at the maximum ebb of neap tide. Free surface (exaggerated by 30 times) and bottom topography have been shown as dotted lines.

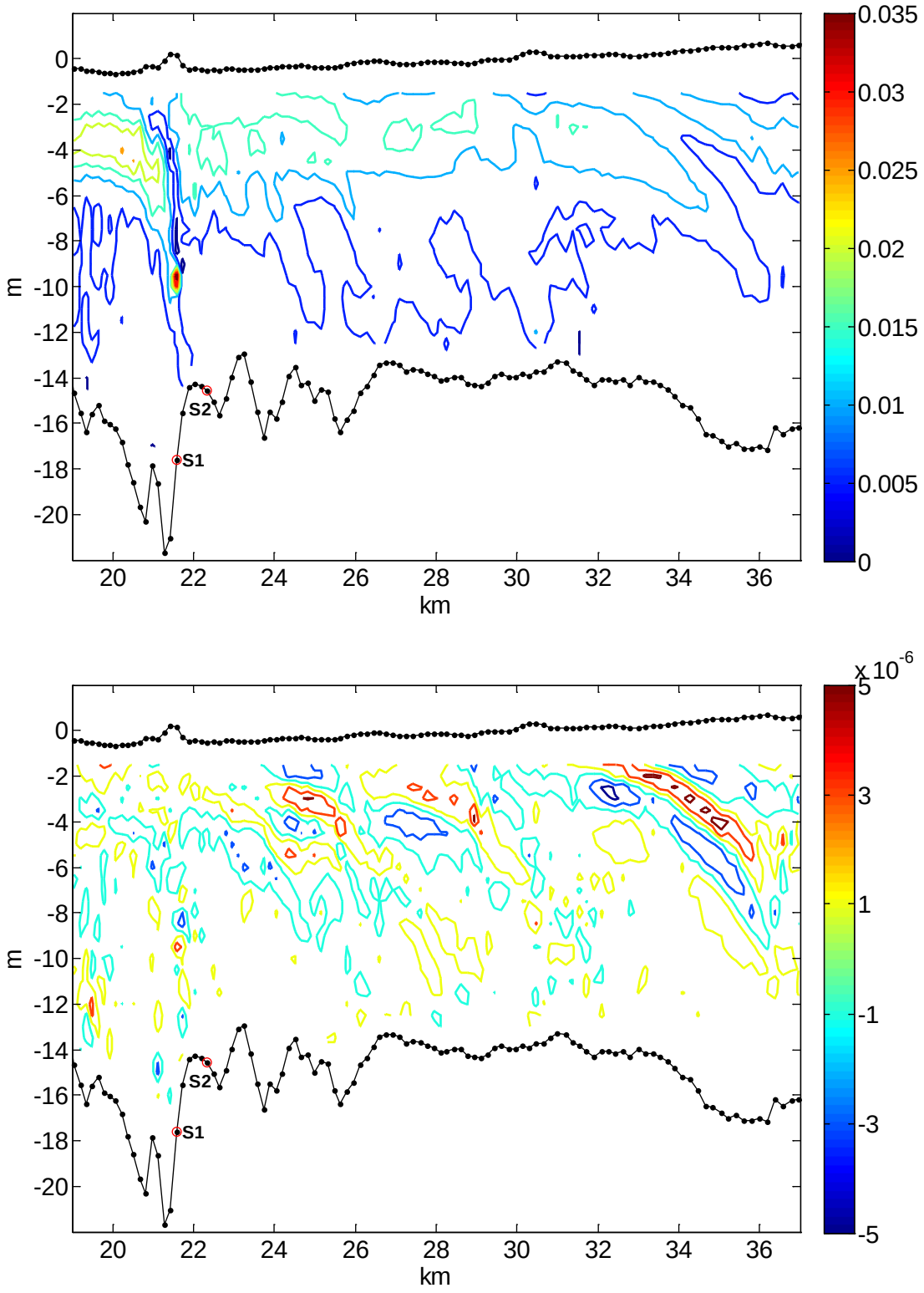

Figure 2.22 Model Brunt–Väisälä frequency N^2 [s^{-1}] (upper panel) and its local time rate $\partial N^2/\partial t$ [s^{-2}] (lower panel) in a longitudinal section at the maximum ebb of neap tide. Free surface (exaggerated by 30 times) and bottom topography have been shown as dotted lines.

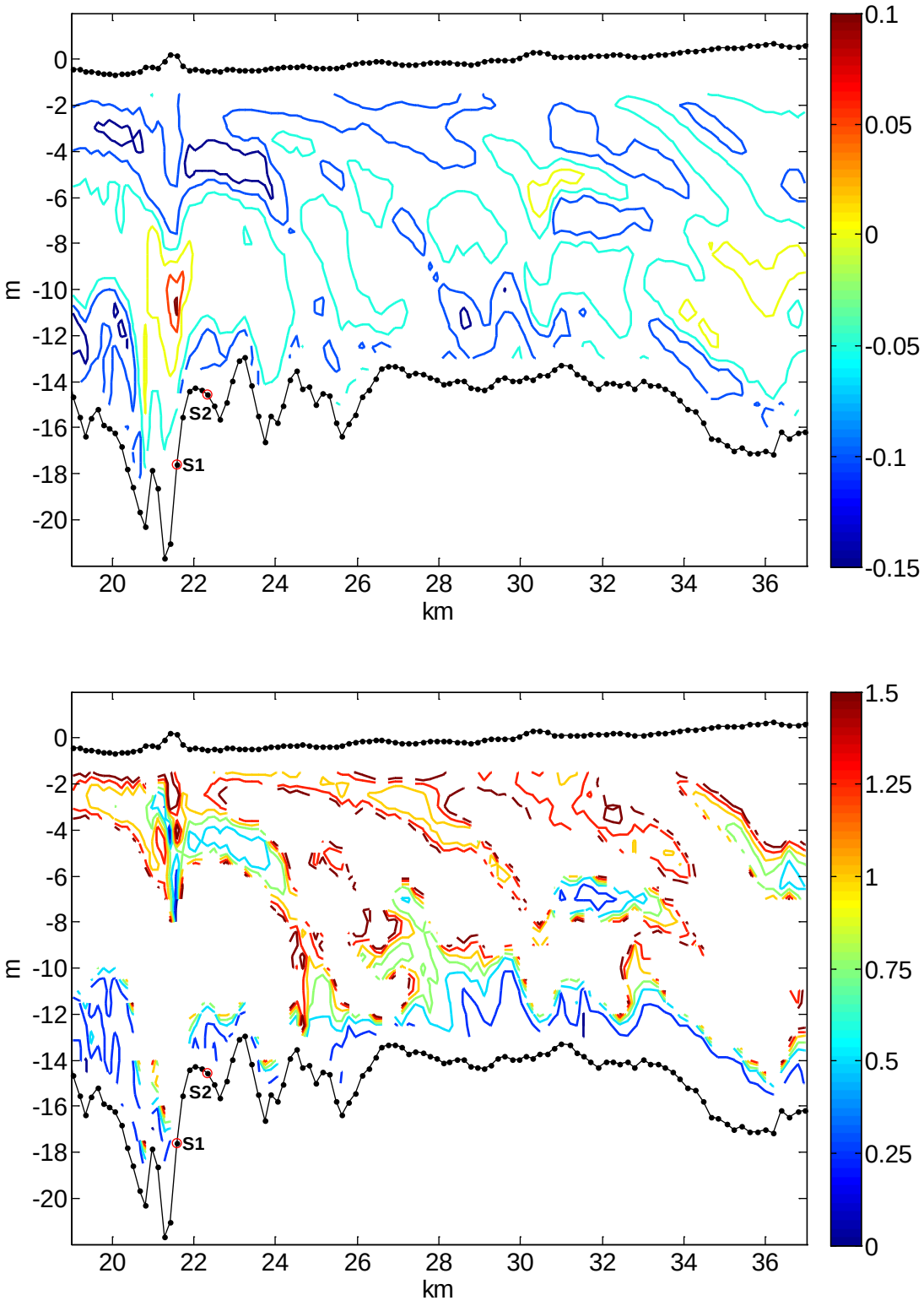

Figure 2.23 Model vertical shear $\partial u/\partial z$ [s^{-1}] (upper panel) and Richardson Number R_i (lower panel) in a longitudinal section at the maximum ebb of neap tide. Free surface (exaggerated by 30 times) and bottom topography have been shown as dotted lines.

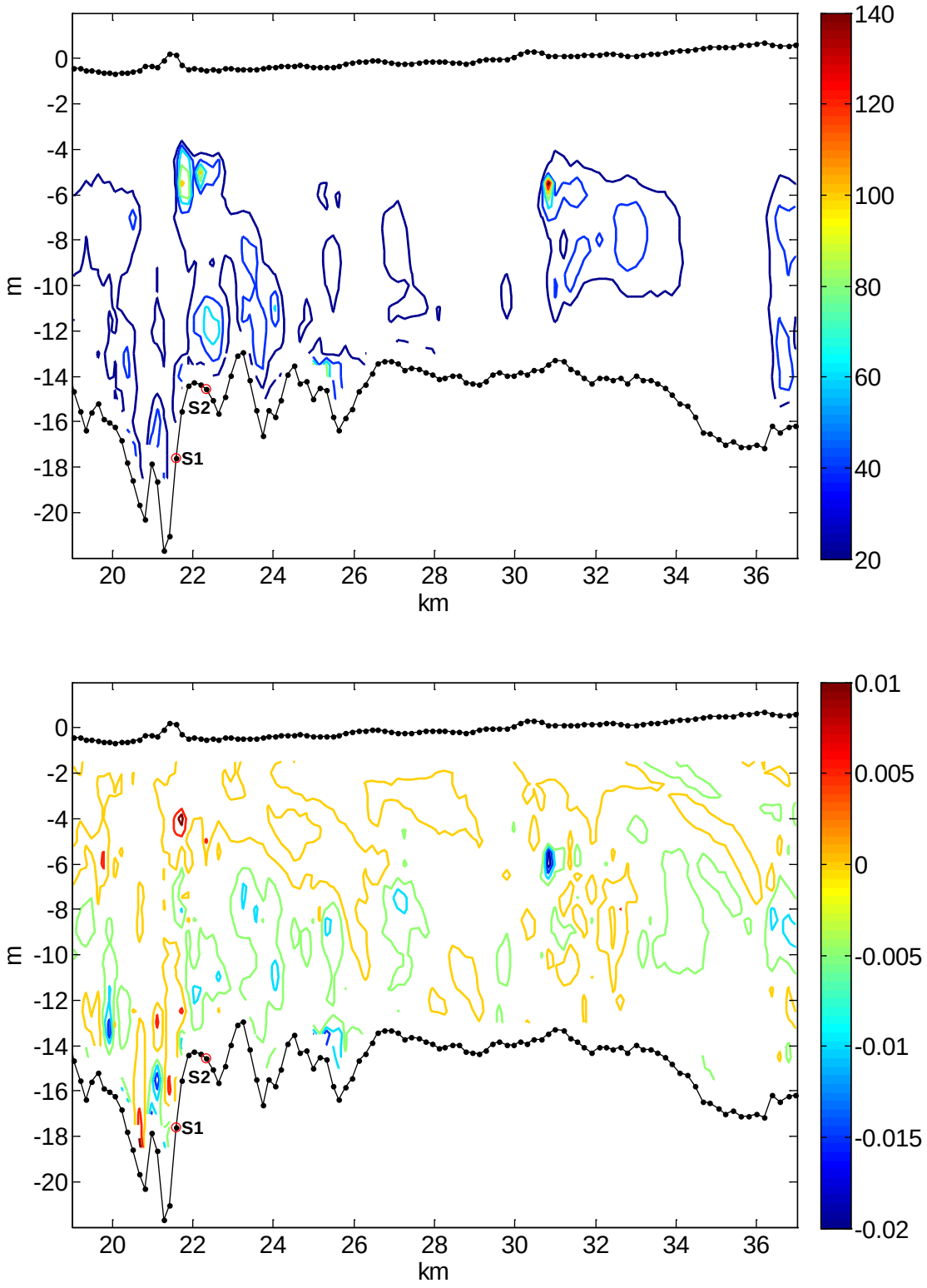

Figure 2.24 Model available potential energy APE [J/m^3] (upper panel) and its local time rate ∂APE/∂t [W/m^3] (lower panel) in a longitudinal section at the maximum ebb of neap tide. Free surface (exaggerated by 30 times) and bottom topography have been shown as dotted lines.

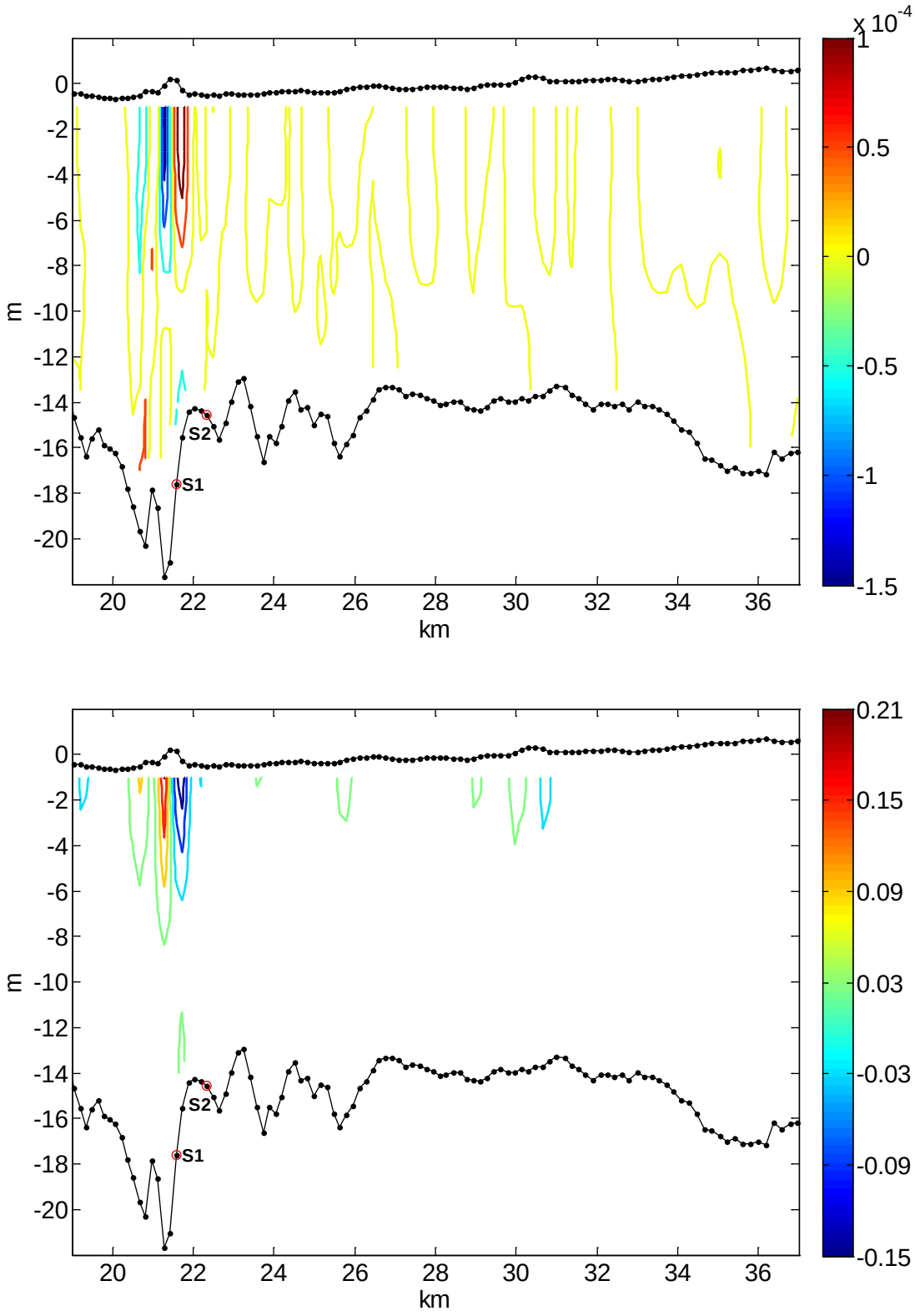

Figure 2.25 Model pressure gradient force [m/s^2] (upper panel) and its power (or divergence of energy flux) [W/m^3] (lower panel) in a longitudinal section at the maximum ebb of neap tide. Free surface (exaggerated by 30 times) and bottom topography have been shown as dotted lines.

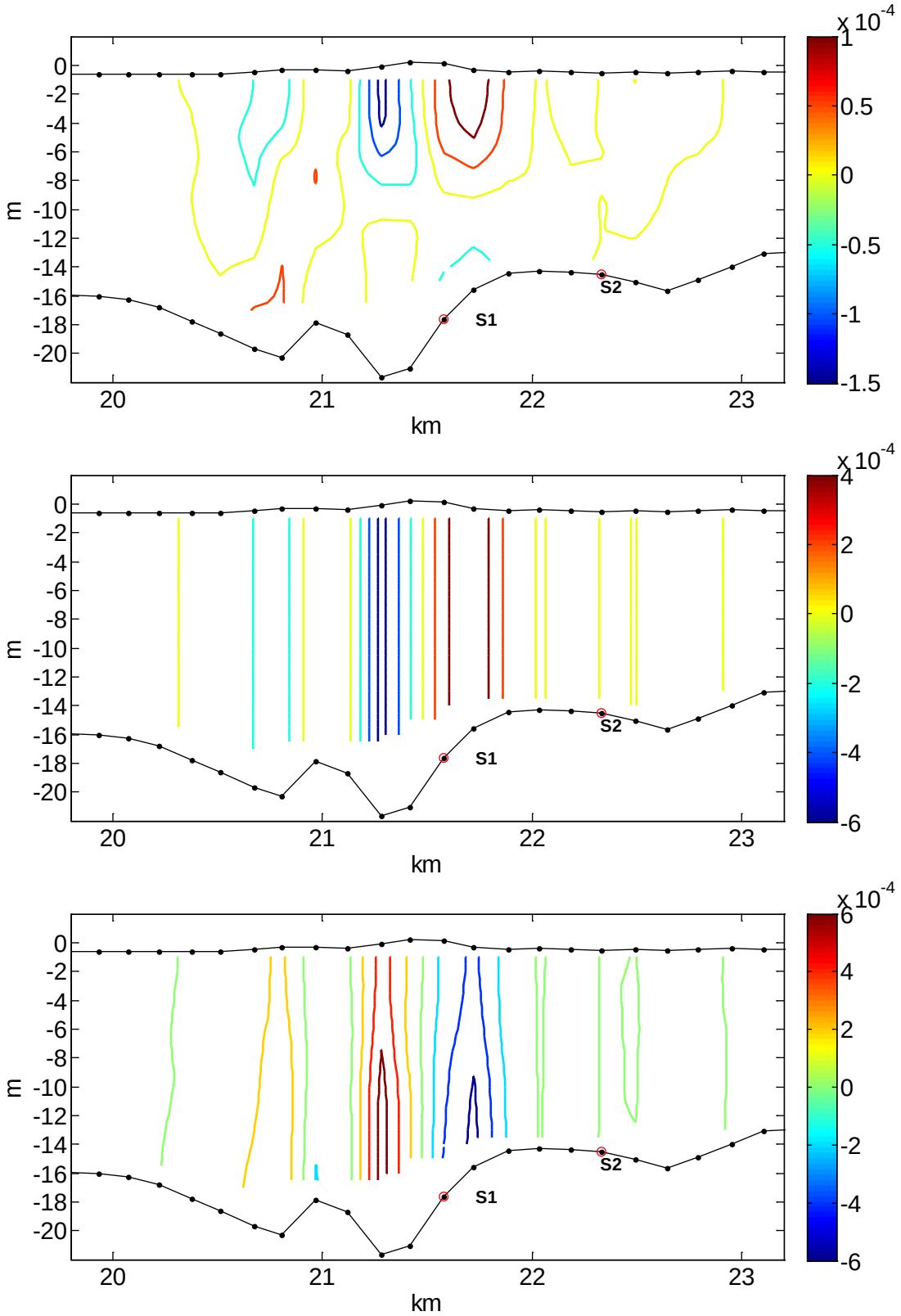

Figure 2.26 Model pressure gradient force [m/s^2] (top panel), barotropic pressure gradient force [m/s^2] (middle panel) and baroclinic pressure gradient force [m/s^2] (bottom panel) in the vicinity of the big valley at ~21 km at the maximum ebb of neap tide.

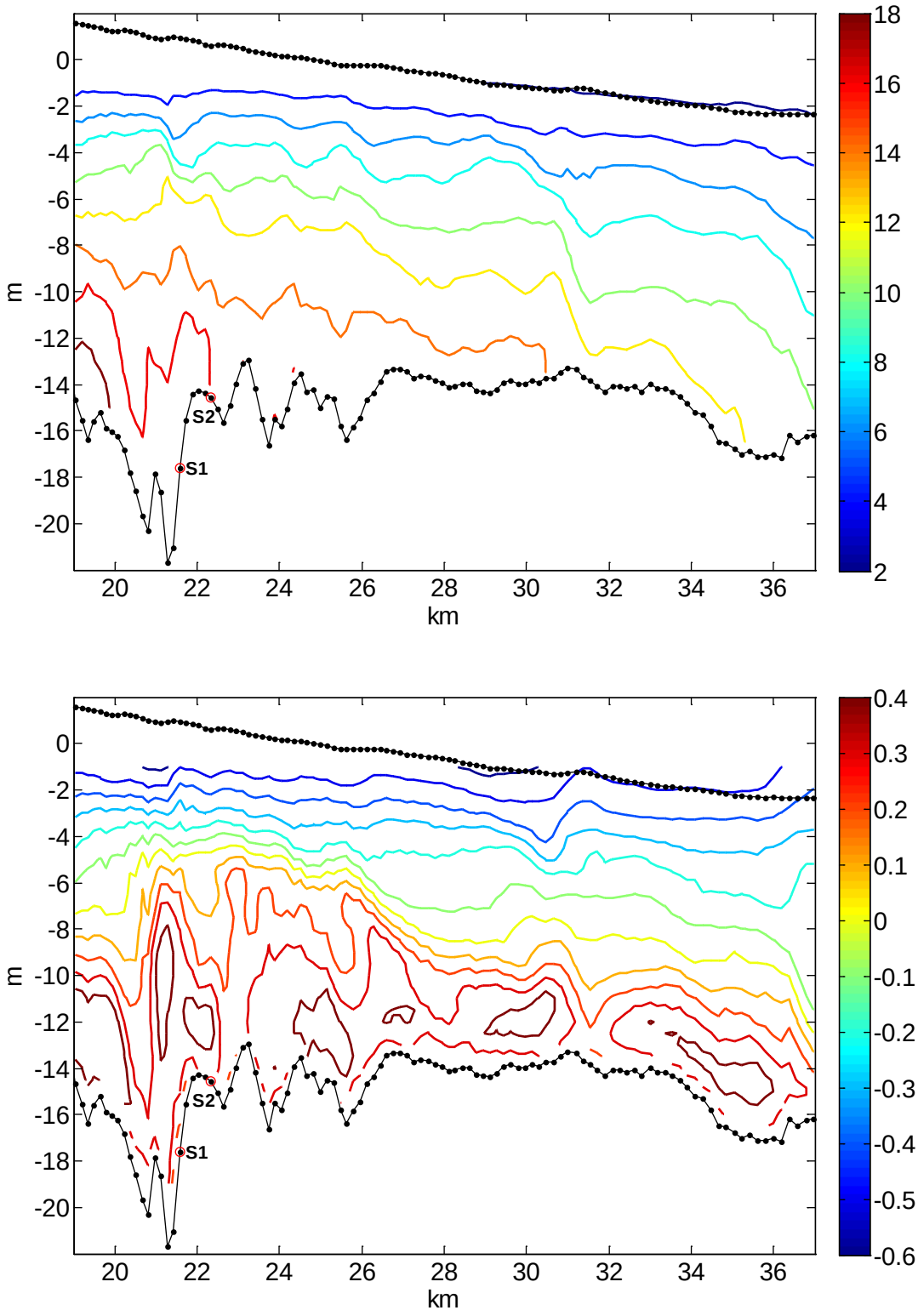

Figure 2.27 Model salinity [*psu*] (upper panel) and along-channel velocity *u* [*m/s*] (lower panel) in a longitudinal section at the early flood (**t2** in tidal cycle Figures 2.38~2.51) of neap tide. Free surface (exaggerated by 30 times) and bottom topography have been shown as dotted lines.

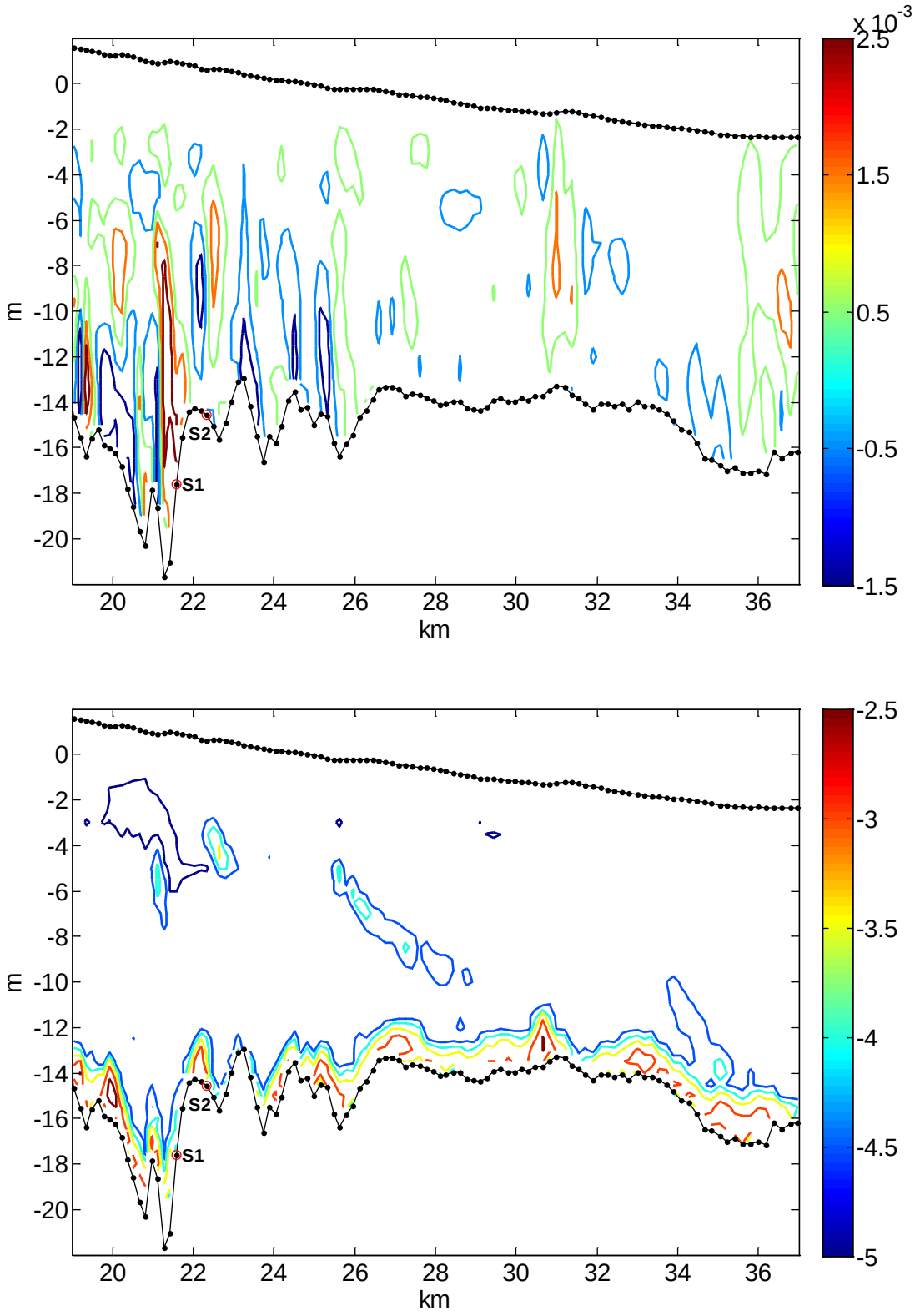

Figure 2.28 Model vertical advection *w* [*m/s*] (upper panel) and logged viscosity [m^2/s] (lower panel) in a longitudinal section at the early flood of neap tide. Free surface (exaggerated by 30 times) and bottom topography have been shown as dotted lines.

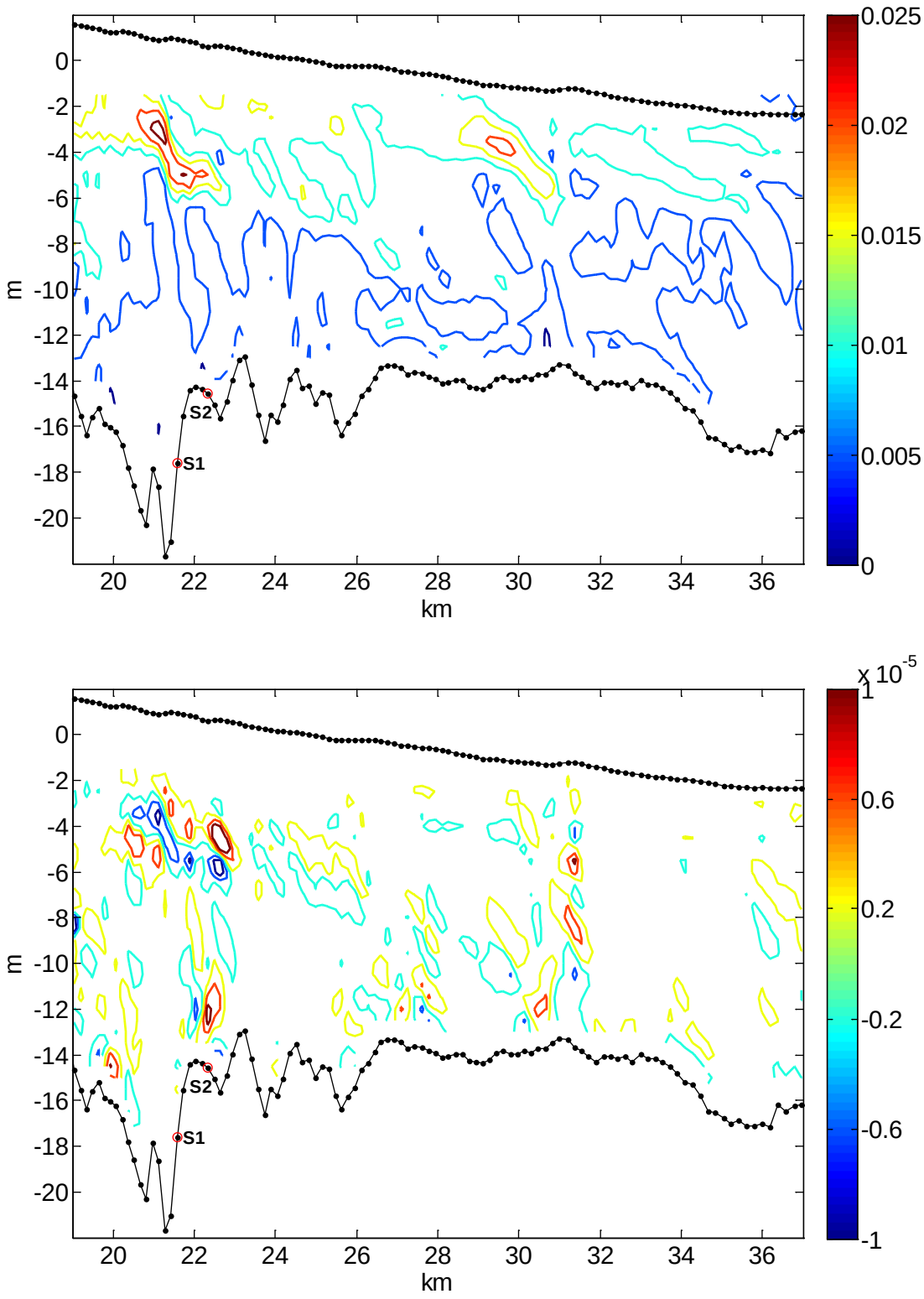

Figure 2.29 Model Brunt–Väisälä frequency N^2 [s^{-1}] (upper panel) and its local time rate $\partial N^2/\partial t$ [s^{-2}] (lower panel) in a longitudinal section at the early flood of neap tide. Free surface (exaggerated by 30 times) and bottom topography have been shown as dotted lines.

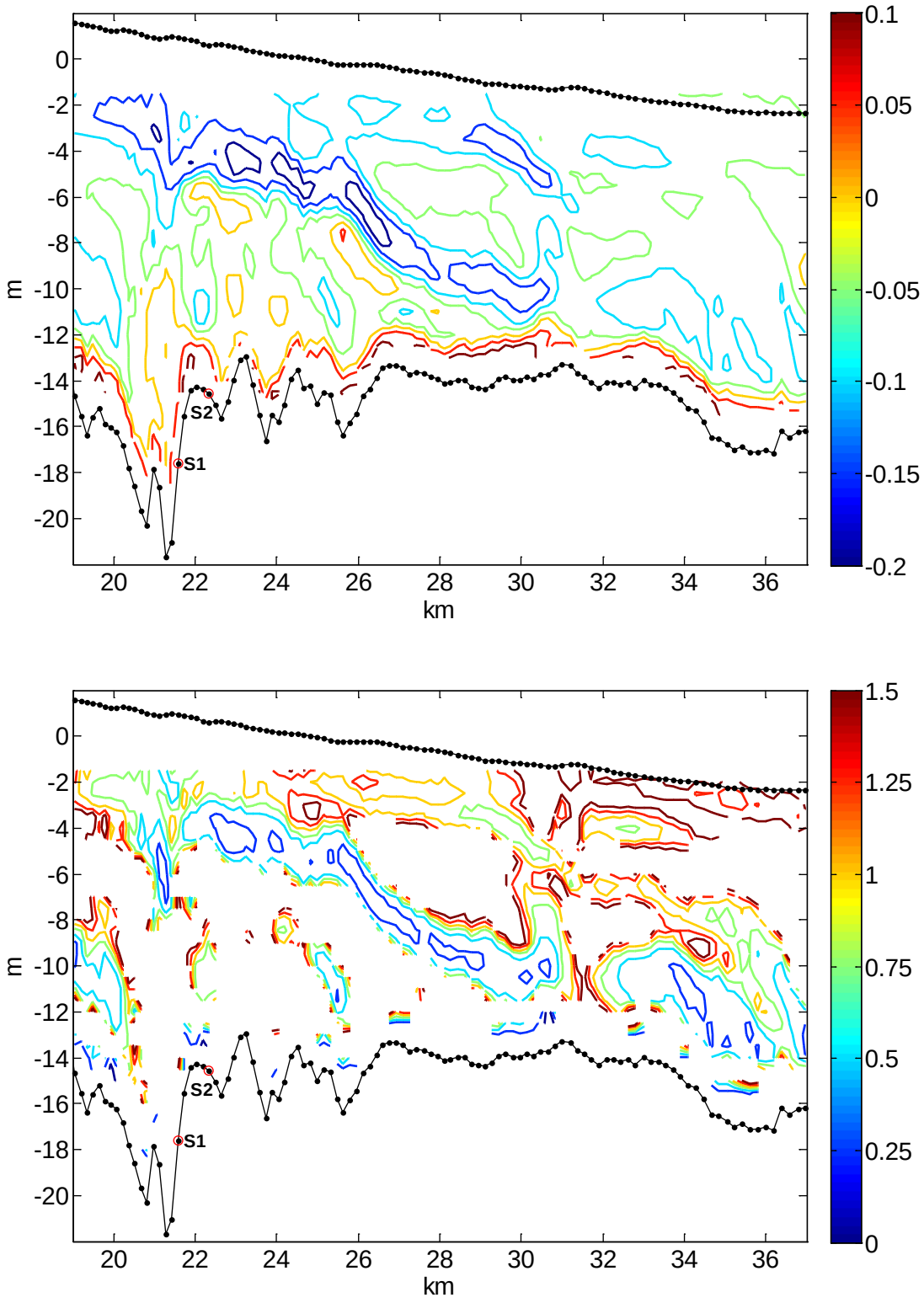

Figure 2.30 Model vertical shear $\partial u/\partial z$ [s^{-1}] (upper panel) and Richardson Number R_i (lower panel) in a longitudinal section at the early flood of neap tide. Free surface (exaggerated by 30 times) and bottom topography have been shown as dotted lines.

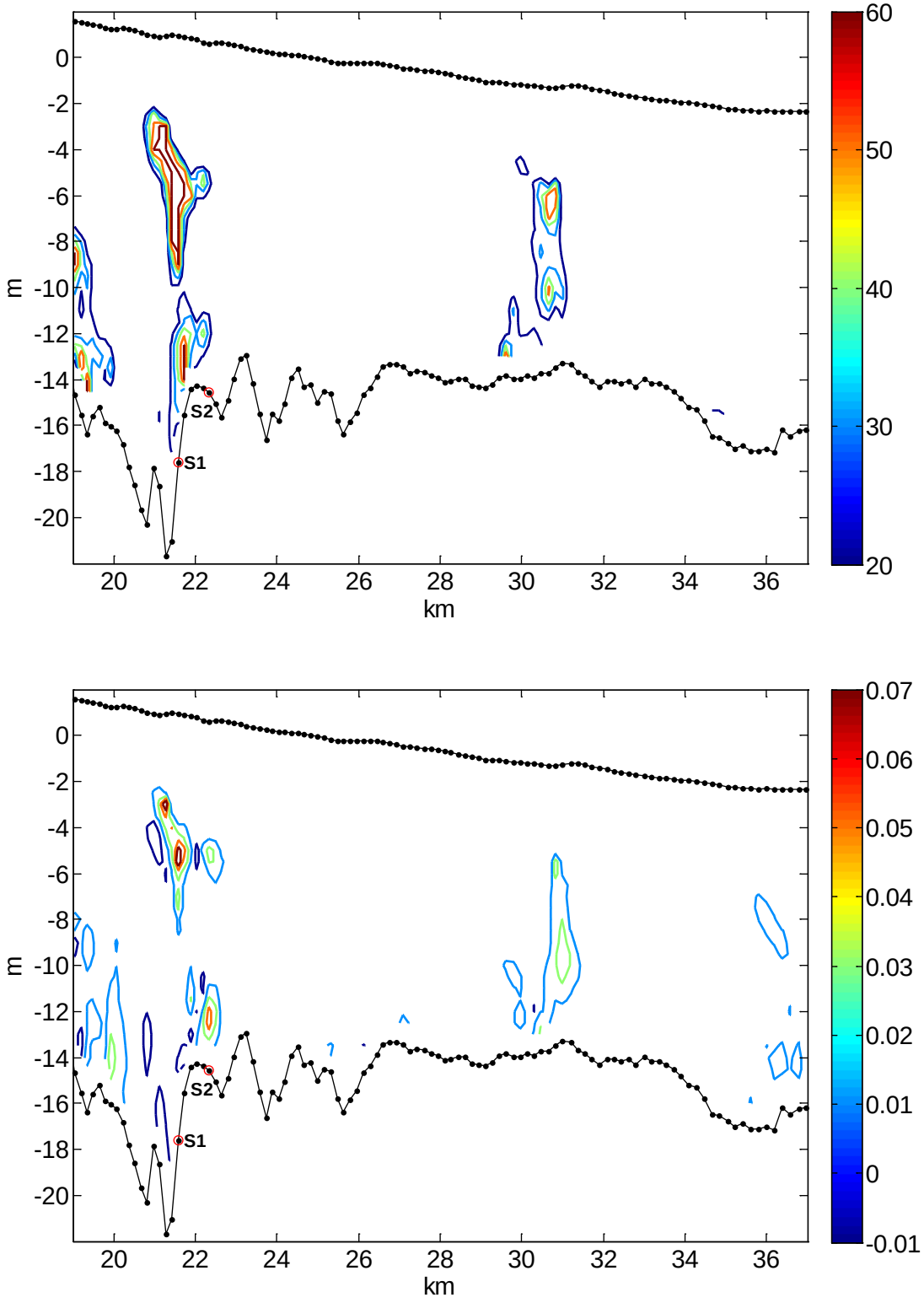

Figure 2.31 Model available potential energy APE [J/m^3] (upper panel) and its local time rate ∂APE/∂t [W/m^3] (lower panel) in a longitudinal section at the maximum ebb of neap tide. Free surface (exaggerated by 30 times) and bottom topography have been shown as dotted lines.

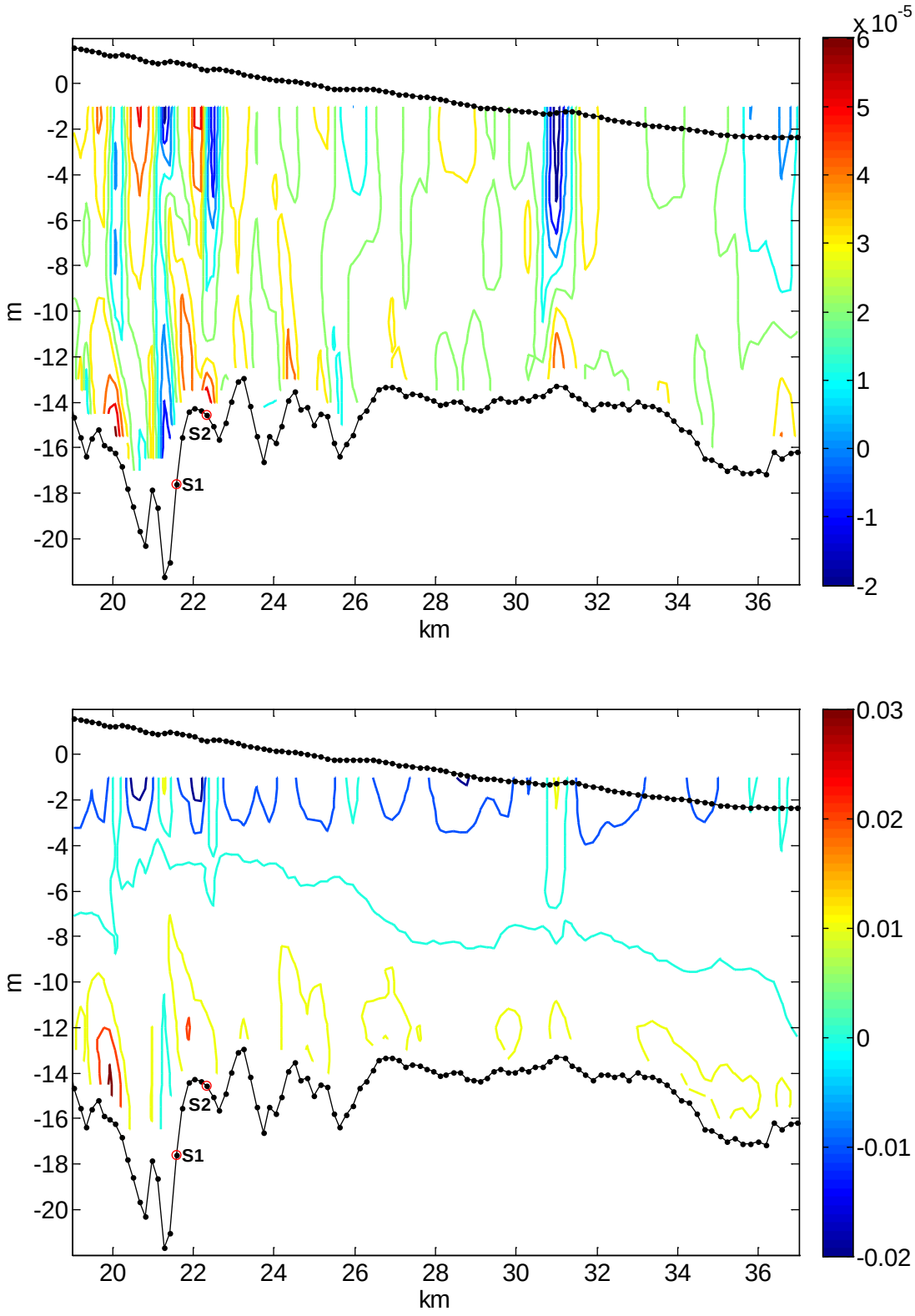

Figure 2.32 Model pressure gradient force [m/s^2] (upper panel) and its power (or divergence of energy flux) [W/m^3] (lower panel) in a longitudinal section at the early flood of neap tide. Free surface (exaggerated by 30 times) and bottom topography have been shown as dotted lines.

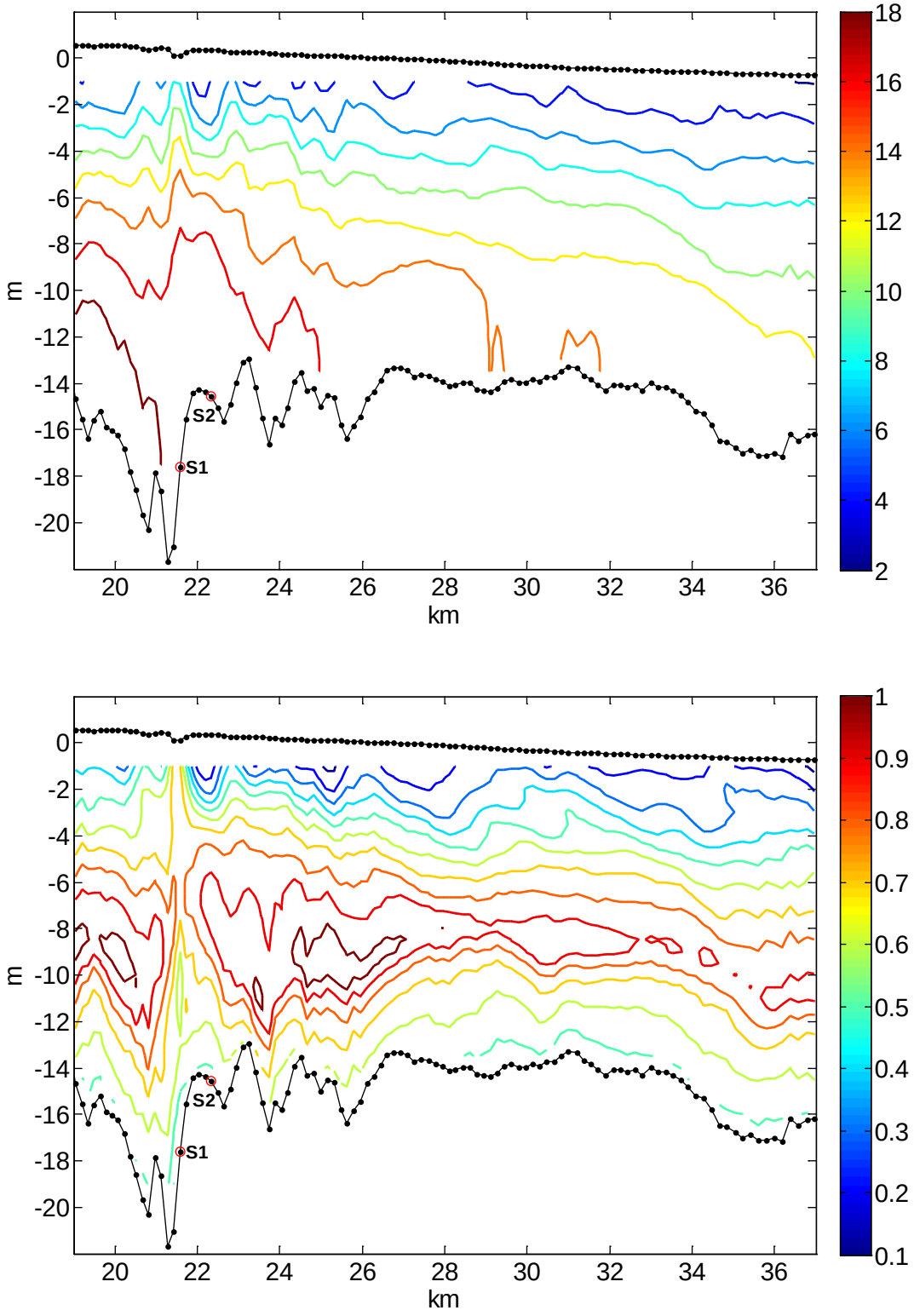

Figure 2.33 Model salinity [*psu*] (upper panel) and along-channel velocity *u* [*m/s*] (lower panel) in a longitudinal section at the maximum flood (**t3** in tidal cycle Figures 2.38~2.51) of neap tide. Free surface (exaggerated by 30 times) and bottom topography have been shown as dotted lines.

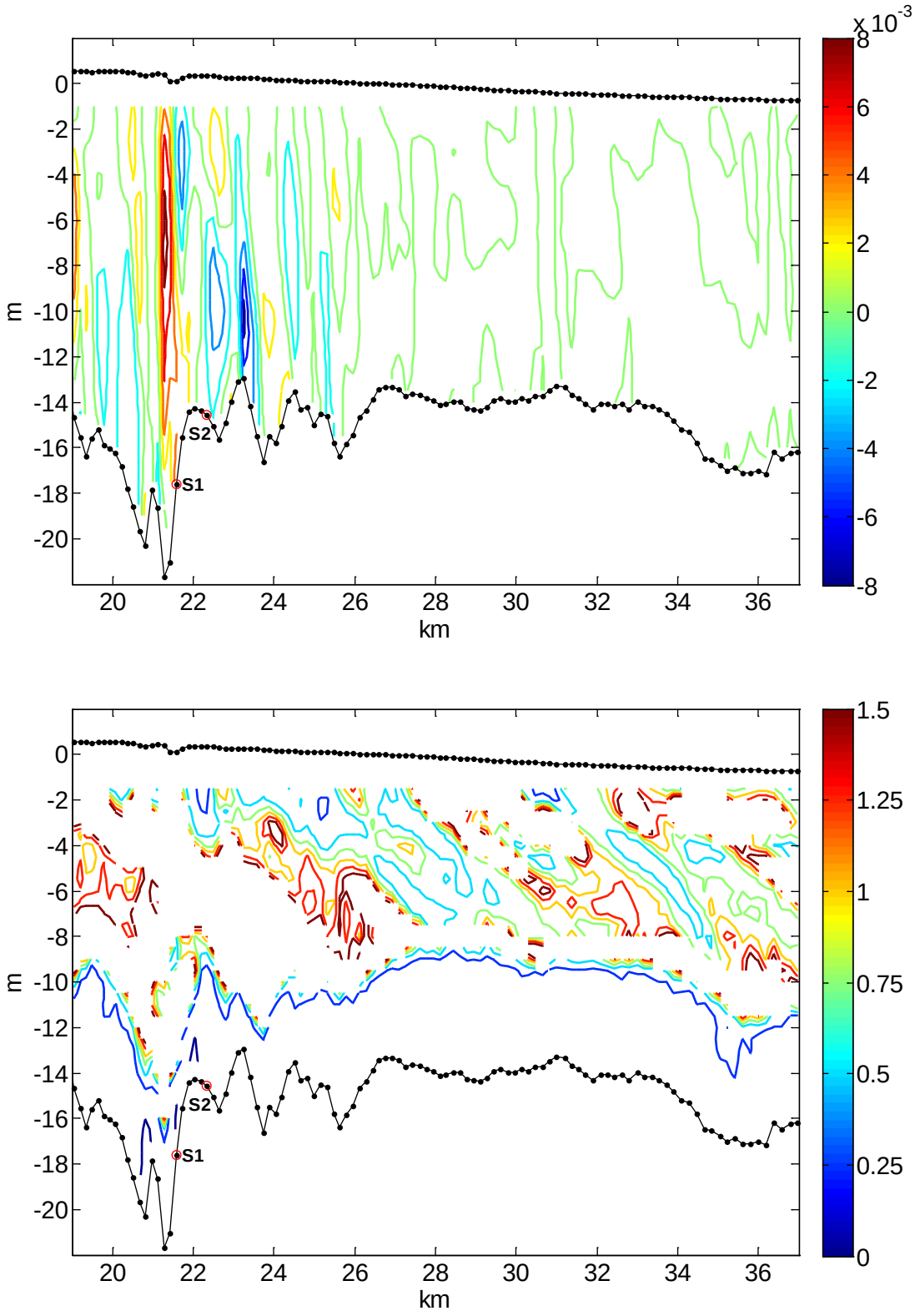

Figure 2.34 Model vertical advection w [m/s] (upper panel) and Richardson Number R_i (lower panel) in a longitudinal section at the maximum flood of neap tide. Free surface (exaggerated by 30 times) and bottom topography have been shown as dotted lines.

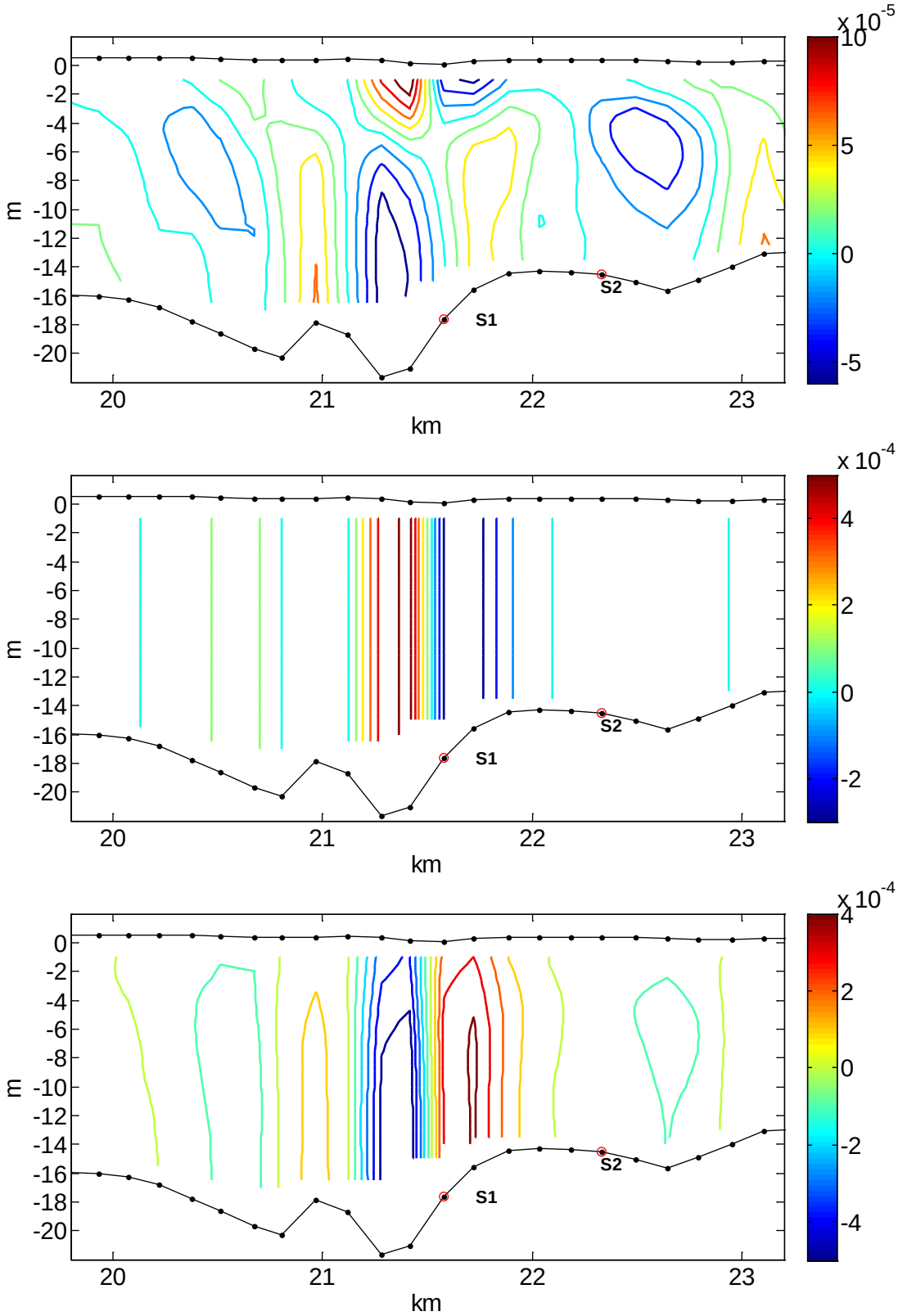

Figure 2.35 Model pressure gradient force [m/s^2] (top panel), barotropic pressure gradient force [m/s^2] (middle panel) and baroclinic pressure gradient force [m/s^2] (bottom panel) in the vicinity of the big valley at ~21 km at the maximum flood of neap tide.

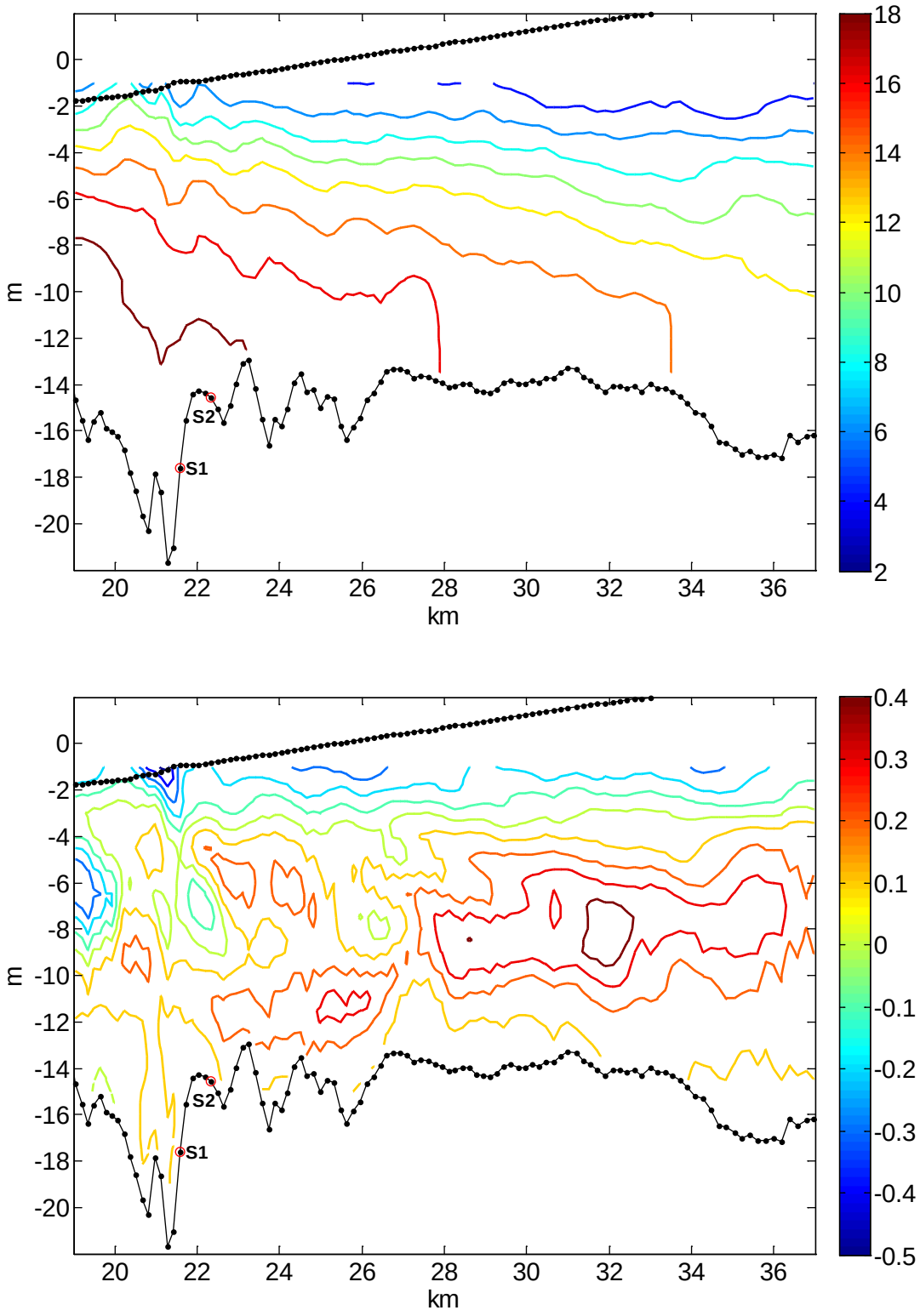

Figure 2.36 Model salinity [*psu*] (upper panel) and along-channel velocity *u* [*m/s*] (lower panel) in a longitudinal section at the late flood (**t4** in tidal cycle Figures 2.38~2.51) of neap tide. Free surface (exaggerated by 30 times) and bottom topography have been shown as dotted lines.

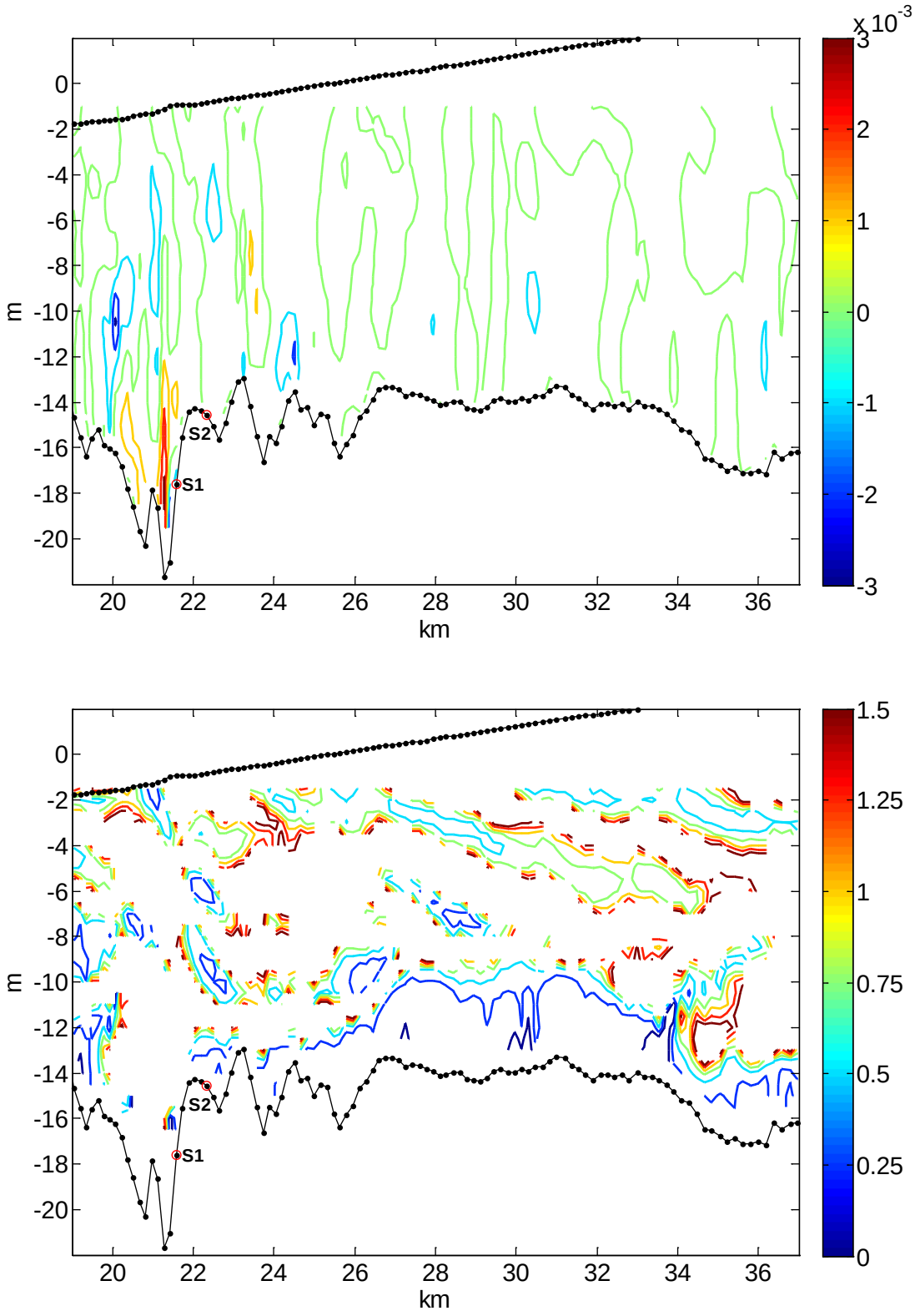

Figure 2.37 Model vertical advection w [m/s] (upper panel) and Richardson Number R_i (lower panel) in a longitudinal section at the late flood of neap tide. Free surface (exaggerated by 30 times) and bottom topography have been shown as dotted lines.

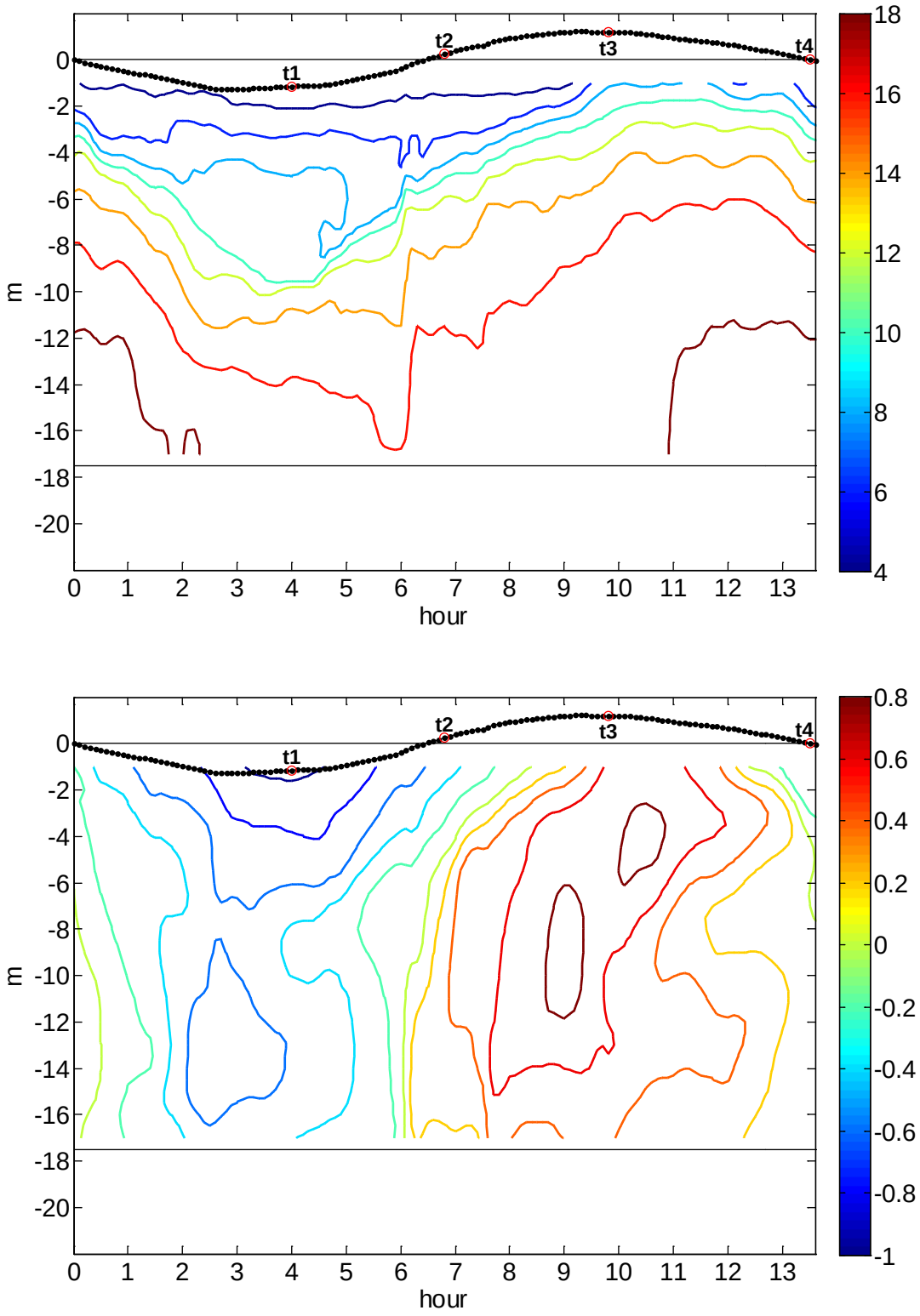

Figure 2.38 Model salinity [*psu*] (upper panel) and along-channel velocity *u* [*m/s*] (lower panel) in a tidal cycle at the landward slope of the big valley (**S1** in longitudinal Figures 2.20~2.37). Depth-averaged *u* (doubled in magnitude) has been shown as dotted line.

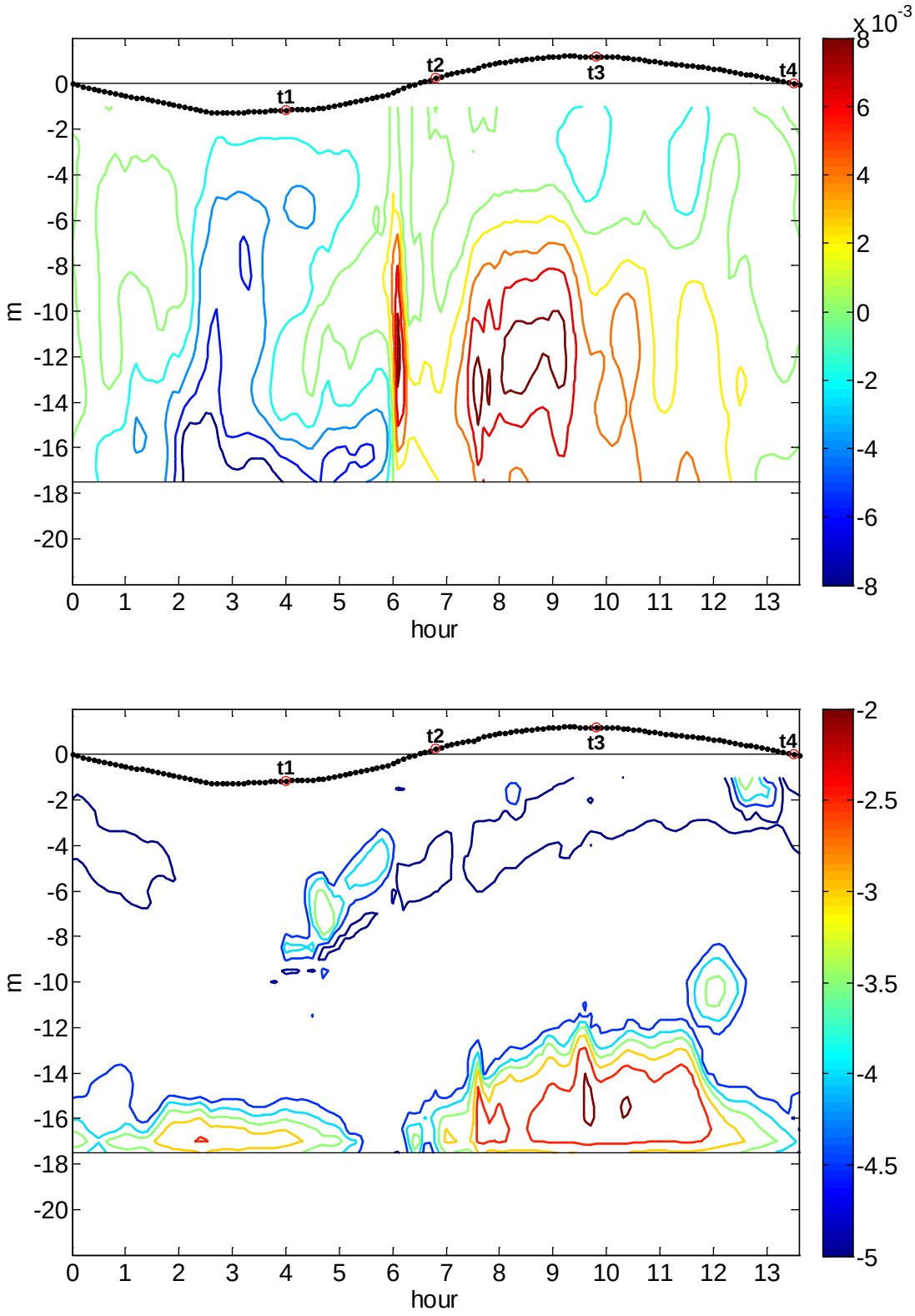

Figure 2.39 Model vertical advection *w* [*m/s*] (upper panel) and logged viscosity [m^2/s] (lower panel) in a tidal cycle at the landward slope of the big valley. Depth-averaged *u* (doubled in magnitude) has been shown as dotted line.

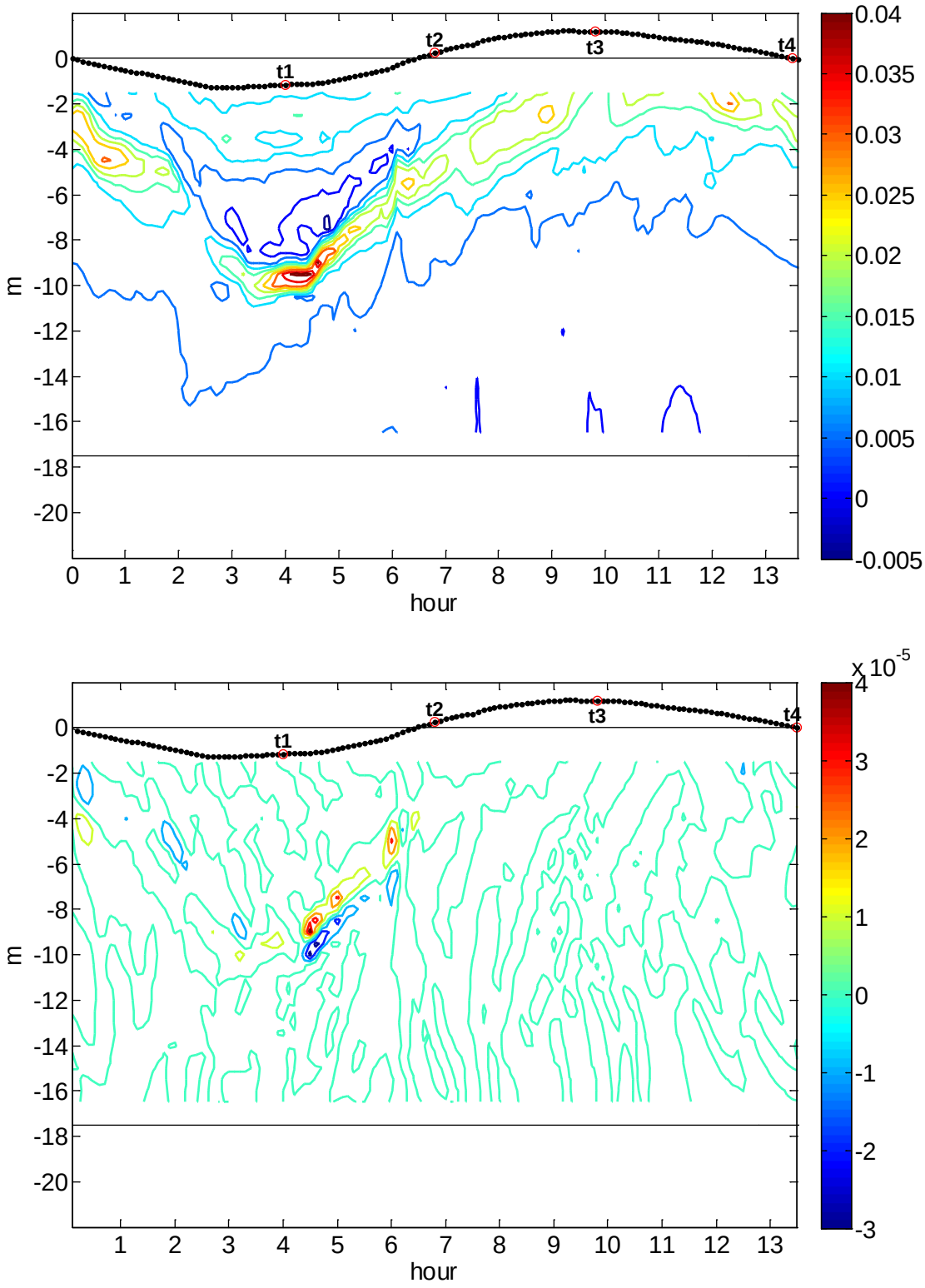

Figure 2.40 Model Brunt–Väisälä frequency N^2 [s^{-1}] (upper panel) and its local time rate $\partial N^2/\partial t$ [s^{-2}] (lower panel) in a tidal cycle at the landward slope of the big valley. Depth-averaged u (doubled in magnitude) has been shown as dotted line.

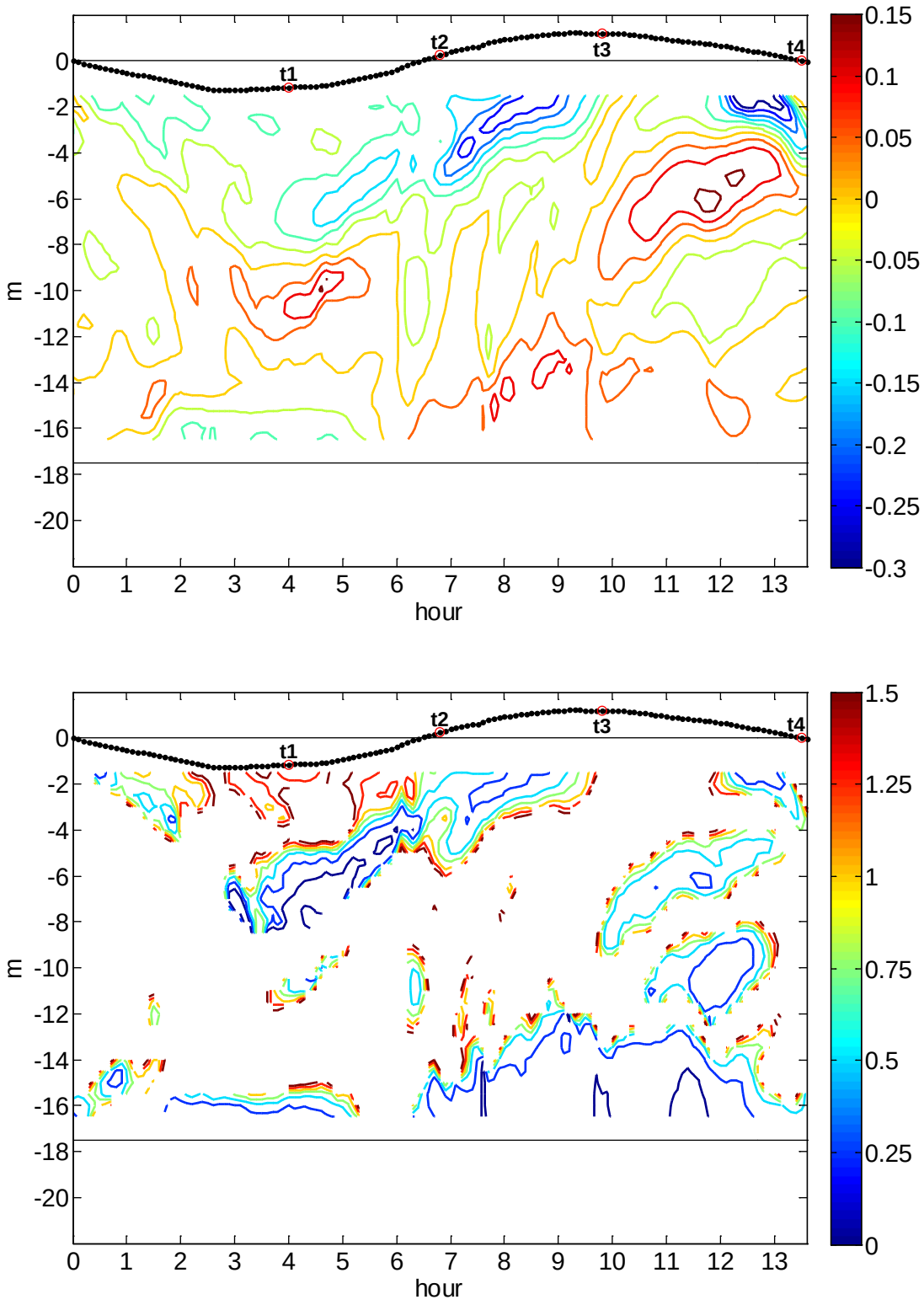

Figure 2.41 Model vertical shear $\partial u/\partial z$ [s^{-1}] (upper panel) and Richardson Number R_i (lower panel) in a tidal cycle at the landward slope of the big valley. Depth-averaged u (doubled in magnitude) has been shown as dotted line.

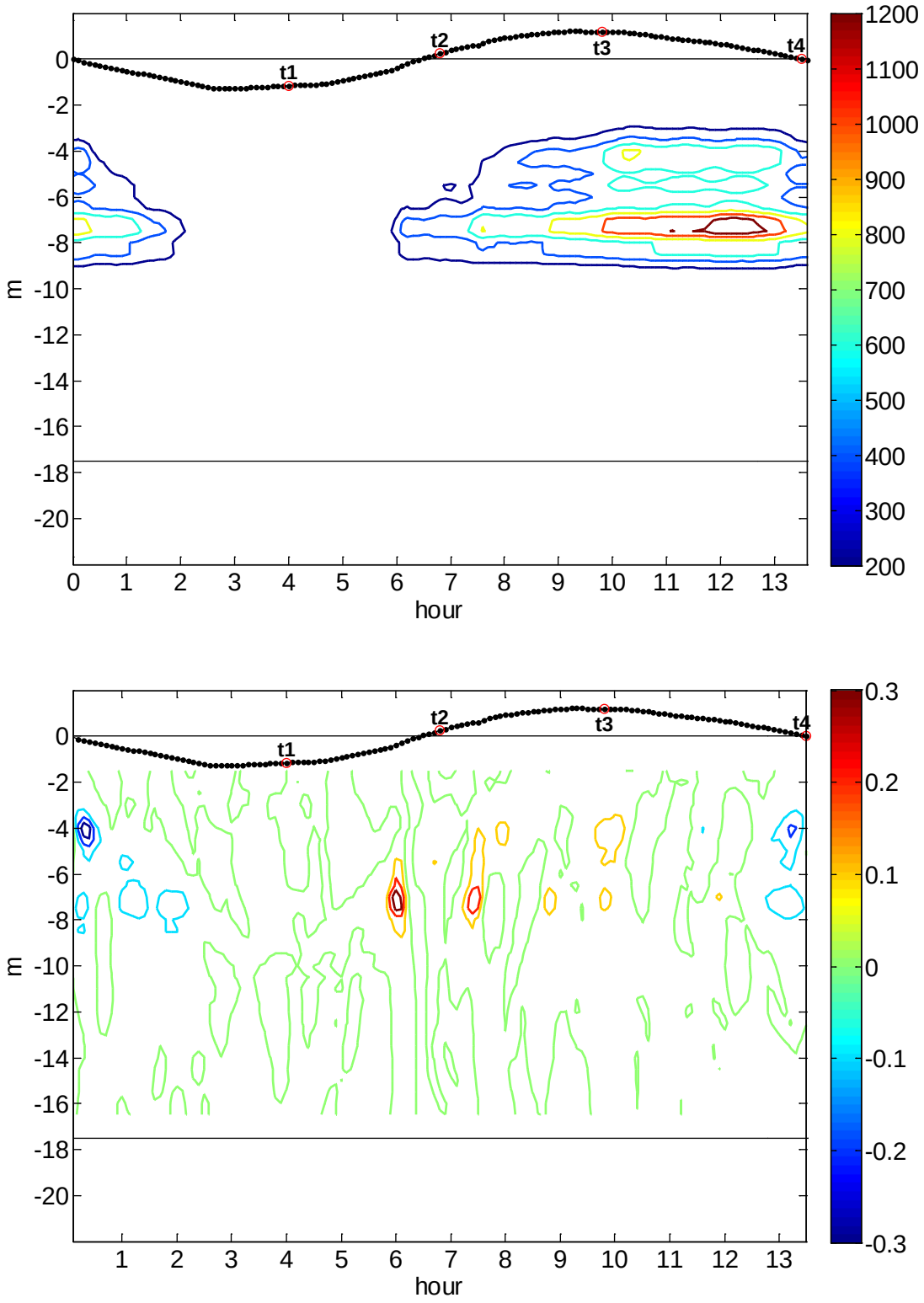

Figure 2.42 Model available potential energy APE [J/m^3] (upper panel) and its local time rate ∂APE/∂t [W/m^3] (lower panel) in a tidal cycle at the landward slope of the big valley. Depth-averaged u (doubled in magnitude) has been shown as dotted line.

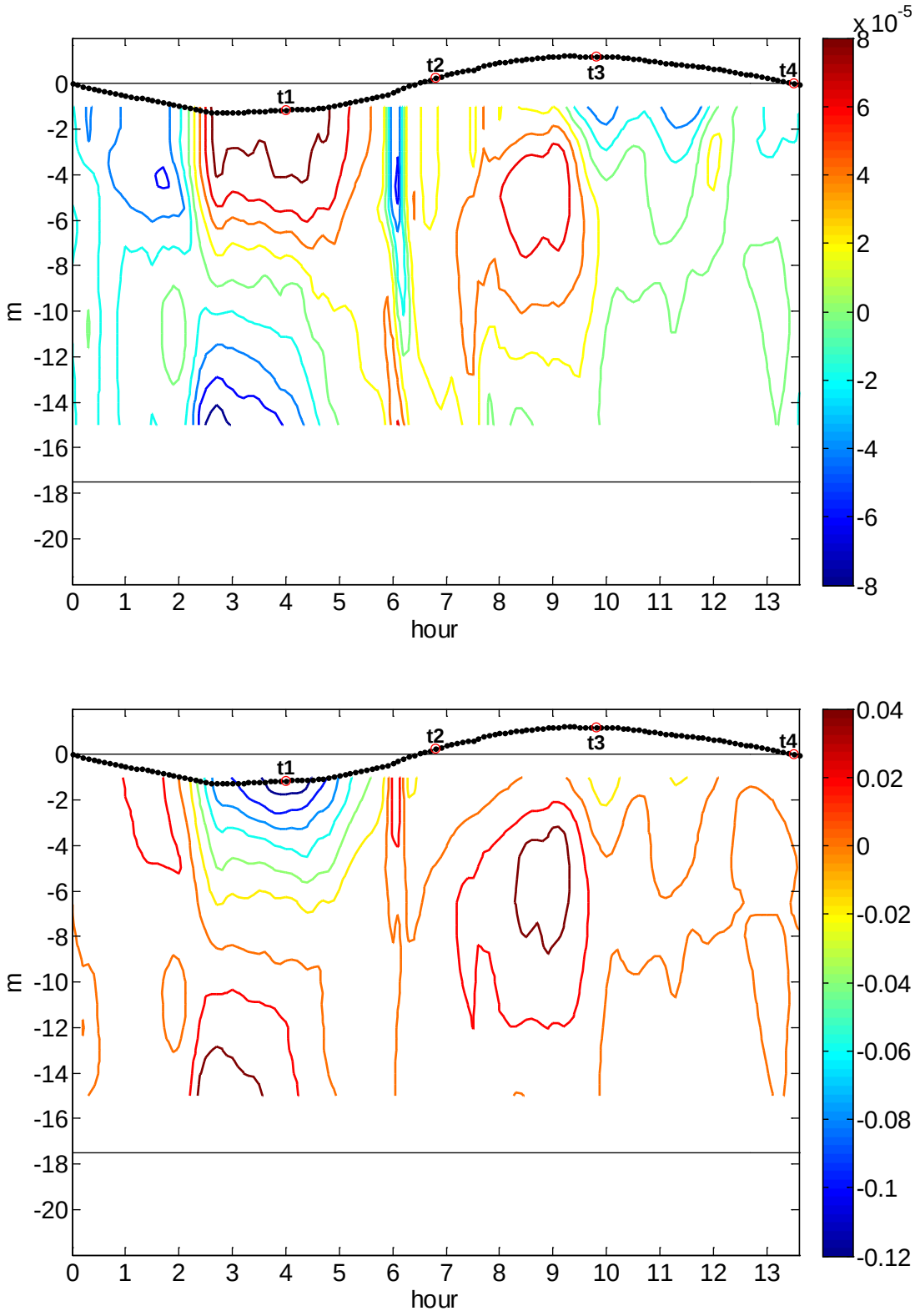

Figure 2.43 Model pressure gradient force [m/s^2] (upper panel) and its power (or divergence of energy flux) [W/m^3] (lower panel) in a tidal cycle at the landward slope of the big valley. Depth-averaged *u* (doubled in magnitude) has been shown as dotted line.

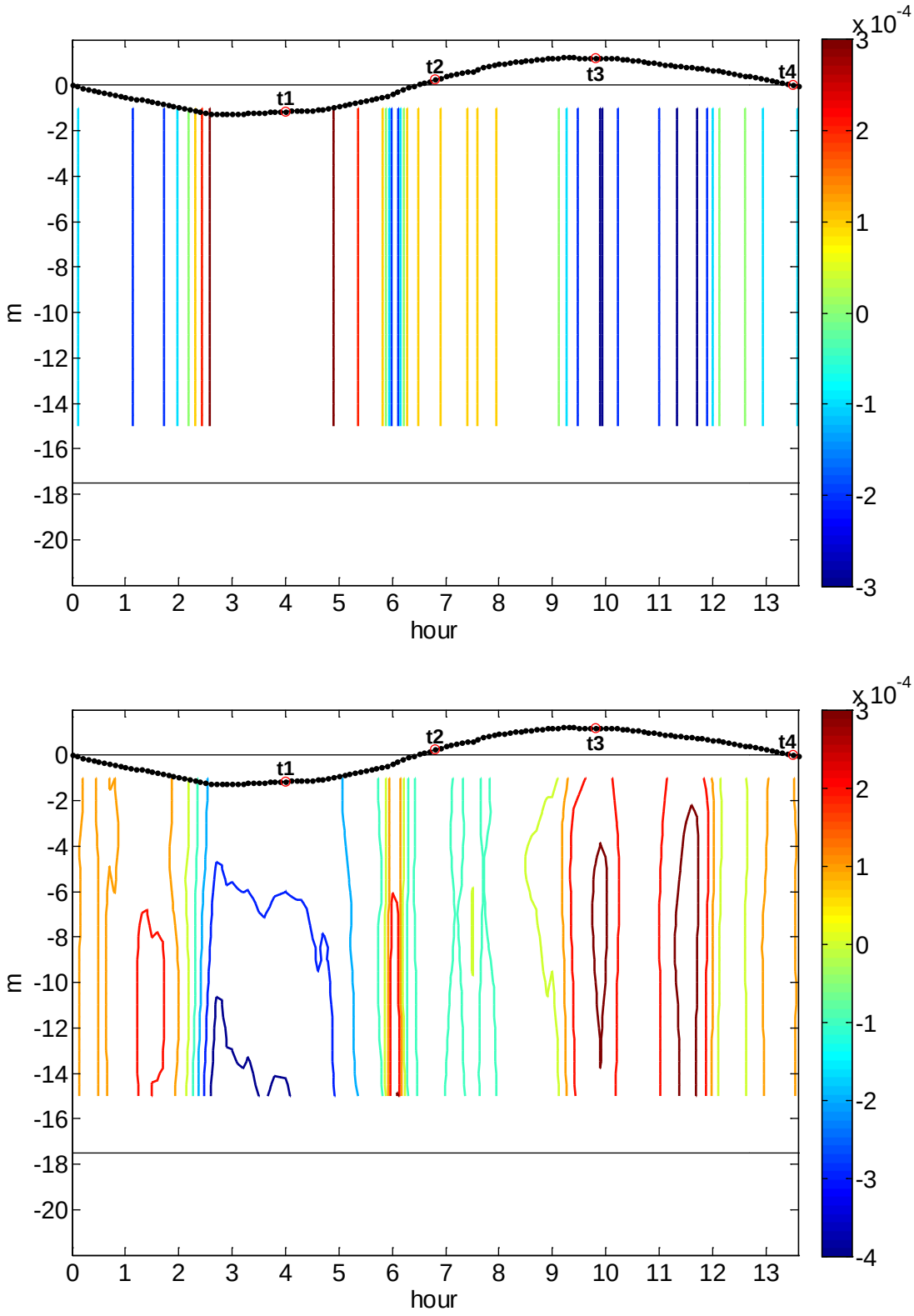

Figure 2.44 Model barotropic (upper panel) and baroclinic (lower panel) pressure gradient forces [m/s^2] in a tidal cycle at the landward slope of the big valley. Depth-averaged *u* (doubled in magnitude) has been shown as dotted line.

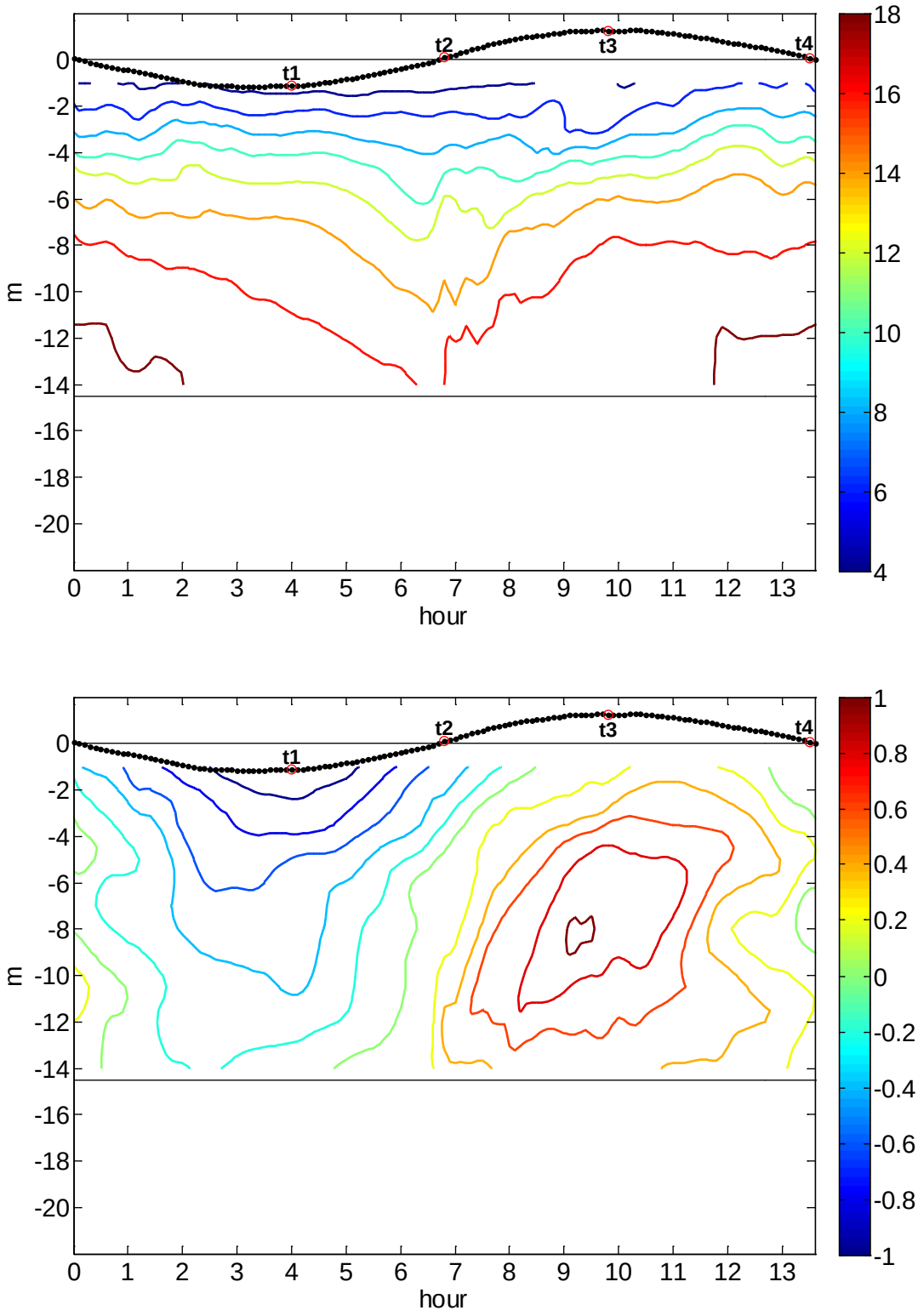

Figure 2.45 Model salinity [*psu*] (upper panel) and along-channel velocity *u* [*m/s*] (lower panel) in a tidal cycle at the upstream of the big valley (**S2** in longitudinal Figures 2.20~2.37). Depth-averaged *u* (doubled in magnitude) has been shown as dotted line.

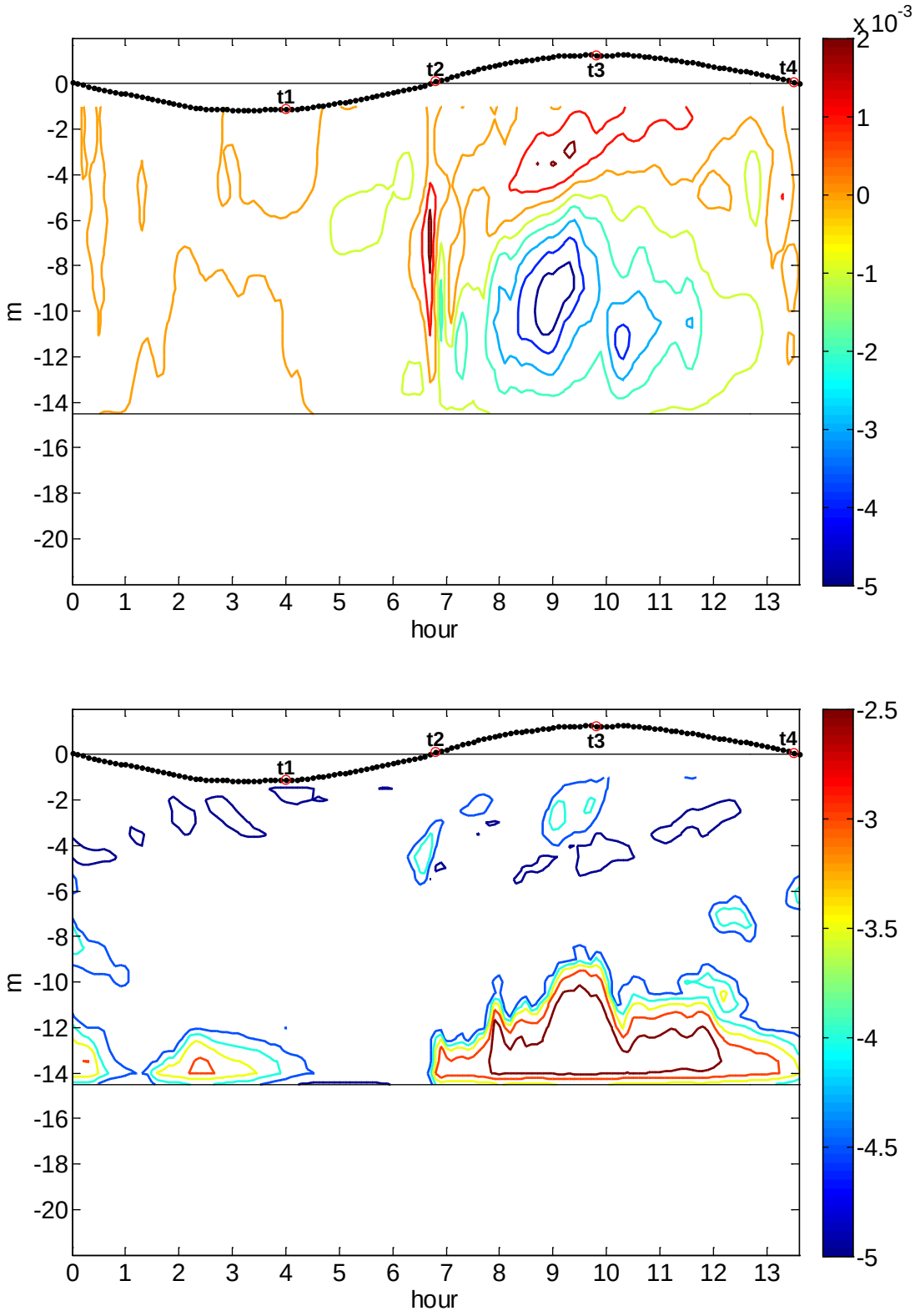

Figure 2.46 Model vertical advection *w* [*m/s*] (upper panel) and logged viscosity [m^2/s] (lower panel) in a tidal cycle at the upstream of the big valley. Depth-averaged *u* (doubled in magnitude) has been shown as dotted line.

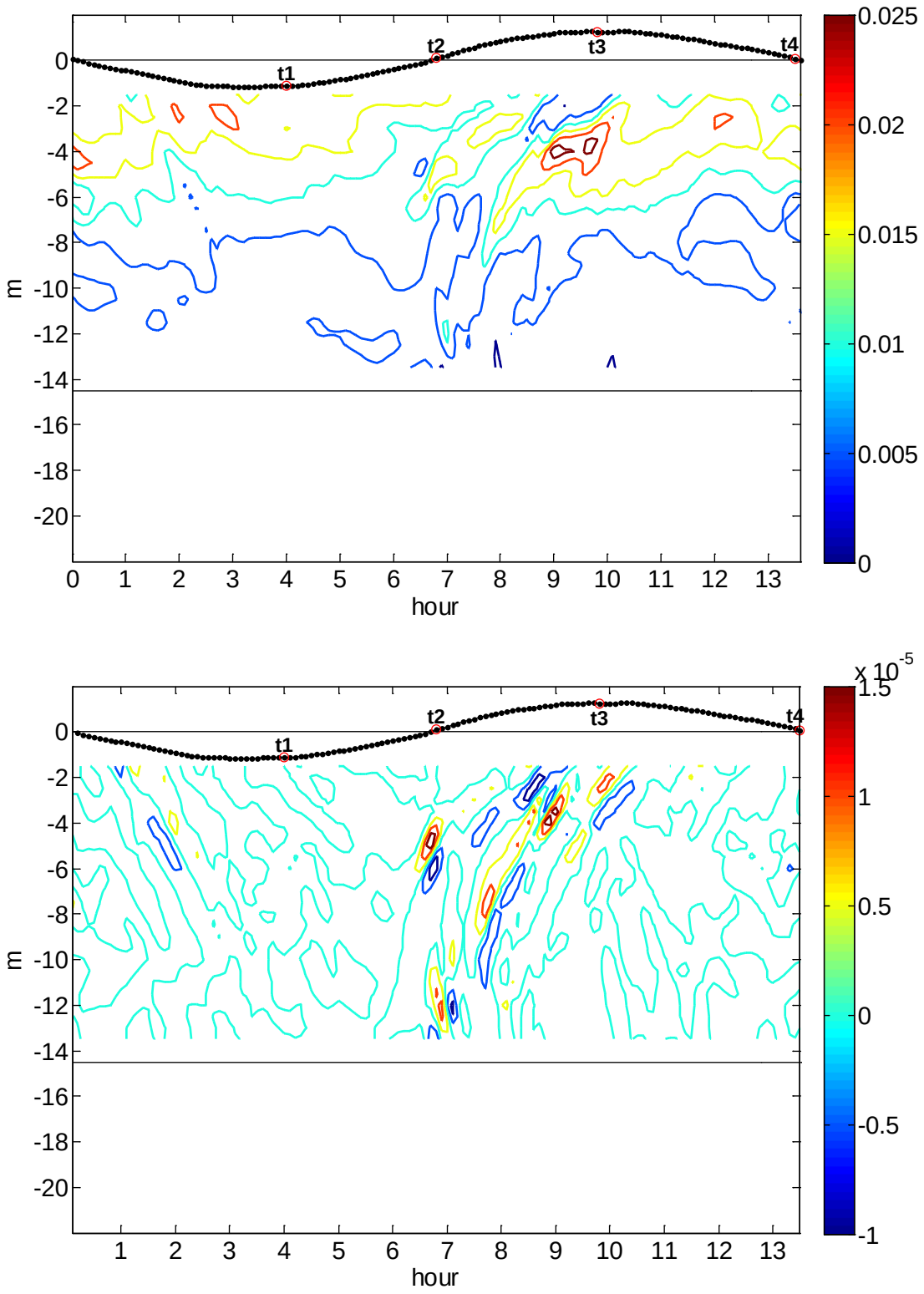

Figure 2.47 Model Brunt–Väisälä frequency N^2 [s^{-1}] (upper panel) and its local time rate $\partial N^2/\partial t$ [s^{-2}] (lower panel) in a tidal cycle at the upstream of the big valley. Depth-averaged u (doubled in magnitude) has been shown as dotted line.

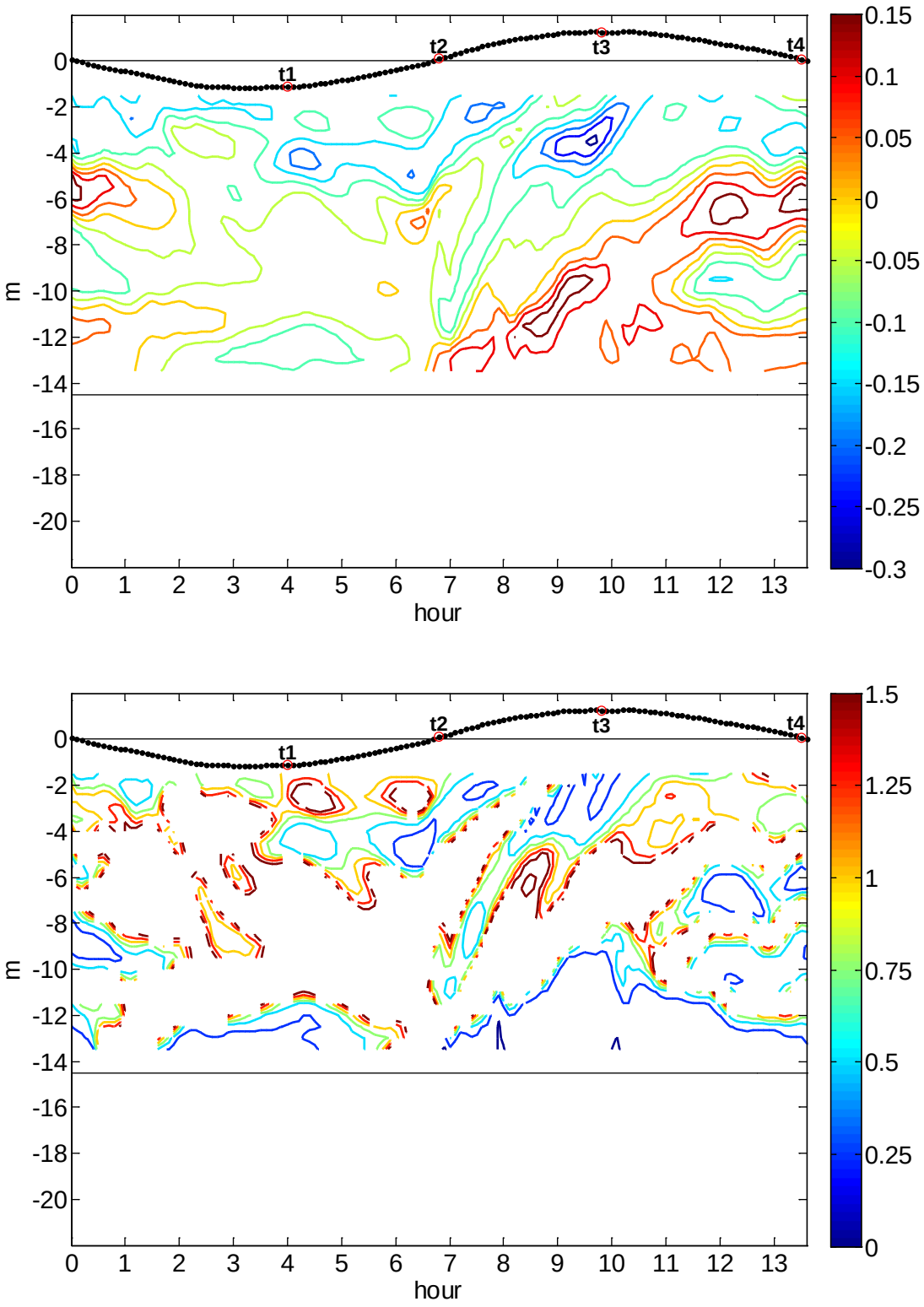

Figure 2.48 Model vertical shear $\partial u/\partial z$ [s^{-1}] (upper panel) and Richardson Number R_i (lower panel) in a tidal cycle at the upstream of the big valley. Depth-averaged u (doubled in magnitude) has been shown as dotted line.

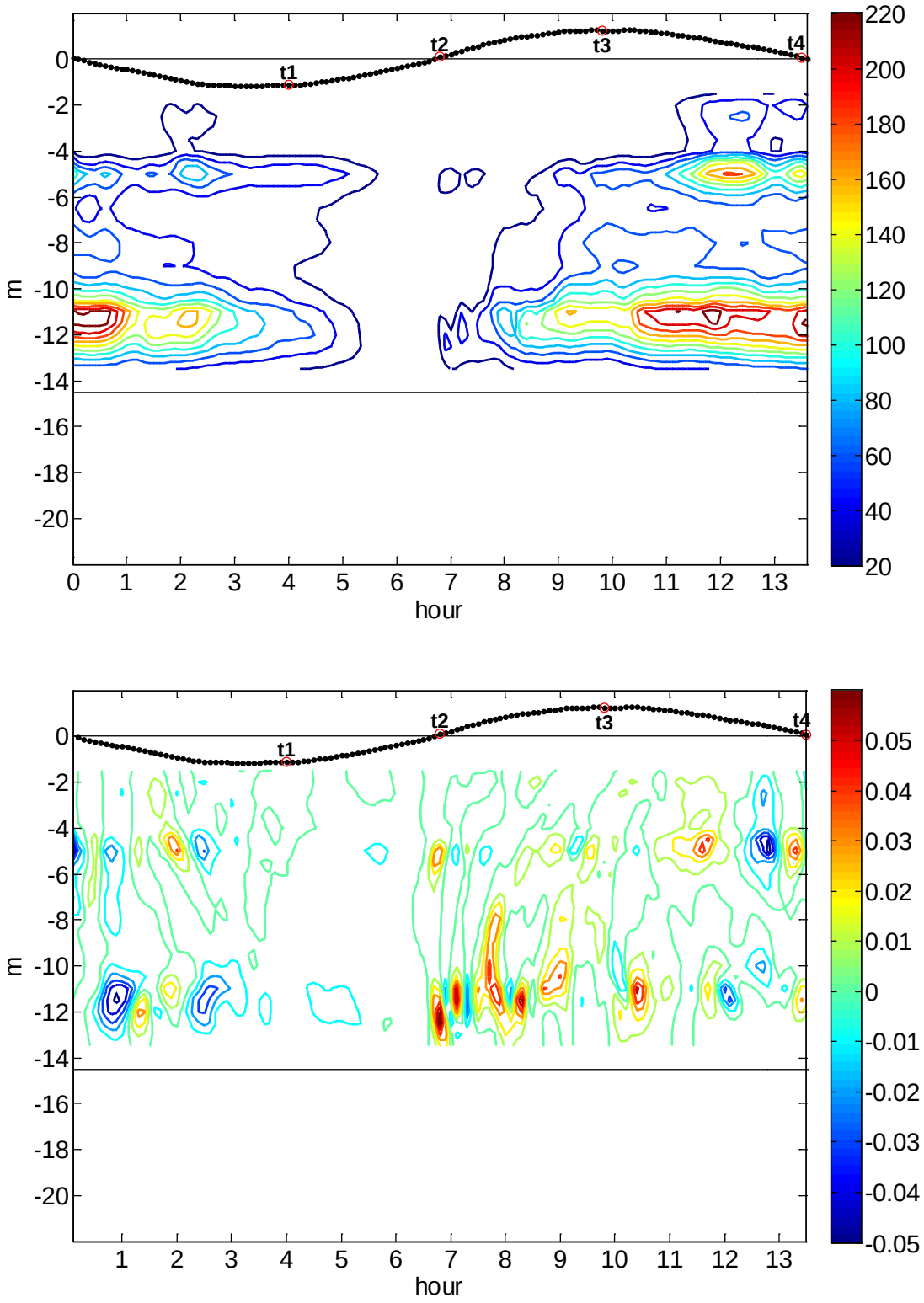

Figure 2.49 Model available potential energy APE [J/m^3] (upper panel) and its local time rate ∂APE/∂t [W/m^3] (lower panel) in a tidal cycle at the upstream of the big valley. Depth-averaged u (doubled in magnitude) has been shown as dotted line.

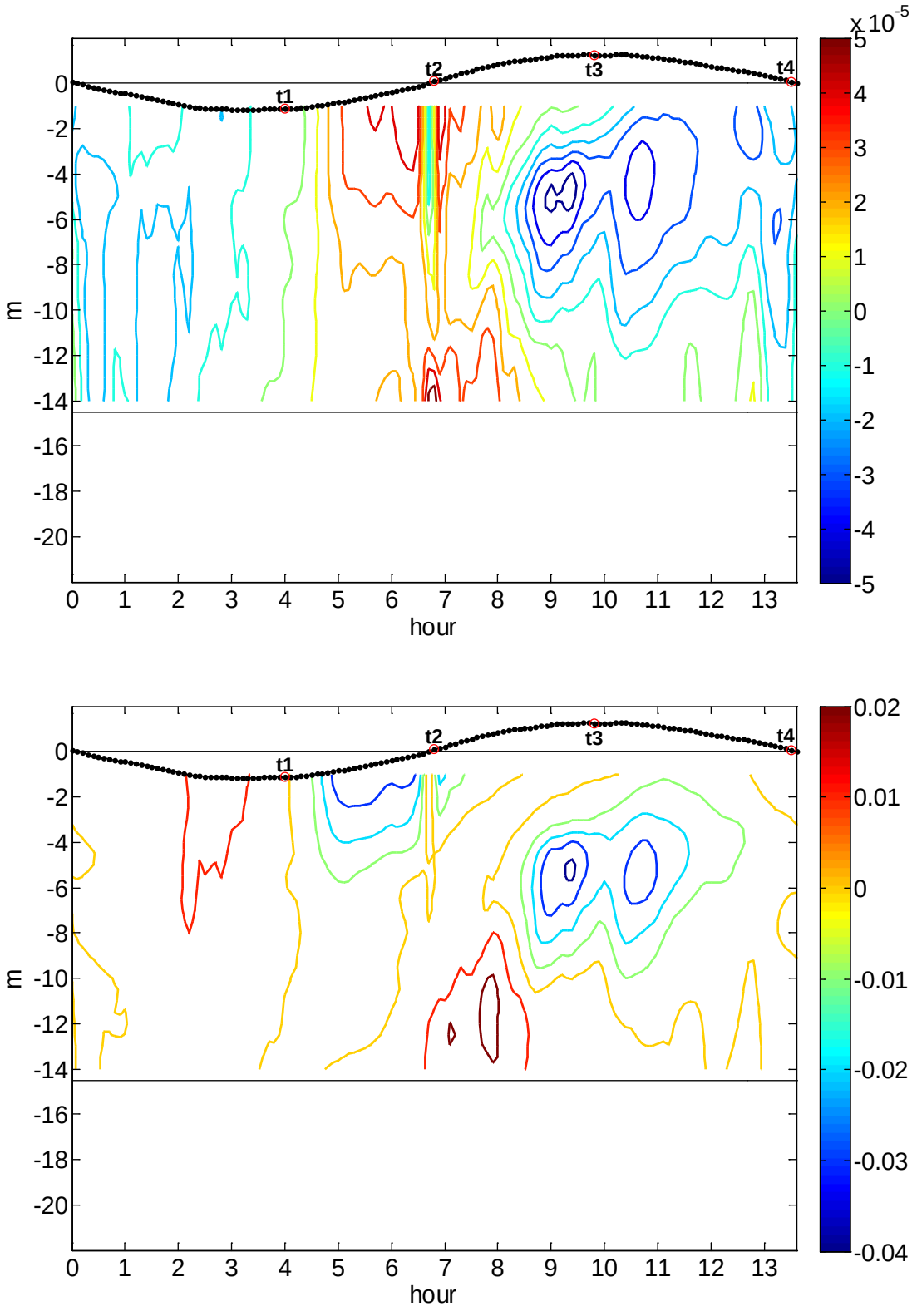

Figure 2.50 Model pressure gradient force [m/s^2] (upper panel) and its power (or divergence of energy flux) [W/m^3] (lower panel) in a tidal cycle at upstream of the big valley. Depth-averaged *u* (doubled in magnitude) has been shown as dotted line.

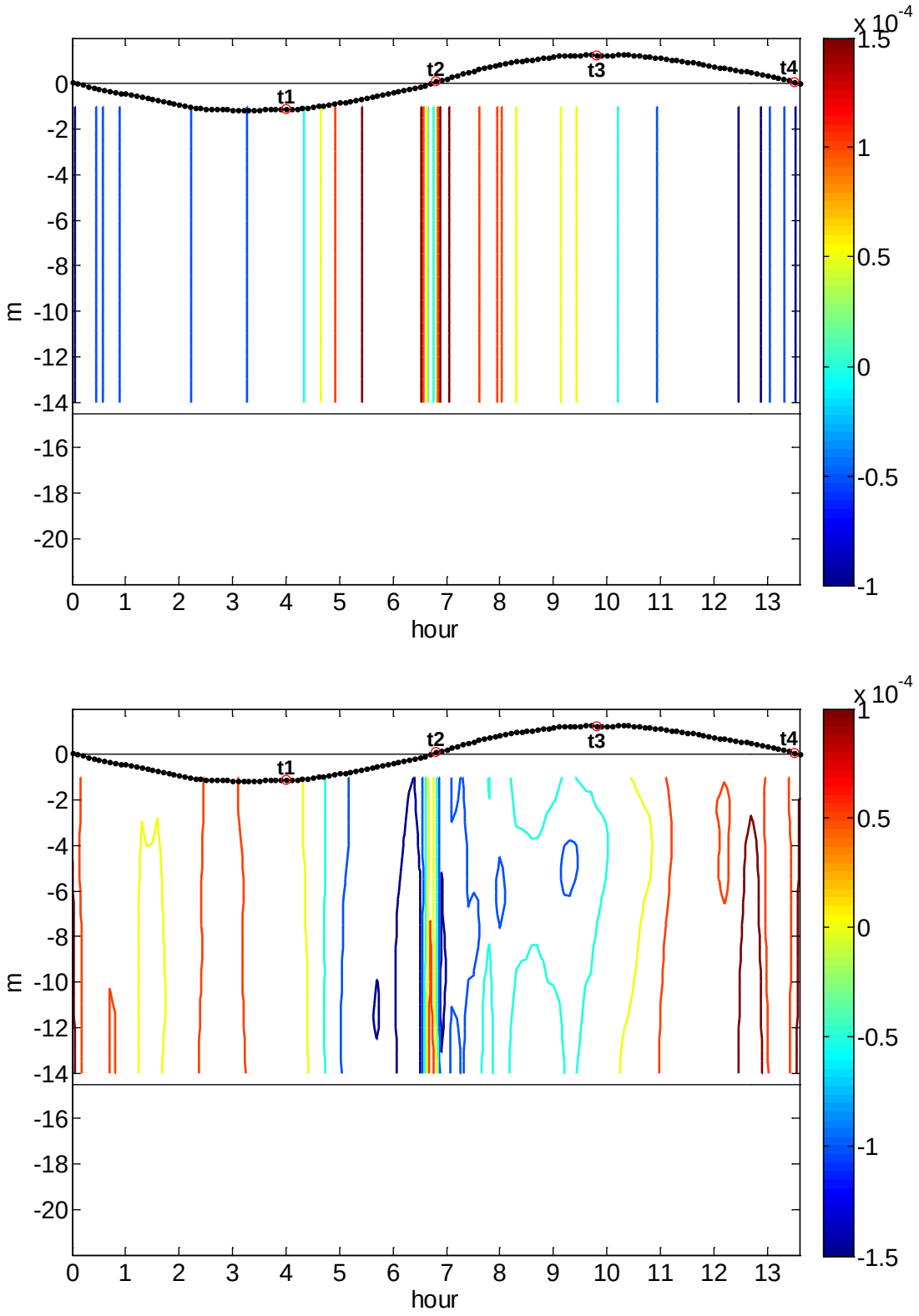

Figure 2.51 Model barotropic (upper panel) and baroclinic (lower panel) pressure gradient forces [m/s^2] in a tidal cycle at upstream of the big valley. Depth-averaged *u* (doubled in magnitude) has been shown as dotted line.

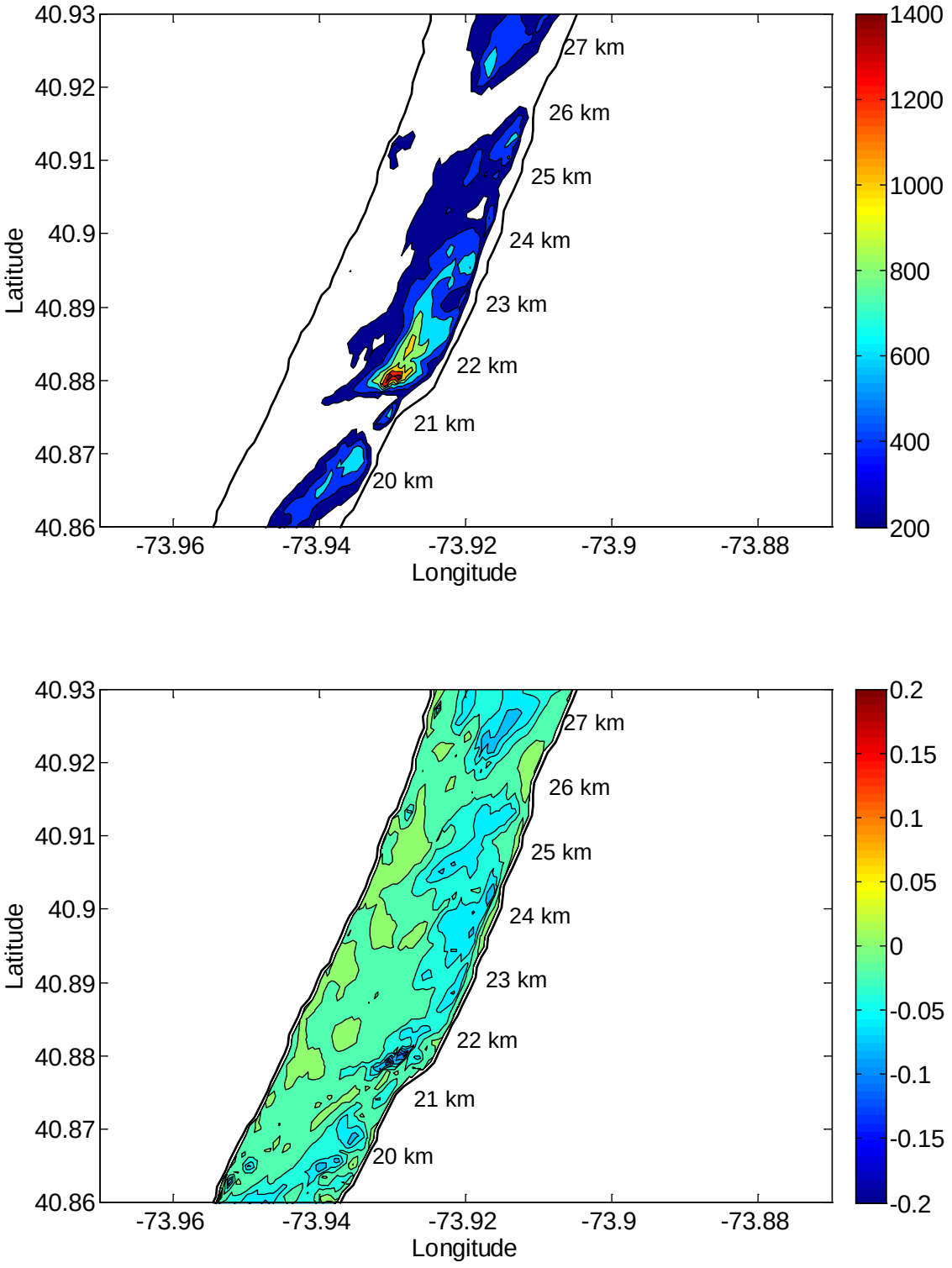

Figure 2.52 Model depth-integrated available potential energy $\int$ APE dz [J/m^2] (upper panel) and its local time rate $\int \partial \text{APE}/\partial t \, dz$ [W/m^2] (lower panel) at the maximum ebb of neap tide in the lower Hudson Estuary.

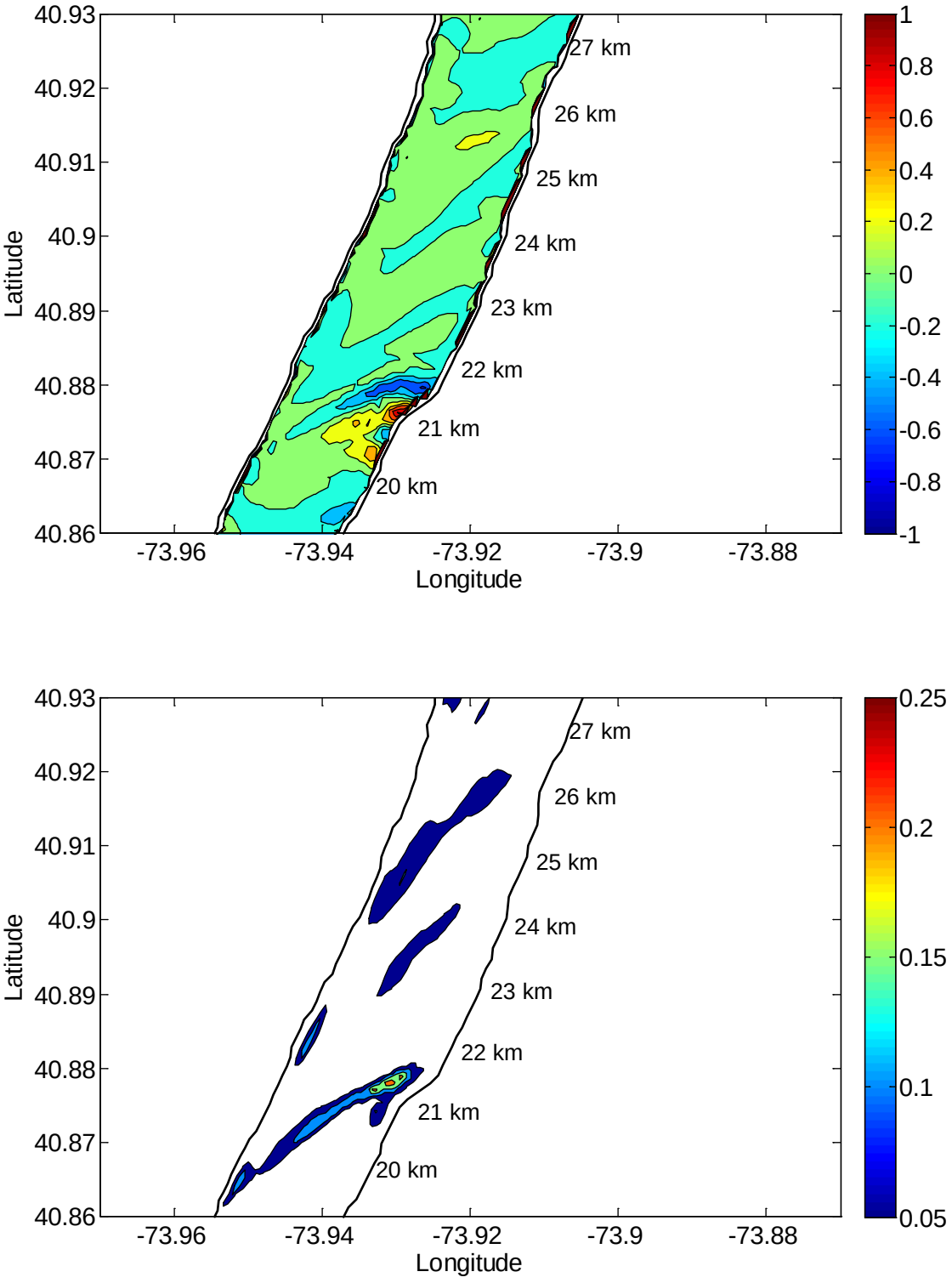

Figure 2.53 Model depth-integrated pressure gradient power (or divergence of energy flux) [W/m^2] (upper panel) and dissipation rate [W/m^2] (lower panel) at the maximum ebb of neap tide in the lower Hudson Estuary.

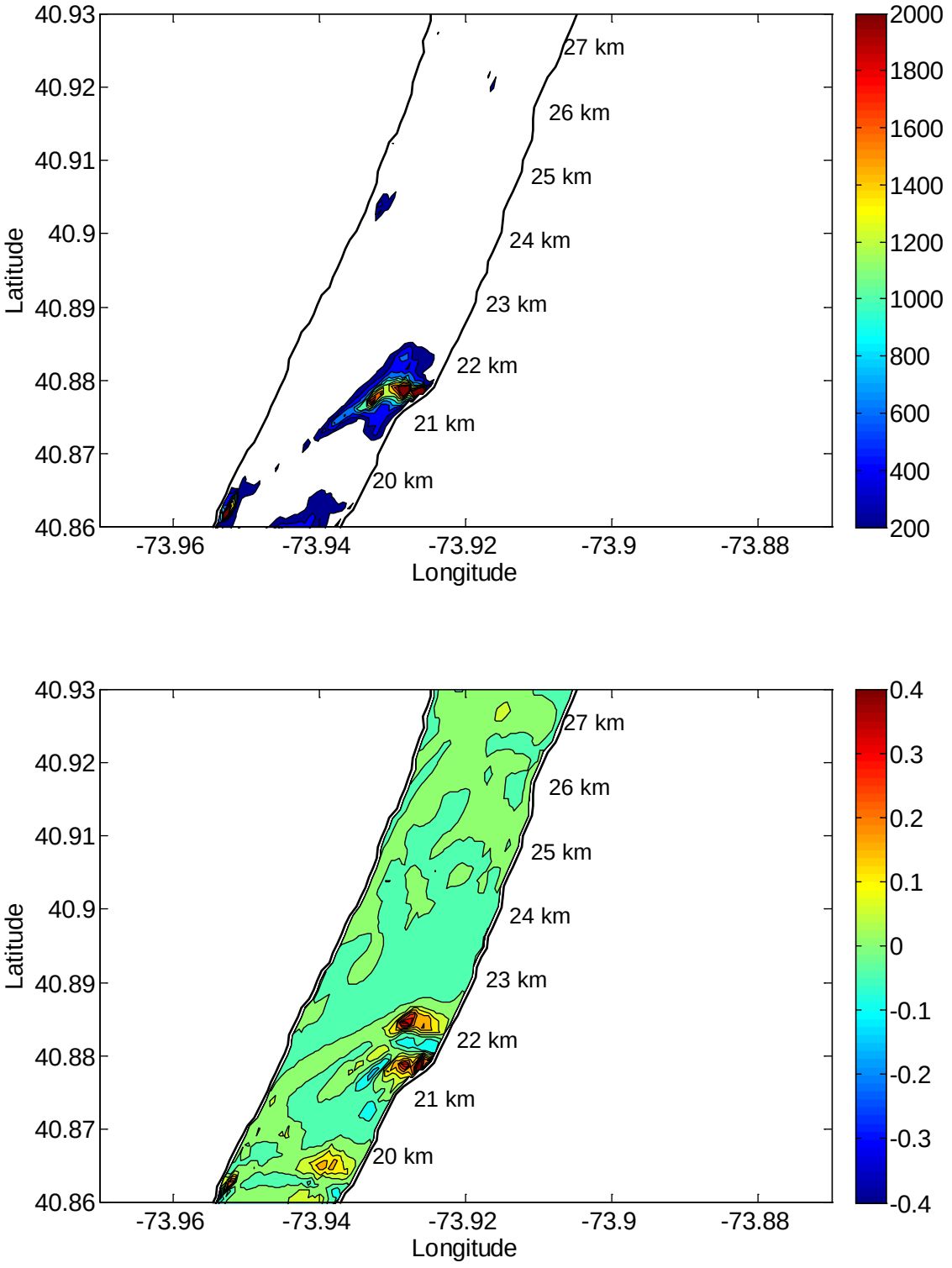

Figure 2.54 Model depth-integrated available potential energy $\int$ APE dz [J/m^2] (upper panel) and its local time rate $\int \partial \text{APE}/\partial t \, dz$ [W/m^2] (lower panel) at the early flood of neap tide in the lower Hudson Estuary.

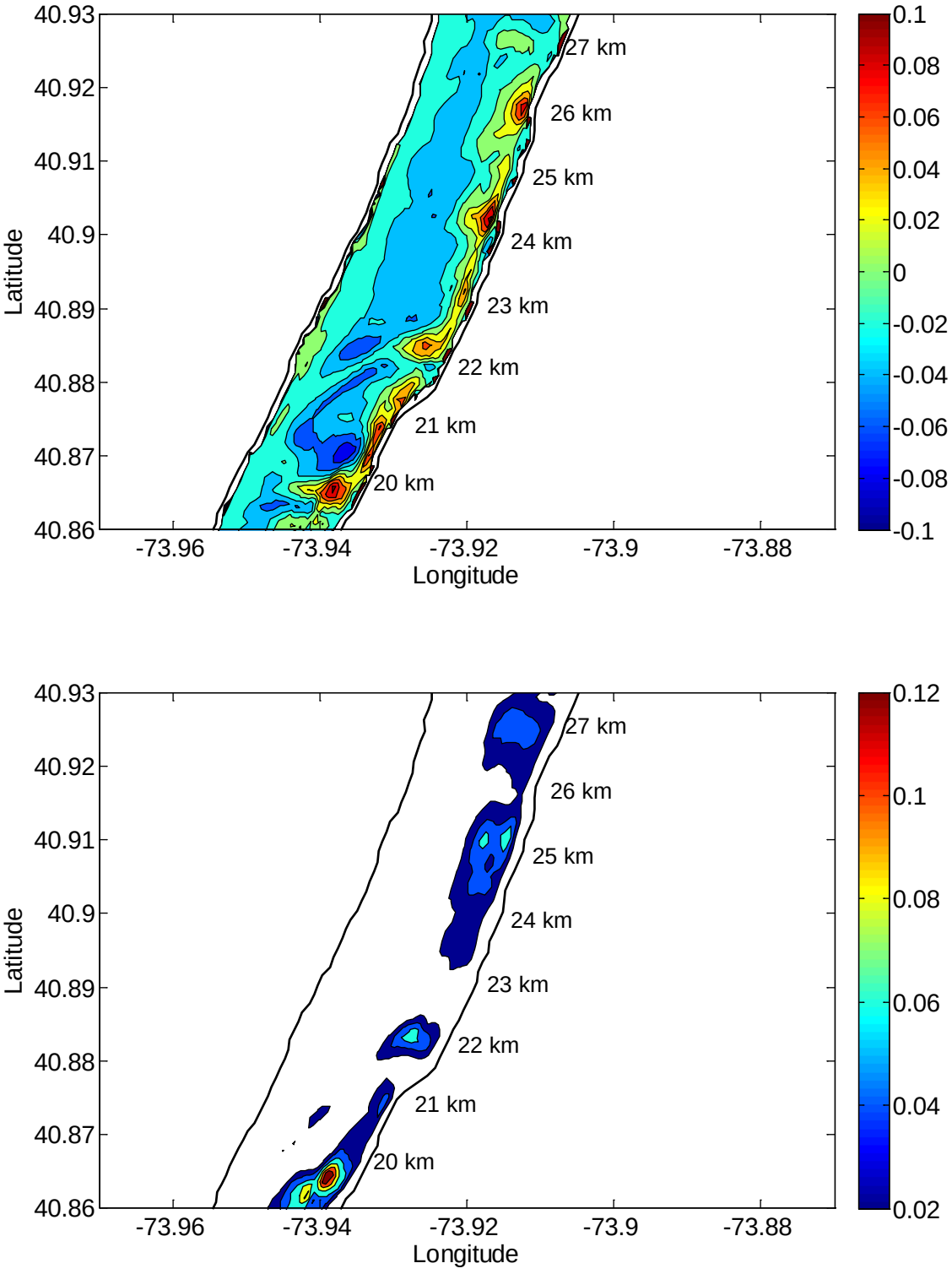

Figure 2.55 Model depth-integrated pressure gradient power (or divergence of energy flux) [W/m^2] (upper panel) and dissipation rate [W/m^2] (lower panel) at the early flood of neap tide in the lower Hudson Estuary.

Table 2.1 Skill statistics of 3D Hudson simulation

Parameters	Skill	RMSE
Depth-averaged current	0.99	0.06
Surface current	0.98	0.16
Bottom current	0.97	0.10
Surface salinity	0.89	1.63
Bottom salinity	0.95	1.56

Chapter 3
Overtide generation and tidal wave propagation in the Hudson River

Abstract

The influence of the strong variations in topography of the channel from the lower Hudson to Troy on the barotropic tide and major over-tides is described using extensive observations from both tide gauges and moored ADCPs. These observations reveal significant over-tides and changes in tidal amplitude and phase coincident with topographic variations. Mechanisms of over-tide generation and tidal wave propagation are investigated using both one-dimensional model and two-dimensional ROMS simulations. Results emphasize the importance of variations in channel topography, as well as the contributions of specific nonlinear terms on over-tide generation, and the importance of tidal wavelength to channel length. Significant longitudinal variations in river channel geometry lead to partial reflection of the tidal waves, i.e. the generation of the additional waves which combine with the original waves. As a result, both the tidal water levels and currents are significantly changed depending on the longitudinal position in the river and the spatial scales of the channel convergence or divergence.

3.1 Objectives and Introduction

The objective of this chapter is to investigate the nonlinear interactions leading to generation of the overtides and modification of the tidal waves by the longitudinally-varying channel morphology in the Hudson River.

The astronomical tides originating in the ocean propagate over the continental shelf and into bays and estuaries, where they are changed in amplitude and phase and distorted from the sinusoidal waves. These tidal changes in the shallow water are mainly due to the changed geometry and depth of the waterway. The distortion of the shallow-water tide can be represented by development of the overtides and the compound tides through nonlinear interactions. The tides, overtides and compound tides are all characterized as shallow-water waves. Understanding the characteristics of shallow-water waves and the related dynamics is important to better comprehend coastal inundation, biogeochemical processes and transport of pollutant, sediment and aquatic species.

The analytical analysis of shallow-water waves has an extensive literature [Redfield, 1950; Ippen and Harleman, 1960; Hunt, 1964; Dronkers, 1964; LeBlond, 1978; Prandle and Rahman, 1980; Parker, 1984; Friedriches and Aubrey, 1994] over the last fifty years. The simplified continuity and momentum equations have been applied to the shallow waterways, assuming that the wave amplitude is less than the depth of waterway and is much less than the wavelength. The friction term in the momentum equation is in a linearized form, i.e. is proportional to longitudinal velocity. All nonlinear terms are ignored.

$$\frac{\partial \eta}{\partial t} + h\frac{\partial u}{\partial x} = 0 \tag{3.1}$$

$$\frac{\partial u}{\partial t} = -g\frac{\partial \eta}{\partial x} - Fu \tag{3.2}$$

where η is the tidal water elevation, u is the cross-sectionally averaged tidal current, h is the width-averaged depth, F is the linearized friction coefficient which can be related with the drag coefficient C_d used in a quadratic frictional form [Friedriches and Aubrey, 1994; Prandle, 2003].

$$F = \frac{8}{3\pi}\frac{C_d U}{h} \tag{3.3}$$

A solution of the simplified continuity and momentum equations is an exponentially damped progressive wave.

$$\eta_i = A_\eta \cos(\sigma t - k x)\, e^{-\mu x} \tag{3.4}$$

where η is the tidal water elevation induced by the incident wave. A_η is the tidal amplitude at the closed end of the waterway (x=0). σ is the wave frequency. k is the wave number. μ is the damping coefficient and is related with F by $\mu = Fk_0/(2kc_0)$ [Parker, 1984; Parker, 2007]. For a waterway with the limited length, an incident damped progressive wave is superimposed by a reflected damped progressive wave. As a result, the wave is characterized by combination of the progressive wave and the standing wave depending mainly on the length of the waterway relative to the tidal wavelength.

$$\eta = \eta_i + \eta_r = A_\eta \cos(\sigma t - kx)\, e^{-\mu x} + A_\eta \cos(\sigma t + kx)\, e^{\mu x} \tag{3.5}$$

The analytical solution of shallow-water waves has been applied to the study of many bays and estuaries in the world [Redfield, 1978; Prandle and Rahman, 1980; Friedriches and Aubrey, 1994]. Comparison between the analytical solution and the observational data indicates that the analytical analysis is able to catch the main characteristics of shallow-water waves. However we can still see significant discrepancy between the analytical solution and the observational data, especially in the tidal river with relatively complicated topography and shape, like the Hudson River (Figure 3.1).

The discrepancy between the analytical solution and the observational data leads us to think about the roles that the nonlinear interactions play in tidal hydrodynamics. The nonlinear interactions are represented by the presence of the product of the variables (e.g. the elevation, current, channel width, depth) in the continuity and momentum equations. The nonlinear interactions play important roles in modifying the tides and generating the overtides, compound tides, residual mean sea level and residual current in shallow waterways [Uncles, 1981; Parker, 1984; Dronkers, 1986; Speer and Aubrey, 1985; Friedrichs and Aubrey, 1988; Jay, 1991; Lanzoni, 1998]. Most of the previous research has been focused on analytical and numerical analysis of generation of the overtides and modification of the tidal waves by the varying channel geometry in relatively short waterways. Both the tides and overtides behave more like a standing wave (combination of the incident wave and the reflected wave). Little previous analysis has been done for the incident wave separated from the standing wave in relatively long waterways. In this study, it can be seen that the analytical and numerical analysis of the incident

wave is a big help to better understand the mechanisms of overtide generation and tidal wave modification. The use of the relatively long generic waterways in this study also provides a complete picture of shallow-water wave characteristics.

In this study, we use both one- and two- dimensional models to investigate the nonlinear interactions leading to generation of the overtides and modification of the tidal waves by the varying channel morphology in the Hudson River. In section 3.2, we describe the data and methods. In section 3.3, we describe the model setup and the model performance. In section 3.4, we analyze the tides and overtides in the Hudson River based on both the observed and model harmonics. In section 3.6, we discuss the mechanisms of overtide generation and the effect of channel geometry on tidal wave propagation. We summarize the chapter in section 3.7.

3.2 Observations

The Hudson River, as a tidal river, is connected with the North Atlantic Ocean through New York Harbor. The tides coming from the North Atlantic Ocean propagate through the river up to Troy. The Hudson River (Figure 3.1) has the length of ~250 km from the Battery up to Troy, about a half semidiurnal tidal wavelength, and with complicated topography and shape, provides with a good experimental place for understanding shallow-water wave characteristics. A lot of measurements of water elevation and current have been done in the Hudson River by NOAA, USGS, HRECOS, Columbia University, and Stony Brook University since 2001. Considering the continuity and completeness of data records, we choose seven data sets of current at June, July, and September, 2005 and April, May, August, and October, 2006 and four data sets of water elevation at May 2001, September 2006, July and September 2009 for analysis. All the data sets have the same time length of 32 days. Each of the data sets is combination of the observed currents or water levels from a certain number of ADCPs or tide gauges in the Hudson River. We use harmonic analysis to separate important tidal constituents M_2, S_2, N_2, K_1, O_1, M_4, and M_6 based on these data sets. The tides in the Hudson are dominated by M_2 and also show spring-neap variation represented mainly by S_2 and N_2, diurnal variation represented mainly by K_1 and O_1, and asymmetry or distortion represented mainly by M_4 and M_6 (Figure 3.2 ~ 3.5). In the present study, we will focus on the discussion of M_2, M_4, and M_6.

Figure 3.2 shows longitudinal variation in amplitude and phase of M_2, M_4, and M_6 elevation calculated from the above four data sets of water elevation using harmonic analysis. Basically M_2 has the minimum amplitude at West Point, about 155 km away from the river head (Troy), much longer than a quarter of the M_2 wavelength (~90 km). However, according to the standing wave theory, the first node of M_2 should be located at a quarter of the M_2 wavelength away from the closed end of the waterway. In addition, the along-channel amplitude of both M_4 and M_6 shows obvious standing wave pattern. The first M_4 antinode and the second M_6 node coincide with each other and are located around 90 km away from Troy, confirming that a quarter of the M_2 wavelength is about 90 km in the upper reach. It also should be noted that the amplitude of M_2, M_4, and M_6 is significantly amplified within the upper ~50 km reach. Thus the downstream shift of the M_2 node and the upper-reach amplification of M_2, M_4, and M_6 lead us to rethinking the tidal propagation in the channel with longitudinally-varying shape.

Figure 3.3 shows longitudinal variation in amplitude of M_2, M_4, and M_6 currents. The M_2, M_4, and M_6 currents are significantly affected by the local channel geometry. However their general patterns look like long waves in the channel. The magnitude of M_2 currents is reduced in the upper reaches of the Hudson River. However the magnitude of M_4 and M_6 currents is significantly enhanced in the upper reaches.

The along-channel phase of M_2, M_4, and M_6 and their phase relations also vary at different reaches of the river, showing very interesting patterns. These important and special features suggested by the observed M_2, M_4, and M_6 need to be further investigated to provide more insights into shallow-water wave characteristics.

3.3 Model configuration and performance

One-dimensional model and experiment design

A one dimensional hydrodynamic model, which is able to represent longitudinal variation in depth, cross-sectional area, and bottom friction coefficient, is used here to investigate the

characteristics of M_2, M_4, and M_6 in a long channel with the closed end on the land and the open mouth connected with the ocean. The model is based on discretization of the equations of continuity and momentum by using the finite-difference technique. The equations of continuity and momentum including all nonlinear terms can be obtained following Parker (1984):

$$\frac{\partial \eta}{\partial t} + \frac{1}{b}\frac{\partial}{\partial x}(b(h+\eta)u) = 0 \tag{3.6}$$

$$\frac{\partial u}{\partial t} + u\frac{\partial u}{\partial x} = -g\frac{\partial \eta}{\partial x} - \frac{1}{h+\eta}C_d\, u\,|u| \tag{3.7}$$

where b is the width of the channel. The equations of (3.6) and (3.7) are then discretized by using the finite-difference technique with a staggered spatial scheme and a centered second-order temporal scheme:

$$\frac{\eta_x^{t+\Delta t} - \eta_x^{t-\Delta t}}{2\Delta t} + \frac{1}{b_x}\frac{1}{2\Delta x}[b_{x+\Delta x}(h_{x+\Delta x} + \eta_{x+\Delta x}^t)u_{x+\Delta x}^t - b_{x-\Delta x}(h_{x-\Delta x} + \eta_{x-\Delta x}^t)u_{x-\Delta x}^t] = 0 \tag{3.8}$$

$$\frac{u_x^{t+\Delta t} - u_x^{t-\Delta t}}{2\Delta t} + \frac{1}{2}\frac{(u_{x+\Delta x}^t)^2 - (u_{x-\Delta x}^t)^2}{2\Delta x} = -g\frac{\eta_{x+\Delta x}^t - \eta_{x-\Delta x}^t}{2\Delta x} - \frac{C_{dx}}{h_x + \eta_x^{t-\Delta t}}u_x^{t-\Delta t}\,|u_x^{t-\Delta t}| \tag{3.9}$$

The elevation $\eta_x^{t+\Delta t}$ is calculated at odd grid points by using (3.8) and the current $u_x^{t+\Delta t}$ is calculated at even grid points by using (3.9). A backward, first-order time difference is applied to the friction term for modeling stability.

The model is forced at the channel entrance with tidal elevation and with river flow at the closed end. If the clamped boundary condition (i.e. specified sinusoidal function) is applied at the open boundary, the outgoing waves would be fully bounced back into the domain, resulting in false wave characteristics along the channel, especially at the downstream reach. If the radiation boundary condition is applied at the open boundary, the outgoing wave speed needs to be precisely estimated. Otherwise errors would be introduced back into the domain. However, tidal wave speed depends on tidal wave length if the bottom friction is considered (see (3.14)). It is hard to radiate all outgoing waves without introducing errors into the domain. In this study, an extended uniform channel is used to damp significantly outgoing waves in order to diminish their effects on tidal waves in the interest channel. Its function is similar to a sponge layer in other numerical models. It is assumed that tidal waves propagating in the extended uniform channel conform to the equations (3.1) and (3.2). The extended channel length and the corresponding

linear friction coefficient can be estimated by analytical relations (3.4), (3.12), (3.13), and (3.14) if the incident wave amplitude at the mouth of the interest channel has been known. If the linear bottom friction term is used for the interest channel, the linear friction coefficient for the extended channel is set to be equal to that for the interest channel. If the quadratic bottom friction term is used for the interest channel, the linear friction coefficient for the extended channel is set to be equal to $C_d A_u / h$ at the point connecting the extended channel with the interest channel. A_u is the estimated current amplitude of the incident wave at the connecting point. Given the linear friction coefficient for the extended channel, the extended channel length and the incident wave amplitude at the mouth of the extended channel can then be specified according to the damping request. Then a sinusoidal wave with larger amplitude is specified at the open boundary of the extended channel. In the following numerical experiments, the ratio of the incident wave amplitude at the mouth of the extended channel to that at the mouth of the interest channel is set to be about 10. Under this condition, an outgoing wave with the amplitude of *A* at the interest channel mouth would be damped to be *0.1A* after the first-time propagating through the extended channel. Once this wave is reflected back from the extended channel mouth due to the clamped open boundary condition, it would be damped again to be *0.01A* at the interest channel mouth and only have very little effect on the waves within the interest channel after the second-time propagating through the extended channel.

Assume that the variable η and u change with x and t and the variable b and h change with x, there are two nonlinear terms $\partial(bhu)/\partial x$ and $\partial(b\eta u)/\partial x$ in the continuity equation (3.6). In a uniform channel, b and h are constant. There is only one nonlinear term $\partial(\eta u)/\partial x$ in the continuity equation. If the friction term is broken into two pieces [Parker, 1984]:

$$-\frac{1}{h+\eta} C_d u|u| \approx -\frac{C_d}{h} u|u| + \frac{C_d}{h^2} \eta u|u| \qquad (3.10)$$

then there are three nonlinear terms $u\partial u/\partial x$, $C_d u|u|/h$, and $C_d \eta u|u|/h^2$ in the momentum equation (3.7). In the following discussion, we will use the product of different variables to represent the corresponding nonlinear term. These nonlinear terms play different roles in generating the overtides and modifying the tidal waves. In addition, the river flow introduced into the system also has significant effects on overtide generation. We will use r to represent the

river flow effects. Parker (1984) applied Fourier decomposition onto each of the nonlinear terms and found that the nonlinear term ηu (or $b\eta u$), uu, $\eta u|u|$, and $u|u|+r$ could generate asymmetric overtide M_4 and the nonlinear term $u|u|$ could generate symmetric overtide M_6. Actually the nonlinear term *bhu* plays an important role in modifying the tidal waves propagating in the channel with spatially-varying width and depth. Each of the nonlinear terms can be activated or shutdown at certain reaches of the interest channel in order to evaluate their individual effect on overtide generation or tidal wave modification.

We designed two basic types of generic numerical experiments. The first type of experiments is to investigate overtide generation and tidal wave modification based on the analysis of the progressive wave in a relatively long channel. The other type is based on the analysis of the quasi-standing wave in a relatively short channel. In order to simulate propagation of the progressive wave, two extended channels are connected respectively with two ends of the interest channel. The downstream extended channel is used to damp the wave reflected at the clamped open boundary. The upstream extended channel is used to damp the wave reflected at the closed end of the channel. Thus the wave that propagates within the middle interest channel is very little affected by the reflected waves and can be seen as the progressive wave. The linearized bottom friction term is used in the momentum equation for the two extended channels and the interest channel. In order to simulate the quasi-standing wave, only one extended channel is used to mitigate the effects of the clamped open boundary condition. The quadratic bottom friction term is used for the interest channel.

For all generic numerical experiments, the model is forced by the M_2 elevation at the open boundary. The model runs to produce the results with 30 days record. The last four days are used in harmonic analysis to obtain the amplitude and phase of M_2, M_4, and M_6 along the channel. Then the amplitude ratio and the phase difference between M_2 and M_4, M_6 are then calculated.

Model setup in the Hudson River

The model grid used for two-dimensional barotropic simulations is the same as described in 2.4. The longitudinally-varying width and mean depth extracted from the 2D grid is used for one-dimensional simulations.

Both one- and two- dimensional models are forced by the real-time observed water levels at the Battery and the river discharge at Green Island. Hydrodynamic conditions are simulated for two months. The first 15 days are used for adjustment. The last 32 days are used in harmonic analysis to provide longitudinal amplitude and phase of M_2, S_2, N_2, K_1, O_1, M_4, and M_6 elevation and current throughout the Hudson River.

Model performance

Generally both one- and two- dimensional models reproduce the tides and overtides (Figure 3.2 ~ 3.5) very well in terms of both amplitude and phase of the dominant tidal constituents in the Hudson River. The root-mean-squared errors (RMSE) have been listed in Table 3.1. One-dimensional model performs as well as two-dimensional model except M_4 in terms of amplitude. One-dimensional model tends to overestimate the M_4 amplitude especially in the upstream reaches probably due to the overestimated upstream bathymetry (see the discussion of the shoaling effect). Two-dimensional model reproduces tidal phase a little better than one-dimensional model due to representation of channel/shoal topography in the river. Both one- and two- dimensional models tend to overestimate tidal phase in the vicinity of the river head, which may be due to the overestimated bathymetry.

3.4 Results

3.4.1 Partial reflection of tidal waves in the downstream Hudson

A sharp divergent reach (35~40 km) and a sharp convergent reach (60~65 km) are connected by the wide Haverstraw Bay (41.04 ºN ~ 41.25ºN) in the downstream Hudson River

(Figure 3.1). The width of the sharp divergent reach increases from 1500m to 4500m. The cross-sectional area also increases by ~1.4 times. The convergent reach is even sharper, with the width decreasing from 5000 m to 1000 m and the cross-sectional area decreasing by ~1.7 times. Both the divergent reach and the convergent reach lead to partial reflection of tidal waves in the downstream Hudson. As shown in Figure 3.3b, the phase difference between M_2 elevation and current is elevated to ~30º in the vicinity of the divergent reach. The elevated phase difference between elevation and current can also be seen in other tidal constituents (Figure 3.5bdfh) in the vicinity of the divergent reach. This can be explained by the followed discussion of the effect of the convergent/divergent reach on the incident waves in section 3.5.2 and Figure 3.18. As shown in Figure 3.18e, there is a maximum/minimum of η-u phase difference around the 1/8 M_2 wavelength downstream of the convergent/divergent reach. In the downstream Hudson, the 1/8 M_2 wavelength is approximately 50 km, which is much longer than the distance between the convergent reach and the divergent reach. Thus the η-u phase difference increases downstream of the convergent reach and decreases downstream of the divergent reach, leading to a peak present in the vicinity of the divergent reach.

As the discussion in section 3.5.2, the abrupt convergence/divergence produces the additional wave which propagates at the same time in the two directions, leading to longitudinal variations in amplitude and phase of the combined wave. The upstream-propagating additional wave induced by the abrupt convergence (or divergence) would be superimposed onto (or subtracted from) the original incident wave due to 0 (or π) phase difference. The downstream-propagating additional wave behaves like a reflected wave. As a result, the combined wave amplitude keeps unchanged around the transition point located at the 1/8 wavelength downstream of the sharp convergent/divergent reach. The combined wave amplitude would increase (or decrease) at the upstream of the transition point and decrease (or increase) at the downstream of the transition point due to the abrupt convergence (or divergence). Since the distance between the sharp divergent reach and the sharp convergent reach in the downstream Hudson is only about the 1/16 wavelength of the semidiurnal tides, two opposite effects tend to be cancelled in between, which make the combined wave amplitude close to the incident wave amplitude. The combined wave amplitude is lowered down at the downstream of the divergent reach and is elevated at the upstream of the convergent reach. As a result, the semidiurnal tide

amplitude decreases at a slower rate upstream from the river mouth to the node (Figure 3.2a and Figure 3.4ac). If neither abrupt convergence nor divergence is in the downstream Hudson, the semidiurnal tide amplitude should decrease at a faster rate upstream from the river mouth to the node as shown in Figure 3.6a.

In addition, the combined wave phase keeps unchanged at the upstream of the convergent/divergent reach but would slightly increase (or decrease) at the downstream of the convergent (or divergent) reach. Thus the phase of the semidiurnal tides slightly decreases downstream of the sharp divergent reach (Figure 3.2b and Figure 3.4bd). The effects of the sharp convergent/divergent reach on the diurnal tides can also be seen in Figure 3.4 and Figure 3.5.

It should also note that the distance between the sharp divergent reach and the sharp convergent reach in the downstream Hudson is around the 1/8 M_4 wavelength and exceeds the 1/8 M_6 wavelength. Thus the decreased overtide amplitude by the divergent reach would not be compensated by the upstream convergent reach, leading to a minimum M_4/M_6 in the vicinity of the divergent reach.

The M_2 amplitude from the two-dimensional model is a couple of centimeters higher than that from the one-dimensional model in between the sharp divergent reach and the sharp convergent reach in the downstream Hudson. This may be because the curved channel shape (~41.25 ^{o}N in Figure 3.1a) can only be resolved by the two-dimensional model. The curved channel may also contribute to partial reflection of tidal waves, leading to enhanced wave amplitude at both the upstream and downstream of the convergent reach.

There are large flanks in the Haverstraw Bay. Friedrichs (1995) showed that the channel/shoal topography can modify tidal phase propagation. However, the slight phase difference (Figure 3.2b) between the one- and two- dimensional models suggests that the channel/shoal topography may play a minor role in modifying the tide in the downstream Hudson.

3.4.2 Tides and overtides in the upper Hudson

The upstream Hudson from 150 km to 250 km is characterized as a continuously convergent reach with the width decreasing from 1500 m to 300 m and the cross sectional area decreasing by ~11 times. The upstream M_2 amplitude significantly increases, which is due to both the enhanced incident M_2 by the channel convergence and the superimposition of the reflected M_2. The M_2 node should be located at the 1/4 wavelength downstream of the river head, which is approximately at 150km in a uniform channel (Figure 3.6a). However, the M_2 node (Figure 3.2a) in the Hudson River moves further downstream by ~40km due to the upstream convergence. Both the M_2 η-u phase difference (Figure 3.3b) and the M_2 amplitude (Figure 3.2a) decreases downstream from the river head to the node at a faster rate than that in the uniform channel (Figure 3.6ab), indicating that the reflected M_2 is damped more quickly since the upstream Hudson is convergent to the incident M_2 but divergent to the reflected M_2. As a result, the M_2 current (Figure 3.3a) increases sharply downstream from the river head to the node.

The elevation phase difference between M_2 and M_4 (Figure 3.2d) is close to 90º in the vicinity of the river head, indicating that the time from the high tide to the low tide is shorter than that from the low tide to the high tide (ref. the fourth column of Figure 3.8). In other words, the high tide time is delayed while the low tide time is advanced. The current phase difference between M_2 and M_4 (Figure 3.3d) is close to 0º through the upstream Hudson (170~250 km), suggesting flood dominance (ref. the fourth column of Figure 3.9).

Figure 3.10 and 3.11 display the M_2, M_4, and M_6 elevation and current in the convergent channel and the shoaling channel. These are used to show the effects of the channel morphology of the upstream Hudson on tidal propagation. The channel width linearly decreases from 1000m at 150km to 200m at 250km in the convergent channel. The channel depth linearly decreases from 10m at 150km to 2m at 250km in the shoaling channel. The cross-sectional area decreases by one fifth for each type of channel. The downstream width and depth keep uniform for each type of channel. Generally the upstream channel convergence significantly amplifies the tidal amplitude, moves the tidal node downstream (Figure 3.10a) and makes the phase propagation

faster (Figure 3.10b). The transition between standing wave and progressive wave also moves downstream (Figure 3.11b).

In the shoaling channel, the tidal amplitude in the upstream reach (170~250 km) decreases since the increased damping effect of the bottom friction surpasses the enhancing effect of the channel convergence (Figure 3.10a). On the other hand, the tide amplitude in the middle reach (110~170 km) increases due to the damped reflected tidal wave in the upstream reach. Correspondingly, the tidal phase propagates faster in the middle reach and slower in the upstream reach (Figure 3.10b) relative to the uniform channel. The M_4 elevation is amplified while the M_6 elevation is damped in the upstream reach. It is interesting that the M_2, M_4, and M_6 currents are all significantly amplified in the upstream reach (Figure 3.11ace), leading to upstream movement of the current anti-node. The ways that the overtides distort the tide are also changed (Figure 3.10df and Figure 3.11df).

In the upstream Hudson River, it is the combining effects of both convergence and shoaling that significantly reshape the tides and overtides throughout the upper Hudson (100~250 km) in terms of both elevation and currents relative to the uniform channel.

Figure 3.12 and Figure 3.13 show the effect of the river flow on the tide and overtides in the uniform channel with the same length as the Hudson River. The maximum M_2 current (anti-node) in the upper reach (100~250 km) is approximately 0.6 m/s without the river flow (Figure 13a), which is present around the M_2 elevation node (~150 km). When the river flow increases to be 0.3 m/s, the M_2 and M_6 is damped but the M_4 is significantly enhanced. The M_2 phase is slightly delayed. When the river flow reaches 0.6 m/s, the M_2, M_4, and M_6 are all significantly damped throughout the channel especially in the upstream reach (170~250 km). The M_2 phase is significantly slowed down.

3.5 Discussion

3.5.1 Analytical model for overtide generation

The analytical solution of a tidal wave in a long uniform channel can be expressed by combination of the incident wave and the reflected wave. The combined wave with the form in (3.5) can be further changed into one-wave form:

$$\eta = A_\eta \sqrt{e^{-2\mu x} + e^{2\mu x} + 2\cos(2kx)}\cos(\sigma t - kx + \theta) \tag{3.11}$$

where $\theta = \tan^{-1}\left[\dfrac{e^{\mu x}\sin(2kx)}{e^{-\mu x} + e^{\mu x}\cos(2kx)}\right]$.

Figure 3.14 shows longitudinal variation in amplitude and phase of the incident wave, the reflected wave, and the combined wave. The incident wave amplitude $A_\eta e^{-\mu x}$ is exponentially damped in the positive x direction and becomes A_η at the channel end (x=0). The reflected wave amplitude $A_\eta e^{\mu x}$ has the same value A_η at the channel end and then decreases exponentially in the negative x direction. As a result, the combined wave amplitude, $A_\eta \sqrt{e^{-2\mu x} + e^{2\mu x} + 2\cos(2kx)}$, along the channel looks like a landward-increasingly perturbed curve around an exponential center line (i.e. the along-channel amplitude of the incident wave). The envelop lines of this perturbed curve can be seen as superimposition (or subtraction) of the incident wave amplitude by the reflected wave amplitude everywhere along the channel. The upper (or lower) envelop line is expressed by $A_\eta(e^{-\mu x} \pm e^{\mu x})$. The incident wave phase *kx* linearly increases in the positive x direction, suggesting linearly-delayed high water along the channel. The reflected wave phase *–kx* continues to increase in the negative x direction, suggesting continuingly-delayed high water. The combined wave phase $kx - \theta$ along the channel also looks like a landward-increasingly perturbed curve around the incident wave phase line. The phase difference between the incident wave and the reflected wave is equal to *2kx*. Where $2kx = -m\pi$ (*m*=0, 2, 4 …) or the distance away from the channel end is *m/4* wavelength, the incident wave is in phase with the reflected wave and the combined wave amplitude is superimposition of the incident wave amplitude by the reflected wave amplitude. These

locations $x = \frac{m}{4}\lambda$ are defined as the antinodes. Where $2kx = -n\pi$ (n=1, 3, 5 …) or the distance away from the channel end is *n/4* wavelength, the incident wave is in reversed phase with the reflected wave and the combined wave amplitude is subtraction of the incident wave amplitude by the reflected wave amplitude. These locations $x = \frac{n}{4}\lambda$ are defined as the nodes. Basically the combined wave amplitude and phase suggest that a tidal wave behaves more like a standing wave where it is closer to the channel end and more like a progressive wave where it is further away from the channel end.

For an exponentially damped incident wave in a long channel with uniform width and depth, the current can be obtained by substituting the elevation solution (3.4) into the continuity equation (3.1):

$$u_i = A_u \cos(\sigma t - kx + \alpha)\, e^{-\mu x} \tag{3.12}$$

where $A_u = A_\eta \frac{\sigma}{h\sqrt{\mu^2 + k^2}}$, $\alpha = \tan^{-1}(\mu / k)$.

The damping coefficient μ can be related to the linear friction coefficient F by:

$$\mu = \frac{k_0 F}{2kc_0} \tag{3.13}$$

k_0 and c_0 are the frictionless values of wave number and wave speed. Their relation with k and c can be expressed by:

$$\frac{k_0}{k} = \frac{c}{c_0} = \frac{1}{\sqrt{1 + (\mu / k)^2}} \tag{3.14}$$

For no friction ($\mu = 0$), $A_u = A_\eta \frac{\sigma}{hk_0} = A_\eta \frac{c_0}{h} = A_\eta \sqrt{\frac{g}{h}}$, $\alpha = 0$. The amplitude ratio of current to elevation is $\sqrt{g/h}$. Maximum elevation and maximum current occur at the same time. As friction increases (F in (3.2) increases), the amplitude ratio of current to elevation becomes smaller and smaller than $\sqrt{g/h}$. The time difference between maximum elevation and maximum current increases correspondingly.

Here we use η_{i2nct} (or η_{i2adv}), u_{i2nct} (or u_{i2adv}), $A_{\eta 2nct}$ (or $A_{\eta 2adv}$), A_{u2nct} (or A_{u2adv}) to represent elevation, current, elevation and current amplitude at x=0 of the incident second harmonic constituent (i.e. M_4) produced by M_2 through the nonlinear term $\partial(\eta u)/\partial x$ in the continuity equation (or the advective term $u\partial u/\partial x = \frac{1}{2}\partial u^2/\partial x$ in the momentum equation). The product of elevation and current of the incident M_2 can be expressed by:

$$\eta_i u_i = \frac{1}{2} A_\eta A_u \cos(2\sigma t - 2kx + \alpha) e^{-2\mu x} + \frac{1}{2} A_\eta A_u \cos(\alpha) e^{-2\mu x} \tag{3.15}$$

The first term on the right hand side can be seen as one of the sources of the incident M_4. The second term affects the mean water level. For M_4 generation, only the first term will be considered. Assume that the incident M_4 is arrested at a certain point x_0, its development can be expressed by part of the continuity equation:

$$\frac{\partial \eta_{i2nct}}{\partial t} = -\frac{\partial(\eta_i u_i)}{\partial x} \tag{3.16}$$

Substitute the first term of (3.15) into (3.16):

$$\frac{\partial \eta_{i2nct}}{\partial t} = -A_\eta A_u \sqrt{\mu^2 + k^2} \sin(2\sigma t - 2kx) e^{-2\mu x} \tag{3.17}$$

Then η_{i2nct} at x_0 can be estimated by:

$$\eta_{i2nct}\Big|_{x=x_0} = \frac{A_\eta A_u \sqrt{\mu^2 + k^2}}{2\sigma} \cos(2\sigma t - 2kx_0) e^{-2\mu x_0} \tag{3.18}$$

The magnitude of M_4 is proportional to the square of the magnitude of M_2. If M_4 is arrested at its born point, the magnitude of M_4 along the channel would decrease more quickly ($\sim e^{-2\mu x}$) than that of M_2 ($\sim e^{-\mu x}$). It suggests that the closer to the channel end the smaller the magnitude of the locally-generated M_4.

Once the elevation η_{i2nct} has been fully developed through (3.18) at x_0, the incident M_4 would not actually be arrested but would propagate at the same time in the two directions, i.e., toward the channel end (the positive incident M_4) and toward the channel mouth (the negative

incident M_4). This can be testified by the latter numerical modeling results (Figure 3.8). Both the positive and negative incident M_4 should conform to the equation (3.1) and (3.2) on the first order assumption during their propagation along the channel.

Then η_{i2nct} and u_{i2nct} of the positive incident M_4 through the channel can be estimated:

$$\eta^{+}_{i2nct} = A_{\eta 2nct}\cos(2\sigma t - 2kx)e^{-\mu(x-x_0)} \tag{3.19}$$

$$u^{+}_{i2nct} = A_{u2nct}\cos(2\sigma t - 2kx + \alpha_2)e^{-\mu(x-x_0)} \tag{3.20}$$

where $A_{\eta 2nct} = \dfrac{A_\eta A_u\sqrt{\mu^2+k^2}}{2\sigma}e^{-2\mu x_0}$, $A_{u2nct} = \dfrac{2\sigma A_{\eta 2nct}}{h\sqrt{\mu^2+(2k)^2}} = \dfrac{A_\eta A_u\sqrt{\mu^2+k^2}}{h\sqrt{\mu^2+(2k)^2}}e^{-2\mu x_0}$,

$\alpha_2 = \tan^{-1}\left(\dfrac{\mu}{2k}\right)$

η_{i2nct} and u_{i2nct} of the negative incident M_4 through the channel can be estimated:

$$\eta^{-}_{i2nct} = A_{\eta 2nct}\cos[2\sigma t + 2k(x-2x_0)]e^{\mu(x-x_0)} \tag{3.21}$$

$$u^{-}_{i2nct} = A_{u2nct}\cos[2\sigma t + 2k(x-2x_0) + \alpha_2 - \pi]e^{\mu(x-x_0)} \tag{3.22}$$

It should be noted that the phase of the positive incident M_4 does not depend on its born position x_0. It indicates that the positive incident M_4 waves generated at different locations are in phase where they meet with each other. They tend to be superimposed by each other. On the other hand, the phase of the negative incident M_4 depends on its born position x_0. If another negative incident M_4 is generated at x_1 and the distance between x_0 and x_1 is equal to a quarter of M_4 wave length, i.e. $|x_1 - x_0| = \dfrac{2\pi}{8k}$, the phase difference between these two negative incident M_4 waves would become π. They tend to be canceled by each other.

The positive incident M_4 has almost the same wave speed (shallow-water wave speed) and the same propagating direction with the incident M_2 and is also exponentially ($\sim e^{-\mu x}$) damped on the way of its propagation. When it reaches another point on its way, the damped downstream-born positive incident M_4 is almost in phase with the locally-born positive incident M_4 and they tend to be superimposed by each other. The resulting positive incident M_4 along the

channel can be seen as superimposition of infinite amount of damped downstream-born M_4 with locally-born M_4. The amplitude of the resulting positive incident M_4 would increase in the positive x direction at the starting downstream reach where the amount that the locally-born M_4 adds into the combined M_4 exceeds the exponentially damped amount of the combined M_4. Then the combined positive incident M_4 reaches its maximum in amplitude at a certain point where the newly-supplied amount is equal to the exponentially damped amount. From this maximum point to the channel end, the amplitude of the combined positive incident M_4 decreases but at a slower rate than exponentially-damping rate due to continuous supply from the locally-born M_4. The position of this maximum point mainly depends on the strength of the bottom friction. The weaker the bottom friction is, the closer the maximum point is to the channel end. If the channel length is shorter than the distance between the starting point and the maximum point, the amplitude of the combined positive incident M_4 would increase all through the channel. The above discussion can be confirmed by the numerical results shown in Figure 3.16.

The negative incident M_4 has almost the same wave speed (shallow-water wave speed) but the opposite propagating direction with the incident M_2. It is also exponentially ($\sim e^{\mu x}$) damped on the way of its propagation. When it reaches another point on its way, the damped upstream-born negative incident M_4 is not necessarily in phase with the locally-born negative incident M_4. They are even reversed in phase where they meet with each other if the distance between them is a quarter of the M_4 wavelength. As a result, the negative incident M_4 tends to be canceled by each other and does not accumulate along the channel.

Similarly the incident M_4 at x_0 only generated by the advective term can be obtained by solving part of the momentum equation (3.24).

$$\frac{1}{2}u_i u_i = \frac{1}{4}A_u A_u \cos(2\sigma t - 2kx + 2\alpha)e^{-2\mu x} + \frac{1}{4}A_u A_u e^{-2\mu x} \qquad (3.23)$$

The first term on the right hand side can be seen as another source of the incident M_4. The second term contributes to variation in the mean current. Substitute the first term into (3.24) and solve (3.24):

$$\frac{\partial u_{i2adv}}{\partial t} = -\frac{1}{2}\frac{\partial (u_i u_i)}{\partial x} \tag{3.24}$$

Then u_{i2adv} at x_0 can be estimated by:

$$u_{i2adv}\Big|_{x=x_0} = \frac{A_u A_u \sqrt{\mu^2 + k^2}}{4\sigma}\cos(2\sigma t - 2kx_0 + \alpha)e^{-2\mu x_0} \tag{3.25}$$

Then u_{i2adv} and η_{i2adv} of the positive incident M_4 through the channel can be estimated from (3.25) and the equation (3.1) and (3.2):

$$u^+_{i2adv} = A_{u2adv}\cos(2\sigma t - 2kx + \alpha)e^{-\mu(x-x_0)} \tag{3.26}$$

$$\eta^+_{i2adv} = A_{\eta 2adv}\cos(2\sigma t - 2kx + \alpha - \alpha_2)e^{-\mu(x-x_0)} \tag{3.27}$$

where $A_{u2adv} = \frac{A_u A_u \sqrt{\mu^2 + k^2}}{4\sigma}e^{-2\mu x_0} = \frac{A_\eta A_u}{4h}e^{-2\mu x_0}$,

$A_{\eta 2adv} = \frac{A_{u2adv} h\sqrt{\mu^2 + (2k)^2}}{2\sigma} = \frac{A_\eta A_u \sqrt{\mu^2 + (2k)^2}}{8\sigma}e^{-2\mu x_0}$

u_{i2adv} and η_{i2adv} of the negative incident M_4 through the channel can be estimated:

$$u^-_{i2adv} = A_{u2adv}\cos[2\sigma t + 2k(x - 2x_0) + \alpha]e^{\mu(x-x_0)} \tag{3.28}$$

$$\eta^-_{i2adv} = A_{\eta 2adv}\cos[2\sigma t + 2k(x - 2x_0) + \alpha - \alpha_2 - \pi]e^{\mu(x-x_0)} \tag{3.29}$$

Compared with the analytical results in (3.19) ~ (3.22), the incident M_4 represented by (3.26) ~ (3.29) solely generated by the advective term in the momentum equation is different from that solely generated by the nonlinear term in the continuity equation in terms of their phase difference $\alpha - \alpha_2$ (or $\alpha - \alpha_2 - \pi$) for the positive (or negative) incident M_4 and their amplitude ratio $\frac{A_{\eta 2adv}}{A_{\eta 2nct}} = \frac{A_{u2adv}}{A_{u2nct}} = \frac{\sqrt{\mu^2 + (2k)^2}}{4\sqrt{\mu^2 + k^2}}$. For no friction ($\mu = 0$), their phase difference is 0 (or π) for the positive (or negative) incident M_4 and their amplitude ratio is 0.5. Thus the positive (or negative) incident M_4 waves generated by these two nonlinear terms tend to be superimposed (or canceled) by each other. As friction increases, their phase difference increases and their magnitude ratio decreases. It also can be seen from the latter numerical results that the positive

(or negative) incident M_4 generated by these two nonlinear terms still tends to be strengthened (or weakened) by each other under normal frictional conditions.

If the quadratic form is used for the bottom friction, M_4 can also be generated by M_2 through either the nonlinear term $\eta u|u|$ or the river flow involved term $u|u|+r$. M_6 can be generated by M_2 through $u|u|$ if the river flow is smaller in magnitude than the incident M_2 induced current. The quadratic friction terms have been mathematically proved to contribute to overtide generation by using Fourier decomposition [Parker, 1984; Dronkers, 1964; Fang, 1987]. However the phase relation and the magnitude ratio between the overtides generated by the quadratic friction term and other nonlinear terms are difficult to be analytically solved. These will be investigated based on the following numerical modeling results.

Once the incident M_4 and M_6 have been generated by the incident M_2 through the nonlinear terms, they would be reflected at the channel end and continue to propagate in the negative direction. In addition, the other part of the negatively-propagating M_4 and M_6 are generated by the reflected M_2 through the nonlinear terms. These two parts tend to be superimposed together. The first part plays a dominant role since the incident M_2 is much larger in magnitude than the reflected M_2.

The incident waves in a long uniform channel

In the middle of a long channel, either the nonlinear term ηu or uu is only activated at a short reach (which can be seen as a single "point") in order to testify that the incident M_4 is locally generated by the incident M_2 and then propagates at the same time in the two opposite directions. For a given linear friction coefficient F and the adequate channel length, the reflected waves from both the channel mouth and the channel end are sufficiently damped so that they have little effect on the incident waves.

The modeling results shown in Figure 3.15 agree very well with the analytical results (3.19) ~ (3.22) and (3.26) ~ (3.29). The incident M_4 is generated at -2000km and propagates at the same time in the two opposite directions. The magnitude ratio of the elevation (η_{i2nct} or

η_{i2adv}) to the current (u_{i2nct} or u_{i2adv}) conforms to $\frac{A_{\eta 2nct}}{A_{u2nct}} = \frac{A_{\eta 2adv}}{A_{u2adv}} = \frac{h\sqrt{\mu^2 + (2k)^2}}{2\sigma}$. Under normal friction conditions, the phase difference between the elevation and the current of the positive (or negative) incident M_4 is close to 0 (or π). The magnitude ratio of the incident M_4 solely from ηu to that solely from uu is close to 0.5. The phase difference of the positive (or negative) incident M_4 generated by these two nonlinear terms is close to 0 (or π). Thus the positive (or negative) incident M_4 generated by these two nonlinear terms tends to be superimposed (or cancelled) by each other. In addition, the positive (or negative) incident M_4 generated at two locations x_0 and x_1 tend to be superimposed (or cancelled) by each other if the distance between x_0 and x_1 is equal to a quarter of M_4 wavelength, i.e. $|x_1 - x_0| = \frac{2\pi}{8k}$.

As shown in Figure 3.16, if either the nonlinear term ηu or uu is activated through the middle interest channel (-2000 km ~ -1000 km), the positive (or negative) incident M_4 accumulates (or weakens) along the channel. If both of these two nonlinear terms are activated through the middle reach of the channel, the positive (or negative) incident M_4 induced by uu is superimposed to (or subtracted from) that induced by ηu.

The quasi-standing waves in a uniform channel

M_4 can be generated by M_2 not only through the nonlinear term ηu or uu but also through the nonlinear term $\eta u|u|$ or the river flow involved term $u|u|+r$ if the quadratic bottom friction is used in the momentum equation. The first-order M_6 can be generated by M_2 through $u|u|$. The second-order M_6 results from interaction between M_2 and M_4. In order to test relative contribution of these nonlinear terms to the overtide generation and their relationship, a series of numerical experiments have been done for a closed uniform channel with the same length of 250 km as the Hudson River. For each of the experiments, only one nonlinear terms or one combination of different nonlinear terms is activated. The longitudinal elevation amplitude and phase of M_2, M_4, and M_6 are shown in Figure 3.17. Without the river flow, the magnitude of M_4 induced by ηu is about two times of that by uu, and about six times of that by $\eta u|u|$. The

magnitude of M_4 induced by all these three terms is less than the sum of M_4 induced by individuals due to their phase difference. Assume that two M_4 waves $\eta_{2a} = a\cos(2\sigma t + \phi)$ and $\eta_{2b} = b\cos(2\sigma t + \phi + \Delta\phi)$ are added together and $a > b > 0$, the combined M_4 wave can be expressed by

$$\eta_{2c} = \eta_{2a} + \eta_{2b} = a\cos(2\sigma t + \phi) + b\cos(2\sigma t + \phi + \Delta\phi) = c\cos(2\sigma t + \phi + \psi) \tag{3.30}$$

where $c = \sqrt{a^2 + b^2 + 2ab\cos(\Delta\phi)}$, $\psi = \tan^{-1}\left[\dfrac{b\sin(\Delta\phi)}{a + b\cos(\Delta\phi)}\right]$

If $\Delta\phi = 0$, $c = a + b$ and $\psi = 0$. If $\Delta\phi = \pi/2$, $c = \sqrt{a^2 + b^2}$ and $\psi = \tan^{-1}(b/a)$. If $\Delta\phi = \pi$, $c = a - b$ and $\psi = 0$. When the phase difference $\Delta\phi$ is close to 0 (or π), the combined wave has the amplitude to be equal to the sum (or residual) of two waves' amplitude and has the phase the same as the wave with larger amplitude (i.e. *a*).

The M_4 wave from combination of ηu and uu has the amplitude close to the sum of the amplitude of two individual M_4 waves since their phase difference is only about 20 degrees. The M_4 wave from $\eta u|u|$ can enhance the M_4 wave from combination of ηu and uu by the amount less than itself since its phase is about 90 degrees away from the others. If the river flow is introduced into the system at the channel end, M_4 can be generated by M_2 through the term $u|u|$. The magnitude of M_4 from the river-involved $u|u|$ depends on the ratio of the river velocity to the velocity induced by the incident M_2 at the channel end [Parker 1984; Parker 2007]. Given the river flow with the velocity half of the M_2 velocity, the river-induced M_4 wave shown in Figure 3.17 (c) is even larger than the M_4 wave from combination of ηu, uu and $\eta u|u|$. The phase of the river-induced M_4 wave is close to that of the $\eta u|u|$-induced M_4 and is about 90 degrees different from that of the ηu-induced or uu-induced M_4 wave. As a result, the M_4 wave from combination of all the four nonlinear terms is strengthened by addition of each term into the model but has the amplitude less than the sum of the amplitude of individual M_4 waves due to their phase difference.

When the nonlinear terms are introduced into the model, M_4 generation also affects the amplitude and the phase of M_2 and M_6. Without the river flow, the M_2 amplitude and phase change a little due to existence of ηu, uu and $\eta u|u|$ as shown in Figure 3.17 (a) (b). With the river flow only, the M_2 amplitude drops significantly but the M_2 phase changes a little. With the river flow and involvement of ηu, uu and $\eta u|u|$, the M_2 amplitude changes a little but the M_2 phase changes significantly. According to other numerical experiments, combination of the river flow and ηu plays a dominant role in modifying the M_2 phase since it introduces into the system an additional M_2 wave which is combined with the original M_2 wave. The first-order M_6 in Figure 3.17 (e) (f) comes from $u|u|$. Without the river flow, M_2 interacts with M_4 from ηu, uu and $\eta u|u|$, producing the second-order M_6 superimposed onto the first-order M_6. With the river flow only, the M_6 amplitude reduces significantly due to the reduced momentum input into M_6. With the river flow and involvement of ηu, uu and $\eta u|u|$, the M_6 amplitude is larger than that from the river flow only and the M_6 phase is significantly different from other cases due to the modification of the M_2 phase.

The river flow (i.e. the mean flow) plays an important role in modifying M_2, M_4, and M_6 through the quadratic friction term $u|u|$. Based on the Fourier decomposition of $u|u|$ [Parker 1984], as the river flow increases, M_2 and M_6 decrease and M_4 increase. M_2 keeps decreasing since combination of the river flow and $u|u|$ has the same effect as the friction. When the river flow increases to be larger than the incident M_2 current, M_4 increases and reaches a maximum but M_6 decreases and vanishes since there are already not ebb currents at all.

Distortion of the tidal wave by the overtides

It has been known that the overtides play a significant role in distorting the temporal tidal curve away from the sinusoidal curve. If we use $A\eta_{M2}$ ($P\eta_{M2}$), $A\eta_{M4}$ ($P\eta_{M4}$), and $A\eta_{M6}$ ($P\eta_{M6}$) to represent the amplitude (phase) of M_2, M_4, and M_6 elevation, respectively. Basically the shape of the combined tidal curve depends on the amplitude ratio $A\eta_{M4}/A\eta_{M2}$ and $A\eta_{M6}/A\eta_{M2}$ and the phase difference $2*P\eta_{M2}-P\eta_{M4}$ and $3*P\eta_{M6}-P\eta_{M2}$ [Parker, 2007 page60-61; U.S.C. & G.S., 1952]. As seen in Figure 3.7, the amplitude ratio $A\eta_{M4}/A\eta_{M2}$ tends to have the first peak at the closed

end and the second peak around the first M_2 node. The amplitude ratio $A\eta_{M6}/A\eta_{M2}$ has the first peak at the closed end and twin-peaks around the first M_2 node. The phase differences $2*P\eta_{M2}$-$P\eta_{M4}$ and $3*P\eta_{M6}$-$P\eta_{M2}$ tend to keep uniform for the first quarter wavelength of the overtides away from the closed end and change about 270 degrees around the first M_2 node. We can see that the tidal wave has significant difference in shape at different reaches along the channel. We show time series of the tides at four typical locations: A (x = 110 km), B (x = 140 km), C (x = 170 km), and D (x = 230 km) to see how the overtides distort the tidal curve.

In Figure 3.8, the panels in column 1, 2, 3, and 4 corresponds with the location A, B, C, and D, respectively. The panels in row 1, 2, and 3 show combination of M_2 with M_4, M_2 with M_6, and M_2 with M_4 and M_6, respectively. The amplitude ratio $A\eta_{M4}/A\eta_{M2}$ and $A\eta_{M6}/A\eta_{M2}$ are relatively larger along the channel at these four locations. The phase difference $2*P\eta_{M2}$-$P\eta_{M4}$ and $3*P\eta_{M6}$-$P\eta_{M2}$ change ~180º between the location A and C and have the similar value at the location B and D. The role of the M_4 in the tide at both B and D is to make a faster rising from low water to high water and make a slower falling from high water to low water. The role of the M_6 in the tide at both B and D is to flatten both high water and low water and leads to a shrink in tidal range. The role of both M_4 and M_6 in the tide at A and C is almost reversed. The M_4 tends to steepen high water and flatten low water at A. On the other hand, the M_4 flattens high water and steepens low water at C. The M_6 shrinks the tidal range at A but increases the tidal range at C.

The overtide currents also distort the tidal currents in the way depending on the amplitude ratio Au_{M4}/Au_{M2} and Au_{M6}/Au_{M2} and the phase difference $2*Pu_{M2}$-Pu_{M4} and $3*Pu_{M6}$-Pu_{M2} (Figure 3.7 and Figure 3.9). In particular, the combination of M_2 and M_4 currents leads to flood dominance condition throughout the upstream reach (150~250 km). The M_6 tends to increase the magnitude of both flooding and ebbing currents and shorten the time of the maximum currents in the upstream reach (170~250 km).

3.5.2 The effect of channel morphology on tidal wave propagation

The incident waves in a channel with abrupt change in width or depth

Jay (1991) found that an incident wave in a strongly convergent or divergent channel behaves like a standing wave without the presence of a reflected wave. But he did not specify the relationship between the original incident wave and the standing wave induced by convergence or divergence.

Assume that a very long channel with uniform depth (20 m) has an abrupt convergent (or divergent) reach in the middle, connecting with the wider (or narrower) lower reach and the narrower (or wider) upper reach. Both the lower reach and the upper reach have uniform width. The width ratio of the lower reach to the upper reach is larger (or smaller) than 1 for the convergent (or divergent) geometry. The convergent (or divergent) reach can be seen as the abrupt discontinuity if it has much smaller length than the total channel. In the following numerical experiments, the channel with the total length of 3000 km is set up to have the convergent (or divergent) reach with the length of 20 km. The wider and narrower reaches have the width of 2000 m and 1000 m, respectively. Only one nonlinear term ηu is activated at the middle channel (-2000 km ~ -1000 km) to see the effects of varying geometry on the M_4 wave. The linear friction term is used for the whole channel.

Figure 3.18 displays the longitudinal variations in amplitude and phase of the incident M_2 and M_4 affected by discontinuity in geometry. If we subtract the water level obtained by the simulation in the channel with uniform width from that obtained by the simulation in the channel with convergent (or divergent) discontinuity, we can get the residual water level for the whole channel. We then do a harmonic analysis on the residual water level to extract M_2 and M_4. The longitudinal variations in amplitude and phase of the residual M_2 and M_4 are also shown in Figure 3.18. It suggests that an additional M_2 has been developed at the channel discontinuity through the nonlinear term $\frac{h}{b}\frac{\partial(bu)}{\partial x}$ in the continuity equation. Once this additional M_2 is generated, it also propagates at the same time in the two opposite directions. For the convergent

(or divergent) geometry, the positive additional M_2 has the phase difference of 0 (or π) from the original incident M_2 through the upper reach. As a result, the combined incident M_2 in the upper reach is the sum (or residual) of the original incident M_2 and the positive additional M_2 and is in phase with the original incident M_2. The negative additional M_2 behaves like a reflected wave superimposed onto the original incident M_2, producing a quasi-standing wave through the lower reach. Similarly, the additional M_4 generated through the nonlinear term $\frac{h}{b}\frac{\partial(b\eta u)}{\partial x}$ also propagates in the two opposite directions and is superimposed onto the original incident M4. It should be noted that the magnitude of the additional M_2 or M_4 induced by the channel discontinuity depends on both the magnitude of the original incident M_2 or M_4 and the width ratio of the lower reach to the upper reach. The larger the original incident M_2 or M_4 and the width ratio, the larger is the additional M_2 or M_4.

If the length of the convergent (or divergent) reach is increased to be more than a quarter of the M_2 wave length, the positive additional M_2 wave generated through $-\frac{h}{b}\frac{\partial(bu)}{\partial x}$ at one point is in phase with those generated at other points. Thus the positive additional M_2 tends to be accumulated along the convergent (or divergent) reach. The accumulated positive additional M_2 is superimposed onto (or subtracted from) the original incident M_2 for the convergent (or divergent) reach since their phase difference is 0 (or π). The negative additional M_2 is not able to be accumulated due to the phase difference between the negative additional M_2 waves generated at different locations. The pattern of the additional M_2 is similar to the M_4 generation mentioned in 3.5.1. The additional M_4 is similarly combined with the original incident M_4.

Assume that a very long channel with uniform width (1000 m) has a shoaling (or deepening) reach in the middle, connected with the lower reach and the upper reach. Both the lower reach and the upper reach have uniform depth. The shallower and deeper reaches have the depth of 10 m and 20 m, respectively. The numerical experiments are set to be the same as the above except that the convergent (or divergent) reach is replaced by the shoaling (or deepening) reach.

Figure 3.20 show the longitudinal variations in amplitude and phase of the incident M_2 and M_4 affected by discontinuity in depth. The change in depth affects not only the cross-sectional area of the channel but also the phase speed and the frictional effect. The decrease in depth leads to the significant decrease in phase speed and the increase in the frictional damping effect (i.e. μ in (3.4)) even the linear friction coefficient F keeps unchanged. The additional M_2/M_4 is also generated at the channel discontinuity through the nonlinear term $\frac{\partial(hu)}{\partial x}$ or $\frac{\partial(h\eta u)}{\partial x}$ and propagates at the same time in the two opposite directions. The incident M_2 or M_4 is firstly enhanced by the positive additional M_2 or M_4 and then damped more after it propagates through the shoaling reach. The incident M_2 or M_4 is firstly reduced and then damped less after it propagates through the deepening reach. The negative additional M_2 or M_4 also behaves like a reflected wave superimposed onto the incident M_2 or M_4, producing a quasi-standing wave through the lower reach.

The quasi-standing waves in a channel with abrupt change in width or depth

A series of numerical experiments are set up to test the effects of the abrupt convergence (or divergence) on the quasi-standing waves. In these experiments, a channel is set to have the length of 2000 km and the depth of 20 m. The simplified continuity and momentum equations with the linear friction and without any nonlinear term are used for the lower 1000 km reach. The quadratic friction term $u|u|$ and the nonlinear terms ηu, uu and $\eta u|u|$ are activated for the upper 1000 km reach. The abrupt convergent (or divergent) reach with the length of 20 km can be located at any place in the upper reach.

Figure 3.19 (a) (c) (e) display the longitudinal amplitude of M_2, M_4 and M_6 with the influence of the abrupt convergence. The convergent reach works as a convergent reach for the incident M_2 but works as a divergent reach for the reflected M_2. The incident M_2 is enhanced when it gets through the convergent reach. The phase of the enhanced incident M_2 is the same as the original incident M_2, increasing with x in the positive direction. At the same time a negative additional M_2 is generated and propagates in the negative direction, behaving like a reflected

wave. The phase of the negative additional M_2 is the same as the original incident M_2 only at the convergent reach and then increases with x in the negative direction. When the enhanced incident M_2 hits the channel end, an enhanced reflected M_2 is produced and propagates in the negative direction.

If the convergent reach is located at a half of the M_2 wavelength away from the channel end, the enhanced reflected M_2 arrives at the channel discontinuity just in phase with the local incident M_2. This convergent reach for the incident M_2 is also a divergent reach for the enhanced reflected M_2. The enhanced reflected M_2 is weakened after it propagates through the divergent reach. However, it is strengthened to a larger extent by the negative additional M_2 mentioned above since they are in phase with each other through the lower reach. At the same time a positive additional M_2 is reflected back into the upper reach. This positive additional M_2 weakens the original incident M_2 since their phase difference is close to π. However, the weakened amount of the original incident M_2 by this positive additional M_2 is less than the previously enhanced amount. As a result, the incident M_2 in the upper reach and the reflected M_2 all through the channel are enhanced by a relatively small amount. The additional wave energy induced by the channel convergence tends to be distributed all through the channel.

If the convergent reach is located at a quarter of the M_2 wave length away from the channel end, the enhanced reflected M_2 arrives at the channel discontinuity just in reversed phase (i.e. π) with the local incident M_2. After it propagates through the channel discontinuity, the enhanced reflected M_2 is weakened to a large extent not only by getting through its divergent reach but also by the negative additional M_2 mentioned above since they are in reversed phase with each other through the lower reach. At the same time a positive additional M_2 is reflected back into the upper reach. This positive additional M_2 strengthens the original incident M_2 since their phase difference is close to 0. The additional M_2 induced by the channel discontinuity would "bounce" back and forth within the quarter-wavelength reach until it is damped to nothing by the friction. As a result, both the incident M_2 and the reflected M_2 are reinforced significantly within the quarter-wave-length reach. The reflected M_2 in the lower reach is significantly reduced. The additional wave energy per unit width induced by the channel convergence tends to be arrested within the quarter-wavelength reach. This can be seen as the "resonance" of the

wave when the wave propagates in a convergent channel with the length of a quarter of the wave length. Similar story happens if the convergent reach is located at n/4 (n=1, 3, 5 …) of the M_2 wave length away from the channel end. However, the further away from the channel end, the less is the resonance effect since the more wave energy has been consumed by the friction on the longer way.

Similarly, the relative magnitude and the phase relationship between the M_2 waves from the different sources can be used to explain the final longitudinal M_2 amplitude if the convergent reach is located at other places. If the convergent reach is located between $\lambda/2$ and $\lambda/4$, both the incident M_2 and the reflected M_2 are strengthened in the upper reach. The second antinode of M_2 moves toward the channel end. If the convergent reach is located less than $\lambda/4$ away from the channel end, the first node of M_2 moves toward the channel mouth. This actually can be used to explain the first node of M_2 in the Hudson River also moves toward the river mouth (Figure 2). The convergent reach plays the similar role in modifying M_4 and M_6. If the convergent reach is located at m/4 (m=2, 4, 6 …) of the M_4 or M_6 wavelength, the incident M_4 or M_6 and the reflected M_4 or M_6 in the upper reach and the reflected M_4 or M_6 are enhanced by a relatively small amount. If the convergent reach is located at n/4 (n=1, 3, 5 …) of the M_4 or M_6 wavelength, the incident M_4 or M_6 and the reflected M_4 or M_6 in the upper reach are enhanced significantly. The reflected M_4 or M_6 in the lower reach is weakened.

Figure 3.19 (b) (d) (f) display the longitudinal amplitude of M_2, M_4 and M_6 with the influence of the abrupt divergence. If the divergent reach is located at m/4 (m=2, 4, 6 …) of the wavelength, the incident wave and the reflected wave in the upper reach and the reflected wave in the lower reach are reduced by a relatively small amount. The reduced wave energy per unit width induced by the channel divergence tends to be distributed through the channel. If the divergent reach is located at n/4 (n=1, 3, 5 …) of the wavelength, the incident wave and the reflected wave in the upper reach are reduced significantly. The reflected wave in the lower reach is enhanced. The channel discontinuity tends to stop most of the wave energy to be transferred into the upper reach.

A series of numerical experiments are set up to test the effects of abrupt shoaling (or deepening) of the channel on the quasi-standing waves. In these experiments, a channel is set to have the length of 2000 km and the width of 1000 m. The simplified continuity and momentum equations with the linear friction and without any nonlinear term are used for the lower 1000 km reach. The quadratic friction term $u|u|$ and the nonlinear terms ηu , uu and $\eta u|u|$ are activated for the upper 1000 km reach. The shoaling (or deepening) reach with the length of 20km can be located at any place in the upper reach.

Figure 3.21 (a) (c) (e) display the longitudinal amplitude of M_2, M_4 and M_6 in a channel with abrupt shoaling. Unlike the quasi-standing waves in the channel with abrupt convergence, all the nodes and antinodes move toward the channel end since the wavelength is significantly shortened within the shallower upper reach. If the shoaling reach is located at m/4 (m=2, 4, 6 …) of the wavelength, the incident wave and the reflected wave in the shallower upper reach are reduced due to the increased damping effect of the decreased depth. The reflected wave in the deeper lower reach is also reduced since the antinode discontinuity changes little the reflected wave propagating through it. If the shoaling reach is located at n/4 (n=1, 3, 5 …) of the wavelength, the incident wave and the reflected wave in the shallower upper reach is the result of competition between the damping effect of the decreased depth and the enhancing effect of the node discontinuity. Thus even though the wave is enhanced within the shallower upper reach, the enhancement is much smaller than that induced by the convergent reach. The reflected wave in the deeper lower reach is significantly reduced since the node discontinuity stops most of the reflected wave from propagating through it.

For the waves in a channel with the abrupt deepening reach as shown in Figure 3.21 (b) (d) (f), all the nodes and antinodes move further away from the channel end since the wavelength increases in the deeper upper reach. The magnitude of the waves in the deeper upper reach is the result of the competition between the enhancing effect due to the decreased friction and the weakening effect due to the increased cross-sectional area. The antinode discontinuity still allows most of the reflected waves to propagate through it in the negative direction. As a result, the magnitude of the reflected waves is changed a little through the channel. On the other hand, the node discontinuity tends to stop most of the incident waves to propagate through it in the

positive direction. Thus both the incident waves and the reflected waves in the deeper upper reach are significantly weakened.

3.6 Summary and conclusions

The tidal wave in a shallow long channel can be seen as the combination of the friction-damped incident wave and the friction-damped reflected wave. The wave amplitude and phase vary along the channel. Where the tidal wave is closer to the closed end, it behaves more like a standing wave since the reflected wave has the comparable magnitude to the incident wave. The nodes and antinodes are obvious. The phase changes abruptly around the nodes and changes little around the antinodes. Where the tidal wave is further away from the closed end, it behaves more like a progressive wave since the reflected wave has much smaller magnitude than the incident wave. The amplitude decreases monotonically toward the channel end without obvious nodes or antinodes. The phase also changes monotonically along the channel.

In a shallow channel, the overtides are analytically and numerically shown to be generated by M_2 through nonlinear terms in the continuity and momentum equations. As M_2 propagates along the channel, M_4 is developed at each point of the channel through the nonlinear terms ηu, uu, $\eta u|u|$ and $u|u|$+r. M_6 is developed through the nonlinear term $u|u|$ and the interaction between M_2 and M_4. Then the overtide M_4 or M_6 behaves as a normal tidal wave and propagates at the same time in the two opposite directions. The positive incident overtide generated at one point tends to be in phase with that generated at the other point on the way of its propagation. Thus the incident overtide is accumulated by continuing supply of locally-generated overtide along the channel. At the same time, the incident overtide is damped by the bottom friction. Therefore, the incident overtide is the result of competition between the accumulating effect and the damping effect. The incident overtide is then combined with the reflected overtide by the channel end.

The overtide generated through each individual of the nonlinear terms has different magnitude and phase. Thus the nonlinear terms have different contribution to the overtide generation. In a uniform channel without the river flow, M_4 induced by ηu has the largest

magnitude, about two times of M_4 induced by uu, and ten times of M_4 induced by $\eta u|u|$. If the river flow, about half of the incident M_2 current, is introduced into the channel from the channel end, M_4 induced by $u|u|$+r is comparable to M_4 induced by ηu. M_4 induced by ηu has about 0° phase difference with M_4 induced by uu and has about 90° phase difference with M_4 induced by $\eta u|u|$ or $u|u|$+r. In addition, combination of ηu and the river flow leads to generation of the additional M_2 which is superimposed onto the original M_2. As a result, the nodes and antinodes of M_2, M_4, and M_6 move towards the channel mouth.

The overtides play an import role in distorting the tidal wave from the sinusoidal wave when they are combined with M_2. How the overtides distort the tidal wave depends on the amplitude ratio and the phase difference between the overtides and M_2. The channels with different length, geometry, and topography may have different along-channel patterns of the amplitude ratio and the phase difference between the overtides and M_2. For the uniform channel without the river flow, the amplitude ratio between the overtides and M_2 tends to have peaks at the overtide antinodes. The phase difference $2*P_{M2}-P_{M4}$ and $3*P_{M6}-P_{M2}$ keep about 90° and 180° around the M_2 antinodes and changes abruptly around the M_2 nodes. Thus around the M_2 antinodes, M_4 tends to shorten the flooding time and extend the ebbing time. M_6 tends to extend both the high-water time and the low-water time. Around the M_2 nodes, M_4 tends to either shorten the high-water time and extend the low-water time or shorten the low-water time and extend the high-water time. M_6 tends to shorten both the high-water time and the low-water time.

The abrupt longitudinal change in width or depth has significant effects on the amplitude and phase of the tidal waves in the channel. The abrupt change of the channel width leads to generation of the additional waves. The additional waves propagate at the same time in the two opposite directions and are combined with the original waves. For the quasi-standing wave, the abrupt convergent reach located around the nodes tends to trap the increased wave energy and lead to the "resonance" of the wave within the upper reach. The abrupt divergent reach located around the nodes tends to stop the wave energy going into the upper reach and reflect most of the wave energy back to the lower reach. Either the convergent reach or the divergent reach located around antinodes allows the increased or decreased wave energy to be distributed evenly along the channel. The change of the channel depth not only leads to generation of the addition waves

but also affects the wave speed and the bottom friction. Thus the tidal wave is the result of competition between different factors. However, it is still true that the node discontinuity in depth tends to trap the wave energy within the upper or lower reach and the antinode discontinuity in depth allows the increased or decreased wave energy to be evenly distributed along the channel. The longitudinal change in friction coefficient within the reasonable range also leads to generation of the additional waves but with very little magnitude. No matter where the discontinuity in friction coefficient is located, the increased or decreased wave energy tends to be evenly distributed along the channel.

The tides and overtides in the Hudson River are well reproduced by both one- and two-dimensional models. The abrupt changes in width of the downstream Hudson lead to the combination of the incident waves and the partially reflected waves. As a result, both the tidal water levels and currents have been significantly modified relative to the uniform channel. The continuous convergence of the upstream Hudson leads to downstream movement of tide nodes and significant amplification of tidal amplitude in the upstream reach.

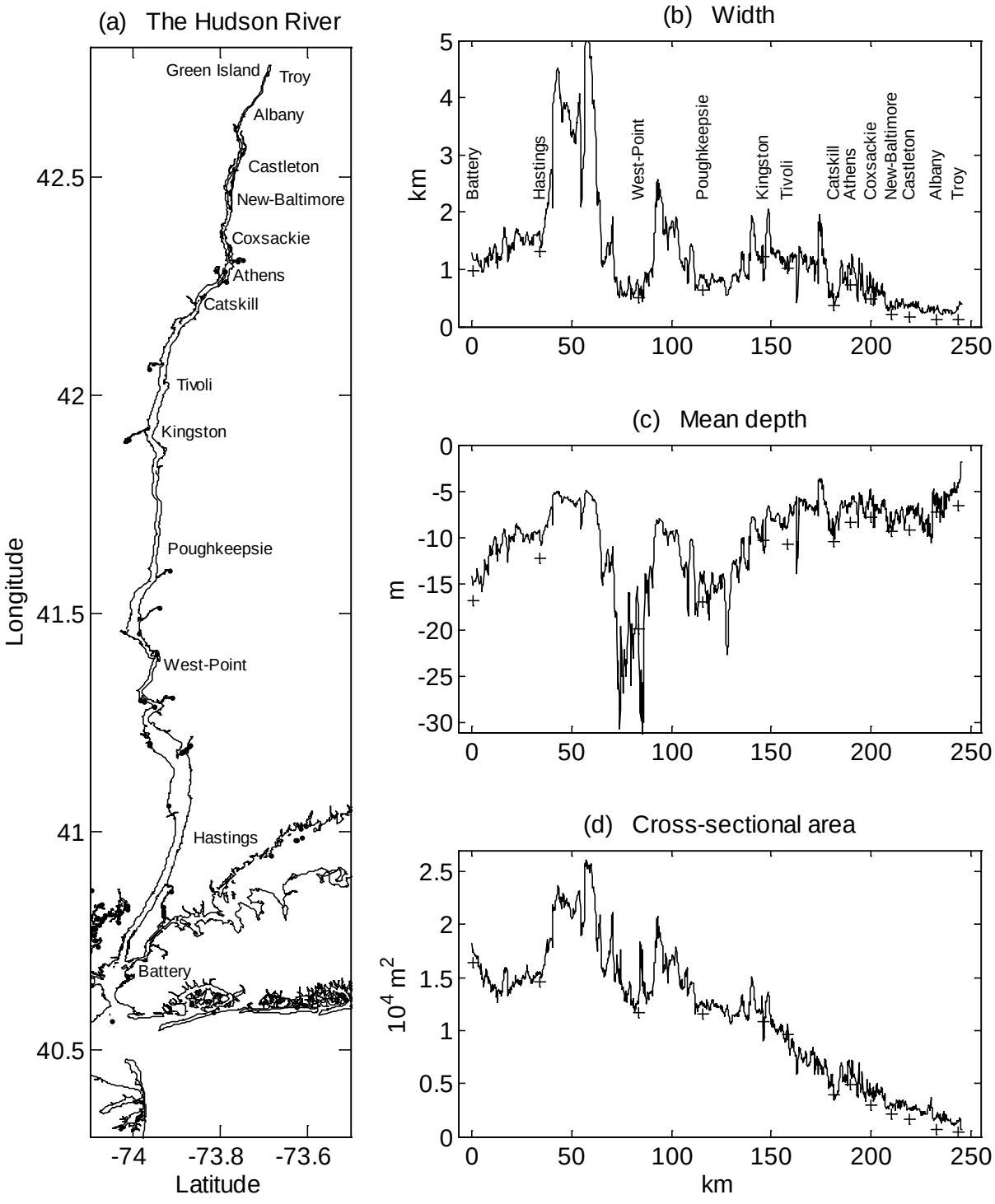

Figure 3.1 (a) The geometry, (b) the channel width, (c) the mean depth, and (d) the cross-sectional area of the Hudson River. The locations of the water level gages have been shown.

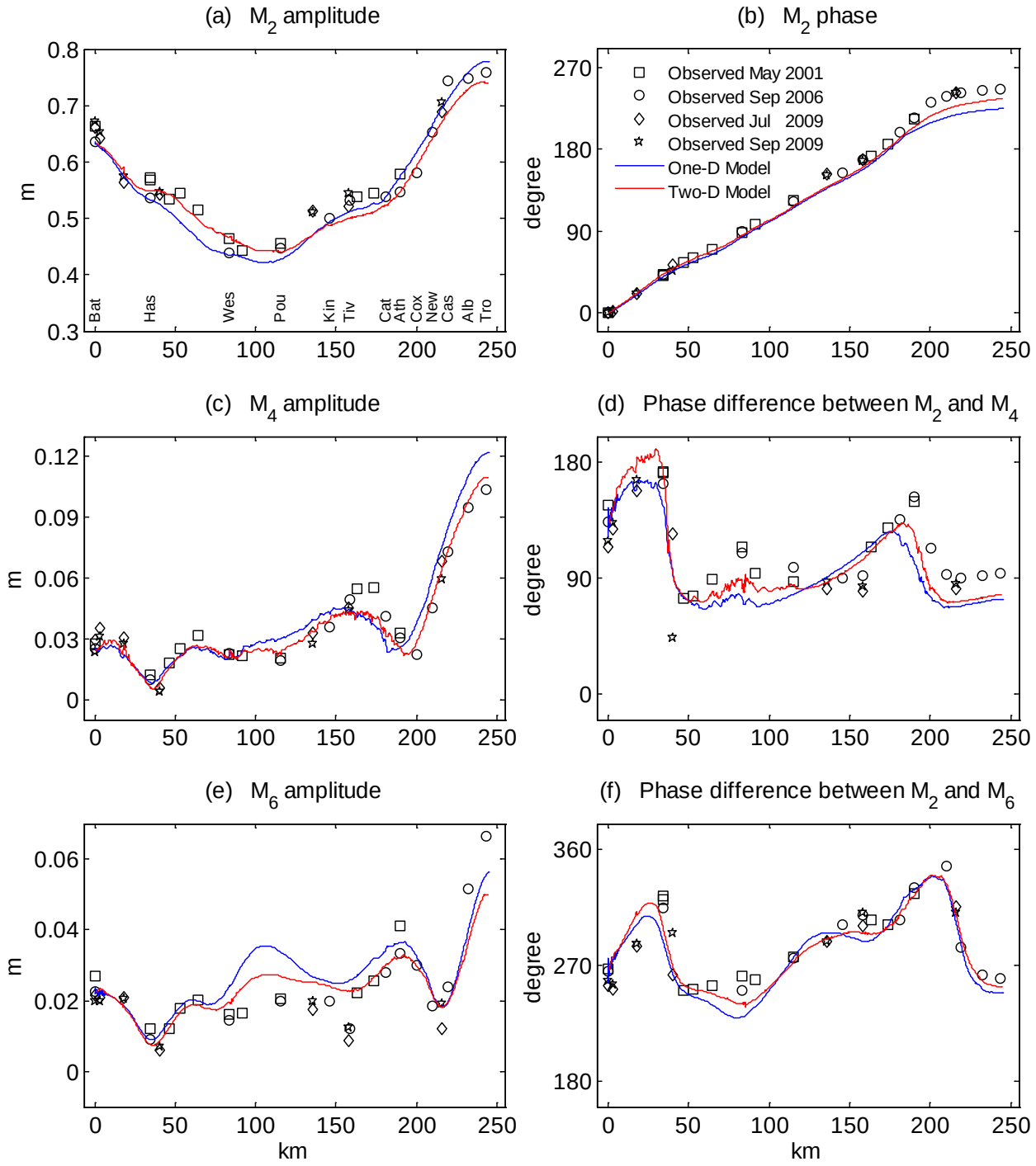

Figure 3.2 The amplitude of M_2, M_4, and M_6 elevation (a, c, e), the phase of M_2 elevation (b), and the phase difference between M_4, M_6 and M_2 elevation (d, f) in the Hudson River. The observed results are from harmonic analysis of the four data sets all having one-month record. Each of the data sets is combination of the observed water levels from a certain number of water level gauges in the Hudson River. Both one- and two- dimensional model harmonics are also calculated from one-month simulations.

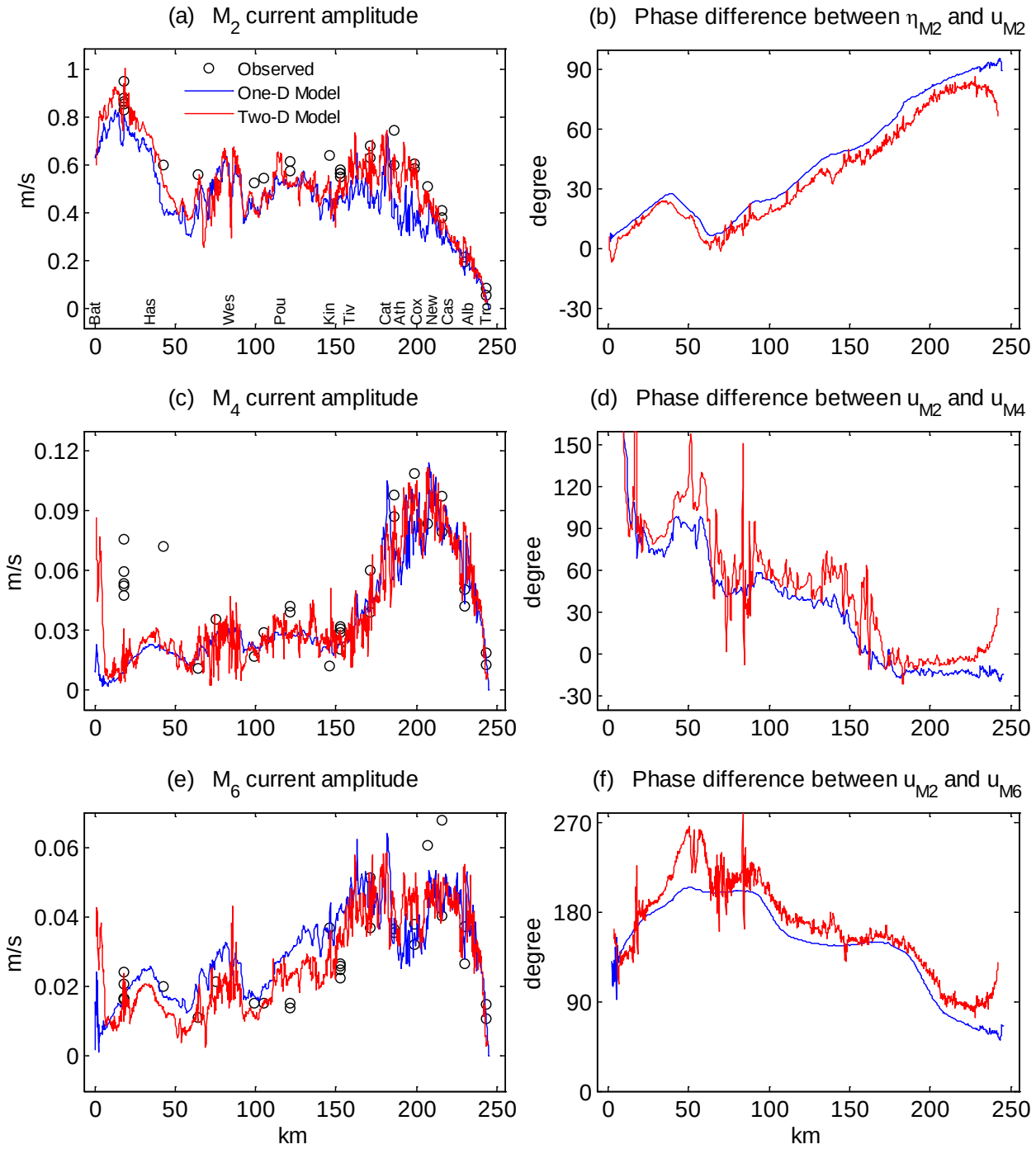

Figure 3.3 The amplitude of M_2, M_4, and M_6 current (a, c, e), the phase difference between elevation and current of M_2 (b), the phase difference between M_4, M_6 and M_2 current (d, f) in the Hudson River. The observed results are from harmonic analysis of one-month time series of depth-averaged currents of the ADCPs moored in the channel of the Hudson River. Both one- and two- dimensional model harmonics are also calculated from one-month simulations.

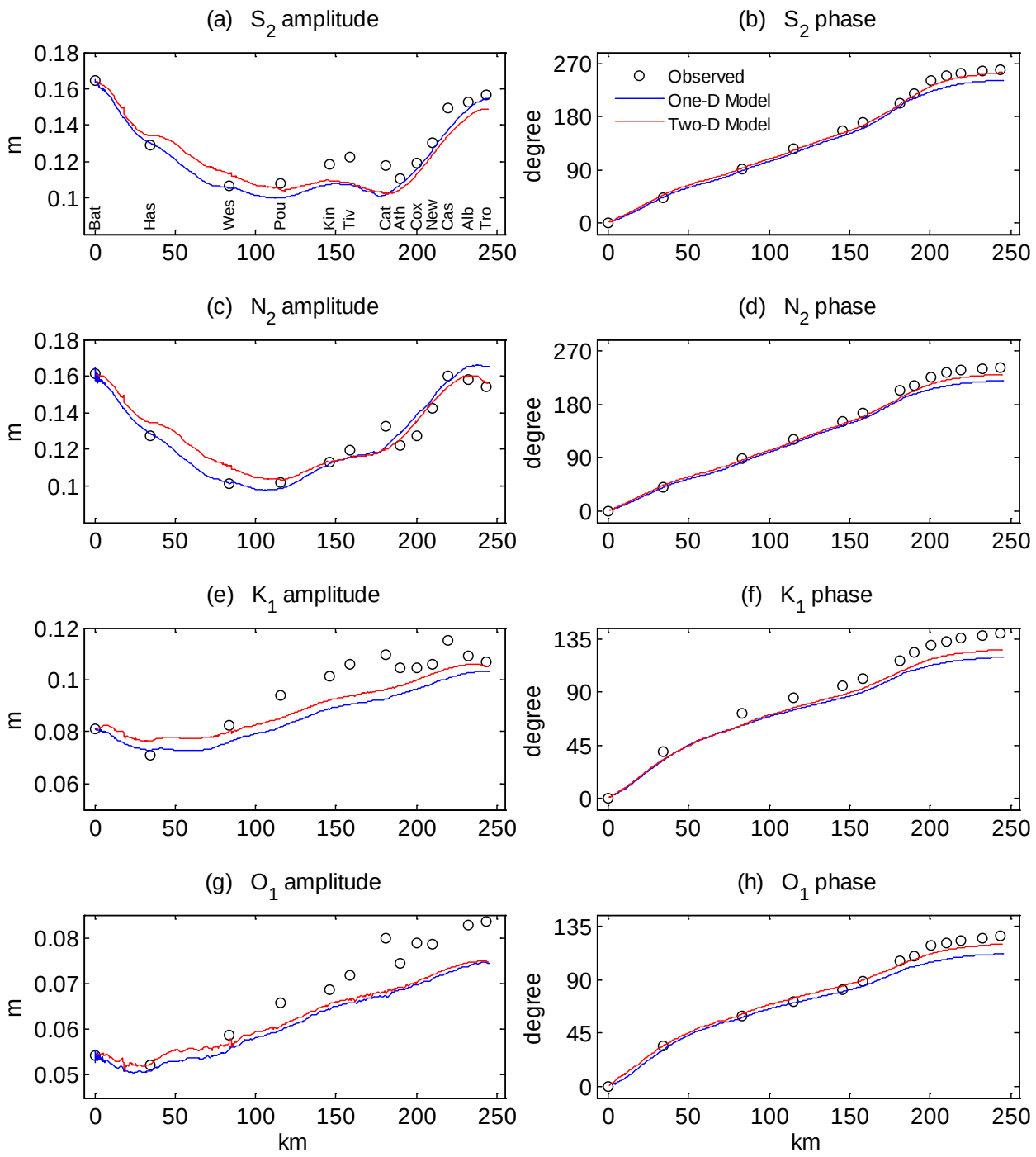

Figure 3.4 The amplitude (a, c, e, g) and the phase (b, d, f, h) of N_2, S_2, K_1 and O_1 elevation in the Hudson River. Both the observed and model harmonics are calculated from one-month time series of water levels.

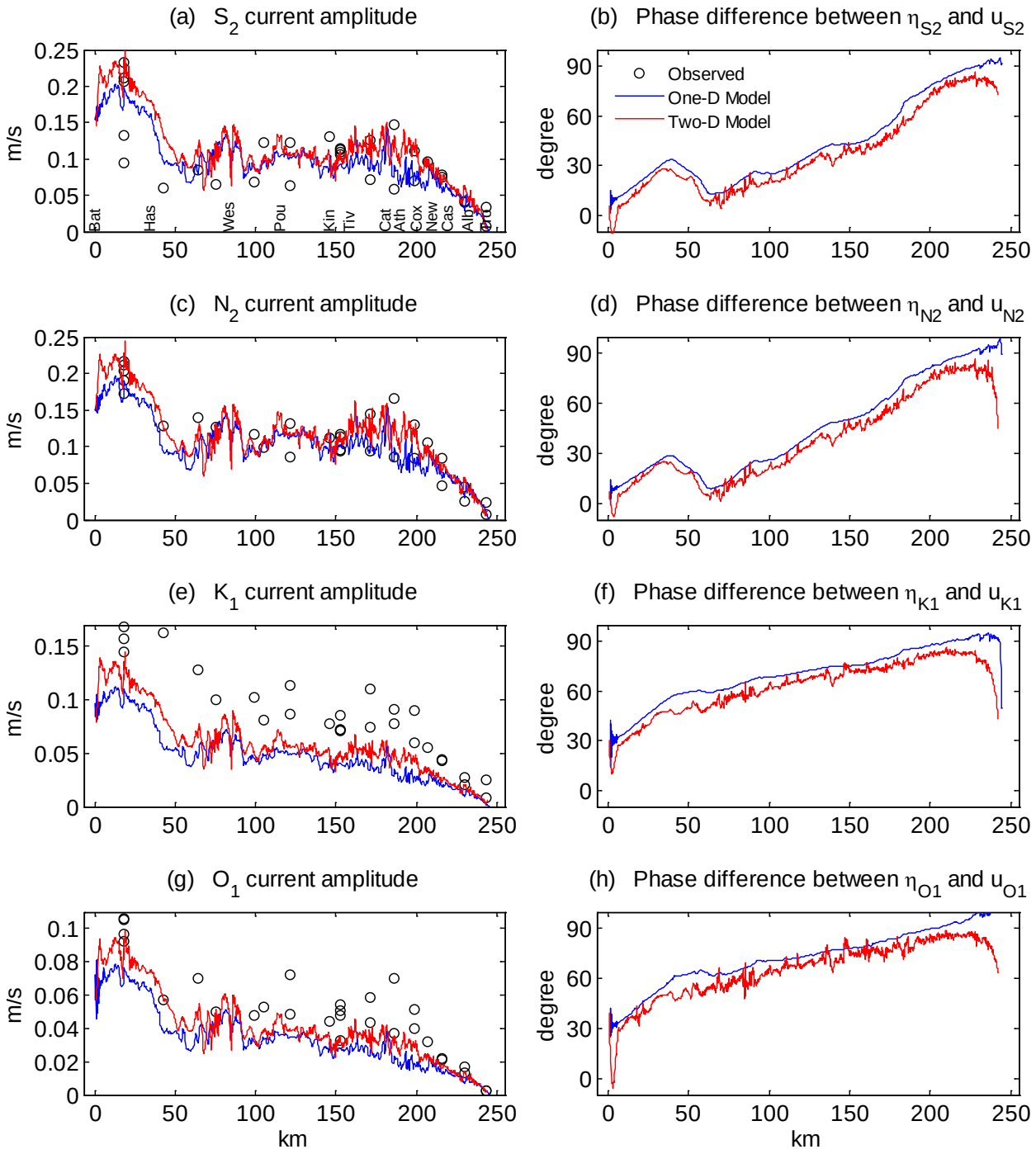

Figure 3.5 The amplitude of N_2, S_2, K_1 and O_1 current (a, c, e, g) and the phase difference between elevation and current of N_2, S_2, K_1 and O_1 (b, d, f, h) in the Hudson River. Both the observed and model harmonics are calculated from one-month time series of depth-averaged currents.

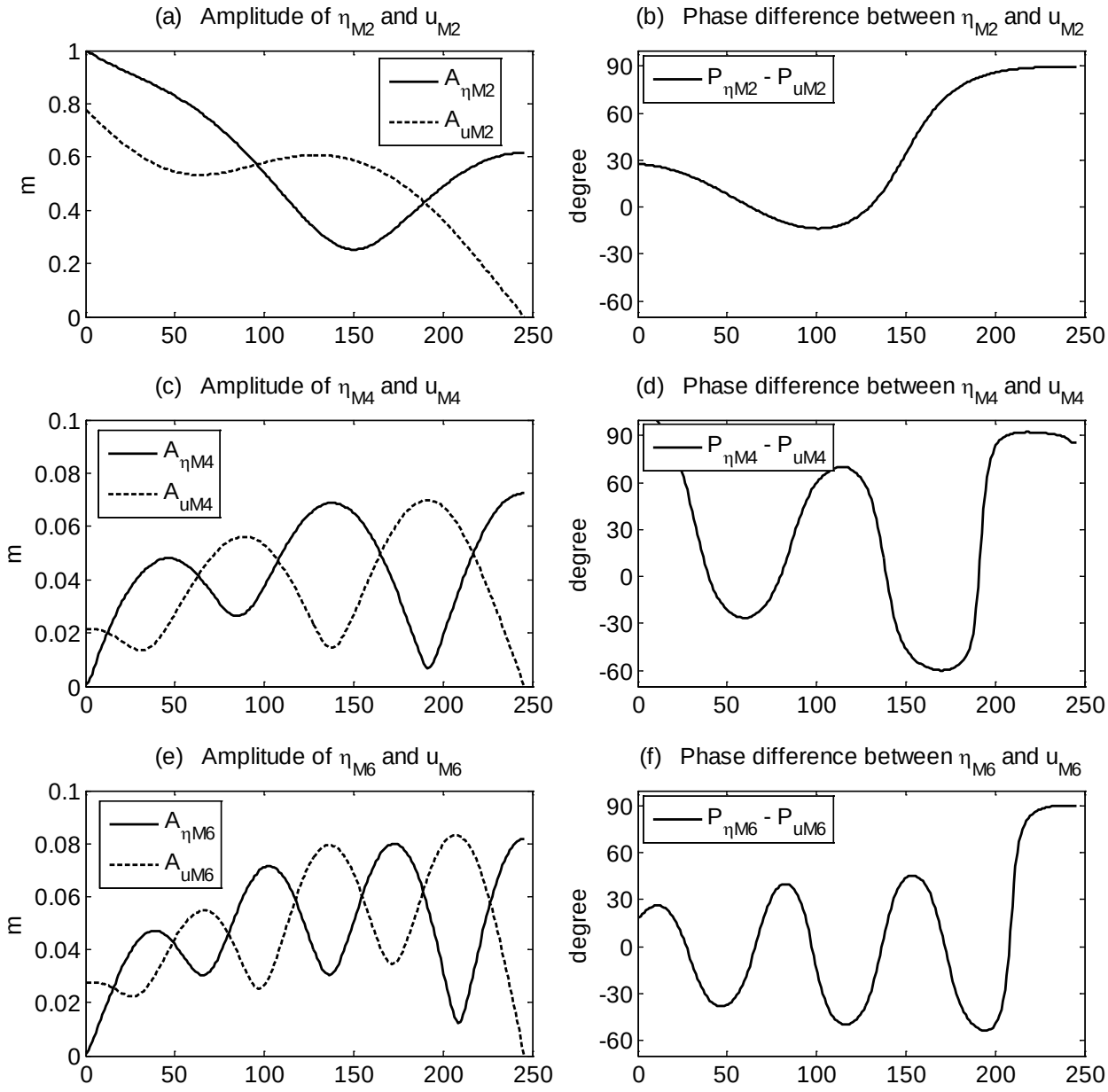

Figure 3.6 The amplitude of M_2, M_4, and M_6 elevation and current (a, c, e), and the phase difference between elevation and current of M_2, M_4, and M_6 (b, d, f) in a uniform rectangular channel.

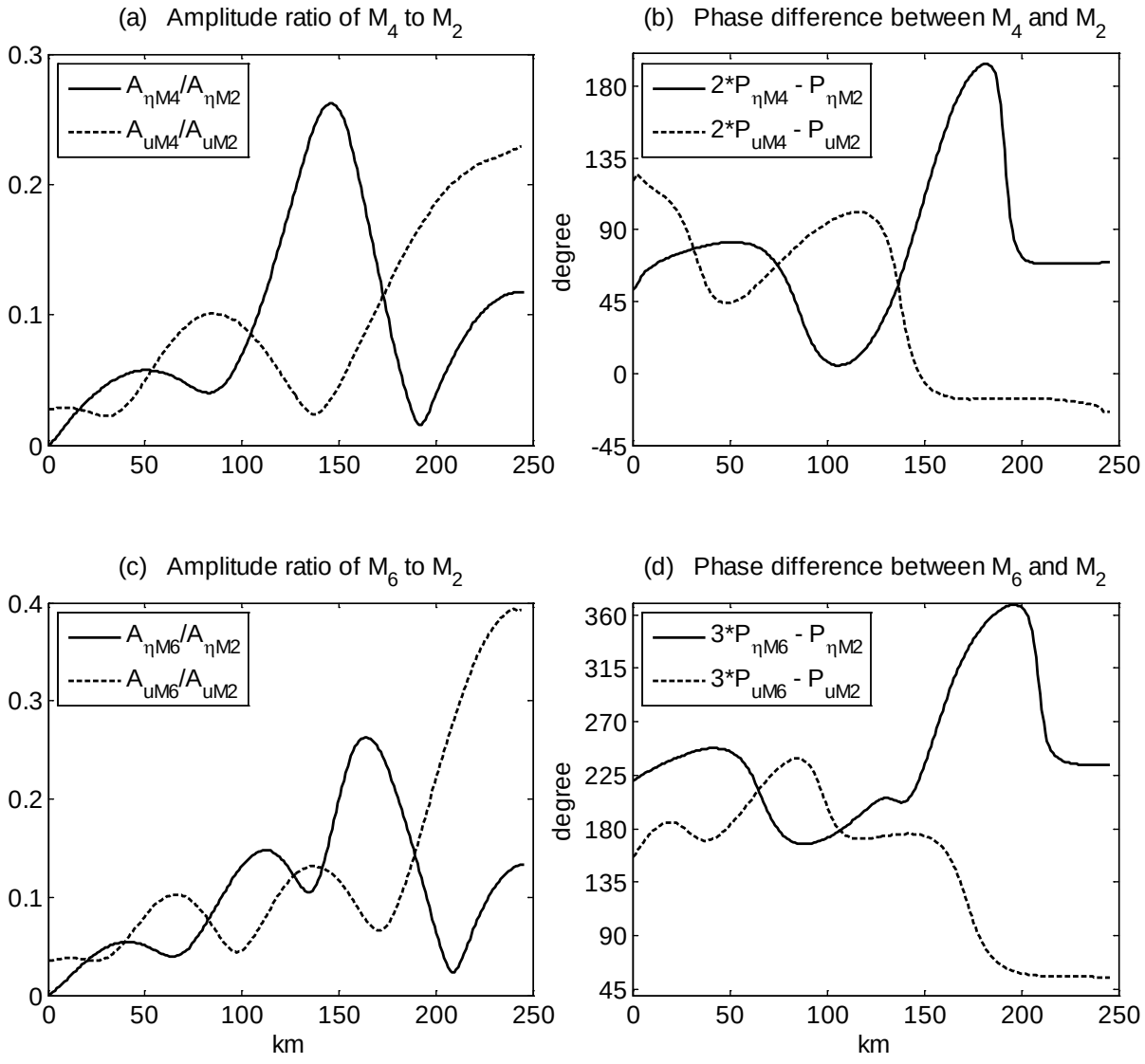

Figure 3.7 The amplitude ratio (a, c) and the phase difference (b, d) between M_4, M_6 and M_2 in a uniform rectangular channel. These two parameters are used to determine how M_4 and M_6 distort the tidal wave at the particular reach of the tidal river.

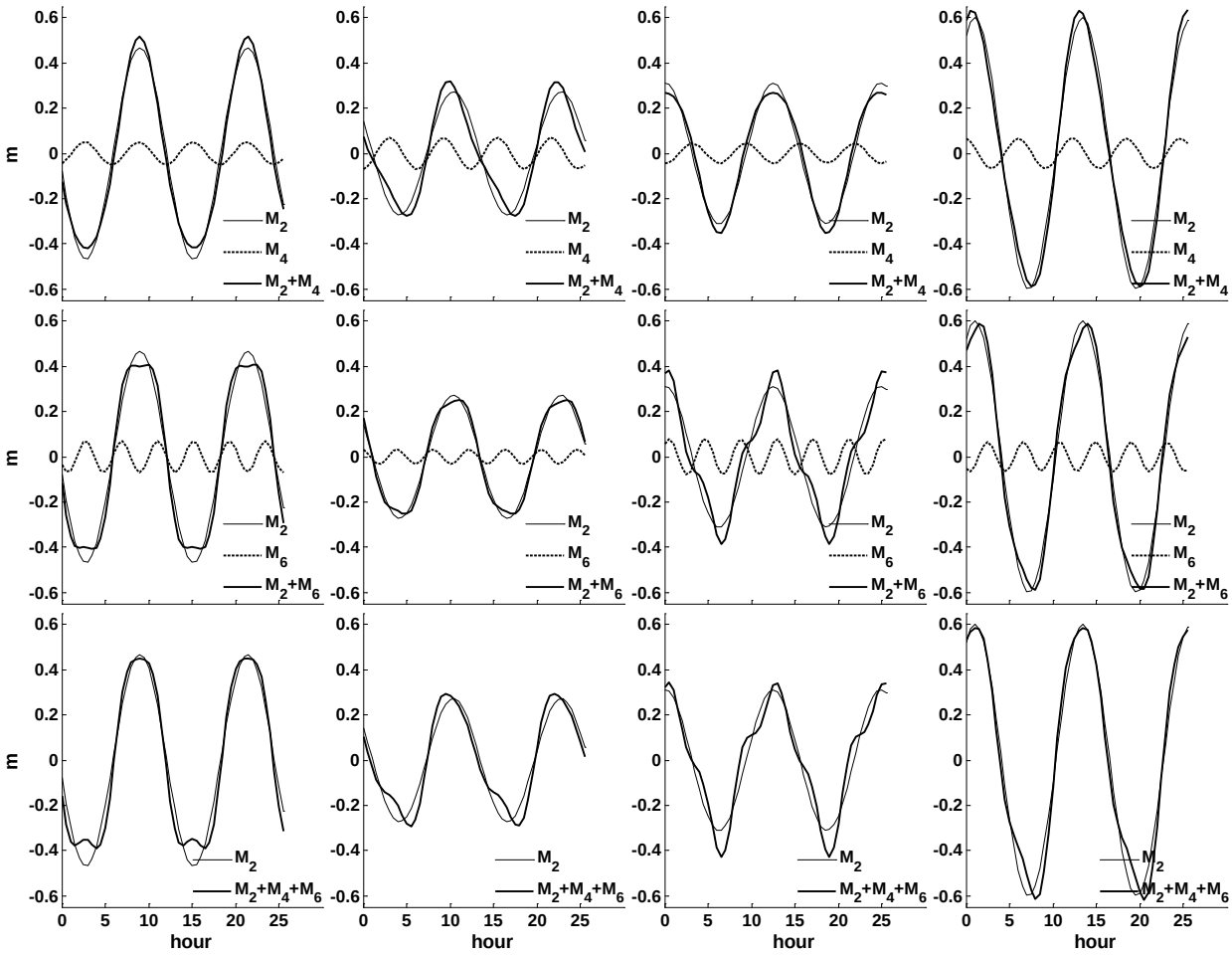

Figure 3.8 M_4 and M_6 distorts the tidal wave in terms of water elevation in different ways at different reaches of the tidal river. The panels in column 1, 2, 3, and 4 show the distortion at x = 110 km, 140 km, 170 km, and 230 km, respectively. These locations are referred in Figure 3.7. The panels in row 1, 2, and 3 show combination of M_2 with M_4, M_2 with M_6, and M_2 with M_4 and M_6, respectively.

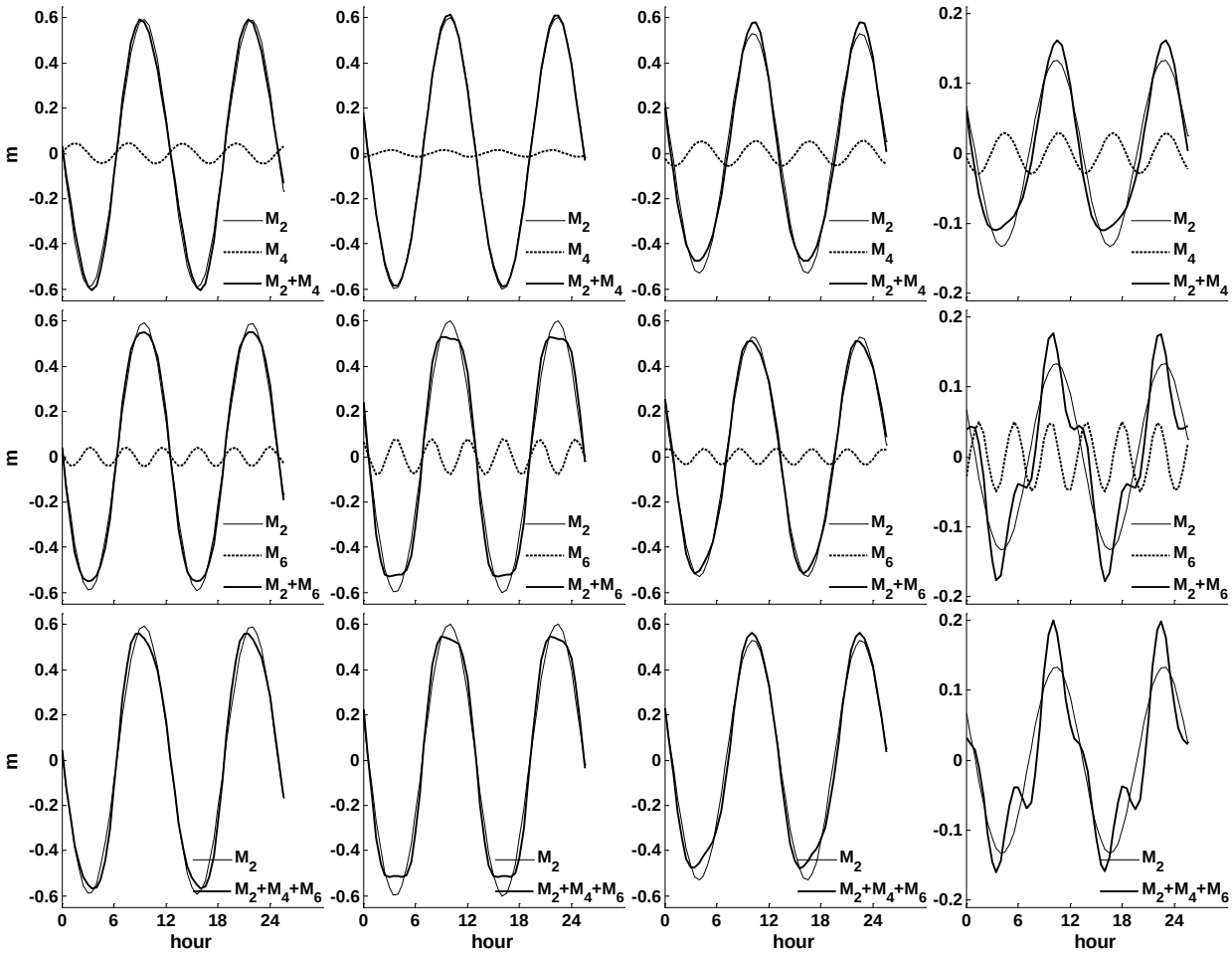

Figure 3.9 M_4 and M_6 distorts the tidal wave in terms of water current in different ways at different reaches of the tidal river. The panels in column 1, 2, 3, and 4 show the distortion at x = 110 km, 140 km, 170 km, and 230 km, respectively. These locations are referred in Figure 3.7. The panels in row 1, 2, and 3 show combination of M_2 with M_4, M_2 with M_6, and M_2 with M_4 and M_6, respectively.

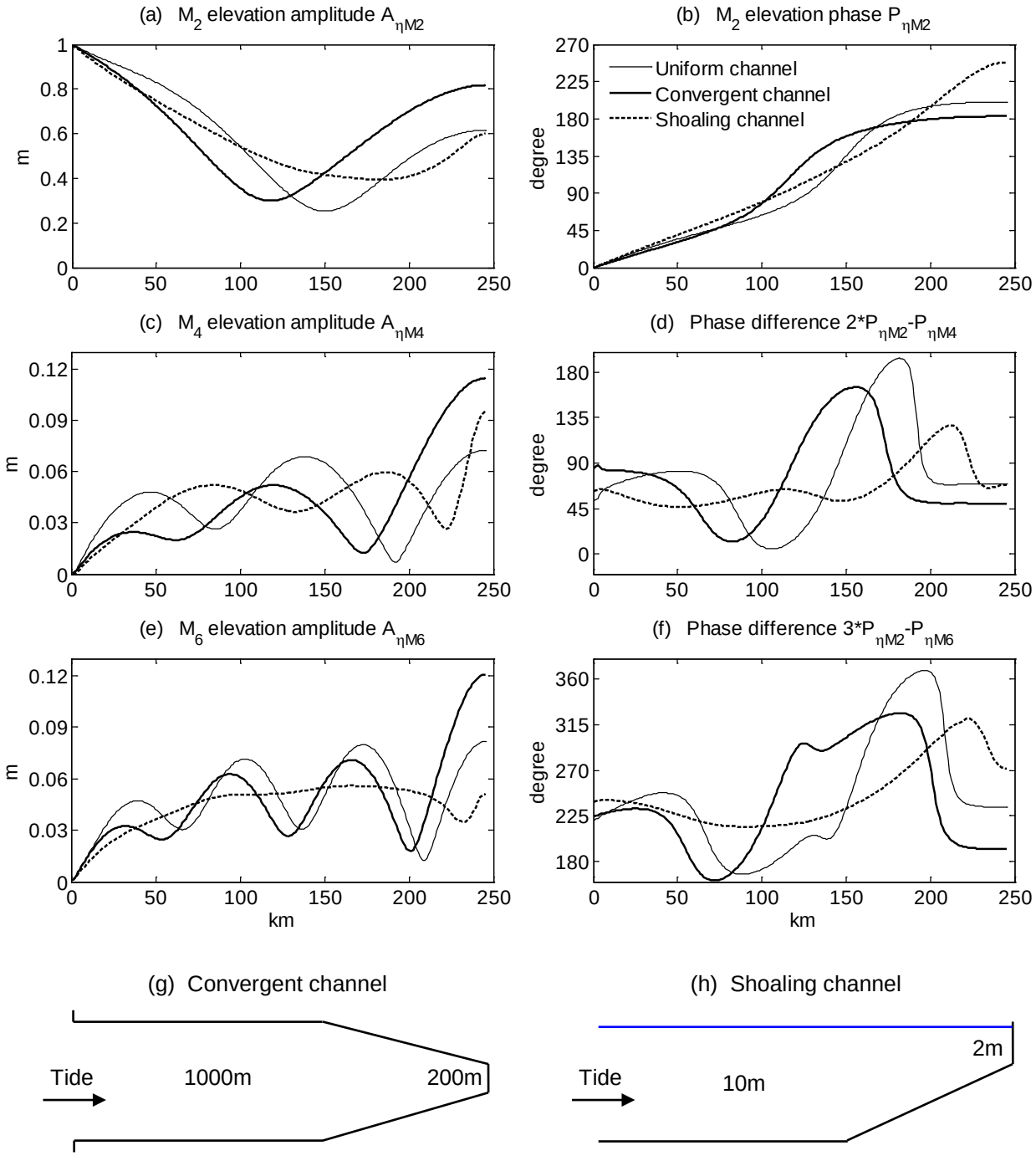

Figure 3.10 The amplitude of M_2, M_4, and M_6 elevation (a, c, e), the phase of M_2 elevation (b), and the phase difference between M_4, M_6 and M_2 elevation (d, f) in an upstream (150 ~ 250 km) convergent channel (g) and an upstream shoaling channel (h). The generic channels are used to simulate the effects of the channel geometry of the upstream Hudson on tidal wave propagation.

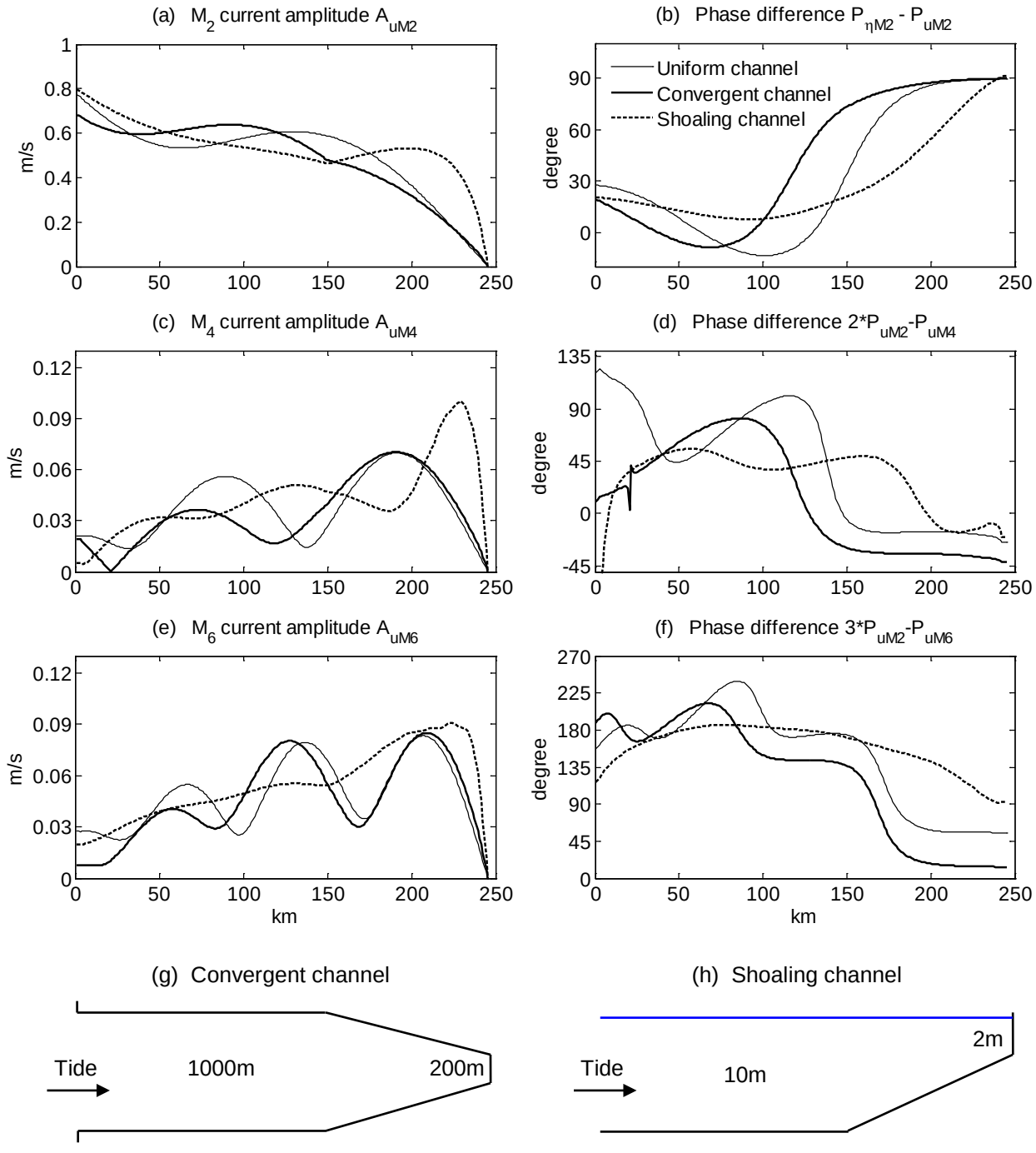

Figure 3.11 The amplitude of M_2, M_4, and M_6 current (a, c, e), the phase difference of elevation and current of M_2 (b), and the phase difference between M_4, M_6 and M_2 current (d, f) in an upstream (150 ~ 250 km) convergent channel (g) and an upstream shoaling channel (h). The generic channels are used to simulate the effects of the channel geometry of the upstream Hudson on tidal wave propagation.

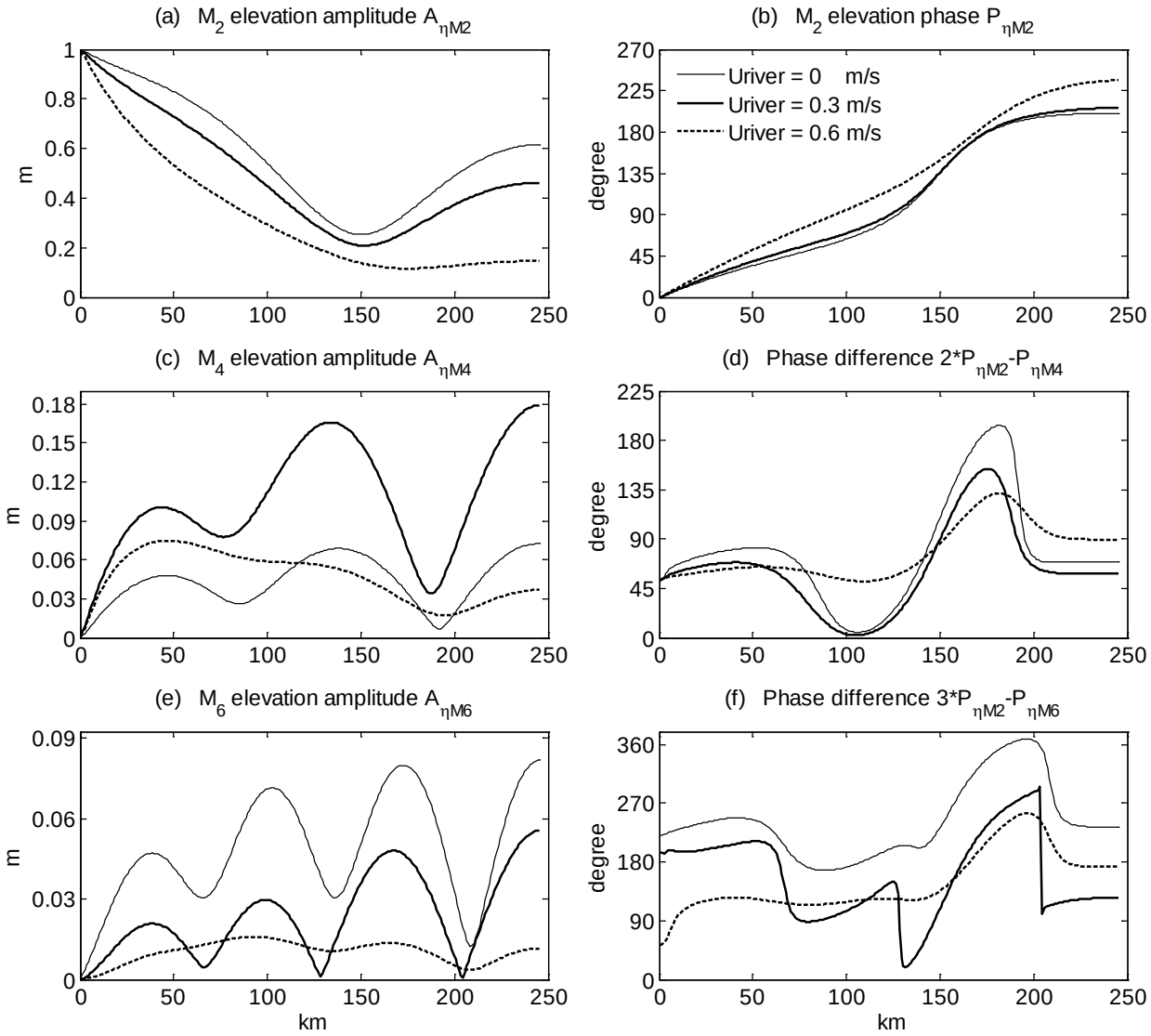

Figure 3.12 The amplitude of M_2, M_4, and M_6 elevation (a, c, e), the phase of M_2 elevation (b), and the phase difference between M_4, M_6 and M_2 elevation (d, f) in a uniform rectangular channel under the conditions of the river flow equal to 0 m/s (thin solid lines), 0.3 m/s (thick solid lines), and 0.6 m/s (thick dashed lines), respectively.

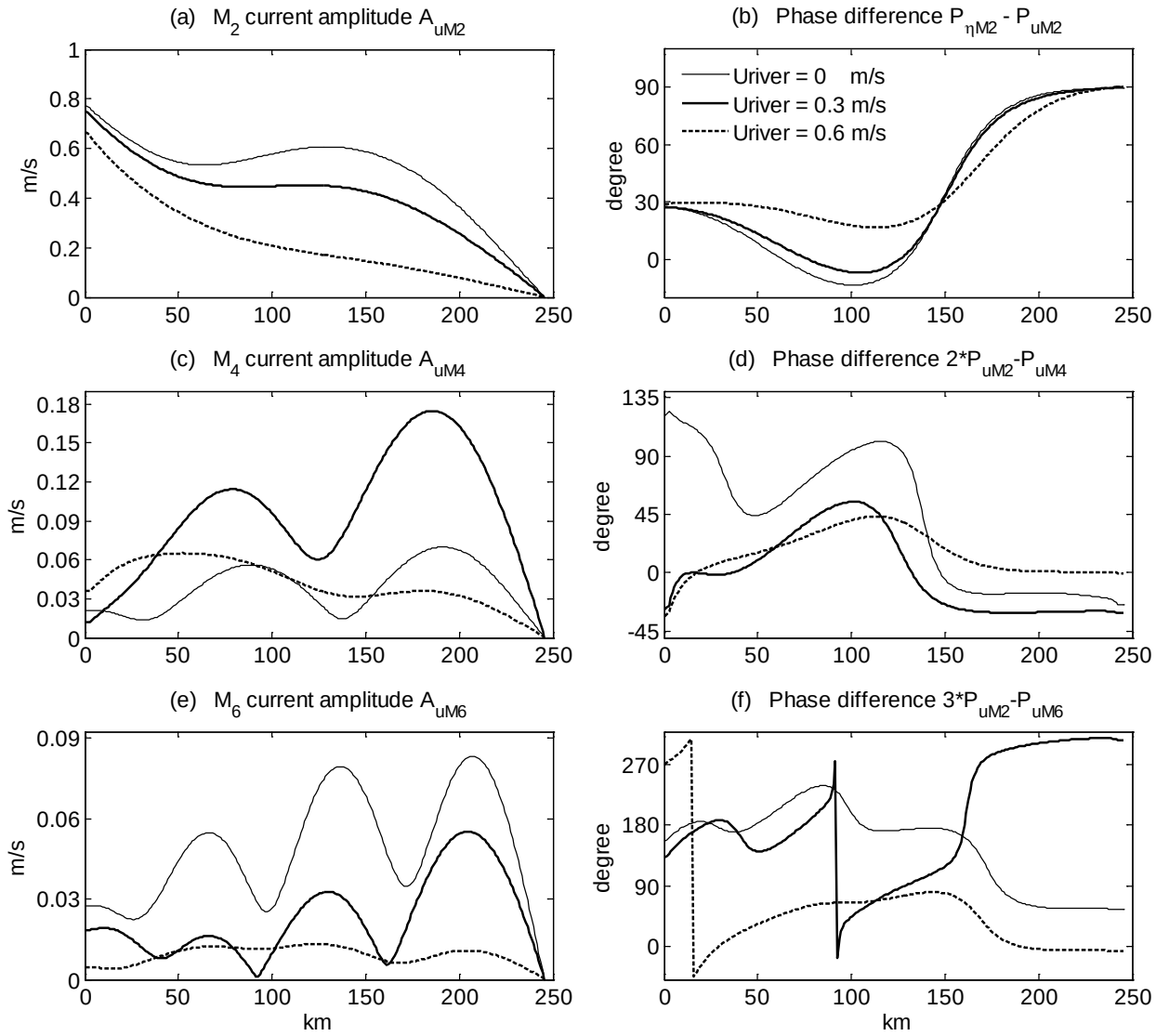

Figure 3.13 The amplitude of M_2, M_4, and M_6 current (a, c, e), the phase difference of elevation and current of M_2 (b), and the phase difference between M_4, M_6 and M_2 current (d, f) in a uniform rectangular channel under the conditions of the river flow equal to 0 m/s (thin solid lines), 0.3 m/s (thick solid lines), and 0.6 m/s (thick dashed lines), respectively.

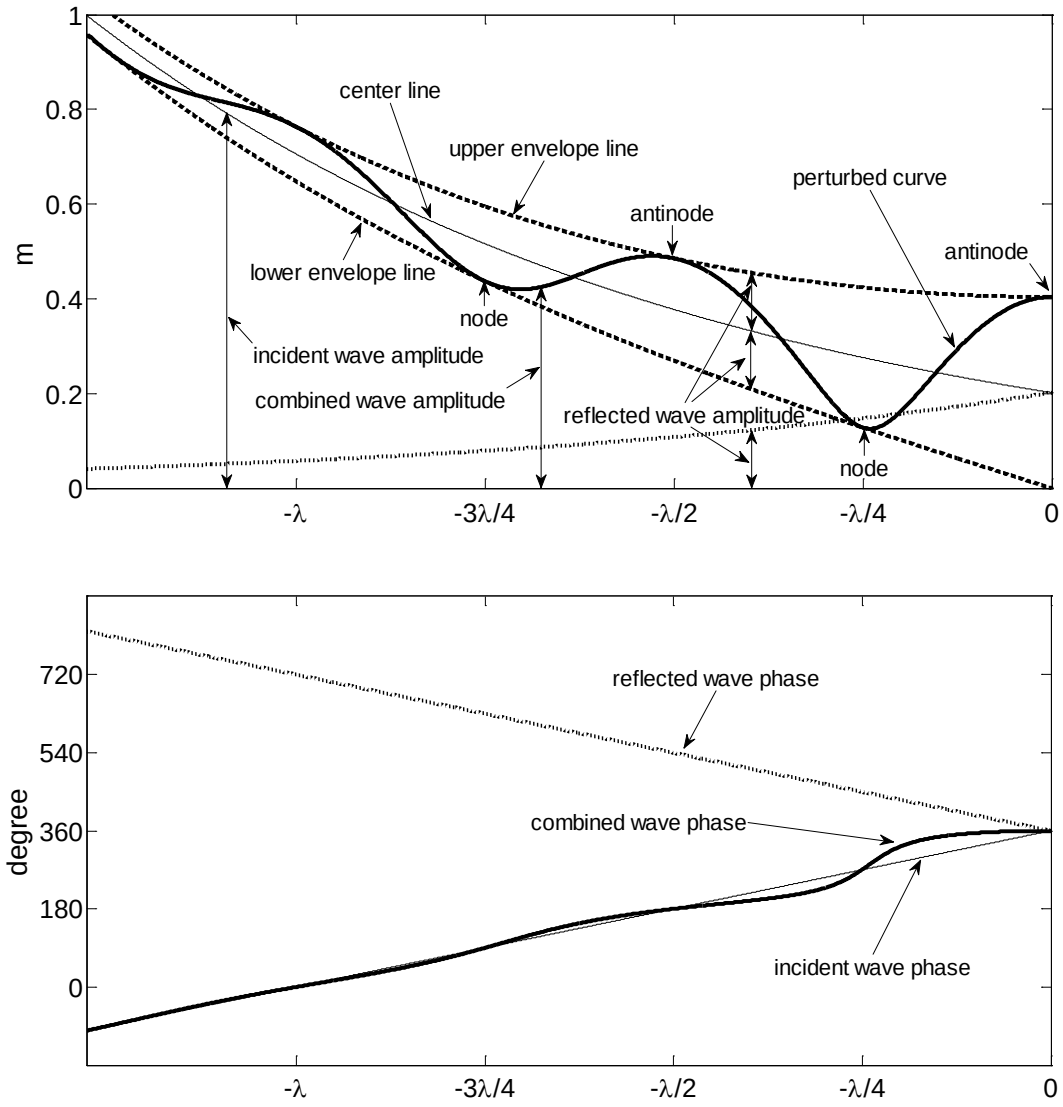

Figure 3.14 The schematic along-channel amplitude (top) and phase (bottom) of the tidal wave in a long uniform rectangular channel. The combined wave (thick solid lines) can be decomposed into the incident wave (thin solid lines) and the reflected wave (dot-dashed lines). The incident wave decreases exponentially in amplitude and increases linearly in phase toward the closed end (x=0). The reflected wave decreases exponentially in amplitude and increases linearly in phase toward the channel mouth.

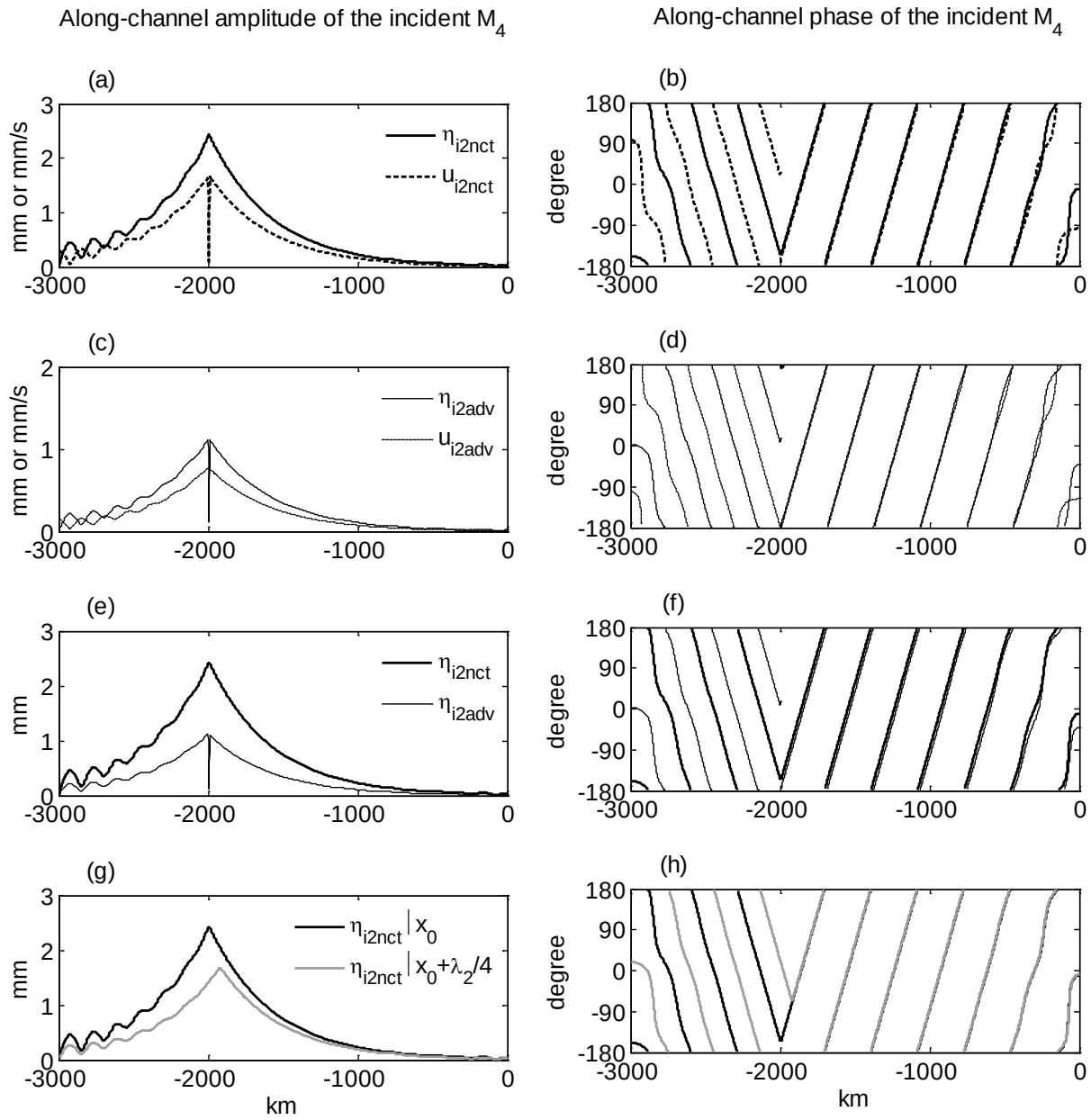

Figure 3.15 The along-channel amplitude (a, c, e, g) and phase (b, d, f, h) of the incident M_4 induced by either the nonlinear term in the continuity equation or the advective term in the momentum equation. Each type of the lines in the figure is from the results of an individual numerical experiment. In each of the experiments, only one nonlinear term is activated at a short (the length of 10 km) reach in the vicinity of -2000 km to simulate M_4 being generated at a local "point" and then propagating in the two opposite directions.

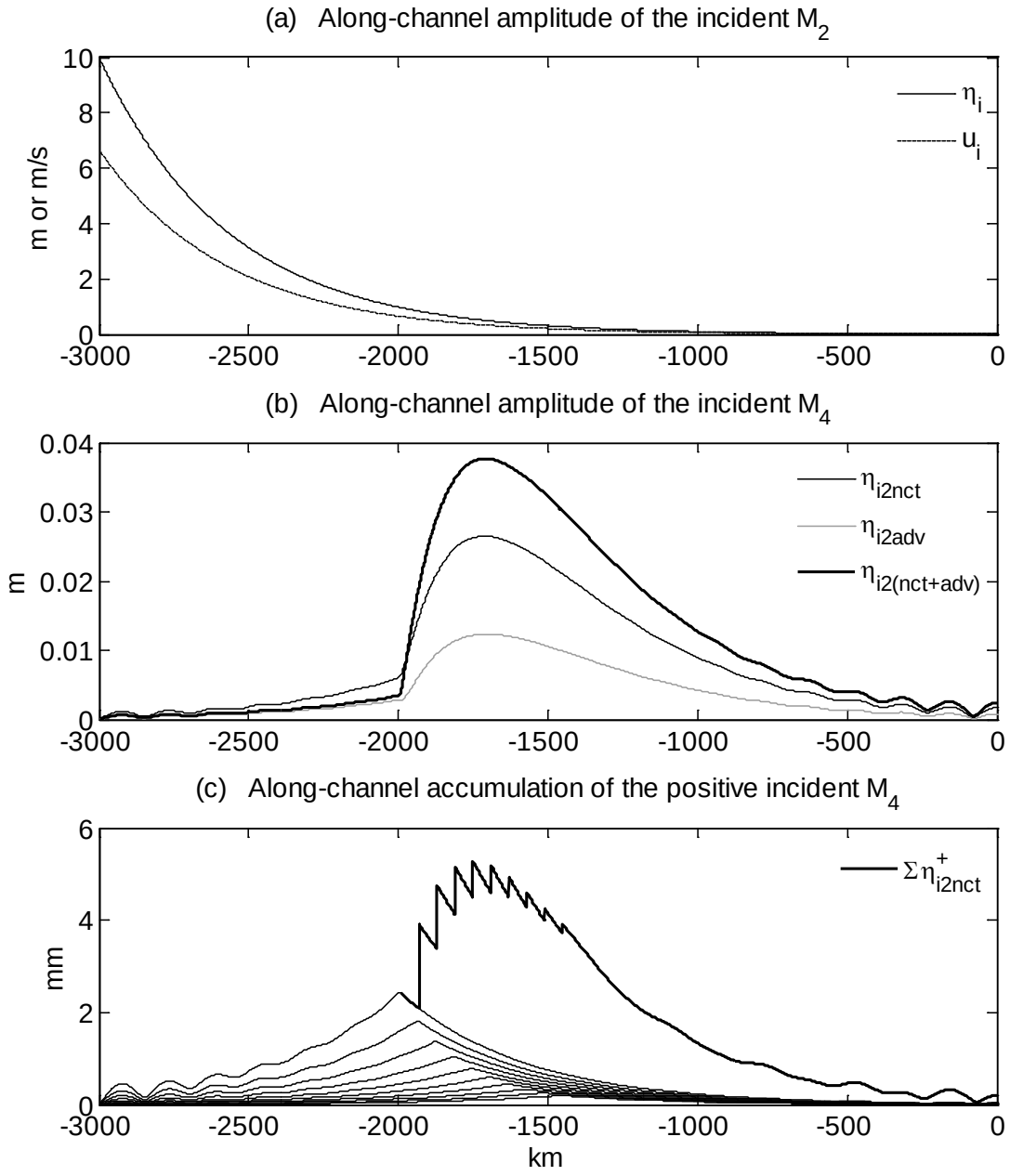

Figure 3.16 The exponentially-damped incident M_2 (a) in a long uniform rectangular channel produces the incident M_4 (b, c) at the certain reaches where the nonlinear term is activated. For (b), each line is from an individual experiment in which one or two nonlinear terms are activated at a long reach (-2000 ~ -1000 km). For (c), each thin line is from an individual experiment in which the nonlinear term is activated at a short (10 km) reach in between -2000 km and -1500 km. The superimposition of the series of positive incident M_4 in (c) is represented by the thick line similar to the lines in (b) in terms of the shape.

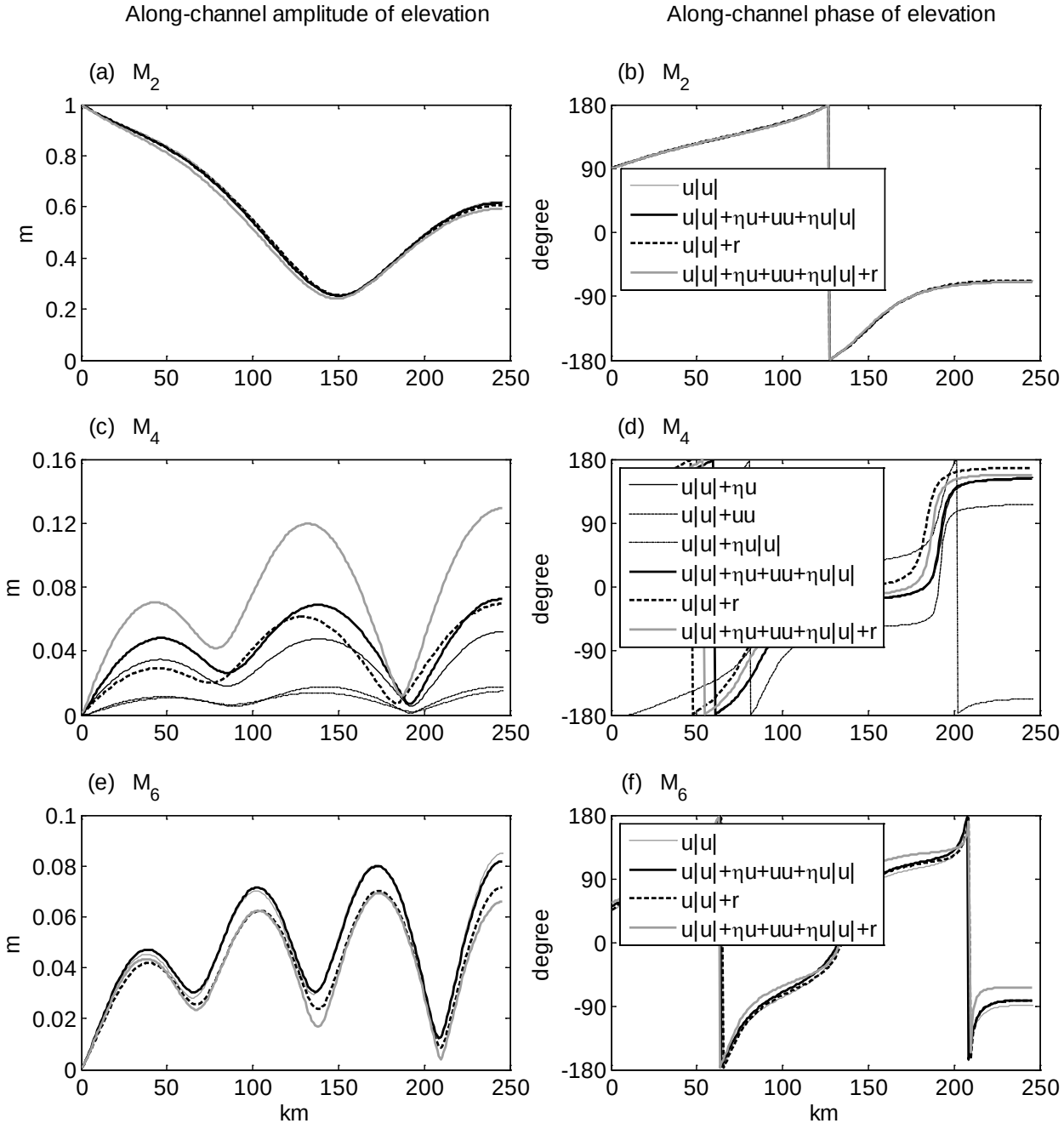

Figure 3.17 M_2 (a, b) in a uniform rectangular channel produces M_4 (c, d) and M_6 (e, f) through different combination of the nonlinear terms. M_2, M_4, and M_6 all show the quasi-standing wave pattern. Each type of the lines in the figure is from the results of an individual experiment in which different nonlinear terms are activated through the channel.

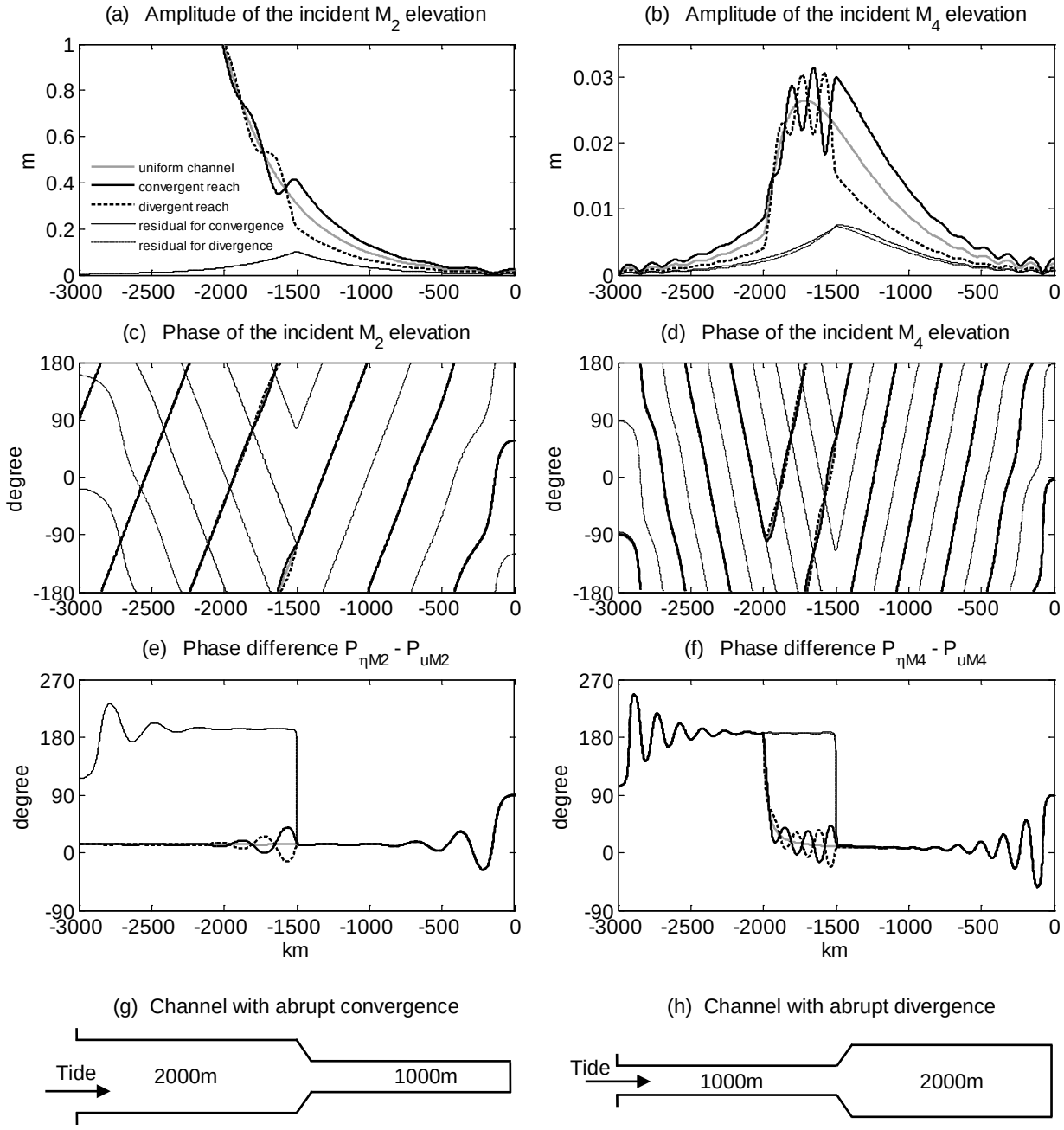

Figure 3.18 The incident M_2 (a, c, e) and M_4 (b, d, f) are modified by the abrupt longitudinal change of the channel width. The thick solid lines in the figure are from the results of an individual experiment in which a short (20 km) convergent reach is connected with the narrower (the width of 1000 m) upper reach (-1490 ~ 0 km) and the wider (2000 m) lower reach (-3000 ~ -1510 km) (g). The gray solid lines are from the experiment in a uniform rectangular channel. The thin solid lines are from the residual results between the convergent and the uniform. The thick dashed lines are from the experiment in a channel with abrupt divergence (h). The thin dashed lines are from the residual results between the divergent and the uniform.

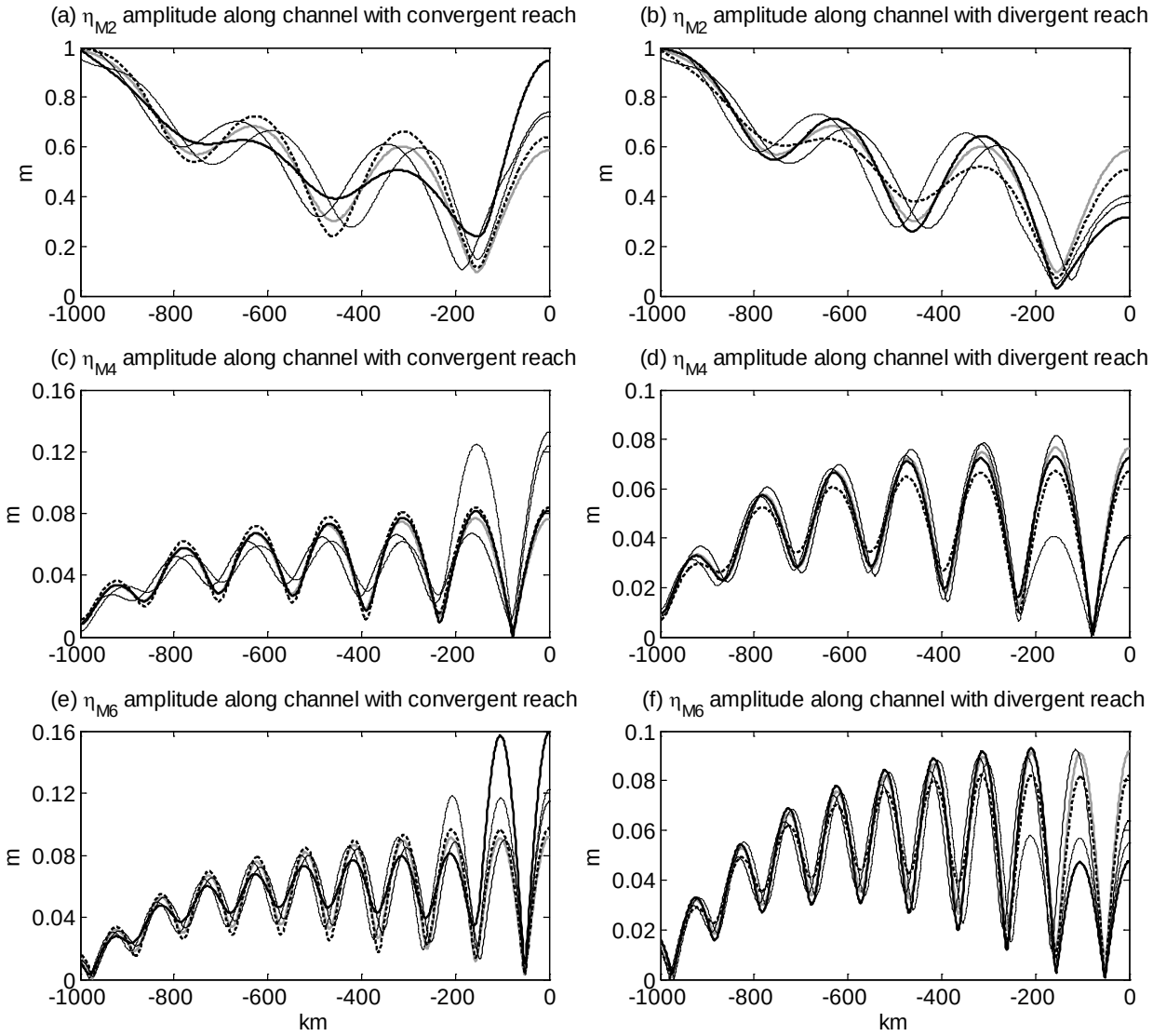

Figure 3.19 The quasi-standing M_2 wave (a, b) and the corresponding M_4 (c, d) and M_6 (e, f) are modified by the abrupt longitudinal change of the channel width. The gray solid lines are from the experiment in a uniform rectangular channel. The thin solid lines in the left panels are from the experiment in which a short (20 km) convergent reach is located at x = -78 km, where it is also the first M_4 node (a quarter of the M_4 wavelength away from the closed end). The thin solid lines in the right panels are for a short (20 km) divergent reach located at x = -78 km. The thick solid lines, the thin dashed lines and the thick dashed lines are for the convergent reach (left panels) or the divergent reach (right panels) located at x = -156 km (the first M2 node, the second M_4 antinode, and the second M_6 node), -234 km (the second M_4 node), and -312 km (the second M_2 antinode, the third M_4 antinode, and the fourth M_6 antinode), respectively.

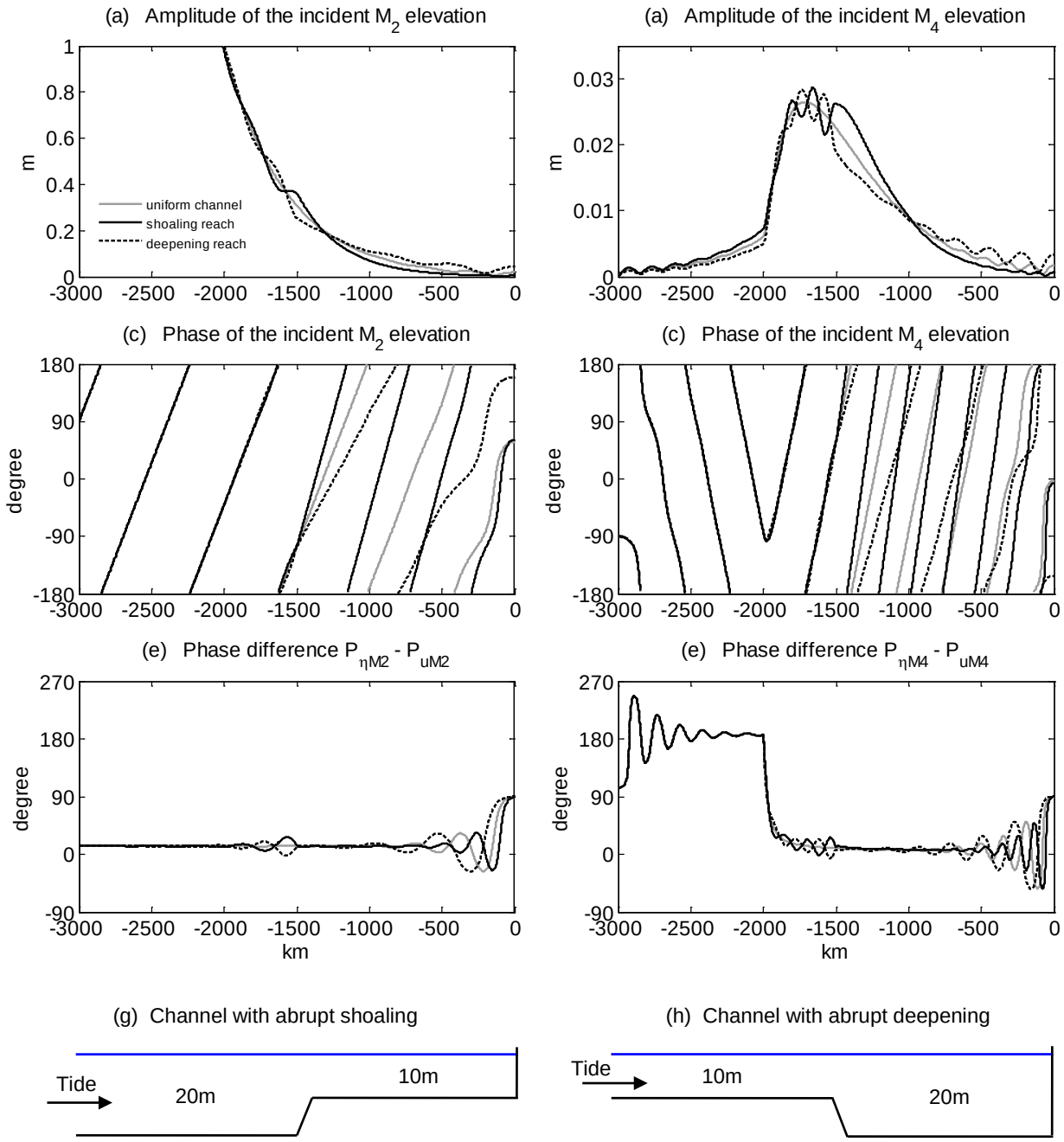

Figure 3.20 The incident M_2 (a, c, e) and M_4 (b, d, f) are modified by the abrupt longitudinal change of the channel depth. The solid lines in the figure are from the results of an individual experiment in which a short shoaling reach (20 km) is connected with the shallower (10 m) upper reach (-1490 ~ 0 km) and the deeper (20 m) lower reach (-3000 ~ -1510 km) (g). The gray solid lines are from the experiment in a uniform rectangular channel. The dashed lines are from the experiment in a channel with abrupt deepening (h).

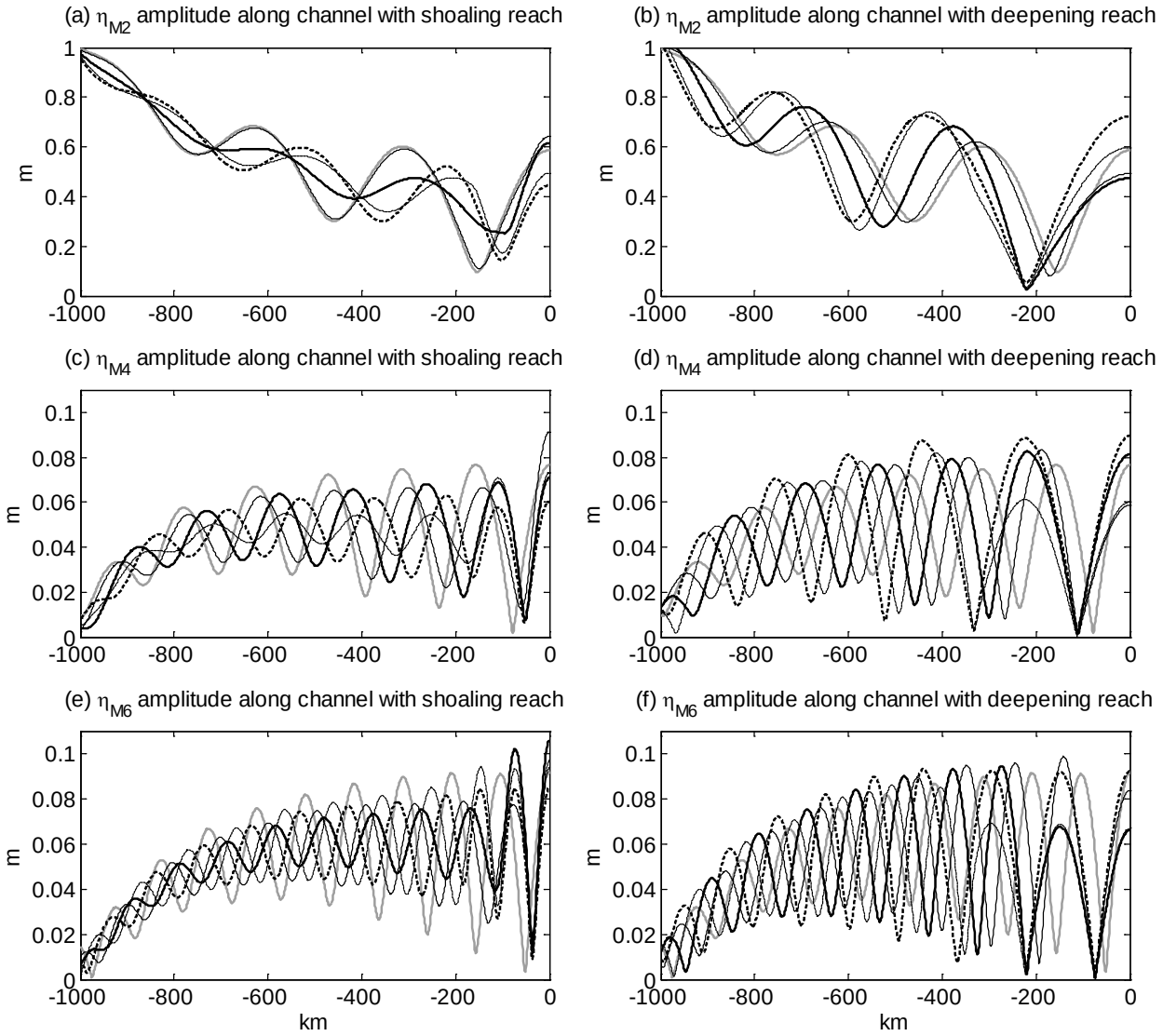

Figure 3.21 The quasi-standing M_2 wave (a, b) and the corresponding M_4 (c, d) and M_6 (e, f) are modified by the abrupt change of the channel depth. The gray solid lines are from the experiment in a uniform rectangular channel. For the left panels, the thin solid lines are from the experiment in which a short (20 km) shoaling reach is located at x = -52 km, where it is also the first M_4 node (a quarter of the M_4 wavelength away from the closed end). The thick solid lines, the thin dashed lines and the thick dashed lines are for the shoaling reach located at x = -108 km (the first M_2 node, the second M_4 antinode, and the second M_6 node), -163 km (the second M_4 node), and -220 km (the second M_2 antinode, the third M_4 antinode, and the fourth M_6 antinode), respectively. For the right panels, the thin solid lines, the thick solid lines, the thin dashed lines, and the thick dashed lines are for the short (20 km) deepening reach located at x = -110 km (the first M_4 node), -220 km (the first M_2 node, the second M_4 antinode, and the second M_6 node), -330 km (the second M_4 node), and -440 km (the second M_2 antinode, the third M_4 antinode, and the fourth M_6 antinode), respectively.

Table 3.1 The RMSE of tidal constants simulated by the one- and two- dimensional models

	RMSE of amplitude (cm)		RMSE of phase (degree)	
	One-D Model	Two-D Model	One-D Model	Two-D Model
M_2	2.2	2.4	15	9
M_4	1.1	0.5	21	12
M_6	0.8	0.8	39	23
S_2	0.8	0.9	12	4
N_2	0.9	0.8	16	10
K_1	1.1	0.8	14	10
O_1	0.8	0.7	10	5

Chapter 4
Interactions between storm surge, river pulse and tide in the Hudson River

Abstract

Storm surge associated with tropical and extra-tropical cyclones can cause severe flooding in coastal areas especially when it occurs at the time of a high tide. Storm surge can be amplified as it propagates from coastal waters into bays or estuaries. In addition, heavy precipitation associated with storms can lead to a river pulse resulting in a surge especially in the upstream reaches of a river. The storm surge propagation will be discussed based on analyses of observed water level data collected during Hurricane Ernesto in September, 2006, Hurricane Irene in August, 2011, and Hurricane Lee in September, 2011 at water level gauge locations in the Hudson River. Hindcast simulations using both one-dimensional and two-dimensional models provide detailed description of water elevation and current throughout the Hudson River from the Battery to Troy to support the analyses. In addition, longitudinal variation in surge height and surge timing, and the effects of nonlinearity and channel morphology change on surge, will be discussed based on the model results in both a generic channel and the Hudson River.

4.1 Objectives and Introduction

The objective of this chapter is to investigate along-channel variations in surge height and surge timing and the effects of all nonlinear terms and channel morphology on the propagation and interaction of storm surge, river pulse and tide in both a generic channel and the Hudson River.

Storm surge is a rapid sea-level rise, predominantly due to piling-up of water by high winds pushing on the ocean's surface and secondarily due to sucking-up of water by low pressure at the center of cyclones [Harris, 1963; Heaps, 1964]. Storm surge generated in the ocean tends to propagate across the continental shelf and into coastal waters, bays and estuaries. Storm surge associated with tropical and extra-tropical cyclones can cause severe flooding and tremendous loss of life and property [Blake et al., 2006] in coastal areas, especially when it occurs at the time of a high tide. In addition, heavy precipitation associated with storms can lead to a river pulse resulting in a surge especially in the upstream reaches of a tidal river (as seen in Figure 4.2). The river-pulse-induced surge can be superimposed on the surge propagating from the ocean, resulting in even more severe flooding. Thus understanding of the propagation of storm surge and the interaction between surge, river pulse and tide in estuaries is important for forecasting of inundation, preparation for evacuation and designing of structures.

The Hudson River is connected with the North Atlantic Ocean through New York Harbor. Either the tide or the storm surge can propagate through the estuary up to the Troy. The Hudson River has the length of ~250 km from the Battery up to Troy, about a half semidiurnal tidal wavelength, and has complicated topography and shape. A storm surge occurred during Hurricane Ernesto in September, 2006 has been captured by the measurements of water level gauges (ref. Figure 3.1) in the Hudson River. The along-channel variations (Figure 4.4) in total water level, surge height, and surge timing provide initial pictures of storm surge propagating in an elongated tidal river. During Hurricane Irene in August, 2011, the surge induced by the related river pulse reached as high as 4.5 meters above the mean tidal level at Albany, in the vicinity of the Hudson River head, emphasizing the impact of river pulse.

The propagation of storm surge and the interactions between surge and tide in coastal waters and estuaries have been extensively studied since the 1950's [Proudman, 1955; Doodson, 1956; Rossiter, 1961; Jelesnianski, 1965; Banks, 1974; Prandle, 1975; Wolf, 1978; Johns 1985; Flather, 1987; Tang et al., 1996; As-Salek and Yasuda, 2001; Bernier and Thompson, 2007; Horsburgh and Wilson, 2007; Rego and Li, 2010; Zhang et al., 2010]. Proudman (1955) analytically analyzed the effects of estuarine contraction and bottom friction on the propagation of tide and surge. Doodson (1956) used a simplified numerical method to investigate the

propagation of the surge in terms of the incident and reflected waves in a uniform channel. A one dimensional model has been extensively used to investigate the propagation of tide and surge in the Thames River [Rossiter, 1961; Banks, 1974; Prandle, 1975; Wolf, 1978]. However, the Thames River with the length ~90km can only represent relatively short tidal rivers. In addition, little attention has been paid to the relationship between the surge propagation and the river length. The quadratic friction term has been widely recognized to play an important role in the interaction between surge and tide [Prandle and Wolf, 1978; Tang et al., 1996; Zhang et al., 2010]. However, little attention has been paid to the difference between the linearized friction scheme and the quadratic friction scheme and the effects of other nonlinear terms in the continuity and momentum equations on the surge propagation and the surge-tide interaction. In addition, the river-pulse-induced surge has not received adequate attention.

In this chapter both the observed and model data will be analyzed to investigate along-channel variations in surge height and surge timing and the effects of all nonlinear terms and channel geometry on the propagation and interaction of storm surge, river pulse and tide in an elongated tidal river. The section 4.2 presents data and methods. The section 4.3 addresses both the observed and model results in the Hudson River. The section 4.4 discusses the idealized simulations. Section 4.5 provides a summary.

4.2 Data and methods

The water level data used in this study are mainly obtained from NOAA, USGS, and SOMAS (by courtesy of Dr. Roger Flood). The water levels at Sandy Hook and the Battery are from NOAA. The water levels at Hastings-on-Hudson, Piermont, West Point, Poughkeepsie, Rondout, and Albany and the river discharge at Green Island are from USGS. The water levels at Kingston, Tivoli, Catskill, Athens, Coxsackie, New Baltimore, Castleton, and Troy are from Dr. Roger Flood in SOMAS, Stony Brook, NY.

In order to extract the surge, the tidal signal has to be removed from the observed water levels. After the significant tidal signals are removed from the total water level, the residual includes the surge itself, the part from the surge-tide interaction, the part from the direct wind

effects, and the errors from the equipment and the tide prediction [Horsburgh and Wilson, 2007]. The surge itself should be a dominant part of the residual if the other parts are in a realistic range. The surge-tide interaction is also a significant part. Since an elongated estuary usually is relatively narrow, the water level change induced by the direct wind effect is assumed to be not as important as the surge propagating from the ocean. The wind effect on the water level change will be further investigated in the future study.

The errors from the tide prediction can be reduced if more significant tidal constituents are involved in harmonic analysis. The problem here is that the time of the data record at certain stations is relatively short (e.g. one month). But these stations are useful for providing more details for the corresponding reaches of a tidal river. For two tidal constituents whose synodic period [Parker, 2007] is longer than the time of the data record, only one of them can be included in the harmonic analysis. Otherwise, significant errors may be introduced into the results.

In a shallow tidal river, principal tidal constituents like M_2, S_2, N_2, K_1, and O_1 interact with each other, generating the overtides like M_4 and the compound tides like $2SM_2$ and MK_3. The relative importance of the tides, overtides, and compound tides varies at the different reaches of the estuary. Basically, the closer to the river head, the more important the overtides and the compound tides are (ref. 3.4). In order to get consistent results along the river, all tidal constituents that can be resolved by using a relatively short record (e.g. one month) of data have been included in harmonic analysis.

In order to get a picture of tide, surge, and river pulse propagating in an elongated tidal river, the water level data collected during three events, Hurricane Ernesto in September, 2006, Hurricane Irene in August, 2011 and Hurricane Lee in September, 2011 have been analyzed. Firstly, the time series with the length of at least one month excluding these events are used in harmonic analysis to get better estimates of mean tidal level, amplitude and phase of tidal constituents. Then these tidal constants are used to predict the tidal signal during the events. The residual is then calculated by subtracting the tidal signal from the total water level.

Model setup in the Hudson River

Both one- and two- dimensional models that have been validated by the tides (ref. 3.3) in the Hudson River would be used in this chapter. Both models are forced by the real-time observed water levels at the Battery. Hydrodynamic conditions are simulated for two months. The first 15 days are used for adjustment. The last 45 days are used in analysis using the method mentioned above to extract residual from total water level throughout the Hudson River.

Model setup in a generic channel

In order to investigate how the tide, the surge, and the river pulse interact with each other, a simple one-dimensional model has been applied to a generic channel representing an elongated tidal river. The detailed description of the model set-up has been provided in 3.3. Here we still solve the linearized continuity and momentum equations to get analytical solutions. We solve the continuity and momentum equations with different combination of nonlinear terms to simulate the different contribution of these nonlinear terms.

The difference here is that a surge or river pulse function has been specified at the open or closed boundary. In 3.3, a sinusoidal function $\eta = A_\eta \sin(\sigma t - \varphi_0)$ representing the tide has been specified at the open boundary. In order to simulate the surge propagating from the ocean, an exponential function $\eta_s = A_s \exp[-(t - t_{peak})^2 / T_s]$ is superimposed to the tide at the open boundary. Here A_s is the magnitude of the surge peak. t_{peak} is the time when the surge peak occurs. The surge peak can occur at the slack water during flood or ebb, high tide or low tide. T_s is the time scale proportional to the surge time span. Here we only consider the positive surge ($\eta_s > 0$) since it has more realistic significance than the negative surge. According to the observed time series, the surge time span can be tens of hours or a couple of days. For most of the following discussion, we will use one day for the normal surge time span. Similarly, an exponential function $u_r = -A_r \exp[-(t - t_{peak})^2 / T_r]$ representing a river pulse is specified at the closed boundary.

Generally two types of simulations were carried out in one experiment in order to extract the residual. Only tide was involved in the first type of simulations. Surge and/or river pulse with tide were involved in the second type of simulations to get the total water levels. Then the residual water levels were obtained by subtracting the tidal water levels in the first type from the total water levels in the second type.

4.3 Results

4.3.1 Storm surge and river pulse during historical hurricanes

The time series of total water level, predicted tide, and residual are shown in Figure 4.1 and 4.2 during the three events for four stations in the Hudson River. The Battery represents the river mouth, West Point for the lower reaches, Kingston for the upper reaches, and Albany for the river head. The corresponding along-channel height and along-channel time are shown in Figure 4.4, 4.6 and 4.7.

Storm surge during Hurricane Ernesto, September, 2006

From the time series of water levels during Hurricane Ernesto, the shape of the residual does not change significantly along the Hudson River. It took about 30 hours for the residual to rise from the mean level to its peak and about 15 hours to drop from its peak down to the mean level. It should be also noted that some small perturbations occur at Albany. These high frequency perturbations may due to stronger surge-tide interaction in the vicinity of the river head. The along-channel height (Figure 4.4ace) shows that both the high tide and the maximum total water level decrease from the river mouth toward the middle reaches and increase from the middle reaches toward the river head. The residual was slightly damped throughout the river except for a little rise at the river head. There were no obvious river pulses in the Hudson River during Hurricane Ernesto. Thus the residual was predominately the surge propagating from the ocean. We will show that the surge behaves much differently without interacting with the tides in the following section 4.4.1. Since the peak time of the residual occurs about three hours later than high tide, i.e. almost the slack water during ebb of neap tide, the maximum total water was

less than 1.5 meters above the mean tidal level throughout the river. It would be much more dangerous if this storm surge occurred at a high tide a week later when it was during spring tide.

Both one- and two- dimensional models reasonably reproduce storm surge in the Hudson River during Hurricane Ernesto, September, 2006 (Figure 4.3 and Figure 4.4). The model surge keeps the shape similar to the observed surge (Figure 4.4). There is only one obvious peak in the time series of the residual at Hastings, West Point, and Kingston. However, multiple peaks are present before the dominant peak arrives at Albany. Both one- and two- dimensional models tend to overestimate the preceding peaks at Albany. Without the significant river pulse, the models reproduce the time series of total water level very well.

As shown in Figure 4.4ef, both one- and two- dimensional models very well predict the high tide and the high tide time in the vicinity of the residual peak compared to those predicted by the observed data. All the time-related figures in this section show the step-like feature because the model data were output every half an hour. The decreased output interval would diminish the step-like feature. Both models tend to overestimate the residual peak and the total water level peak by about 10cm through the channel (Figure 4.4ac). The discrepancy between the model and the observed surge may be because both models have not included the wind forcing, which will be considered in the future work. In addition, both models, especially the one-dimensional model, tend to overestimate the surge propagation speed especially in the upper reaches. This may be due to the overestimated bathymetry in the upstream Hudson (ref. 3.3).

Storm surge and river pulse during Hurricane Irene, August, 2011

Hurricane Irene and Lee brought enormous precipitation to the U.S. East Coast which caused two huge river pulses shown in the time series of the Hudson discharge at the Green Island (Figure 4.2). During Hurricane Irene, the residual peak at the Battery was more than 1 meter and just occurred at the high tide (Figure 4.6). The residual peak continued to increase to more than 2 meters at Kingston and then reached as high as more than 4.5 meters at Albany. The water level at Albany was consistent in time with the river pulse. Here we can see how terrible the river-pulse-induced surge is.

Both models reproduce the dominant peak of total water levels and residuals in the lower reaches (Piermont and West Point) of the Hudson River during Hurricane Irene, August, 2011 (Figure 4.5abcd). Both models are able to capture the extremely high surge induced by the river pulse occurring about one day later than the storm surge propagating from the ocean at Albany (Figure 4.5gh). However, both models significantly underestimate the residual at Kingston (Figure 4.5f). This may be mainly because the Kingston tide gauge is located at a tributary (Rondout Creek) entrance of the Hudson River. There might also be a river pulse occurred in Rondout Creek during Hurricane Irene.

Both models are able to capture along-channel peak of total water level, surge, and tide through the Hudson River (Figure 4.6ace) except the station Kingston which is affected by the tributary river pulse. The storm surge propagating from the ocean changes very little along the lower reaches (0~170km). The river-pulse-induced surge mainly affect the upper reaches (170~250km) with the surge peak occurred ~30 hours later than the peak time of the storm surge from the ocean.

River pulse during Hurricane Lee, September, 2011

The normal method of obtaining the surge is to subtract the predicted tide from the total water level. However, some tidal signals would be introduced into the residual (Figure 4.5fh) if this normal method is applied to the river-pulse-induced surge. This is mainly because the river pulse tends to shrink the tidal range. Thus the predicted tide tends to overestimate the tide during the river pulse, leading to leak of tidal signals into the residual. Here we will use low-pass filtered method to estimate the river-pulse-induced surge for Hurricane Lee, September, 2011.

A cut-off period of 34 hours is used in filtering both current and water level data obtained by both one- and two- dimensional models during Hurricane Lee, September, 2011 when there was almost no storm surge propagating into the Hudson River from the ocean. The surge and current peak is mainly induced by the river pulse. Both models are able to capture the low-pass filtered elevation peak from the observations (Figure 4.7cd). But both models tend to

overestimate the peak time. That is one limitation of this low-pass filter method, which may be improved in the future work. The river pulse (Figure 4.7ab) mainly affect the upper reaches (170~250km). Here 170km can be called as a transition point. The current peak decreases sharply downstream from the river head to the transition point, which is mainly due to the downstream divergence of the channel (ref. Figure 3.1). The two-dimensional model provides thalweg current with larger magnitude than cross-section-averaged current from the one-dimensional model. In addition, the current peak from the one-dimension model takes ~7 hours to reach the transition point, which is 2 hours earlier than that from the two-dimensional model.

Both the tide amplitude and phase (Figure 4.7ef) are significantly affected during the river pulse. The tide amplitude is significantly damped by the high river flow in the upper reaches. In addition, the high tide time is delayed all through the river especially in the vicinity of the river head.

4.3.2 Storm surge and river pulse in a generic channel

Figure 4.8 shows the effects of channel convergence and shoaling on storm surge and river pulse in a generic channel with the same length as the Hudson River. The convergent channel and the shoaling channel have the same shape as that described in 3.4.2.

Generally the storm surge is amplified in the convergent channel and damped in the shoaling channel. The river-pulse-induced surge is damped in both the convergent and shoaling channels. In the upper reach (150~250km), the changes of the total water level peak due to storm surge are mainly dependent on the changes of the tide induced by either the convergent or shoaling effect rather than the changes of the storm surge peak. However, the river-pulse-induced surge significantly contributes to the total water level peak. Thus the upstream convergence or shoaling effect influence the river-pulse-induced surge to a much larger extent than the storm surge propagating from the ocean.

Thus the combined effects of the upstream convergence and shoaling lead to relatively flat storm surge but significantly enhanced river pulse in the upstream Hudson.

4.4 Discussion

4.4.1 Nonlinear effects on surge propagation in a tidal channel

Based on the linearized continuity and momentum equations, the analytical solution of a tidal wave in a long uniform channel is combination of the exponentially-damped incident wave and the exponentially-damped reflected wave (ref. 3.5). If the channel is longer than three fourths of the tidal wave length, there should be at least two nodes where the tidal amplitude has local minimums. The most obvious node tends to be located at about a quarter tidal wave length away from the channel end, where the incident tidal wave has the phase difference of π with the reflected tidal wave. The surge propagates in a similar way to the long shallow-water wave (Figure 4.9). The exponentially-damped incident surge would be superimposed by the exponentially-damped reflected surge. However, the surge here has only one rise and fall of water level. Thus the along-channel height of the surge peak tends to have one "node" where the surge peak reaches the minimum. From the channel mouth to the surge node, the reflected surge has insignificant effects on the combined surge. The reflected surge peak is obviously separated from the incident surge peak. Thus the combined surge peak is as high as the incident surge peak. From the surge node to the channel end, the reflected surge significantly contributes to the combined surge. The combined surge peak is higher than the incident surge peak. Thus the surge peak tends to be damped in the lower reaches and be amplified in the vicinity of the channel end. In addition, the time span of the surge in the channel has been extended due to superimposition of the reflected surge onto the incident surge. The pure surge induced by river-pulse generally decreases in magnitude from the river head to the river mouth due to bottom friction (Figure 4.12).

The nonlinear terms include ηu (or $b\eta u$) in the continuity equation (3.6) and uu, $\eta u|u|$, and $u|u|$ in the momentum equation (3.7). In order to investigate the roles that these nonlinear terms play in surge propagation in a tidal channel, we did the following four experiments. The surge peak at the open boundary is assumed to occur at the slack during flood, i.e. three hours before high tide for all the experiments in this section. First, the propagation of surge and tide was simulated by use of the linearized continuity and momentum equations (3.1) and (3.2)

without any nonlinear term activated. The results are shown as the solid lines in Figure 4.9, representing simple superimposition of surge onto tide. Second, surge and tide propagation was simulated by use of (3.1) and (3.2) with the nonlinear terms ηu and uu added into the equations. The results are shown as the dashed lines in Figure 4.9. Even ηu and uu produce the overtide M_4 deforming the tidal wave (the time series in Figure 4.9), but they change M_2 very little in amplitude. However, ηu and uu increase the surge peak magnitude by about 20% and move the surge node by ~60 km toward the river head. In addition, the high tide, the surge peak, and the maximum total water level (the along-channel time panel) in the vicinity of the river head occur ~40 minutes earlier in the simulation with ηu and uu than the linearized simulation.

In the third experiment, the equations (3.1) and (3.2) were still used in the simulation but with the linearized bottom friction term Fu replaced by the quadratic bottom friction term $C_d u|u|/h$ (solid lines in Figure 4.10). Compared with the first experiment, the along-channel height of the surge peak does not show an obvious node in the middle reaches but does show a sudden rise in the vicinity of the river head. The surge shape (the time series panels) is significantly sharpened in the vicinity of the river head. In other words, the surge rises and falls at a faster rate. A series of perturbations are present during the falling of the surge. In the fourth experiment, the quadratic bottom friction term $C_d u|u|/h$ and the other nonlinear terms ηu and uu, and $\eta u|u|$ are activated in the simulation. The nonlinear terms ηu, uu, and $\eta u|u|$ again increase the surge peak magnitude by about 20%. But the along-channel time of the surge peak changes very little. Thus the quadratic bottom friction term $C_d u|u|/h$ plays a very important role in changing the surge propagating in a tidal channel in terms of the surge magnitude and shape. The other nonlinear terms ηu, uu, and $\eta u|u|$ significantly increase the surge in magnitude but slightly change the shape of the surge. In addition, the results from the simulations with the quadratic friction are more consistent with the observations than those with the linearized friction. Thus the quadratic friction terms and all other nonlinear terms are used in the simulations of the following sections.

Interactions between surge, river pulse and tide

Five experiments were designed to investigate the interactions between surge, river pulse and tide. Pure surge, surge with tide, pure river pulse, river pulse with tide, and surge plus river pulse with tide were set up in each experiment. The results are shown in Figure 4.11, 4.12, and 4.13.

The pure surge simulation results (the dashed lines in Figure 4.11) show the propagation of surge in the rest water of the channel without the influence of the tide, as described at the beginning of 4.4.1. If surge interacts with the tide (the solid lines in Figure 4.11), the surge peak is enhanced at 0~350 km and 470~500 km but is reduced at 350~470 km. The surge shape is sharpened, i.e. the surge rises and falls at a faster rate. In addition, a series of perturbations are present during the falling surge.

The surge peak of pure river pulse almost linearly decreases from the river head to the river mouth without any node (the dashed lines in Figure 4.12). The surge peak tends to lag behind the maximum current by 0~6 hours in the upper reaches. The river flow is exaggerated in this experiment to be 1 m/s, corresponding to the discharge of 2×10^4 m^3/s for this rectangular channel. If river pulse interacts with tide (the solid lines in Figure 4.12), the surge peak is significantly enhanced all through the channel. As a result, the surge peak reaches as high as 4.4 m in the vicinity of river head, which is comparable to the observed surge at Albany during Hurricane Irene. The surge shape is also similar to the observed.

If surge and river pulse interact with the tide (the solid lines in Figure 4.13), the surge peak is much higher than surge with tide and river pulse with tide. At the same time, the time span of the total surge is significantly enlarged, potentially leading to very dangerous flooding, especially in the upper reaches of the estuary.

Timing of the surge peak relative to tide

Two groups of experiments were designed to test the effects of the timing of the surge and river pulse. In each group, four simulations were carried out, specifying the boundary surge (or river pulse) peak occurring at high tide, slack during ebb, low tide, and slack during flood, respectively. The results are shown in Figure 4.14.

If the surge peak at the open boundary occurs at slack during flood, the surge peak throughout the channel is higher than that occurring at other times. As a result, the maximum total water level is almost as high as that occurring at high tide.

The river-pulse-induced surge peak is a little affected by the timing of the river pulse peak specified at the closed boundary. However, the surge peak occurring at slack during flood also leads to a higher total water level in the upper reaches.

Sensitivity to the time span of the boundary surge or river pulse

It usually takes tens of hours to a couple of days for storm surge or river pulse to rise to the peak and fall back based on the observations. Two groups of experiments were designed to test the sensitivity of the along-channel surge height to the time duration of the surge or river pulse specified at the boundary. In each group of experiments, the time spans of the boundary surge or river pulse are given 6 hours, 12 hours, 24 hours, and 48 hours, respectively. The magnitude of the boundary surge or river pulse peak stays unchanged for all the experiments in this section. The results are shown in Figure 4.15.

Generally the longer the surge or river pulse at the boundary, the higher the surge and the maximum total water level throughout the channel, potentially leading to more dangerous flooding. The surge with longer duration has more potential energy, which exceeds to a large extent the consumed energy by the bottom friction. In addition, if the time span of the surge exceeds the period of the semidiurnal tide, the chance that the surge peak hit the high tide will be significantly increased.

4.4.2 The effect of channel morphology on storm surge and river pulse

Storm surge and river pulse in a channel with abrupt change in width

The mechanisms of tidal wave being affected by the abrupt longitudinal change of channel width and depth have been discussed in 3.5.2. Here we mainly focus on the longitudinal variation in the surge height and the maximum total water level affected by the abrupt channel convergence or divergence. Similar to section 3.5.2, the channel with uniform depth (20 m) has a convergent (or divergent) reach in the middle, connecting with the wider (or narrower) lower reach and the narrower (or wider) upper reach. Both the lower reach and the upper reach have uniform width. The wider reach and the narrower reach have the width of 1000 m and 250 m, respectively. The short convergent (or divergent) reach is put at 180 km away from the channel head. The surge or river pulse is specified at the boundary with its peak occurring at slack during flood and its time span of 24 hours. The results are shown in Figure 4.16.

The convergent channel is convergent for the surge propagating from the open boundary while it is divergent for the river pulse propagating toward the river mouth (the upper panels of Figure 4.16). The high tidal level, the surge peak and the maximum total water level are significantly enhanced in the upper reach. The increased height of the surge peak is even larger than that of the high tidal level. The magnitude of the river-pulse-induced surge changes a little in the upper reach but significantly drops down in the lower reach due to channel widening. As a result, the increased height of the maximum total water level mainly comes from the increased height of high tidal level.

Conversely, the high tidal level, the surge peak and the maximum total water level are significantly reduced in the wider upper reach due to channel divergence (the lower panels of Figure 4.16). The decreased height of the surge peak is larger than that of the high tidal level. The magnitude of the surge peak and the maximum total water level changes a little. Thus the widening of the channel upper reach generally reduces the possibility of flooding induced by the surge. However, the narrowing of the channel lower reach also leads to significant amplification of the river-pulse-induced surge and the maximum total water level in the lower reach.

Storm surge and river pulse in a channel with abrupt change in depth

The channel with uniform width (1000 m) has a shoaling (or deepening) reach in the middle, connected with the lower reach and the upper reach. The shallower reach and the deeper reach have the depth of 5 m and 20 m, respectively. The short shoaling (or deepening) reach is put at 180 km away from the channel head. The surge or river pulse is specified at the boundary with its peak occurring at slack during flood and its time span of 24 hours. The results are shown in Figure 4.17.

The cross-sectional area is also decreased by one fourths in the shoaling channel relative to the convergent channel. But the bottom friction is significantly enhanced. As a result, the magnitude of the high tidal level, the surge peak and the maximum total water level of the surge is significantly reduced in the shallower upper reach and changes a little in the lower reach. But the position of the shallow-water wave node changes significantly through the channel. In addition, the magnitude of the high tidal level, the surge peak and the maximum total water level of the river-pulse-induced surge is significantly reduced through the channel.

The high tidal level, the surge peak and the maximum total water level of the surge drops in the deeper upper reach but to a much less extent than in the widening channel due to the reduced bottom friction. However, the magnitude of the high tidal level, the surge peak and the maximum total water level of the river-pulse-induced surge is significantly enhanced throughout the channel.

4.5 Summary and conclusions

In a tidal river, the tidal waves, the surge propagating from the ocean, and the surge induced by the river pulse are all shallow-water waves. The surge and the river pulse can occur independently or simultaneously. But they both interact with tide in a tidal channel. Three historical events have been investigated by the observed, the one- and two- dimensional model data. There was no obvious river pulse during Hurricane Ernesto, September, 2006. The surge in the Hudson River was mainly propagating from the ocean. The magnitude of the surge peak

decreases slightly through the channel except a small rise in the vicinity of the channel head. The maximum total water level is generally less than the sum of the surge peak and the high tidal level since the surge peak occurred at slack during ebb. Hurricane Irene in August, 2011 and Hurricane Lee in September, 2011 brought extremely high precipitation, leading to severe river pulse. The river-pulse-induced surge peak reached as high as 4.5 m at Albany, NY during Hurricane Irene and decreased abruptly in the downstream direction due to the channel widening and bottom friction.

A series of numerical experiments were carried out in the idealized channel to investigate the interactions between surge, river pulse and tide and the effects of nonlinearity on the propagation of surge and river pulse by use of one dimensional model. The quadratic bottom friction term significantly affects the longitudinal variation in the magnitude and shape of the surge. It tends to produce a sudden rise of the surge peak in the vicinity of the channel head. It also causes faster rise and fall and a series of perturbations during the falling of the surge. The other nonlinear terms in the continuity and momentum equations generally increase the magnitude of the surge and the total water levels to some extent. If the surge and the river pulse occur simultaneously, not only the magnitude of the surge is significantly enhanced but also the time duration of the surge is significantly expanded.

The longitudinal height of the surge in the tidal channel is sensitive to both the tidal timing and the time span of the surge or river pulse at the boundary. If the boundary surge occurs at slack before flood, the surge peak is the largest through the channel, leading to comparable total water levels relative to the surge occurring at high tide. In addition, the longer duration of the boundary surge leads to the larger magnitude of the surge peak and the maximum total water level throughout the channel.

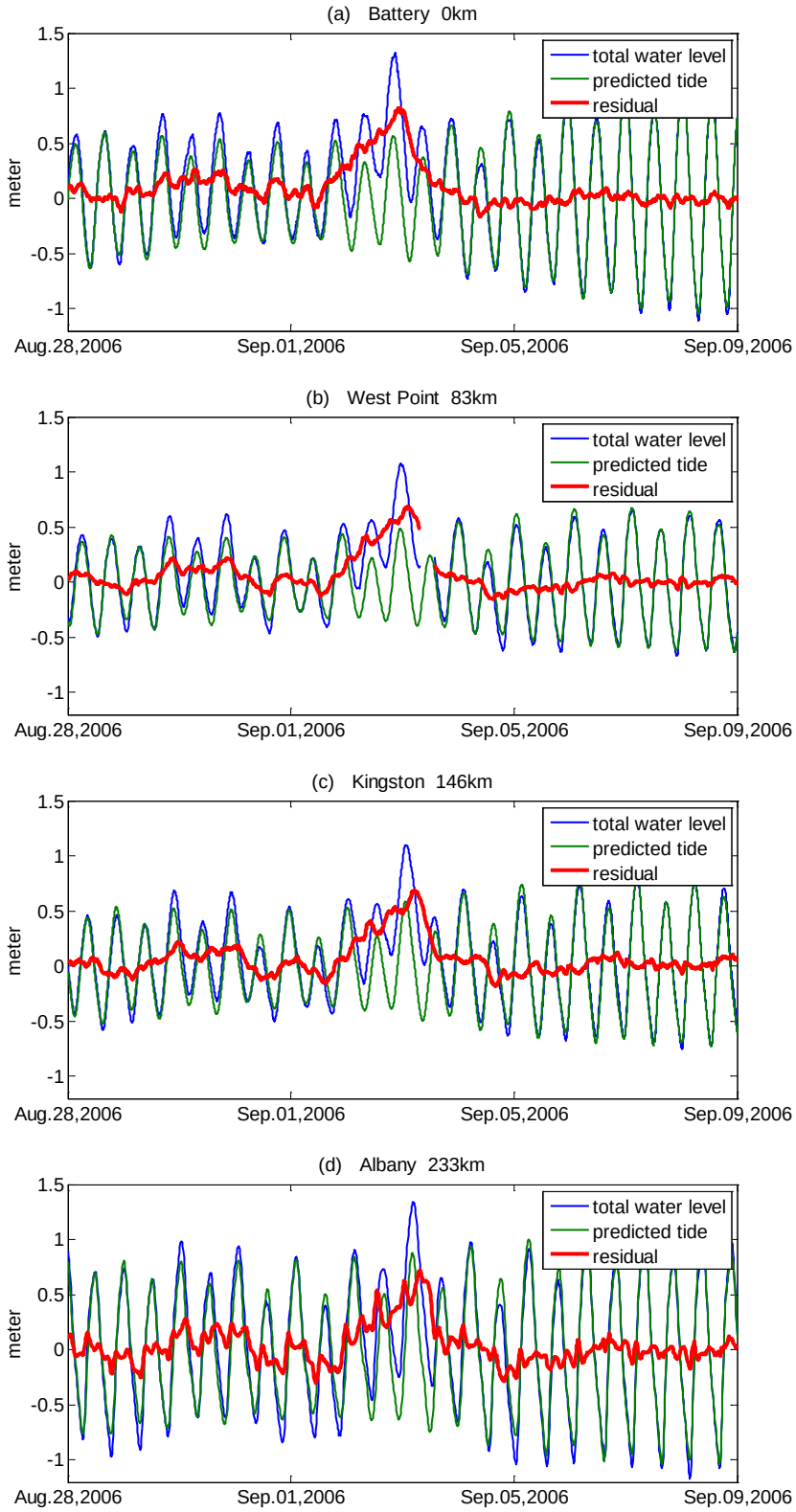

Figure 4.1 Time series of total water level, predicted tide and residual at the (a) Battery, (b) West Point, (c) Kingston, and (d) Albany in the Hudson River during Hurricane Ernesto, September, 2006. The water level gage locations have been shown in Figure 3.1.

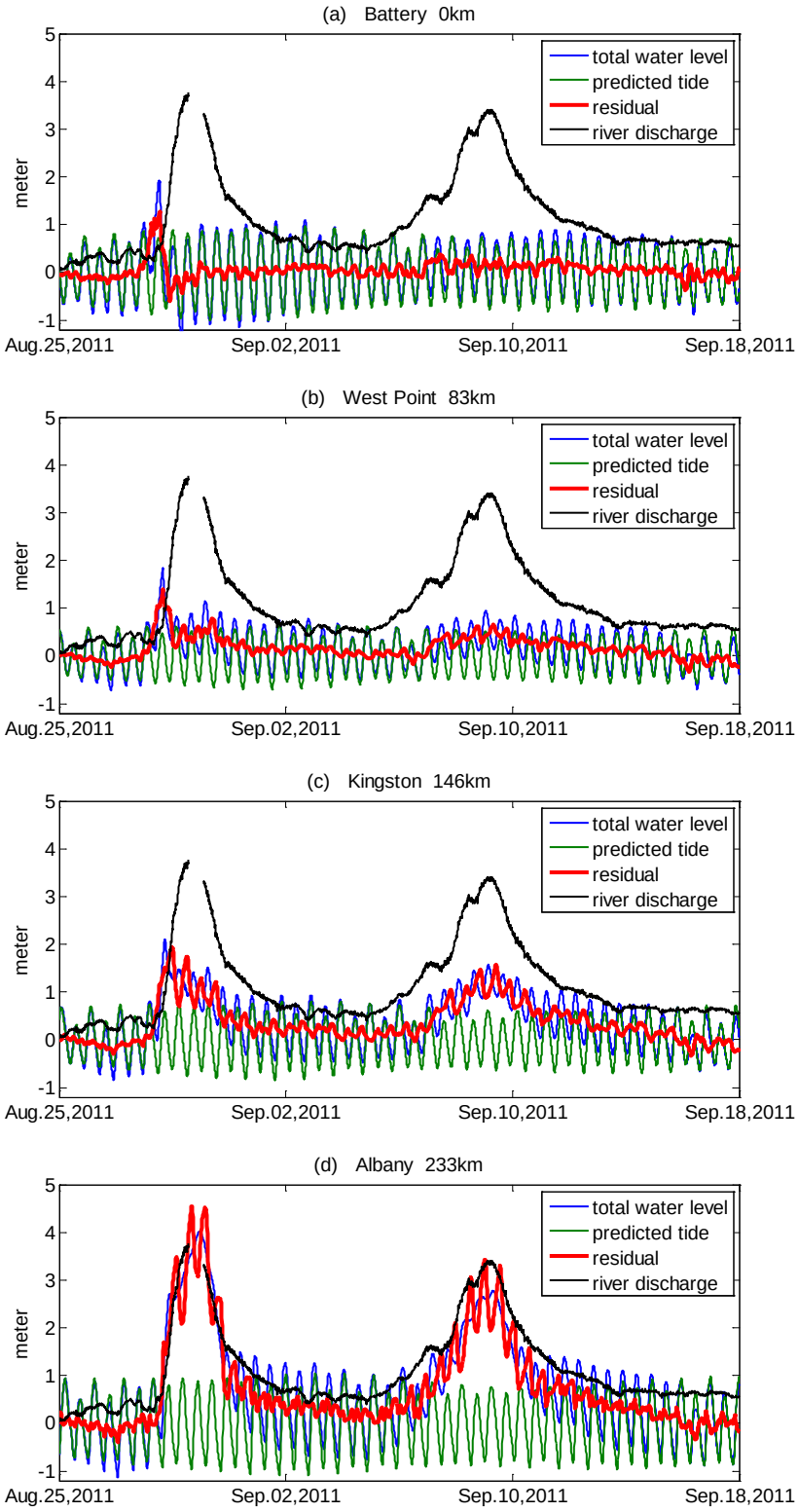

Figure 4.2 Time series of total water level, predicted tide and residual at the (a) Battery, (b) West Point, (c) Kingston, and (d) Albany in the Hudson River during Hurricane Irene, August, 2011 and Hurricane Lee, September, 2011. The black lines show the river discharge in 10^3 m^3/s at the Green Island, NY (ref. Figure 3.1).

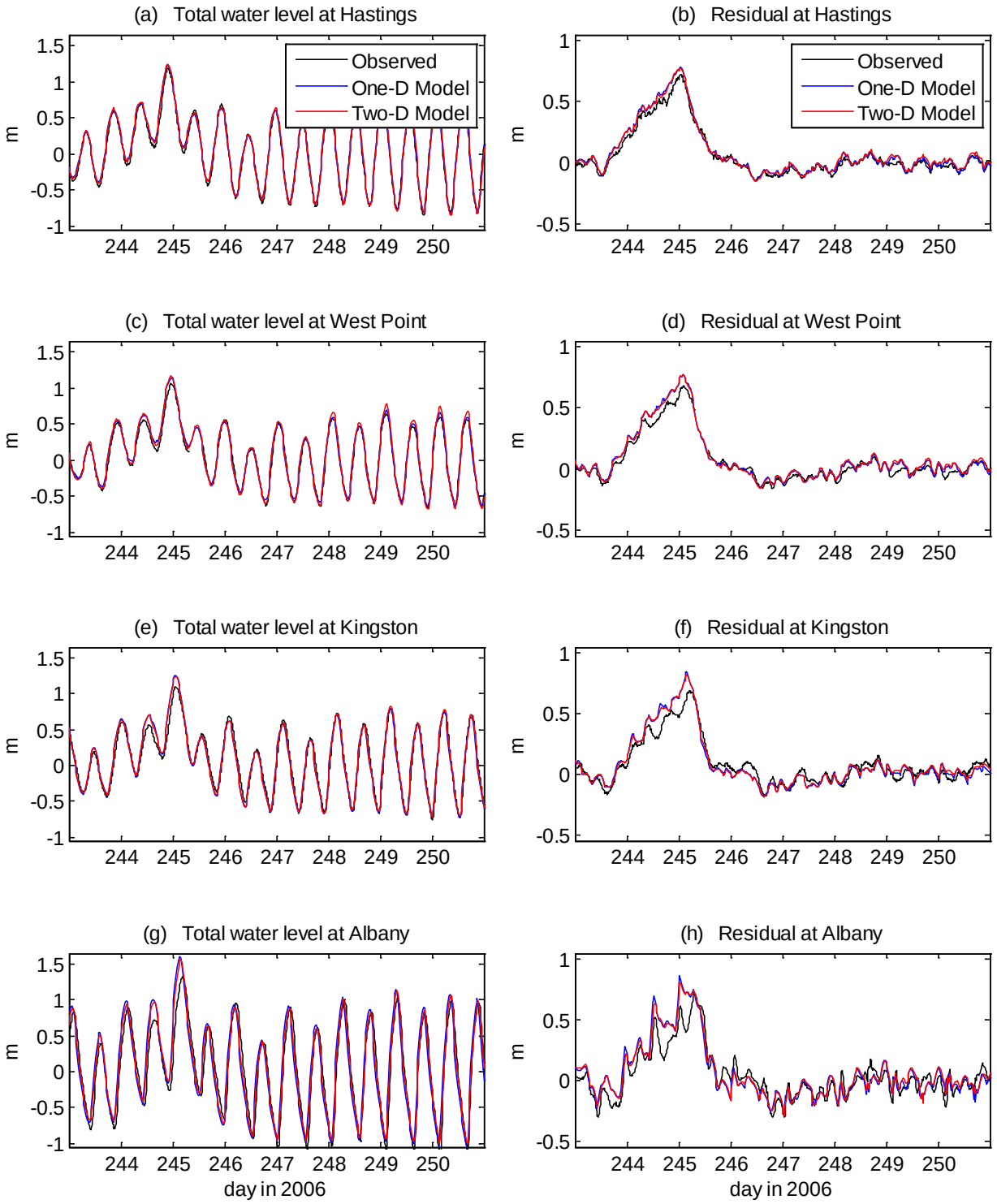

Figure 4.3 Comparison of time series of total water level (left-side panels) and residual (right-side panels) between the one- and two- dimensional model results and the observations at the Hastings (a, b), West Point (c, d), Kingston (e, f), and Albany (g, h) in the Hudson River during Hurricane Ernesto, September, 2006.

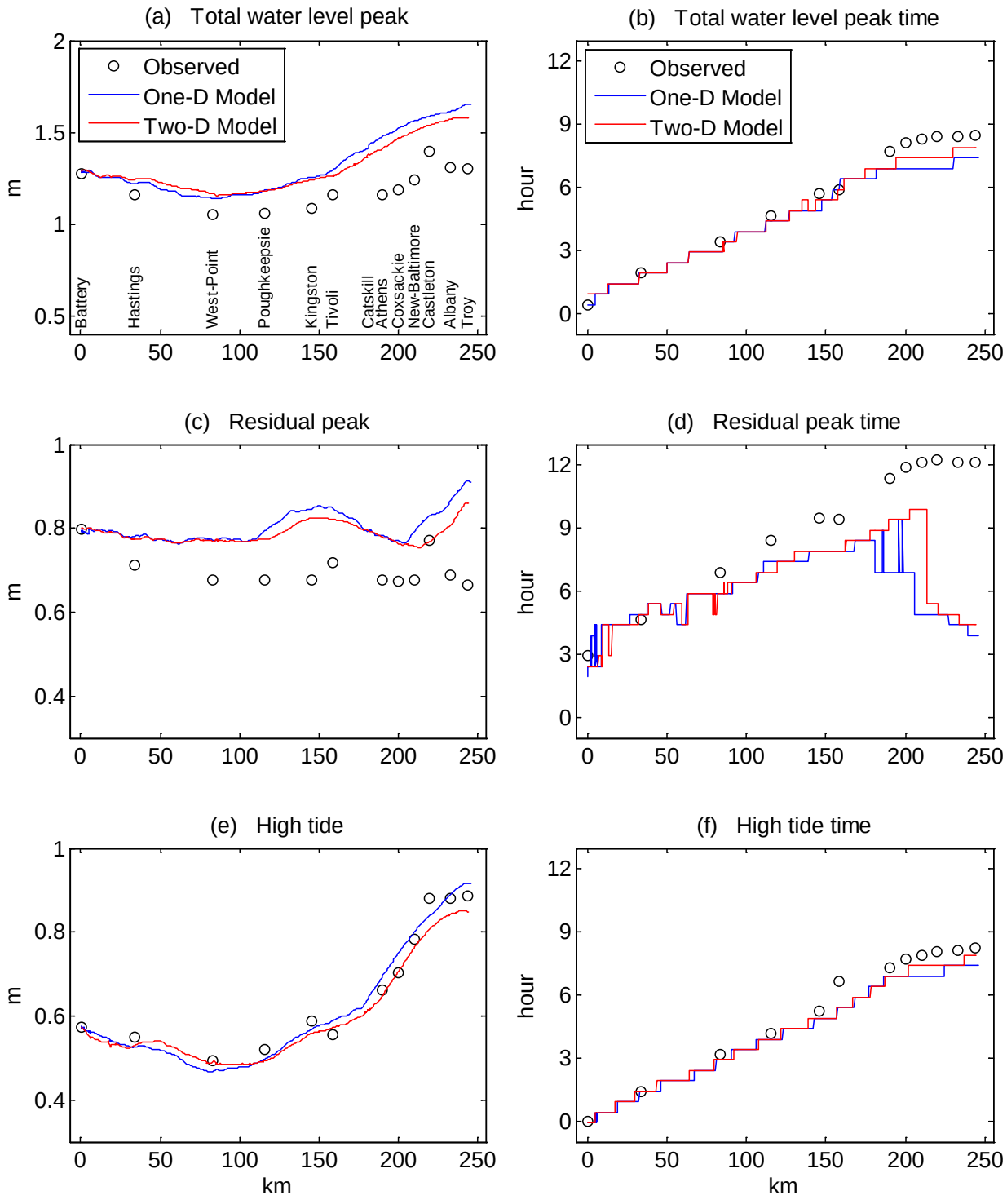

Figure 4.4 Comparison of along-channel height (left-side panels) and time (right-side panels) of total water level peak (a, b), residual peak (c, d), and high tide (e, f) between the one- and two-dimensional model results and the observations in the Hudson River during Hurricane Ernesto, September, 2006.

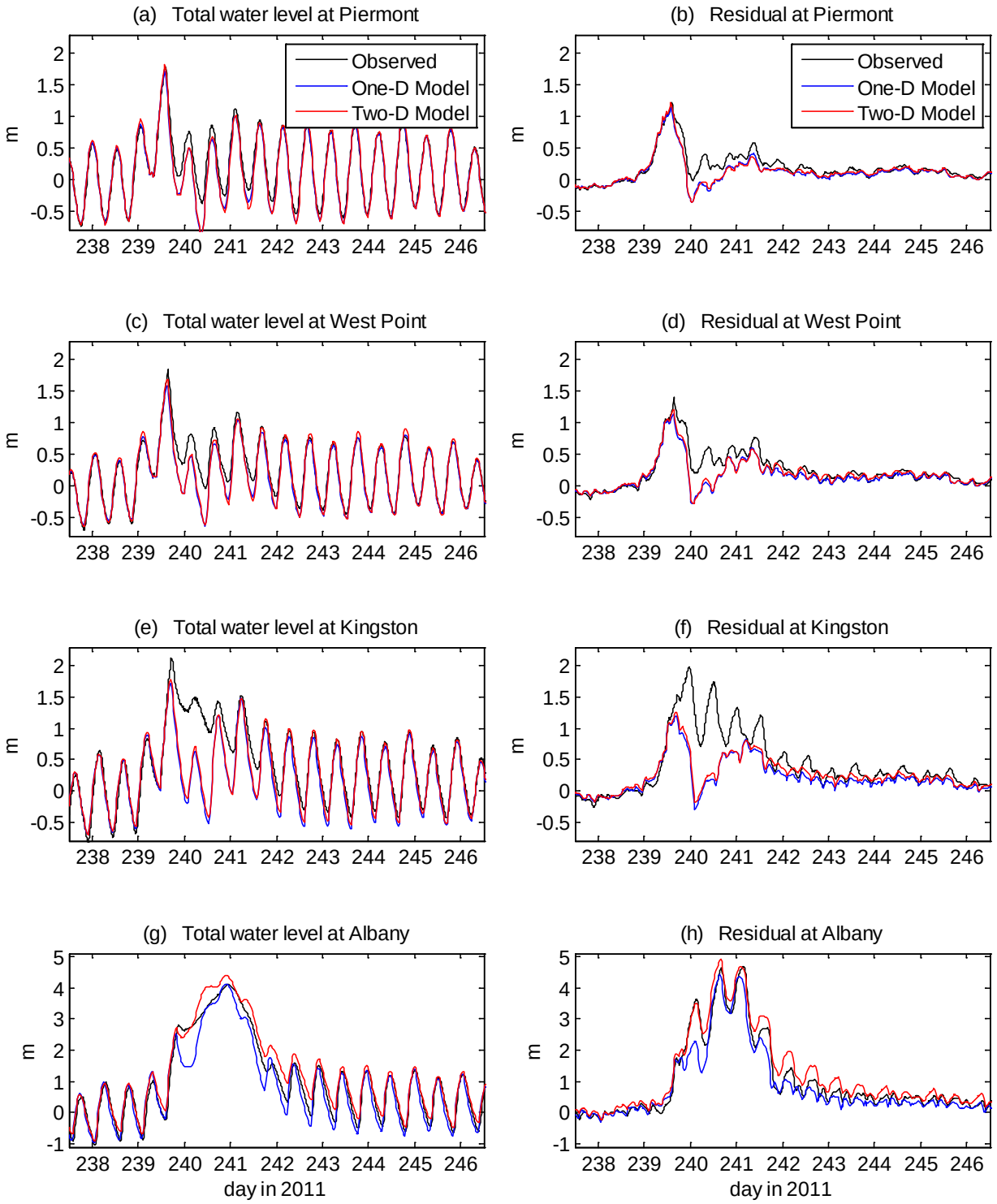

Figure 4.5 Comparison of time series of total water level (left-side panels) and residual (right-side panels) between the one- and two- dimensional model results and the observations at the Piermont (a, b), West Point (c, d), Kingston (e, f), and Albany (g, h) in the Hudson River during Hurricane Irene, August, 2011.

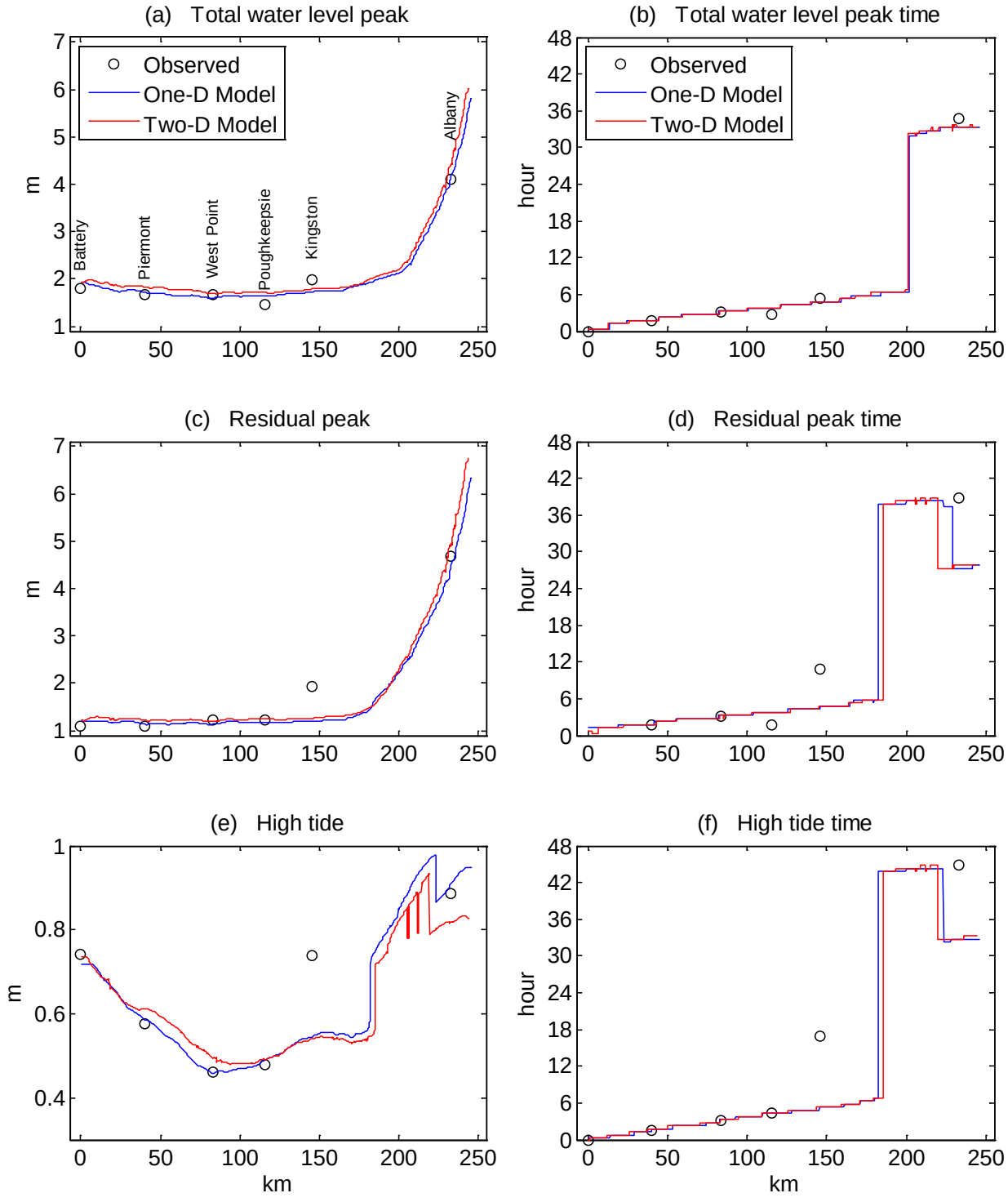

Figure 4.6 Comparison of along-channel height (left-side panels) and time (right-side panels) of total water level peak (a, b), residual peak (c, d), and high tide (e, f) between the one- and two-dimensional model results and the observations in the Hudson River during Hurricane Irene, August, 2011.

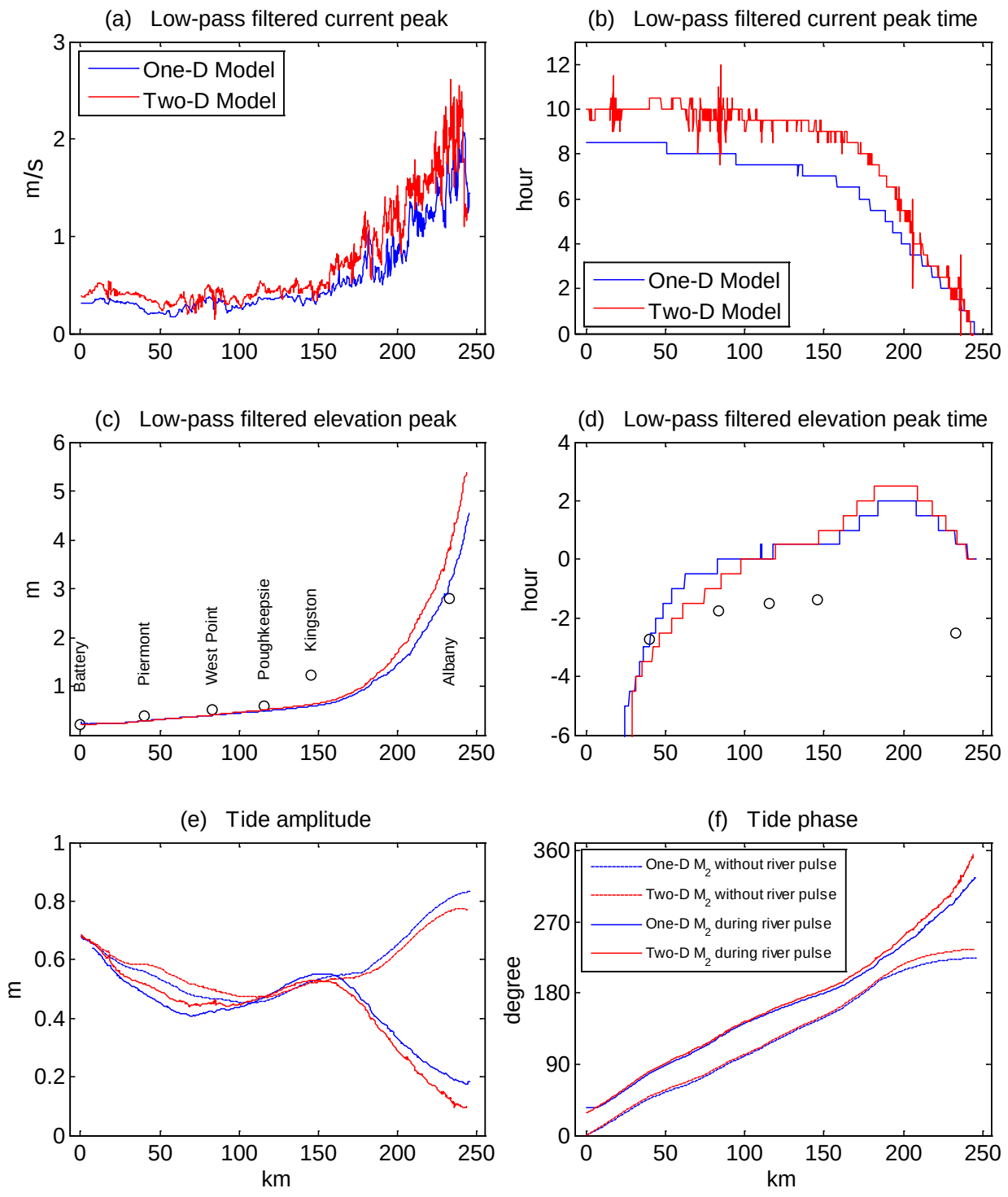

Figure 4.7 Longitudinal variation of low-pass filtered current peak (a) and time (b), low-pass filtered elevation peak (c) and time (d), and tide amplitude (e) and phase (f) in the Hudson River during Hurricane Lee, September, 2011. Both elevation and current especially in the upper reach (150~250 km) are predominantly affected by the river pulse rather than the storm surge from the ocean.

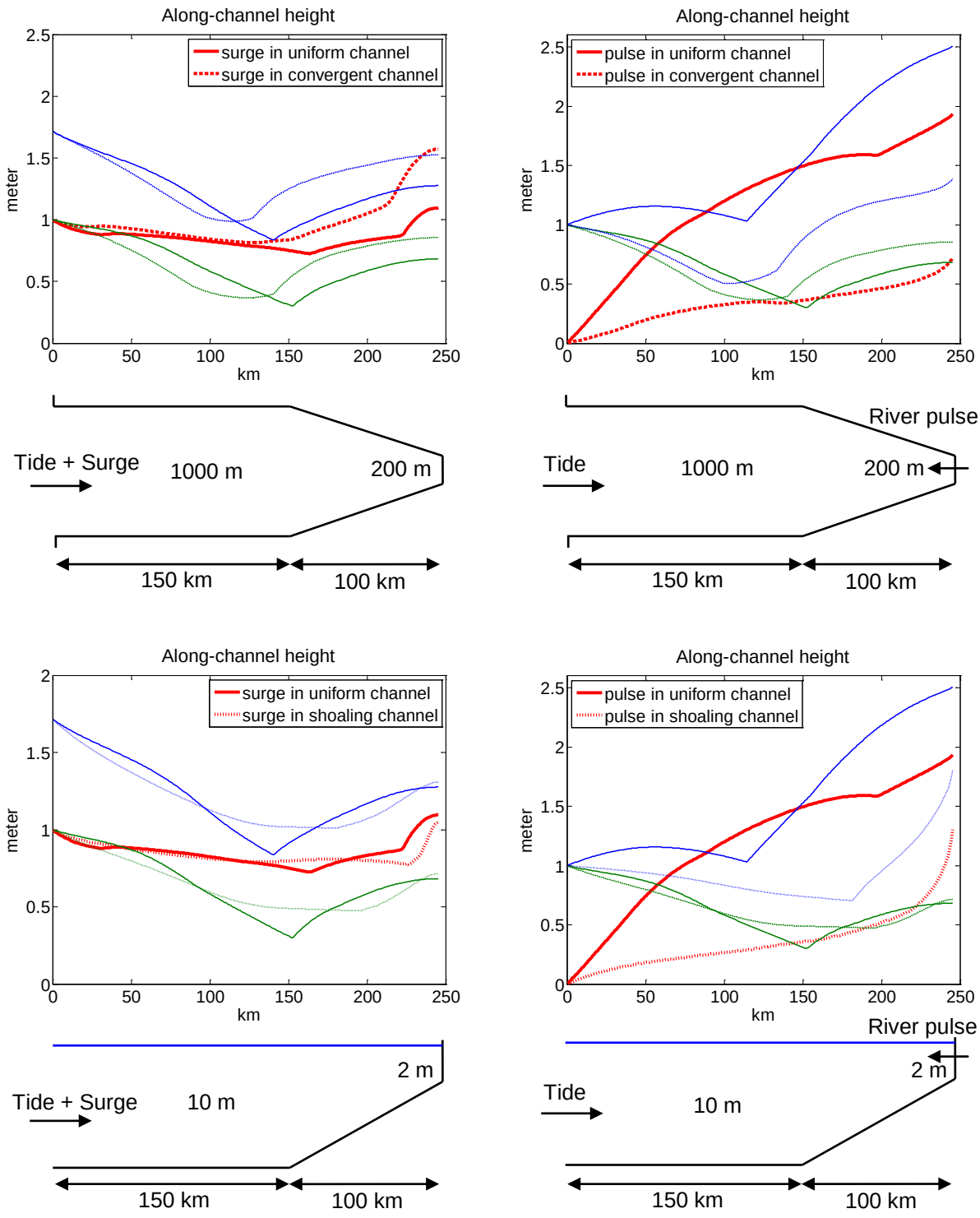

Figure 4.8 Along-channel height of total water level (blue lines), tide (green lines), and residual (red lines) show the effects of channel convergence (upper two panels) and shoaling (lower two panels) on storm surge and river pulse. The solid lines are from the simulations in the uniform channel. The dashed lines and dotted lines are from the simulations in the convergent channel and the shoaling channel, respectively. The generic channels are used to simulate the effects of the channel geometry of the upstream Hudson on storm surge and river pulse.

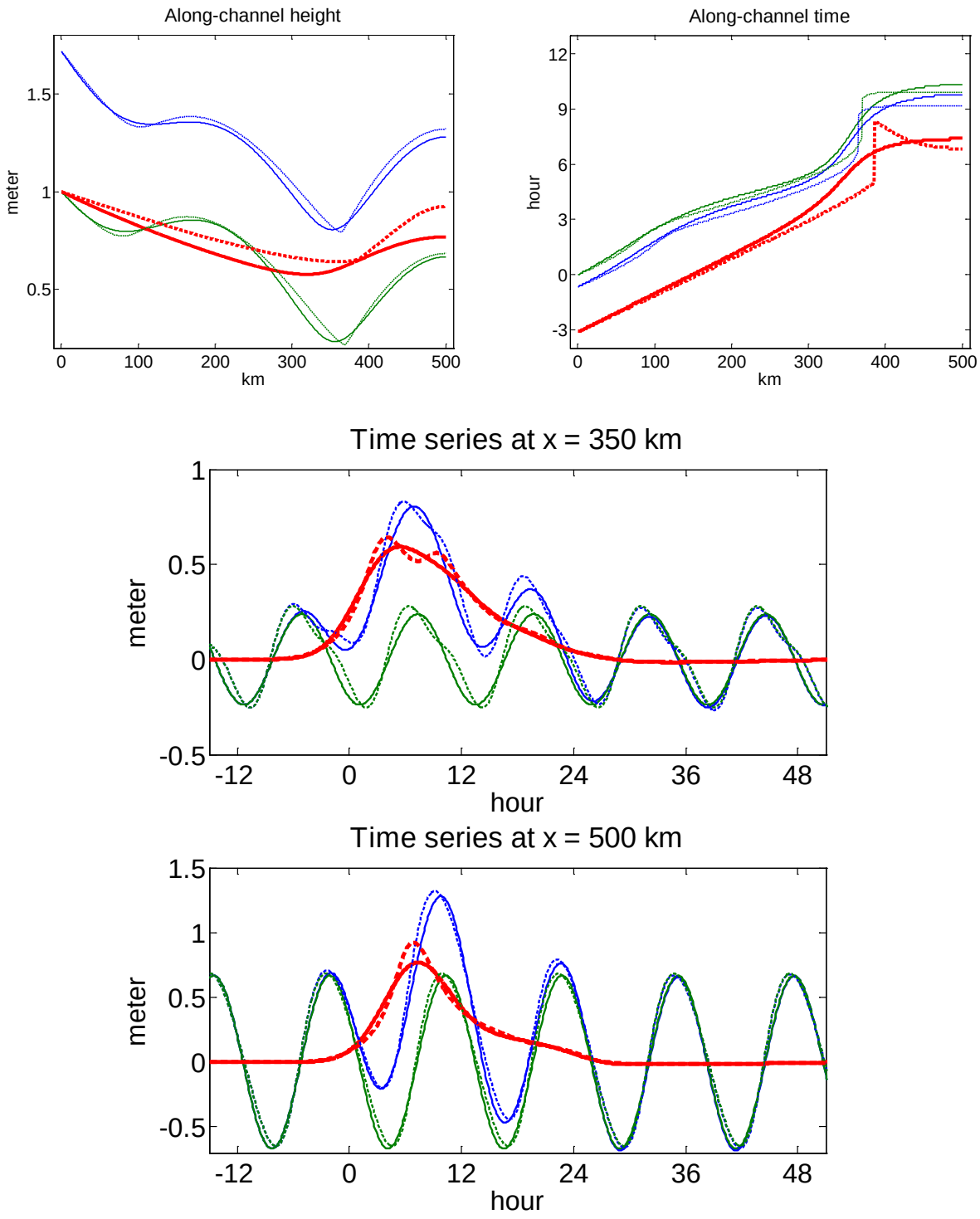

Figure 4.9 Along-channel height and time (upper two panels) and time series (lower two panels) at certain places of total water level (blue lines), tide (green lines), and residual (red lines) show nonlinear effects with linearized bottom friction. The solid lines are from the simulation with linearized bottom friction *Fu* and without any nonlinear term activated. The dashed lines are from the simulation with linearized bottom friction *Fu* and the nonlinear terms ηu and uu.

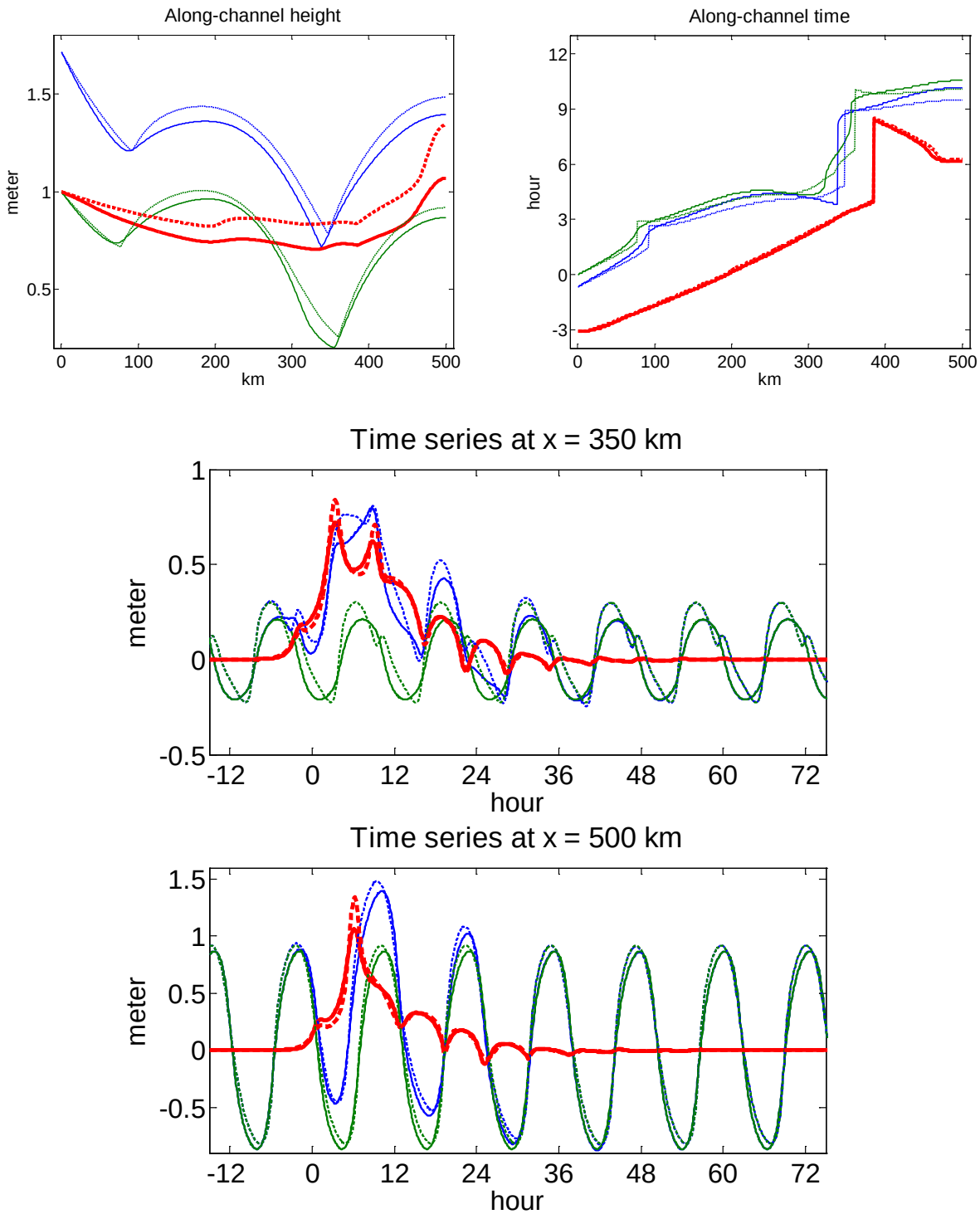

Figure 4.10 Along-channel height and time (upper two panels) and time series (lower two panels) at certain places of total water level (blue lines), tide (green lines), and residual (red lines) show nonlinear effects with quadratic bottom friction. The solid lines are from the simulation with quadratic bottom friction $|u|u$ and without any other nonlinear terms activated. The dashed lines are from the simulation with quadratic bottom friction $|u|u$ and the nonlinear terms ηu, uu *and* $\eta u|u|$.

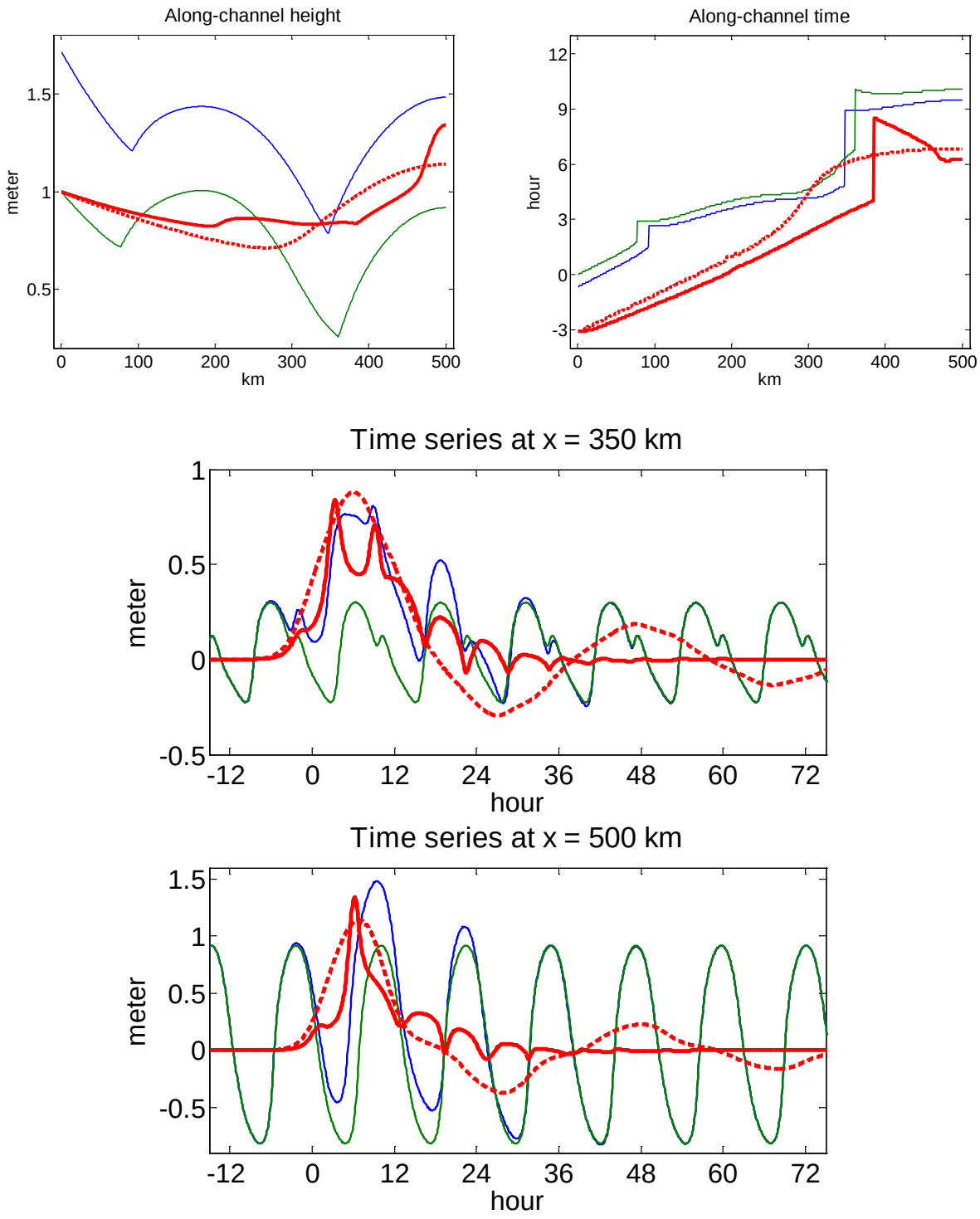

Figure 4.11 Along-channel height and time (upper two panels) and time series (lower two panels) at certain places of total water level (blue lines), tide (green lines), and residual (red lines) show interaction between surge and tide. The solid lines are from the simulation with both surge and tide. The dashed lines are from the simulation only with surge. Quadratic bottom friction and all other nonlinear terms are used in both simulations.

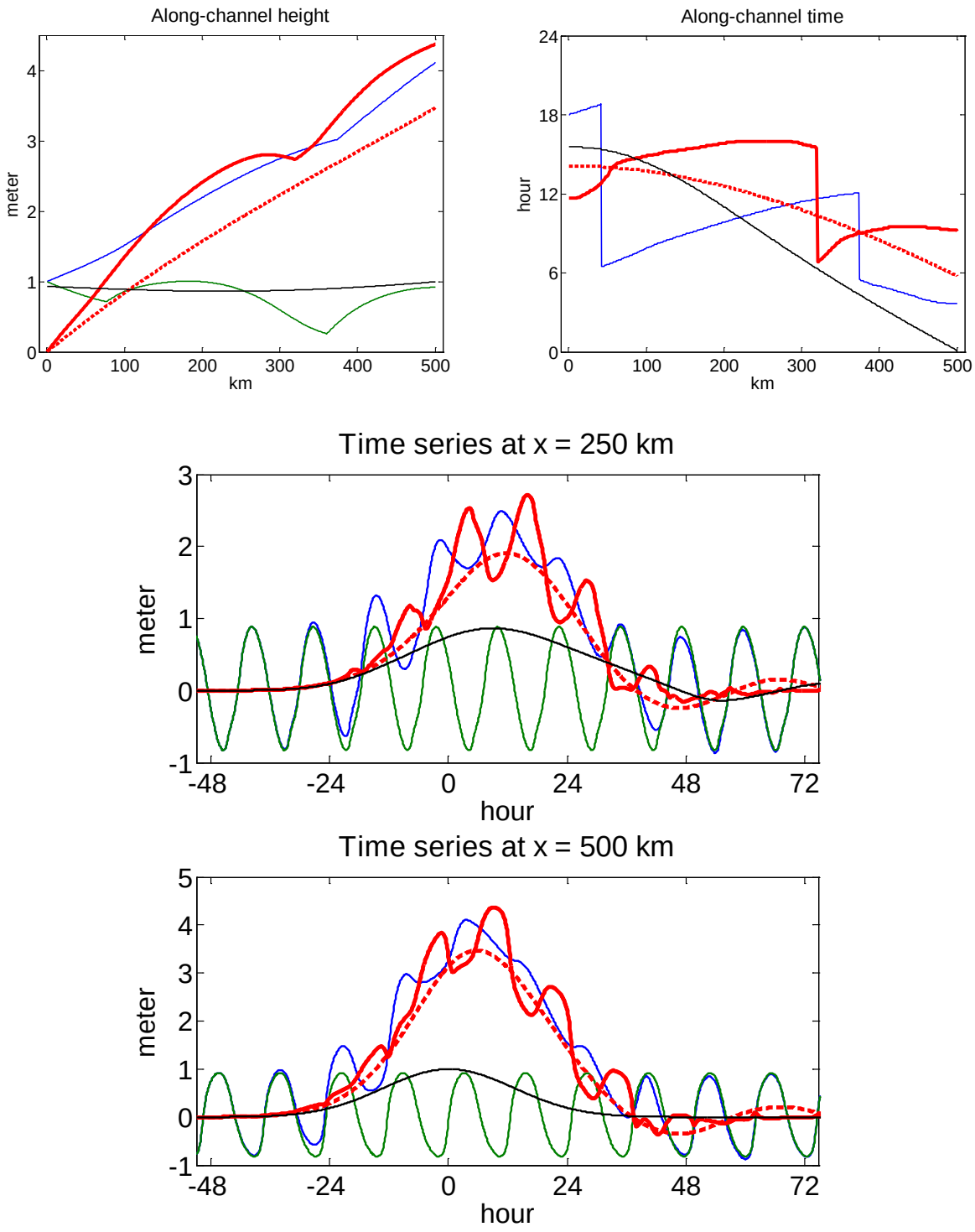

Figure 4.12 Along-channel height and time (upper two panels) and time series (lower two panels) at certain places of total water level (blue lines), tide (green lines), residual (red lines) and river flow (black lines) show interaction between river pulse and tide. The solid lines are from the simulation with both river pulse and tide. The dashed lines are from the simulation only with river pulse. Quadratic bottom friction and all other nonlinear terms are used in both simulations.

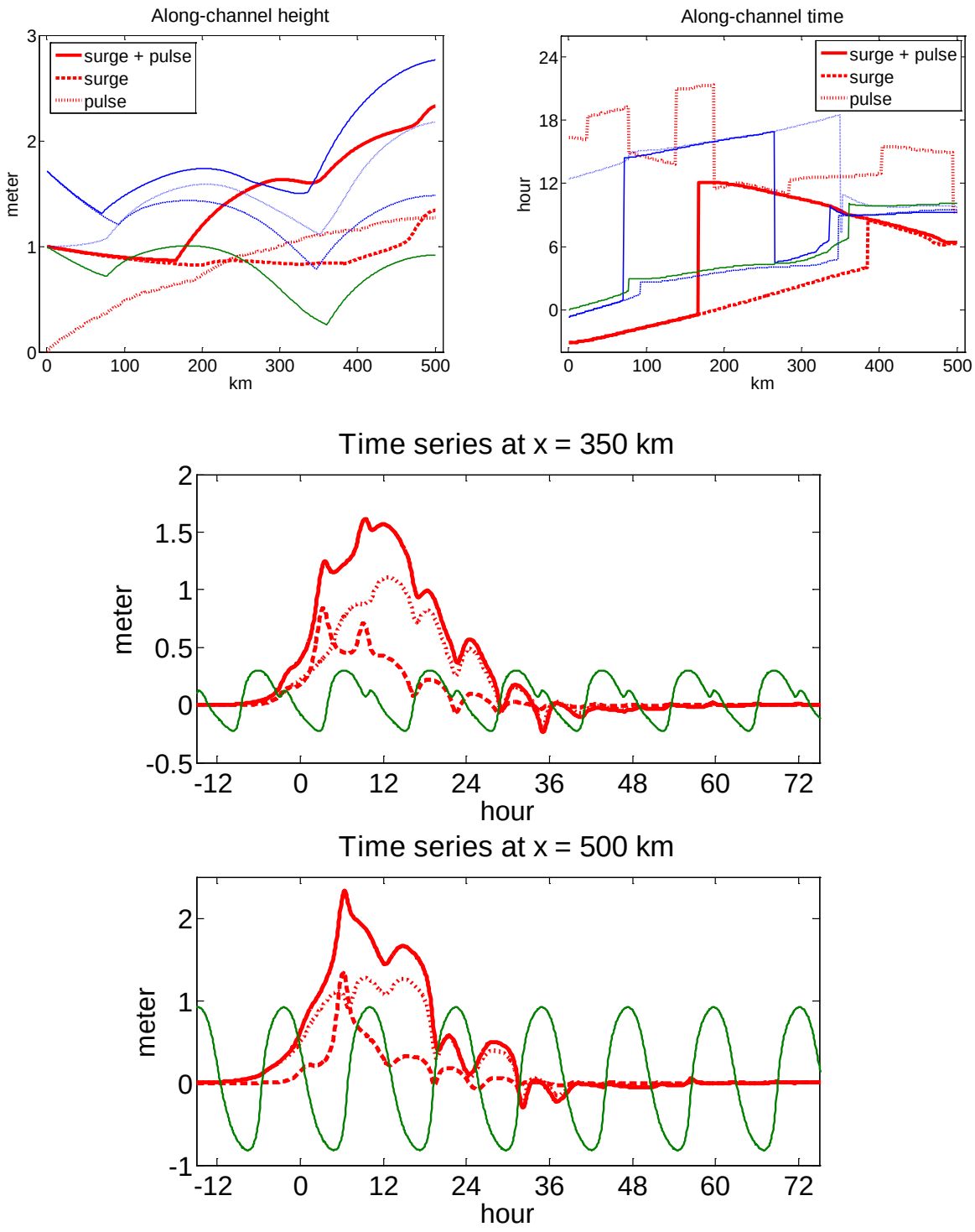

Figure 4.13 Along-channel height and time (upper two panels) and time series (lower two panels) at certain places of total water level (blue lines), tide (green lines), and residual (red lines) show interaction between surge, river pulse and tide. The solid lines are from the simulation with surge, river pulse and tide. The dashed lines are from the simulation only with surge. The dotted lines are from the simulation only with river pulse. Quadratic bottom friction and all other nonlinear terms are used in both simulations.

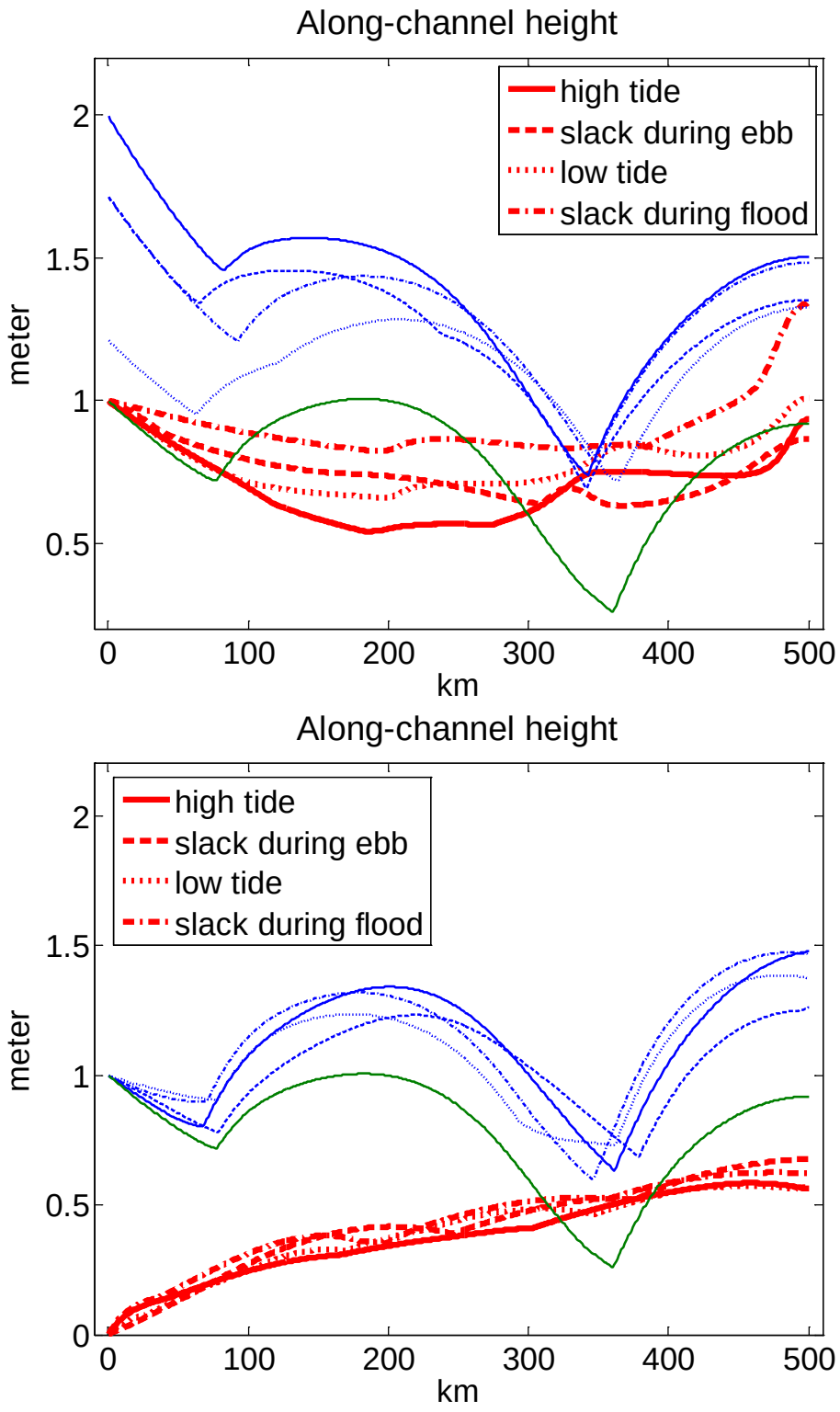

Figure 4.14 Along-channel height of total water level (blue lines), tide (green lines), and residual (red lines) show the effects of the timing of surge (upper panel) and river pulse (lower panel). The surge or river pulse peak at the boundary occurs at high tide (solid lines), slack during ebb (dashed lines), low tide (dotted lines), and slack during flood (dot-dashed lines), respectively.

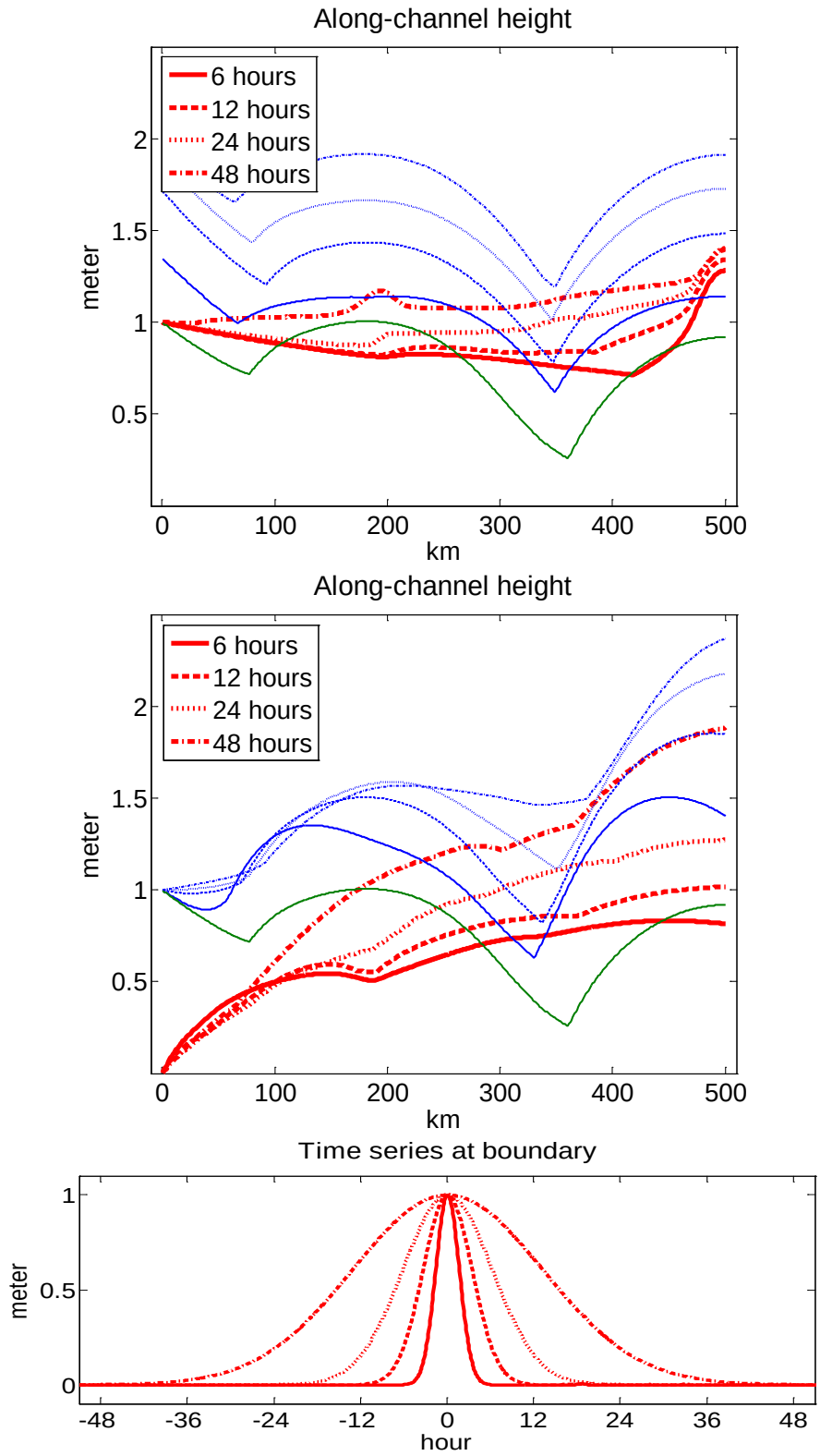

Figure 4.15 Along-channel height of total water level (blue lines), tide (green lines), and residual (red lines) show the sensitivity of surge (upper panel) and river pulse (middle panel) to the time span (bottom panel) of residual specified at the open boundary (for surge) or the closed boundary (for river pulse).

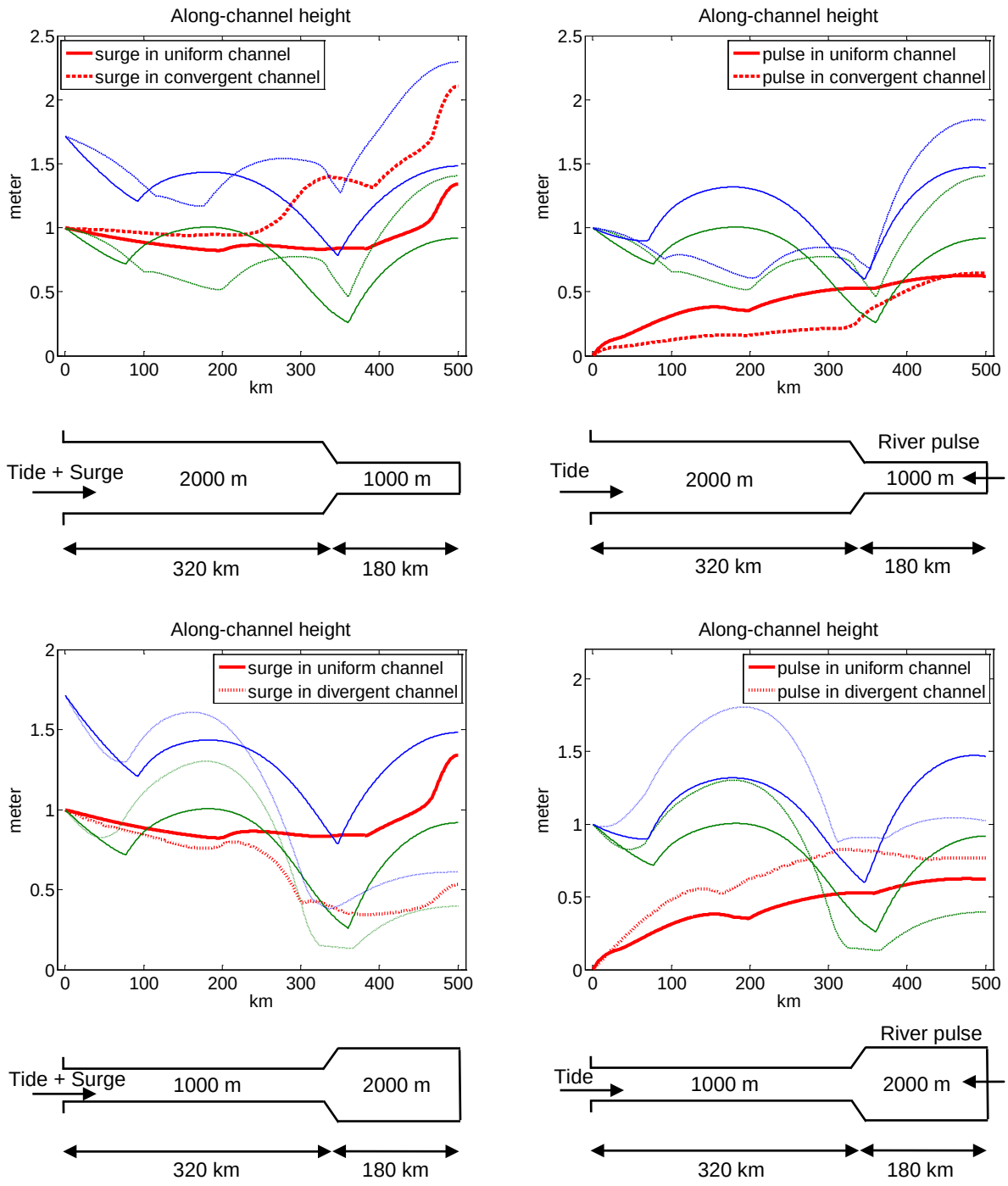

Figure 4.16 Along-channel height of total water level (blue lines), tide (green lines), and residual (red lines) show the effects of abrupt channel convergence (upper two panels) and divergence (lower two panels) on surge (left) and river pulse (right). The solid lines are from the simulations in the uniform channel. The dashed lines and dotted lines are from the simulations in the abrupt convergent channel and divergent channel, respectively.

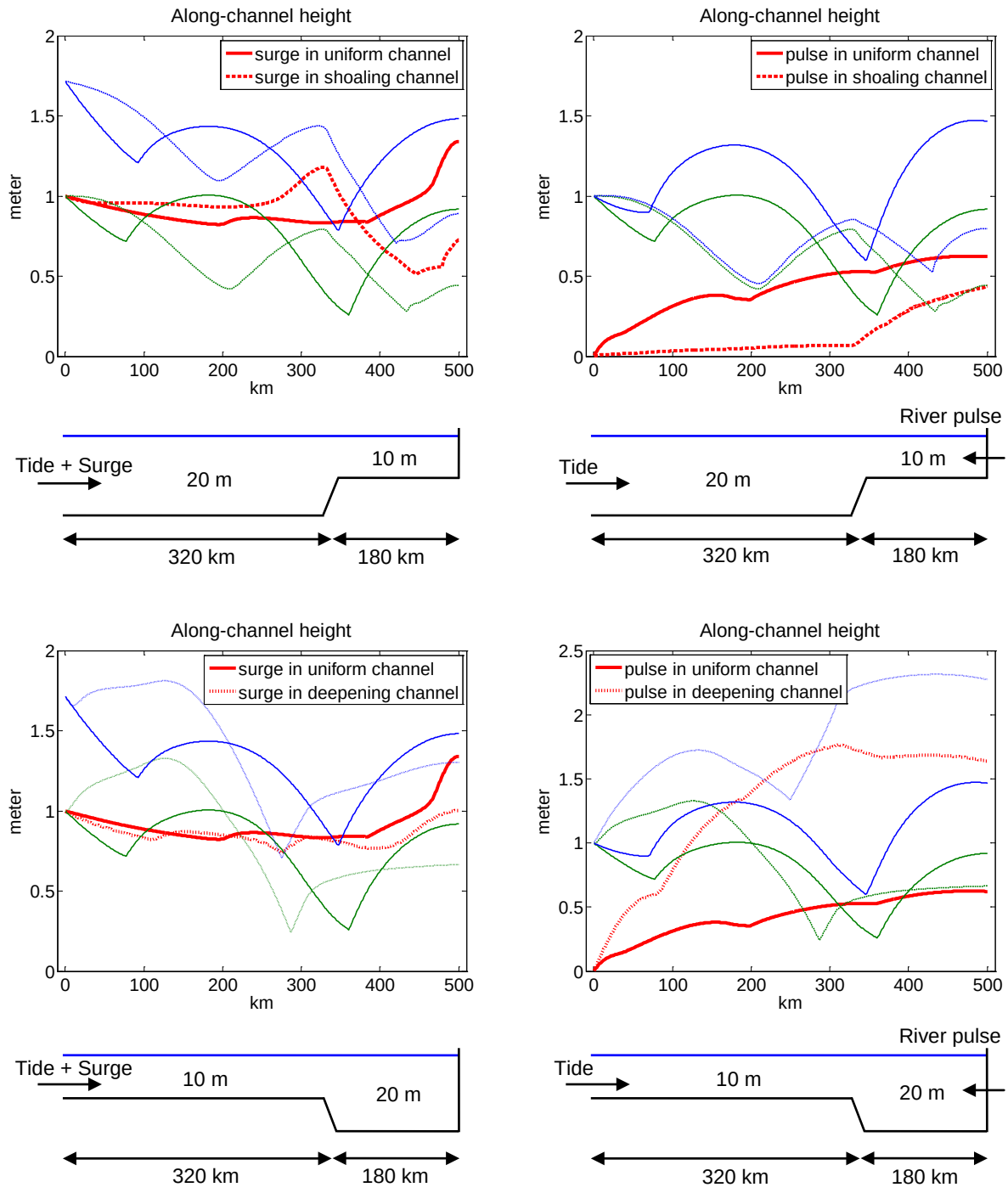

Figure 4.17 Along-channel height and time of total elevation (blue lines), tide (green lines), and residual (red lines) show the effects of abrupt channel shoaling (upper two panels) and deepening (lower two panels) on surge (left) and river pulse (right). The solid lines are from the simulations in the uniform channel. The dashed lines and dotted lines are from the simulations in the abrupt shoaling channel and deepening channel, respectively.

Chapter 5
Summary

5.1 Summary

In a partially-mixed estuary, isohaline slope is generally landward inclined and is smaller during the neap tide than during the spring tide. During the neap tide, the water is more stratified and the obvious halocline is present. Halocline slope and halocline position within the water column during both flood and ebb are shown to be significantly affected by the bottom topographic features in the lower Hudson Estuary based on the analyses of both the observed data and hindcast ROMS simulations. The halocline tends to be significantly displaced in the vertical direction, leading to formation of lee waves over the bottom valleys and hills especially during the maximum ebb and flood. The lee waves are then released when currents decelerate.

Corresponding to the halocline behavior, the movement of the dye patch is also affected by the bottom topography. Generally the dye is significantly moved upward/downward where there is relatively strong upward/downward advection induced by the bottom slope. The dye intruding upward during the ebb is then advected landward at a faster rate, catching up and mixing with the landward bottom dye due to the relatively strong shear in the bottom layer during the flood. As a result, the dye patch as a whole is moved and expanded in both the landward and upward directions. In addition, tracer dispersion is mainly controlled by vertical mixing induced by strong current shear. Strong vertical mixing regions are present not only within the bottom boundary layer during flood but also at the upstream slope of the bottom valleys and hills during ebb and at the current frontal zone during the transition from ebb to flood. The model results also suggest that the sudden release of the internal wave during the transition from ebb to flood leads to enhanced vertical mixing in the vicinity of the halocline.

Analyses of extensive observations from both moored ADCPs and water level gages extending from the lower Hudson to the upper reaches near Troy reveal significant overtides and longitudinal variation in tidal amplitude and phase. In a shallow elongated river, the overtides can be shown, both analytically and numerically to be generated by the M_2 constituent through nonlinear terms in the continuity and momentum equations. The overtides in the upstream Hudson significantly distort the tidal wave, leading to flood dominance condition through the upstream reach. In addition, the tides and overtides are strongly influenced by local topographic variations and the longitudinal position in the river dependent on the ratio of tidal wavelength to channel length. The longitudinal changes in channel geometry tend to produce additional waves combined with the original waves, leading to significant change in tidal amplitude and phase.

In a tidal river, the tidal waves, the surge propagating from the ocean, and the surge induced by the river pulse are all shallow-water waves. The surge and the river pulse can occur independently or simultaneously. The interactions between storm surge and tide could significantly increase the danger of coastal flooding. The longitudinal height of the surge in the tidal channel is sensitive to both the tidal timing and the time span of the surge or river pulse at the boundary. If the boundary surge occurs at slack during flood, the surge peak is the largest through the channel, leading to comparable total water levels relative to the surge occurring at high tide. In addition, the longer duration of the boundary surge leads to the larger magnitude of the surge peak and the maximum total water level through the channel. In addition, the upstream convergence tends to cause sharp increase of both water level and currents in the upstream reach under the condition of river pulse.

5.2 Future work

In order to better estimate the effect of the bottom topographic features on vertical exchange in the water column, passive particle tracer will be introduced into ROMS simulations, providing detailed Lagrangian perspectives. The passive particles will be initiated through the water column in the vicinity of the bottom topographic features at a particular tidal phase. The paths of the particles will be recorded through the tidal period. The potential inter-halocline exchange will be investigated based on the particle movement.

Non-hydrostatic model will be used to investigate the development of internal waves induced by bottom topographic features in a partially-mixed estuary. The comparison between non-hydrostatic model and the ROMS model may provide more insights into internal waves in an estuary.

The wind-induced mixing in the surface layer of the Hudson Estuary will also be considered in the future work. The estimated Richardson Number during flood of neap tide suggests relatively strong mixing in the surface layer in the lower Hudson Estuary. The surface layer mixing needs to be further investigated by introducing the wind forcing into ROMS simulations.

The currents induced by tides, overtides, storm surge and river pulse in a channel with longitudinally varying morphology will be further investigated in a Lagrangian perspective by introducing passive particles into the model, providing more insights into the effects of shallow-water wave propagation on river transport.

Reference

As-Salek, J. A. and T. Yasuda 2001: Tide-surge interaction in the Meghna estuary: Most severe conditions. *Journal of Physical Oceanography*, 31: 3059-3072.

Armi, L. 1986: The hydraulics of two flowing layers with different densities. *Journal of Fluid Mechanics*, 163: 27-58.

Baines, P. G. 1973: The generation of internal tides by flat-bump topography. *Deep Sea Research*, 20: 179-205.

Baines, P. G. 1985: Topographic effects in stratified flows. 489 pp. Cambridge University Press.

Banks, J. E. 1974: A mathematical model of a river-shallow sea system used to investigate tide, surge and their interaction in the Thames-southern North Sea region. *Philosophical Transactions of the Royal Society of London* A, 275: 567-609.

Bernier, N. B. and K. R. Thompson 2007: Tide-surge interaction off the east coast of Canada and northeastern United States. *Journal of Geophysical Research*, 112, C06008, doi:10.1029/2006JC003793.

Blake, E. S., E. N. Rappaport, J. D. Jarrell, and C. W. Landsea 2006: The deadliest, costliest, and most intense United States tropical cyclones from 1851 to 2005 (and other frequently requested hurricane facts), NOAA Tech. Memo., NWS TPC 4, 48 pp., Syst. Dev. Off., Natl. Weather Serv., Silver Spring, Md.

Blumberg, A. F., D. J. Dunning, H. H. Li, D. Heimbuch, and W. R. Geyer 2004: Use of a particle-tracking model for predicting entrainment at power plants on the Hudson River. *Estuaries*, 27(3): 515-526.

Chant, R. J. and R. E. Wilson 2000: Internal hydraulics and mixing in a highly stratified estuary. *Journal of Geophysical Research*, 105: 14215-14222.

Chant, R. J., W. R. Geyer, R. Houghton, E. Hunter, and J. A. Lerczak 2007: Bottom boundary layer mixing processes: insights from Dye Experiments. *Journal of Physical Oceanography*, 37: 1859-1877.

Doodson, A. T. 1956: Tides and storm surges in a long uniform gulf. *Proceedings of the Royal Society* A, 237, 325-343.

Dronkers, J. J., Tidal Computations in Rivers and Coastal Waters, 518 pp., North-Holland, New York, 1964.

Dronkers, J. J. 1986: Tidal asymmetry and estuarine morphology, *Netherlands Journal of Sea Research*, 20: 117-131.

Dyer, K. R. 1997: Estuaries: a physical introduction (2nd edition), 195 pp., John Wiley & Sons Ltd.

Engel, P.A. 2009: Spatial and temporal variability of tide-induced salt flux in a partially mixed estuary. Masters Thesis, Massachusetts institute of Technology, Cambridge, MA, 45 pp.

Farmer, D. M. & Smith, J. D. 1980: Tidal interaction of stratified flow over the sill in Knight Inlet. Deep Sea Research I, 27: 239-254.

Flather, R. A. 1987: Estimates of extreme conditions of tide and surge using a numerical model of the north-west European continental shelf. *Estuarine, Coastal and Shelf Science*, 24: 69-93.

Friedrichs, C. T., and D. G. Aubrey 1988: Non-linear tidal distortion in shallow well-mixed estuaries: A synthesis. *Estuarine, Coastal and Shelf Science*, 27: 521-545.

Friedriches C. T. and D. G. Aubrey 1994: Tidal propagation in strongly convergent channels. *Journal of Geophysical Research*, 99: 3321-3336.

Friedrichs, C.T., 1995. Stability shear stress and equilibrium cross-sectional geometry of sheltered tidal channels. *Journal of Coastal Research*, 11: 1062-1074.

Geyer, R. and H. Nepf 1996: Tidal pumping of salt in a moderately stratified estuary. In Coastal and Estuarine Studies, 53: 213-226.

Geyer, R., R. Chant, and R. Houghton. 2008. Tidal and spring-neap variations in horizontal dispersion in a partially mixed estuary. *Journal of Geophysical Research*, 113 (C07023), doi: 10.1029/2007JC004644.

Gill, A. E., 1982: Atmosphere–Ocean Dynamics. Academic Press, 662 pp.

Haidvogel, D. B., H. G. Arango, K. Hedstrom, A. Beckmann, P. Malanotte-Rizzoli, and A. F. Shchepetkin 2000: Model evaluation experiments in the North Atlantic Basin: Simulations in nonlinear terrain-following coordinates, *Dynamics of Atmospheres and Oceans*, 32: 239-281.

Harris D. L. 1963: Characteristics of the hurricane storm surge. U.S. Dept. of Commerce, Weather Bureau. Technical Paper No. 48. 139 pp.

Heaps, N. S. 1965: Storm surges on a continental shelf. *Philosophical Transactions of the Royal Society of London* A, 257: 351-383.

Hibiya, T. 1986: Generation mechanism of internal waves by tidal flow over a sill. *Journal of Geophysical Research*, 91: 7697-7708.

Hibiya, T. 1988: The generation of internal waves by tidal flow over Stellwagen Bank. *Journal of Geophysical Research*, 93: 533-542.

Hibiya, T. 2004: Internal wave generation by tidal flow over a continental shelf slope. Journal of Oceanography, 60: 637-643

Horsburgh, K. J. and C. Wilson 2007: Tide-surge interaction and its role in the distribution of surge residuals in the North Sea. *Journal of Geophysical Research*, 112, C08003, doi:10.1029/2006JC004033.

Hunt, J. N. 1964: Tidal oscillations in estuaries. *Geophysical Journal Royal Astronomical Society*, 8: 440-455.

Ippen, A. T. and D. R. F Harleman 1966: Tidal dynamics in estuaries, in Estuary and Coastline Hydrodynamics, edited by A. T. Ippen, pp. 493-545, McGraw-Hill Book Company, New York.

Jay, D. A. 1991: Green's law revisited: Tidal long-wave propagation in channels with strong topography. *Journal of Geophysical Research*, 96: 20585-20598.

Jelesnianski, C. P. 1965: A numerical calculation of storm tides induced by a tropical storm impinging on a continental shelf. *Monthly Weather Review*, 93: 343-358.

Johns, B., A. D. Rao, S. K. Dube and P. C. Sinha 1985: Numerical modeling of tide-surge interaction in the Bay of Bengal. *Philosophical Transactions of the Royal Society of London* A, 313: 507-535.

Kang, D. and O. Fringer, 2010: On the calculation of available potential energy in internal wave fields. *Journal of Physical Oceanography*, 40: 2539-2545.

Kranenburg, C., J. D. Pietrzak, and G. Abraham 1991: Trapped internal waves over undular topography. *Journal of Fluid Mechanics*, 226: 205-217.

Lamb, K. G., 2007: Energy and pseudoenergy flux in the internal wave field generated by tidal flow over topography. *Continental Shelf Research*, 27: 1208-1232.

Lanzoni, S. and G. Seminara 1998: On tide propagation in convergent estuaries. *Journal of Geophysical Research*, 103: 30793-30812.

Lawrence, G. A. 1993: The hydraulics of steady two-layer flow over a fixed obstacle. *Journal of Fluid Mechanics*, 254: 605-633.

LeBlond, P. H. 1978: On tidal propagation in shallow rivers. *Journal of Geophysical Research*, 83: 4717-4721.

Lerczak, J. A., W. R. Geyer, and R. J. Chant 2006: Mechanisms driving the time-dependent salt flux in a partially stratified estuary. *Journal of Physical Oceanography*, 36(12): 2296-2311.

Lorenz, E. N., 1955: Available potential energy and the maintenance of the general circulation. *Tellus*, 7: 157-167.

Parker, B. B. 1984: Frictional effects on the tidal dynamics of a shallow estuary. Ph.D. Dissertation, Johns Hopkins University, Baltimore, MD, 292 pp.

Parker, B. B. 2007: Tidal analysis and prediction. NOAA Special Publication NOS CO-OPS 3, 345 pp.

Prandle, D. 1975: Storm surges in the southern North Sea and River Thames. *Proceedings of the Royal Society* A, 344: 509-539.

Prandle, D. 2003: Relationships between tidal dynamics and bathymetry in strongly convergent estuaries. *Journal of Physical Oceanography*, 33(12): 2738-2750.

Proudman, J. 1955: The propagation of tide and surge in an estuary. *Proceedings of the Royal Society* A, 231: 8-24.

Redfield, A. 1950: The analysis of tidal phenomena in narrow embayments, Papers in Physical Oceanography and Meteorology, 11(4), [page], Massachusetts Inst. Of Tech. and Woods Valley.

Redfield, A. C. 1978: The tide in coastal waters. *Journal of Marine Research*, 36: 255-294.

Rego, J. L. and C. Li 2010: Nonlinear terms in storm surge predictions: Effect of tide and shelf geometry with case study from Hurricane Rita. *Journal of Geophysical Research*, 115, C06020, doi:10.1029/2009JC005285.

Rossiter, J. R. 1961: Interaction between tide and surge in the Thames. *Geophysical Journal of the Royal Astronomical Society*, 6: 29-53.

Shchepetkin, A. F., and J. C. McWilliams 2005: The Regional Ocean Modeling System: A split-explicit, free-surface, topography following coordinates ocean model. *Ocean Modelling*, 9: 347-404.

Simpson, J. H., J. Brown, J. Matthews, and G. Allen 1990: Tidal Straining, Density Currents, and Stirring in the Control of Estuarine Stratification. *Estuaries*, 13(2):125-132.

Speer, P. E., and D. G. Aubrey 1985: A study of non-linear tidal propagation in shallow inlet/estuarine systems, II: Theory. *Estuarine, Coastal and Shelf Science*, 21: 207-224.

Stacey, Mark T., and David K. Ralston. 2005. The scaling and structure of the estuarine bottom boundary layer. *Journal of Physical Oceanography* 35 (1):55-71.

Stommel, H. M. and H. G. Farmer 1953: Abrupt change in width in two-layer open channel flow. *Journal of Marine Research*, 11:205-214.

Tang, Y. M., R. Grimshaw, B. Sanderson and G. Holland 1996: A numerical study of storm surges and tides, with application to the North Queensland coast. *Journal of Physical Oceanography*, 26: 2700-2711.

Uncles, R. J. 1981: A note on tidal asymmetry in the Severn estuary. *Estuarine, Coastal and Shelf Science*, 13: 419-432.

Wang, D-P. 2006: Tidally generated internal waves in partially mixed estuaries. *Continental Shelf Research*, 26: 1469–1480.

Warner, J. C., C. R. Sherwood, H. G. Arango, and R. P. Signell 2005: Performance of four turbulence closure models implemented using a generic length scale method, *Ocean Modeling*, 8: 81-113.

Warner, J. C., W. R. Geyer, and J. A. Lerczak 2005: Numerical modeling of an estuary: A comprehensive skill assessment. *Journal of Geophysical Research*, 110, C05001, doi:10.1029/2004JC002691.

Winters, K. B., P. N. Lombard, J. J. Riley, and E. A. D'Asaro, 1995: Available potential energy and mixing in stratified fluids. *Journal of Fluid Mechanics*, 289: 115–128.

Wolf, J. 1978: Interaction of tide and surge in a semi-infinite uniform channel, with application to surge propagation down the east coast of Britain. Applied Mathematical Modelling, 2: 245-253.

Zhang, W.-Z. F. Shi, H.-S. Hong, S.-P. Shang, and J. T. Kirby 2010: Tide-surge interaction intensified by the Taiwan Strait. *Journal of Geophysical Research*, 115, C06012, doi:10.1029/2009JC005762.